

**BEAM NORMAL SINGLE SPIN ASYMMETRY IN FORWARD ANGLE  
INELASTIC ELECTRON-PROTON SCATTERING USING THE Q-WEAK  
APPARATUS**

A Dissertation

By

NURUZZAMAN

Submitted to the Graduate College of Hampton University in  
partial fulfillment of the requirements for the degree of

**DOCTOR OF PHILOSOPHY**

December 2014

This dissertation submitted by Nuruzzaman in  
partial fulfillment of the requirements for the degree of Doctor of Philosophy at  
Hampton University, Hampton, Virginia is hereby approved by the committee  
under whom the work has been completed.

---

Liguang Tang, Ph.D.  
Committee Chair

---

David J. Mack, Ph.D.

---

Eric Christy, Ph.D.

---

Alberto Accardi, Ph.D.

---

Patrena N. Benton, Ph.D.  
Dean, The Graduate College

---

Date

Copyright by  
NURUZZAMAN  
2014

## ABSTRACT

Beam Normal Single Spin Asymmetry in Forward Angle Inelastic Electron-Proton Scattering

Using the Q-weak Apparatus. (December 2014)

Nuruzzaman, B. Sc., University of Kalyani;

M. Sc., Indian Institute of Technology Roorkee;

M. S., Mississippi State University

Chair of Advisory Committee: Liguang Tang

The Q-weak experiment in Hall-C at the Thomas Jefferson National Accelerator Facility has made the first direct measurement of the weak charge of the proton through the precision measurement of the parity-violating asymmetry in elastic electron-proton scattering at low momentum transfer. The electron-proton scattering rate largely depends on the five beam parameters: horizontal position, horizontal angle, vertical position, vertical angle, and energy. Changes in these beam parameters when the beam polarization is reversed create false asymmetries. Although attempt has been made to keep changes in beam parameters during reversal as small as possible, it is necessary to correct for such false asymmetries. To make this correction precisely, a beam modulation system was implemented to induce small position, angle, and energy changes at the target to characterize detector response to the beam jitter. Two air-core dipoles separated by  $\sim 10$  m are pulsed at a time to produce position and angle changes at the target, for virtually any tune of the beamline. The beam energy was modulated using an SRF cavity. The hardware, associated control instrumentation will be described in this dissertation. Preliminary detector sensitivities were extracted which helped to reduce the width of the measured asymmetry. The beam modulation system also has proven valuable for tracking changes in the optics, such as dispersion at the target and beam position coupling.

There is a parity conserving Beam Normal Single Spin Asymmetry or transverse asymmetry ( $B_n$ ) on  $H_2$  with a  $\sin(\phi)$ -like dependence due to two-photon exchange. The size of  $B_n$  is few ppm, so a few percent residual transverse polarization in the beam, in addition to potentially small broken azimuthal symmetries in the detector, might lead to few ppb corrections to the Q-weak data. As part of a program of  $B_n$  background studies, we made the first measurement of  $B_n$  in the N-to-Delta transition using the Q-weak apparatus.  $B_n$  from electron-nucleon scattering is also a unique tool to study the  $\gamma^*\Delta\Delta$  form factors. This dissertation presents the analysis of the first measurement

of the beam normal single spin asymmetry in inelastic electron-proton scattering at a  $Q^2$  of 0.0209 (GeV/c)<sup>2</sup>. This measurement will help to improve the theoretical models on beam normal single spin asymmetry and thereby our understanding of the doubly virtual Compton scattering process.

Dedicated to my parents Md. Shamsuzzoha, Nurun Nahar, my sister Arjun Nahar, my friend Shampa Samanta, my mentors Dave Mack, Liguang Tang, Dipangkar Dutta, Probodh Mondal, Biswanath Mondal, Malay Dutta and Subrto Kundu.

## ACKNOWLEDGEMENTS

This experiment was sponsored by the Department of Energy Office of Science (DOE), National Science Foundation (NSF), NSERC and the State of Virginia. I am very grateful for the support I received and the opportunities that were available during this time. I am indebted to seemingly countless people for what I have accomplished and, first of all, I would like to say thank you to all of these people.

My supervisor, Liguang Tang, provided me with many opportunities and I am very grateful for his support through the entire process. When I first joined Hampton University (HU) graduate program, Dr. Tang welcomed me to his research group and explained all the opportunities I can have. He provided many interesting projects to work on, including the weak charge measurement of proton at Jefferson Lab. He encouraged me to attend several conferences during my time at HU, including those in APS Atlanta, California and Washington conferences. I feel very proud and fortunate to work with my Jefferson Lab supervisor Dave Mack. It was delight working with him. He helped to understand the lab environment and equipment in many ways. We used to discuss different topics of experimental nuclear physics field regularly, which helped me to built my knowledge about the field. He always encouraged me to think about great ideas. His deep knowledge and understanding of the field also helped me to solve problems very quickly. I can not thank enough to Dr. Dipangkar Dutta for his encouragement and help in my professional and personal life. My research career started at Mississippi State University with Dr. Dutta. He introduced me to the Jefferson Lab and allowed me to work in different projects with him as my advisor, including the nuclear transparency of kaons and weak charge measurement of the proton at Jefferson Lab.

I am grateful to all of the friends and colleagues I have come to know at MSU, HU and at JLab. During the three years stay at MSU I had a wonderful experience with our medium energy physics group. Dr. James Dune along with Dr. Dipangkar Dutta helped me a lot. My colleges at MSU, Amrendra Narayan, Luwani Ndukum, Adesh Subedi, Jed Leggett and Azmi al Masalha were also stretched their helping hand all the time. My special thanks to Amrendra and Shloka Chandavar for their enormous help and support. They were with me always in my ups and downs. Our graduate coordinator of the physics department was nicest person I can think of. He was there with me always whenever I needed any help. I can't thank enough to my closest friends in the department Saurabh Dayal, Nimisha Srivastava, Markandey Tripathi, Peeyush Sahay, Hazem Abusura, Chandrasiri Ihalawela and Ruiyuan Mu for their support throughout.

During the three years stay at HU I had a wonderful experience with our nuclear physics group. Michael Kohl, Cynthia Keppel along with Dr. Liguang Tang helped me a lot. I would like to thank Monique Howard, Ebony Majeed, and Rashinda Davis for their help in administration . My colleges in the group Chunhua Chen, Anusha Liguang, Asgur Ates, Debaditya Biswas were with me all the time.

I spent maximum time of my Ph.D career at Jefferson Lab. So many people were involved in my work and helped me throughout at Jefferson Lab. My experience with Paul King in the software work was great. He was brilliant and kind to help me whenever I needed him. Buddhini Waidyawansa and Rakitha Beminiwattha were very nice and helpful throughout the experiment. Wouter Deconinck and Jeong Han Lee was always with me with their helping hand. Their hard work and dedication also inspired us.

A special thanks goes to my roommate Jonathan Miller who was been with me through my MS thesis. There aren't words to describe the importance of our friendship. John has been there with me in the best and worst of times.

I would like to thank the members of the  $Q_{weak}^p$  collaboration whose tireless efforts made the experiment a success. This includes the spokespeople; Roger Carlini, Stanley Kowalsk and Shelley Page, and the other outstanding physicists involved in the core collaboration. I thank Dave Mack for his successful leadership of the testing, installation, commissioning and operation throughout. I wish to thank the entire Hall-C scientific and technical staff for their operational support of these experiments. I thank Steve Wood for his expertise with the Hall-C data acquisition system. I would like to thank Brad Sawatzky for his kind help to build several new online softwares. I wish to recognize the efforts of the target group, and particularly Greg Smith, Silviu Covrig and Dave Meekins, for ensuring the successful operation of one of the most complex target used in Jefferson Lab. I want to thank Dave Gaskell for his outstanding contributions as a coordinator for running the experiment smoothly, including performing the Møller and arc energy measurements. I thank all the scientists and students who took shifts on the experiment so that it could run continuously.

I also wish to thank the accelerator staff and operators for their tireless and outstanding work delivering the high-energy, high-intensity, high-polarization, 100% duty-factor, stable CW electron beam to Hall-C. I want to thank accelerator operators I worked with, specially Sarin Philip for his great help during the hardware assemble and testing. I want to thank Scott Higgins for his great work in the control system for beam modulation system. Special thanks to Mike Tiefenback for his brilliant ideas and Jay Benesch for his helping hand in my initial days at Jefferson Lab. Pitt

Fransis, Simon Wood and Lee Broeker were very helpful in hardware installation and their valuable thoughts.

Also, I want to thank my committee members who read and provided useful feedback on this thesis: Liguang Tang, Michael Kohl, Eric Christy and Dave Mack.

## TABLE OF CONTENTS

Section	Page
<b>1 INTRODUCTION</b>	<b>1</b>
1.1 The Standard Model and the Electroweak Interaction	1
1.2 The Q-weak Experiment	3
1.3 Inelastic Parity Violating Asymmetry	6
1.3.1 The $\Delta$ Resonance	7
1.3.2 Formalism and Measurement	8
1.4 The Beam Normal Single Spin Asymmetry	8
1.5 Inelastic Beam Normal Single Spin Asymmetry	9
1.6 Thesis Outline	9
<b>2 THEORY</b>	<b>10</b>
2.1 Electron Scattering Beyond the Born Approximation	10
2.1.1 2-photon Exchange	11
2.2 Experimental Observation of Beam Spin Asymmetry	12
2.2.1 Measurement of the Beam Normal Single Spin Asymmetry	13
2.2.2 Imaginary Part of Two-photon Diagram	15
2.3 The $\gamma^*\Delta\Delta$ Form Factors	15
2.4 Model Calculations	16
2.5 Goals of the Inelastic Transverse Physics Program	17
<b>3 EXPERIMENTAL SETUP</b>	<b>19</b>
3.1 Q-weak Kinematics	19
3.2 Experimental Techniques	20
3.3 TJNAF Overview	22
3.3.1 Polarized Source and Helicity Reversal	23
3.4 Accelerator	24
3.5 Beamlne	25
3.6 Beam Monitoring	25
3.6.1 Beam Position Monitor	26

Section	Page
3.6.2 Superharp . . . . .	27
3.6.3 Beam Current Monitor . . . . .	27
3.6.4 Beam Energy . . . . .	28
3.6.4.1 Absolute Beam Energy . . . . .	28
3.6.4.2 Energy Asymmetry . . . . .	28
3.6.5 Beam Modulation . . . . .	29
3.6.6 Halo Monitors . . . . .	29
3.6.7 Fast Feed Back . . . . .	30
3.7 Polarimetry . . . . .	30
3.7.1 Møller Polarimetry . . . . .	30
3.7.2 Compton Polarimetry . . . . .	31
3.8 Targets . . . . .	32
3.8.1 Liquid Hydrogen Target . . . . .	32
3.8.1.1 Raster . . . . .	34
3.8.2 Solid Target . . . . .	35
3.9 Collimators and Shielding . . . . .	36
3.10 Q-weak Toroidal Magnetic Spectrometer: QTor . . . . .	36
3.10.1 Hall Probe . . . . .	37
3.11 Detector System . . . . .	38
3.11.1 Main Čerenkov Detectors . . . . .	38
3.11.1.1 Low Noise Electronics . . . . .	40
3.11.1.2 Focal Plane Scanner . . . . .	40
3.11.2 Luminosity Monitors . . . . .	40
3.12 Tracking Detector System . . . . .	41
3.13 Data Acquisition . . . . .	42
3.14 Online Displays and Data Monitoring . . . . .	42
3.15 Parity Analysis . . . . .	43
<b>4 BEAM MODULATION . . . . .</b>	<b>45</b>
4.1 Introduction . . . . .	45
4.2 Measurement Time vs Modulation Asymmetry . . . . .	45

Section	Page
4.3 Modulation Amplitude . . . . .	47
4.4 Optics Calculation . . . . .	49
4.4.1 Simulation using OptiM . . . . .	49
4.4.2 Inverse Beamline . . . . .	49
4.4.3 Forward Beamline with Position or Angle Kicks . . . . .	50
4.4.4 Forward Rays with Energy Kick . . . . .	52
4.5 Beam Modulation Hardware . . . . .	54
4.5.1 Air-Core Coils . . . . .	55
4.5.2 IOC . . . . .	56
4.5.3 VME 4145 Signal Generator . . . . .	56
4.5.4 Relay Board . . . . .	57
4.5.5 Trim Power Amplifier . . . . .	57
4.5.6 LEM Current Transducer . . . . .	58
4.5.7 Energy Modulation Hardware . . . . .	59
4.5.8 ADCs . . . . .	59
4.6 Hardware Components Calibration and Important Constraints . . . . .	60
4.6.1 Coil Positioning . . . . .	61
4.6.2 Waveform . . . . .	62
4.6.3 Waveform Phase . . . . .	62
4.6.4 Frequency Range . . . . .	62
4.6.5 Maximum Current . . . . .	63
4.6.6 Magnetic Field Calibration of the MAT Coils . . . . .	63
4.7 Controls and Software Sketch . . . . .	64
4.8 Modulation Modes . . . . .	66
4.9 Machine Protection Analysis . . . . .	66
4.10 Beam Modulation Cycle . . . . .	68
4.11 Response to Modulation Signal and Applications . . . . .	69
4.12 Extension to Other JLab Parity Violation Experiments . . . . .	71
4.13 Summary . . . . .	72

Section	Page
<b>5 BEAMLINE OPTICS AND FALSE ASYMMETRIES . . . . .</b>	<b>73</b>
5.1 Detector Sensitivities . . . . .	73
5.2 Beamline Optics . . . . .	75
5.2.1 Beam Modulation Tune Parameter Scan . . . . .	77
5.2.2 Effect of Fast Feed Back on Beam Modulation . . . . .	78
5.2.3 BPM Sign Corrections . . . . .	80
5.3 BPM Resolution . . . . .	80
5.3.1 Position Resolution . . . . .	81
5.3.2 Target BPM Angle Resolution . . . . .	84
5.3.3 Consistency Check of Target Variable . . . . .	85
5.4 Helicity Correlated Pedestal Analysis . . . . .	86
5.4.1 Motivation . . . . .	86
5.4.2 Analysis Procedure and Goal . . . . .	86
5.4.3 Experimental Method . . . . .	87
5.4.4 Results . . . . .	87
5.4.4.1 Helicity Correlated Pedestal Signal Pickup . . . . .	88
5.4.4.2 Helicity Correlated Pedestal Sensitivities . . . . .	89
5.4.4.3 Stability of Pedestal Subtracted Signal . . . . .	91
5.4.4.4 Detector Resolution . . . . .	92
5.4.5 Summary of Helicity Correlated Pedestal Survey . . . . .	93
<b>6 BEAM NORMAL SINGLE SPIN ASYMMETRY . . . . .</b>	<b>94</b>
6.1 Introduction . . . . .	94
6.2 Experimental Method . . . . .	94
6.2.1 Available Data Set and Condition of Experimental Data Taking . . . . .	94
6.3 Extraction of Raw Asymmetries . . . . .	95
6.4 Asymmetry Correction using Linear Regression . . . . .	96
6.4.1 Azimuthal Acceptance Correction . . . . .	99
6.5 Corrections and Systematic Uncertainties . . . . .	103
6.5.1 Regression Scheme Dependence . . . . .	103
6.5.2 Regression Time Dependence . . . . .	104

Section	Page
6.5.3 Nonlinearity . . . . .	106
6.5.4 Cut Dependence . . . . .	106
6.5.5 Fit Scheme Dependence . . . . .	107
6.5.6 Summary of Systematic Uncertainties . . . . .	107
6.6 Extraction of Physics Asymmetry . . . . .	108
6.6.1 Beam Polarization . . . . .	110
6.6.2 Background Corrections . . . . .	110
6.6.2.1 Target Aluminum Windows . . . . .	110
6.6.2.2 Beamline Scattering . . . . .	112
6.6.2.3 Other Neutral Background . . . . .	113
6.6.2.4 Elastic Radiative Tail . . . . .	114
6.6.3 Other Corrections . . . . .	116
6.6.3.1 Radiative Correction . . . . .	116
6.6.3.2 Detector Bias Correction . . . . .	117
6.6.3.3 $Q^2$ Precision . . . . .	117
6.6.4 Beam Normal Single Spin Asymmetry . . . . .	118
6.7 Comparison With Model Calculation . . . . .	120
6.8 BNSSA in Nuclear Targets . . . . .	121
6.9 Conclusion . . . . .	121
<b>7 DISCUSSION AND CONCLUSIONS . . . . .</b>	<b>123</b>
7.1 Summary of Results . . . . .	123
7.2 Contribution Towards Q-weak Experiment . . . . .	123
7.2.1 Beam Modulation . . . . .	123
7.2.2 Beamline Work . . . . .	124
7.2.3 Beam Normal Single Spin Asymmetry in Inelastic e+p Scattering . . . . .	125

## APPENDICES

<b>A BEAM MODULATION . . . . .</b>	<b>127</b>
A.1 Beam Modulation . . . . .	127
A.1.1 Introduction . . . . .	127

Section	Page
A.1.2 Measurement Time vs Modulation Asymmetry . . . . .	127
A.1.3 Modulation Amplitude . . . . .	129
A.2 Optics Calculation . . . . .	130
A.2.1 Inverse Beamline . . . . .	130
A.2.2 Forward Rays with Position or Angle Kicks . . . . .	131
A.2.3 Forward Rays with Energy Kick . . . . .	131
A.3 Beam Modulation Hardware . . . . .	132
A.3.1 Air-Core Coils . . . . .	132
A.3.2 Coil Siting . . . . .	133
A.3.3 Energy Modulation Hardware . . . . .	133
A.4 Bench Tests . . . . .	134
A.5 Waveform . . . . .	134
A.5.1 Waveform . . . . .	134
A.5.2 Frequency Range . . . . .	134
A.5.3 Maximum Current . . . . .	135
A.6 OBSERVATIONS . . . . .	135
A.7 EXTENSION TO OTHER JLAB PARITY VIOLATION EXPERIMENTS . . . . .	136
A.8 SUMMARY . . . . .	136
A.8.0.1 Details1 . . . . .	137
A.9 Simulation . . . . .	138
A.9.1 OPTIM . . . . .	138
<b>B QTOR . . . . .</b>	<b>140</b>
B.1 QTOR . . . . .	140
B.2 Hall Probe . . . . .	140
B.3 QTOR Corrector Magnet . . . . .	141
B.4 QTOR Corrector Magnet Design . . . . .	142
B.4.1 TOSCA . . . . .	142
<b>C HELICITY CORRELATED PEDESTAL ANALYSIS . . . . .</b>	<b>147</b>
C.1 Background Detectors . . . . .	147
C.2 Helicity Corelated Pedestal Analysis . . . . .	148

Section	Page
C.2.1 Condition of Experimental Data Taking . . . . .	148
C.2.2 Condition of This Analysis . . . . .	149
C.2.3 Configuration . . . . .	150
C.2.4 List of Variables . . . . .	151
C.2.4.1 Main Cerenkov Detector(17) . . . . .	151
C.2.4.2 Downstream Luminosity Detector(9) . . . . .	151
C.2.4.3 Uptream Luminosity Detector(9) . . . . .	151
C.2.4.4 Beam Current Monitor(9) . . . . .	152
C.2.5 List of Runs . . . . .	152
C.2.5.1 Wien 0 . . . . .	152
C.2.5.2 Wien 1 . . . . .	152
C.2.5.3 Wien 2 . . . . .	152
C.2.5.4 Wien 3 . . . . .	152
C.2.5.5 Wien 4 . . . . .	152
C.2.5.6 Wien 5 . . . . .	153
C.2.5.7 Wien 6 . . . . .	153
C.2.5.8 Wien 7 . . . . .	153
C.2.5.9 Wien 8 . . . . .	153
C.2.5.10 Wien 9 . . . . .	153
C.2.5.11 Wien 10 . . . . .	154
<b>D Beam Normal Single Spin Asymmetry in Inelastic e-p Scattering . . . . .</b>	<b>155</b>
D.1 Condition of Experimental Data Taking . . . . .	155
D.2 Uncertainty in Physics Asymmetries . . . . .	156
D.3 Corrections . . . . .	157
D.4 Barsum vs PMTavg Asymmetries . . . . .	157
D.5 Detector Sensitivities . . . . .	161
D.6 Regression Scheme Dependence . . . . .	161
D.6.1 Regression Time Dependence . . . . .	161
D.6.2 Cut Dependence . . . . .	161

Section	Page
<b>E Miscellaneous . . . . .</b>	<b>165</b>
E.1 Target BPM Angle Resolution . . . . .	165
<b>BIBLIOGRAPHY . . . . .</b>	<b>166</b>
<b>REFERENCES . . . . .</b>	<b>166</b>
<b>VITA . . . . .</b>	<b>186</b>

## LIST OF FIGURES

Figure	Page
1.1 The Standard Model of elementary particles. . . . .	2
1.2 The Feynman diagrams for the parity conserving and parity violating semileptonic electroweak interactions. . . . .	3
1.3 Q-weak will be most precise (relative and absolute) PVES result to date. . . . .	6
1.4 The Feynman diagrams for the parity violating inelastic electron-proton scattering. . . . .	7
2.1 Electron-proton $\rightarrow$ electron- $\Delta$ in $\Delta$ region. . . . .	10
2.2 Transverse Feynman Diagram. . . . .	11
2.3 Ratio $\mu_p G_E/G_M$ extracted from the polarization transfer and LT measurements. . . . .	12
2.4 The schematic of transverse electron-nucleon scattering reaction. . . . .	14
2.5 The two-photon exchange diagram. The filled blob represents the response of the nucleon to the scattering of the virtual photon. . . . .	14
2.6 Inelastic transverse asymmetry model from Pasquini et al. . . . .	16
2.7 Beam normal single spin asymmetry with decay of $\Delta$ in the final state for one-photon exchange. . . . .	17
3.1 Sketch of the elastic electron-proton scattering process. . . . .	20
3.2 Jefferson Lab and its beamline schematic. . . . .	22
3.3 Schematic showing the process of producing circularly polarized light. . . . .	23
3.4 Beam position and current monitors. . . . .	25
3.5 Layout of the Hall C Møller polarimeter. . . . .	31
3.6 Schematic of the Hall C Compton polarimeter. . . . .	32
3.7 Q-weak target system. . . . .	33
3.8 Raster studies. . . . .	34
3.9 Schematic diagram of the Q-weak apparatus. . . . .	35
3.10 Q-weak torodial magnetic spectrometer (QTor). . . . .	37
3.11 QTor controls and hall probe. . . . .	38

Figure	Page
3.12 Q-weak main Čerenkov detector system. . . . .	39
3.13 Schematic of a TRIUMF made ADC and current mode signal chain. . . . .	39
3.14 Luminosity monitors. . . . .	41
4.1 Simple schematic cartoon of the accelerator. . . . .	46
4.2 Jefferson Lab and its beamline schematic for all three experimental halls. . . . .	48
4.3 Inverse orbit excursions simulation from OptiM. . . . .	50
4.4 A sketch of beam modulation concept. . . . .	51
4.5 Forward orbit excursions simulation from OptiM. . . . .	52
4.6 Forward orbit excursions simulation for energy modulation from OptiM. . . . .	54
4.7 Beam modulation hardware sketch. . . . .	55
4.8 LEM current transducer output response to input sine drive signal. . . . .	58
4.9 The effect of Fast Feed Back (FFB) system on energy modulation. . . . .	60
4.10 Beam modulation hardware bench test setup. . . . .	61
4.11 Zoomed ramp and drive signal from a beam modulation cycle during a typical production run. . . . .	63
4.12 Field map of MAT coil for different input coil currents. . . . .	64
4.13 Orbit excursions using a pair of coils with incorrect polarity on one of the coil. . . . .	67
4.14 Orbit excursions with only one coil energized. . . . .	68
4.15 Beam modulation cycle during a typical production run. . . . .	69
4.16 Main detector response to $X$ position modulation. . . . .	70
4.17 Target BPM response to $X$ position modulation. . . . .	71
5.1 Main detector sensitivities with respect to target BPM X position for X Position Modulation. . . . .	74
5.2 Main detector sensitivities for $X$ , $X'$ , $E$ , $Y$ , and $Y'$ . . . . .	75
5.3 Corrected asymmetry using BMod and natural motion grouped by Wien. . . . .	76
5.4 Beam position response of all the BPMs in the Hall-C beamline to X modulation. . . . .	77
5.5 Beam position response of all the BPMs in the Hall-C beamline to X modulation.. . . . .	78
5.6 Beam position response of all the BPMs in the Hall-C beamline to X modulation. . . . .	79
5.7 Hall-C target BPM responses due to modulation kick using a pair of coil in X. . . . .	80

Figure	Page
5.8 Beam position response of all the BPMs in the Hall-C beamline to X modulation. . . . .	81
5.9 Beam position response of all the BPMs in the Hall-C beamline to X modulation. . . . .	82
5.10 BPM position resolution. . . . .	83
5.11 BPM resolution cartoon. . . . .	83
5.12 Target BPM angle resolution at beam current of 180 $\mu$ A. . . . .	84
5.13 A typical beam off pedestal run distributions from Hel_Tree and Mps_Tree. . . . .	88
5.14 The mean of the pedestal differences from Hel_Tree. . . . .	89
5.15 Sigma distribution of helicity correlated pedestal differences. . . . .	90
5.16 The width of the pedestal differences from Hel_Tree. . . . .	90
5.17 The mean of pedestal subtracted signal from Mps_Tree. . . . .	91
5.18 The width of pedestal subtracted signal from Mps_Tree. . . . .	92
6.1 Simulated missing mass, W, distribution at the inelastic QTor setting. . . . .	94
6.2 Azimuthal dependence of the main detector sensitivities to HCBA in the vertical LH <sub>2</sub> transverse data set. . . . .	97
6.3 Beam parameter differences for the Hydrogen transverse data set. . . . .	98
6.4 Main detector corrections vs octant for vertical transverse data set. . . . .	100
6.5 Total corrections vs octant for vertical transverse data set. . . . .	100
6.6 Main detector corrections for horizontal and vertical LH <sub>2</sub> transverse data sets are shown here. . . . .	101
6.7 Main detector asymmetry for horizontal, vertical transverse data set. . . . .	102
6.8 Regressed main detector asymmetry for horizontal, vertical transverse data set on LH <sub>2</sub> . .	103
6.9 Charge sensitivity for horizontal and vertical transverse polarization data set. . . . .	105
6.10 Cut dependence study. . . . .	106
6.11 Summary of uncertainties on measured asymmetry for horizontal and vertical data set.	109
6.12 Azimuthal dependence of asymmetry from the 4% downstream aluminum target. . . . .	111
6.13 Regressed (5+1) USLumi asymmetries from longitudinal running. . . . .	112
6.14 Simulation of contributions from elastic and inelastic e+p and elastic Al from upstream and downstream target windows. . . . .	114
6.15 The residual of yield using Data and simulation from GEANT 3. . . . .	115

Figure	Page
6.16 The variation of beam normal single spin asymmetry with elastic dilution. . . . .	116
6.17 The $Q^2$ from GEANT 3 simulation. . . . .	117
6.18 Summary of uncertainties in inelastic beam normal single spin asymmetry extraction. .	119
6.19 BNSSA asymmetry calculation from Pasquini et al. . . . .	120
6.20 BNSSA asymmetry calculation from Pasquini et al. and its extension. . . . .	121
A.1 Beam modulation hardware sketch. . . . .	132
A.2 Beam modulation sketch. . . . .	133
A.3 The caption. . . . .	139
B.1 QTOR hall probe locations. . . . .	141
B.2 QTOR corrector magnet design. . . . .	142
B.3 QTOR qtor allenergy 0Gcm. . . . .	144
B.4 QTor all energy 4000Gcm dump. . . . .	145
B.5 QTor corrector field integral. . . . .	145
B.6 QTOR qtor corrector field integral variation. . . . .	146
C.1 Mean of the helicity correlated differences for important background detectors. . . . .	147
C.2 Mean of the helicity correlated differences for other background detectors. . . . .	148
C.3 Width of the helicity correlated differences for important background detectors. . . . .	149
C.4 Width of the helicity correlated differences for other background detectors. . . . .	150
D.1 Main detector sensitivities with respect to 5+1 regression scheme for horizontal transverse data set. . . . .	158
D.2 Main detector correction vs octant using to 5+1 regression scheme and differences for horizontal transverse data set. . . . .	159
D.3 Total correction vs octant using to 5+1 regression scheme and differences for horizontal transverse data set. . . . .	159
D.4 Beam position differences for horizontal transverse data set. . . . .	160
D.5 Beam position differences for vertical transverse data set. . . . .	160
D.6 Cut dependence for horizontal transverse. . . . .	163
D.7 Cut dependence for vertical transverse. . . . .	163
D.8 Cut dependence cartoon. . . . .	164

## LIST OF TABLES

Table	Page
1.1 The electric and weak charges of elementary particles in the Standard Model. . . . .	3
1.2 Nucleons and $\Delta$ resonances and their associated properties. . . . .	7
3.1 Proposed error budget of the Q-weak experiment. . . . .	19
3.2 Basic parameters and typical operating conditions of the Q-weak experiment. . . . .	21
3.3 Definition of different variables used in the experiment. . . . .	44
4.1 Dead time calculation for beam modulation. . . . .	47
4.2 A crude estimate of the modulation amplitudes to generate 10 ppm whole detector asymmetries. . . . .	48
4.3 Required field integrals for the modulation dipole pair from OptiM. . . . .	52
4.4 Basic properties of the air core MAT coils used for the beam modulation system. . . .	56
4.5 Different beam modulation modes and related pattern numbers. . . . .	66
5.1 Typical amplitudes used for driven beam modulation. BPM differences and sensitivities during Run 2. . . . .	74
5.2 BPM position resolution. . . . .	84
5.3 Summary of helicity correlated pedestal survey. . . . .	93
6.1 Run numbers for transverse N-to- $\Delta$ data set. . . . .	95
6.2 Beam parameter differences for the Hydrogen horizontal and vertical transverse data sets. . . . .	99
6.3 Asymmetries from different regression schemes for horizontal and vertical transverse data set. . . . .	104
6.4 Fit scheme dependence of the measured asymmetry. . . . .	108
6.5 Summary of uncertainties on measured asymmetry for combined horizontal and vertical data sets. . . . .	108
6.6 Beam polarization using Møller polarimeter for Run 2 transverse data set. . . . .	110
6.7 Measured asymmetry on aluminum target. . . . .	112
6.8 Summary of input quantities to extract the BNSSA. . . . .	119

Table	Page
6.9 Measured regressed (5+1) asymmetries in inelastic electron-nucleon scattering for transverse polarized beam. . . . .	122
A.1 Dead time calculation for beam modulation. . . . .	128
A.2 A crude estimate of the modulation amplitudes to generate 10 ppm whole detector asymmetries. . . . .	129
A.3 Beam modulation bench test. . . . .	134
D.1 Systematic error table. . . . .	157
D.2 Barsum and PMTavg asymmetries. . . . .	157
D.3 MD Sensitivities for X and Y. . . . .	158
D.4 MD Sensitivities for X' and Y'. . . . .	161
D.5 MD Sensitivities for E and A <sup>Q</sup> . . . . .	161
D.6 Regression scheme dependence for vertical transverse polarization. . . . .	161
D.7 Regression scheme dependence for horizontal transverse polarization. . . . .	162
D.8 Regression scheme dependence corrections. . . . .	162
D.9 Regression time dependence. . . . .	162
D.10 Cut dependence. . . . .	162

## SECTION 1

### INTRODUCTION

The Q-weak experiment at the Thomas Jefferson National Accelerator Facility, USA, (TJNAF or JLab) is aimed to measure the weak charge of the proton by measuring parity-violating asymmetry of elastic electron-proton scattering at low four-momentum-transfer squared ( $Q^2$ ). The weak charge of the proton in the Standard Model (SM) is suppressed and any observed deviations from the SM predictions found in this high precision measurement will suggest signatures of new physics.

#### 1.1 The Standard Model and the Electroweak Interaction

The development of the SM in the twentieth century is one of the greatest achievements of the particle physics which is a theory concerning the electromagnetic, weak, and strong nuclear interactions [1]. The SM states that the fundamental particles that make up all matter are quarks and leptons, and that they interact through the strong, weak, and electromagnetic fundamental interactions by exchanging force carrier particles. A summary of the SM particles with their mass, charge, and spin is shown in Figure 1.1. The weak interaction is unique among the four known forces, because it is the only force known to violate parity. A parity transformation is defined as a discrete change of spatial coordinates from  $(x,y,z)$  to  $(-x,-y,-z)$ . The electromagnetic and weak interactions have been unified in an electroweak theory is one of several successes of the SM. The Prescott experiment [2] at the Stanford Linear Accelerator Center (SLAC) first experimentally confirmed SM predictions of the weak neutral current [3–5] by measuring parity violating asymmetry in deep inelastic electron-deuteron scattering. Over the past half-a-century, the general structure of the SM was confirmed by many experiments.

Despite the many successes, there are also many reasons why the SM is not a complete theory. The missing phenomena from the SM are dark matter, dark energy, gravity, etc. The recently observed  $3\sigma$  deviation of the anomalous magnetic moment of muon [7] at Brookhaven National Laboratory could also be related to new physics extensions beyond the SM. The SM falls short of being a complete theory of fundamental interactions, one of them being parity violation. The SM incorporates parity violation by expressing the weak interaction as a chiral gauge interaction.

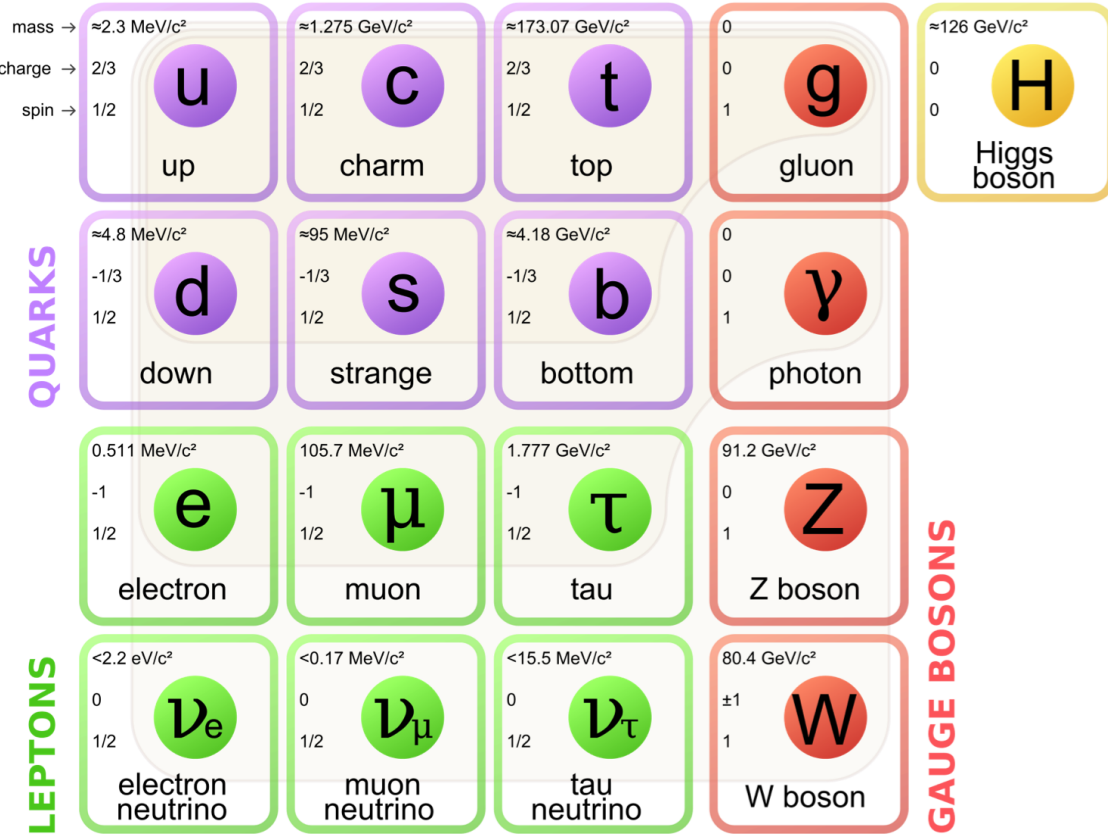


Figure 1.1 The Standard Model of elementary particles [6]. The three generations of matter, gauge bosons are shown in the fourth column, whereas the newly discovered Higgs boson in the fifth.

Over last couple of decades, parity-violating electron scattering (PVES) has become an important experimental tool to investigate the contribution of the quark-antiquark sea of the nucleon to its electromagnetic structure. The advanced technologies and improved experimental techniques allowed us to do challenging parity-violating experiments to measure of the parity-violating asymmetries at the parts-per-billion level. Figure 1.3 shows a brief history of the measured asymmetry in different PVES experiments. The difficulty level of an experiment increases with the decrease of the size and precision of the asymmetry. As shown in the Figure, the Q-weak experiment is expected to measure the most precise value of the PV asymmetry in e+p scattering to date.

Table 1.1 The electric and weak charges of elementary particles in the Standard Model.

Particle	EM Charge	Weak Charge		
u	2/3	$-2C_{1u}$	$1 - (8/3)\sin^2 \theta_W$	$\sim 1/3$
d	1/3	$-2C_{1d}$	$1 - (8/3)\sin^2 \theta_W$	$\sim 1/3$
p (uud)	1	$-2(2C_{1u} + C_{1d})$	$1 - 4\sin^2 \theta_W$	$\sim 0.07$
n (udd)	0	$-2(2C_{1u} + C_{1d})$		$\sim 1$

## 1.2 The Q-weak Experiment

The SM makes a firm prediction of the weak charge of the proton ( $Q_W^p$ ), based on the running of the weak mixing angle  $\sin^2 \theta_W$  from the  $Z^0$  pole down to low energies. Any significant deviation of  $\sin^2 \theta_W$  from the SM prediction at low  $Q^2$  would be a signal of new physics, whereas agreement would place new and significant constraints on possible SM extensions. The weak charge of the proton is suppressed in SM (as shown in Table 1.1) and a precise measurement of the quantity will challenge the SM predictions and search for new physics.

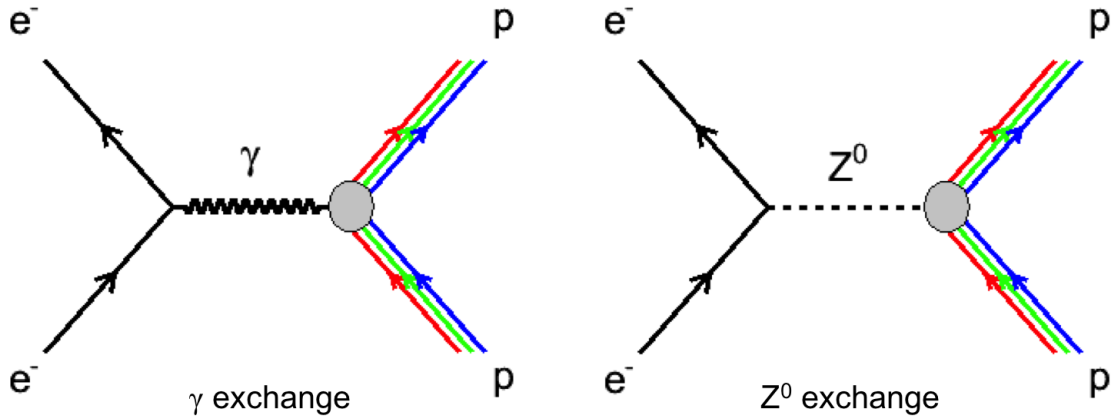


Figure 1.2 The Feynman diagrams for the parity conserving and parity violating semileptonic electroweak interactions.

The electron-proton scattering can involve either an exchange of a photon or a  $Z^0$  boson (Figure 1.2). The scattering cross section is a summation and an interference of the two invariant amplitudes.

$$\sigma \approx |\mathcal{M}_{EM} + \mathcal{M}_{weak}|^2 \approx |\mathcal{M}_{EM}|^2 + 2\Re \mathcal{M}_{EM}^* \mathcal{M}_{weak} + |\mathcal{M}_{weak}|^2, \quad (1.2.1)$$

Here  $\mathcal{M}_{EM}$ , and  $\mathcal{M}_{weak}$  are the amplitudes for the exchange of a photon and  $Z^0$  boson respectively. The sign of  $\mathcal{M}_{weak}$  changes the sign of the interference term under a parity transformation. Experimentally, this is achieved by changing the helicity of a longitudinally polarized electron scattering from an unpolarized nucleon. The parity-violating asymmetry is then defined as

$$A_{PV} = \frac{\vec{\sigma} - \overleftarrow{\sigma}}{\vec{\sigma} + \overleftarrow{\sigma}}, \quad (1.2.2)$$

where  $\vec{\sigma}(\overleftarrow{\sigma})$  is the cross section for the electrons scattering with spin polarized parallel (anti-parallel) to their direction of motion. Given that  $|\mathcal{M}_{weak}| \ll |\mathcal{M}_{EM}|$ , this asymmetry reduces to being proportional to

$$A_{PV} \sim \frac{2\mathcal{M}_{weak}\mathcal{M}_{EM}}{|\mathcal{M}_{EM}|^2}. \quad (1.2.3)$$

At tree level, the full form of the asymmetry for electron-proton scattering can be written as [8]

$$A_{PV} = \left[ \frac{-G_F Q^2}{4\sqrt{2}\pi\alpha} \right] \left[ \frac{\varepsilon G_E^{p\gamma} G_E^{pZ} + \tau G_M^{p\gamma} G_M^{pZ} - (1 - 4\sin^2\theta_W)\varepsilon' G_M^{p\gamma} G_A^e}{\varepsilon(G_E^{p\gamma})^2 + \tau(G_M^{p\gamma})^2} \right], \quad (1.2.4)$$

where the Fermi constant is denoted by  $G_F$ . The kinematic factors in terms of proton mass  $M$ , scattering angle  $\theta$ , and four-momentum transfer squared  $Q^2$  are given by

$$\varepsilon = \frac{1}{1 + 2(1 + \tau)\tan^2\frac{\theta}{2}}, \varepsilon' = \sqrt{\tau(1 + \tau)(1 - \varepsilon^2)}, \tau = \frac{Q^2}{4M}, \quad (1.2.5)$$

and electromagnetic form factors can be expressed as

$$G_{E,M}^{pZ} = (1 - 4\sin^2\theta_W)G_{E,M}^{p\gamma} - G_{E,M}^{n\gamma} - G_{E,M}^s. \quad (1.2.6)$$

The weak charge of the proton in the SM is given by

$$Q_W^p = (1 - 4\sin^2\theta_W). \quad (1.2.7)$$

Defining

$$A_0 = \frac{-G_F Q^2}{4\sqrt{2}\pi\alpha}, \quad (1.2.8)$$

and using equations 1.2.4, 1.2.5, 1.2.6, 1.2.7, the reduced asymmetry can be written as

$$\frac{A_{PV}}{A_0} = \left[ \frac{\varepsilon G_E^{p\gamma} (Q_W^p G_E^{p\gamma} - G_E^{n\gamma} - G_E^s) + \tau G_M^{p\gamma} (Q_W^p G_M^{p\gamma} - G_M^{n\gamma} - G_M^s) - (1 - 4 \sin^2 \theta_W) \varepsilon' G_M^{p\gamma} G_A^e}{\varepsilon (G_E^{p\gamma})^2 + \tau (G_M^{p\gamma})^2} \right] \quad (1.2.9)$$

$$\frac{A_{PV}}{A_0} = Q_W^p \left[ \frac{\varepsilon (G_E^{p\gamma})^2 + \tau (G_M^{p\gamma})^2}{\varepsilon (G_E^{p\gamma})^2 + \tau (G_M^{p\gamma})^2} \right] + \left[ (-1) \frac{\varepsilon G_E^{p\gamma} G_E^{n\gamma} + \tau G_M^{p\gamma} G_M^{n\gamma}}{\varepsilon (G_E^{p\gamma})^2 + \tau (G_M^{p\gamma})^2} \right] + \left[ (-1) \frac{(1 - 4 \sin^2 \theta_W) \varepsilon' G_M^{p\gamma} G_A^e}{\varepsilon (G_E^{p\gamma})^2 + \tau (G_M^{p\gamma})^2} \right]. \quad (1.2.10)$$

The reduced asymmetry can be expressed as a combination of three asymmetries as following

$$\frac{A_{PV}}{A_0} = A_{Q-weak} + A_{hadronic} + A_{axial}. \quad (1.2.11)$$

Here individual asymmetries are given as

$$A_{Q-weak} = Q_W^p, \quad (1.2.12)$$

$$A_{hadronic} = Q_W^n \left[ \frac{\varepsilon G_E^{p\gamma} G_E^{n\gamma} + \tau G_M^{p\gamma} G_M^{n\gamma}}{\varepsilon (G_E^{p\gamma})^2 + \tau (G_M^{p\gamma})^2} \right], \quad (1.2.13)$$

$$A_{axial} = -G_A^e \left[ \frac{(1 - 4 \sin^2 \theta_W) \varepsilon' G_M^{p\gamma}}{\varepsilon (G_E^{p\gamma})^2 + \tau (G_M^{p\gamma})^2} \right], \quad (1.2.14)$$

where the contribution from the strange form factors is ignored.

Under the kinematic condition of  $\theta \rightarrow 0$ ,  $\varepsilon \rightarrow 1$ , and  $\tau \ll 1$ , the asymmetry simplifies as

$$\frac{A_{PV}}{A_0} = Q_W^p + Q^2 B(Q^2, \theta), \quad (1.2.15)$$

where the  $B(Q^2, \theta)$  term contains the hadronic contribution to the asymmetry and is about 30%.

Previous PVES experiments constrain this contribution.

The goal of the Q-weak experiment is aimed to measure this parity violating asymmetry ( $\sim 250$  ppb) in elastic electron-proton scattering at  $Q^2 = 0.025$  (GeV/c) $^2$  and forward angles to determine the proton's weak charge with 4% combined statistical and systematic uncertainties [8]. The experiment will also provide a  $\sim 0.3\%$  measurement of the weak mixing angle. A 2200 hours measurement using a 88% polarized electron beam of 180  $\mu$ A on a 35 cm liquid Hydrogen target was performed during 2010 - 2012.

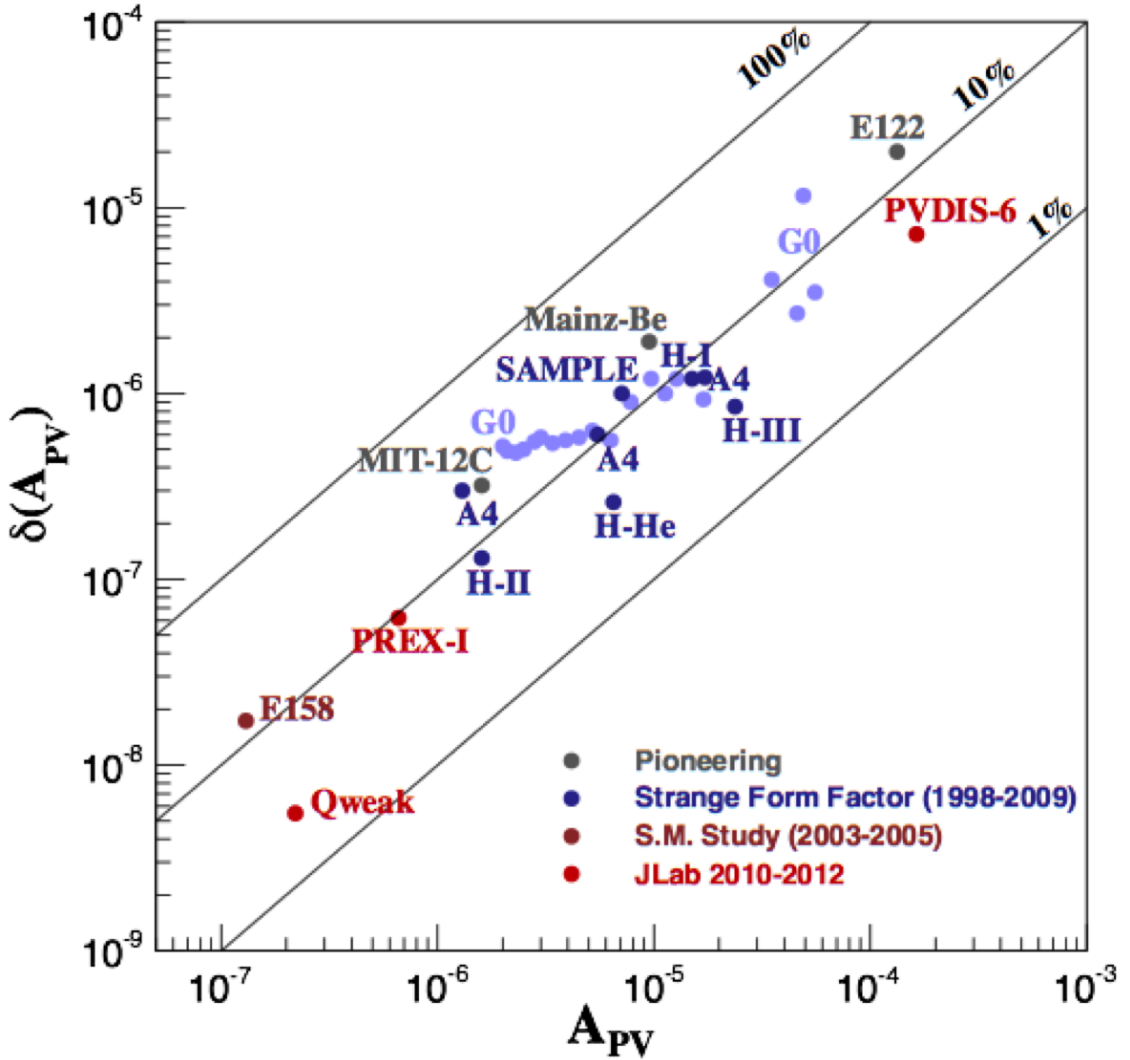


Figure 1.3 Q-weak will be most precise (relative and absolute) PVES result to date.

### 1.3 Inelastic Parity Violating Asymmetry

In addition of measuring the elastic PV asymmetry for the Q-weak, a dedicated data were taken to extract the inelastic PV asymmetry in electron-proton scattering. During normal production running, the detector signals were integrated to obtain the yield and inelastic events also make into the detector acceptance. There is no clear way to separate the inelastic signal from the elastic signal. The inelastic asymmetry is expected to be a factor of 10 larger than the elastic asymmetry and hence was critical to measure the inelastic dilution and correct for it. The inelastic contribution in the Q-weak acceptance is mainly dominated by the production of the resonance.

### 1.3.1 The $\Delta$ Resonance

The  $\Delta$  is the first resonance of the nucleon with nucleon spin  $J=3/2$  and mass 1232 MeV. In the ground state, the total spin of the proton is  $J=1/2$  and is the sum of the spins of its constituent quarks (uud). The nucleon has two valence quark spins aligned parallel and one antiparallel, and hence only two possible flavor states (uud, udd) exist corresponding to isospin 1/2, whereas the  $\Delta$  baryons have all three quark spins aligned parallel [9]. A list of allowed  $\Delta$  resonance states and their properties is given in Table 1.2.

Table 1.2 Nucleons and  $\Delta$  resonances and their associated properties.

Particle	Quarks	EM Charge	Spin	Isospin	$I_3$
p	uud	+1	$\uparrow\uparrow\downarrow$	1/2	+1/2
n	udd	0	$\uparrow\downarrow\downarrow$	1/2	-1/2
$\Delta^{++}$	uuu	+2	$\uparrow\uparrow\uparrow$	3/2	+3/2
$\Delta^+$	uud	+1	$\uparrow\uparrow\uparrow$	3/2	+1/2
$\Delta^0$	udd	0	$\uparrow\uparrow\uparrow$	3/2	-1/2
$\Delta^-$	ddd	-1	$\uparrow\uparrow\uparrow$	3/2	-3/2

A photon or Z boson can interact with a nucleon and flip the spin of one of the quarks to make them all parallel to produce a  $\Delta$  baryon. Only a  $\Delta^+$  or  $\Delta^0$  can be created by this kind of interaction if the target particle is a proton or neutron, respectively. On the other hand, weakly interacting particle, such as a neutrino, a quark can change flavor and flip the spin to produce  $\Delta^{++}$  and  $\Delta^-$ . An electron-proton interaction induces a quark spin flip and can reveal information about how the quark spin is redistributed during the transition. For the Q-weak experiment where the interactions were predominantly electron-proton, only the relevant resonance  $\Delta^+$  is considered.

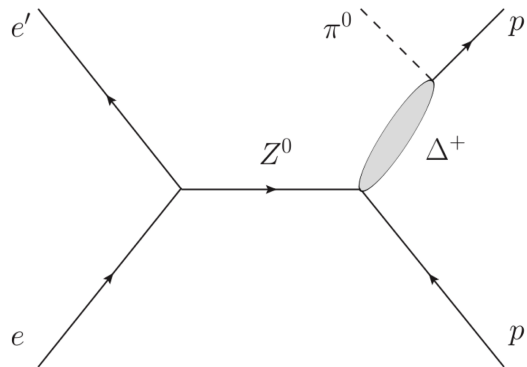


Figure 1.4 The Feynman diagrams for the parity violating inelastic electron-proton scattering [10].

### 1.3.2 Formalism and Measurement

In inelastic PV electron-proton scattering, the incident electron interacts with the proton and loses energy. The proton absorbs this energy and gets excited to its first resonance ( $\Delta^+$ ), then decays to a neutral pion ( $\pi^0$ ) and a proton (as shown in Figure 1.4). The parity-violating asymmetry in the nucleon  $\rightarrow \Delta$  transition can be expressed as [11, 12]

$$A_{PV}^{in} = \left[ \frac{-G_F Q^2}{4\sqrt{2}\pi\alpha} \right] [\Delta_{(1)}^\pi + \Delta_{(2)}^\pi + \Delta_{(3)}^\pi], \quad (1.3.1)$$

where  $\Delta_{(1)}^\pi$  contains the resonant terms, which are all isovector,  $\Delta_{(2)}^\pi$  contains the nonresonant terms including both isovector and isoscalar, and  $\Delta_{(3)}^\pi$  contains all axial-vector reactions at the hadron vertex. The contribution of the inelastic PV to the Q-weak asymmetry is small. The asymmetry for the  $N \rightarrow \Delta$  transition was measured as a part of the Q-weak background studies.

## 1.4 The Beam Normal Single Spin Asymmetry

The beam normal single spin asymmetry (BNSSA) is generated by polarized electrons when scattered from unpolarized protons and is a possible false background asymmetry in parity violating electron scattering experiments (PVES). The BNSSA is a parity conserving asymmetry. Theoretical calculations [13] indicates that, the size of this asymmetry can be several orders of magnitude larger than that of the parity violating asymmetry. For a precision experiment like Q-weak, it was important to estimate the background due to BNSSA and a dedicated measurement was performed.

Elastic electron-nucleon scattering in the one-photon exchange approximation gives a direct access to the electromagnetic form factors of the nucleon which contains information about its structure. The ratio of the proton's electric to magnetic form factors ( $G_{Ep}/G_{Mp}$ ) has been measured precisely up to large momentum transfer ( $Q^2$ ) in precision experiments using two different methods namely the polarization transfer [14, 15] and unpolarized measurements [16–18] using the Rosenbluth separation technique. These two different methods show inconsistent results. This puzzle may be explained by a two-photon exchange amplitude whose magnitude is a few percent of the one photon exchange term as shown in [19]. A beam normal single spin asymmetry measurement provides a direct access to the two-photon exchange process which is required to properly estimate the electron-nucleon scattering cross-sections beyond the Born approximation.

## 1.5 Inelastic Beam Normal Single Spin Asymmetry

There is a parity conserving BNSSA or transverse asymmetry ( $B_n$ ) on  $H_2$  with a  $\sin(\phi)$ -like dependence due to 2-photon exchange. The size of  $B_n$  is few ppm, so a few percent residual transverse polarization in the beam, in addition to potentially small broken azimuthal asymmetries in the main detector, might lead to few ppb corrections to the Q-weak data. As part of a program of  $B_n$  background studies, the first measurement of  $B_n$  in the N-to- $\Delta$  transition was performed using the Q-weak apparatus.

## 1.6 Thesis Outline

This dissertation will present a preliminary analysis of the beam normal single spin asymmetry measured from inelastic electron-proton scattering using the Q-weak apparatus. The outline of this dissertation is organized as follows:

- chapter 1: INTRODUCTION - an introduction and motivation for the Q-weak experiment,
- chapter 2: THEORY - an brief overview of the theory of beam normal single spin asymmetry measurements,
- chapter 3: EXPERIMENTAL SETUP - a brief description of the experimental apparatus,
- chapter 4: BEAM MODULATION - provides a detailed description of the beam modulation system,
- chapter 5: BEAMLINE OPTICS AND FALSE ASYMMETRIES - application of beam modulation system, beamline characterization, and pedestal survey,
- chapter 6: BEAM NORMAL SINGLE SPIN ASYMMETRY - gives details of the data analysis and treatment of systematic uncertainties of beam normal single spin asymmetry in inelastic e+p scattering,
- chapter 7: DISCUSSION AND CONCLUSIONS - a summary of the emphasized work and analysis status.

## SECTION 2

### THEORY

The electromagnetic form factors depicts non-local nature of the nucleon in its interactions with photons. The form factors have been studied extensively both experimentally and theoretically as the basic observables of the nucleon compositeness [20]. Increased precision of electron-proton scattering experiments allowed to extract the form factors precisely and using two alternative methods: the Rosenbluth method - also known as the longitudinal-transverse separation technique [16, 21, 22], and the polarization-transfer technique [14, 15]. The two methods show incompatible results by considering traditional one-photon exchange approximation, called the Born approximation, to extract the form factors. It is important to find an explanation of this discrepancy for the use of the electron-proton scattering as a precise and reliable tool in hadronic physics. Theoretical studies [23, 24] have indicated that the discrepancy could be partially resolved by including higher-order two-photon exchange corrections in the analysis in addition to the lowest-order one-photon exchange approximation. The calculation in Ref. [23] for the two-photon exchange diagrams considered only nucleons in the intermediate state. The  $\Delta$  resonance has an important role in many hadronic reactions and is essential to evaluate its contribution to the two-photon exchange in electron-proton scattering.

#### 2.1 Electron Scattering Beyond the Born Approximation

Beyond the Born approximation, the calculation of the amplitude of the scattering process becomes very complicated. Two or more photons are exchanged in the scattering process and the calculation gets complex as it needs to include all of the excited states of the proton. There are several existing models to calculate multi-photon processes [25], but they are incomplete.

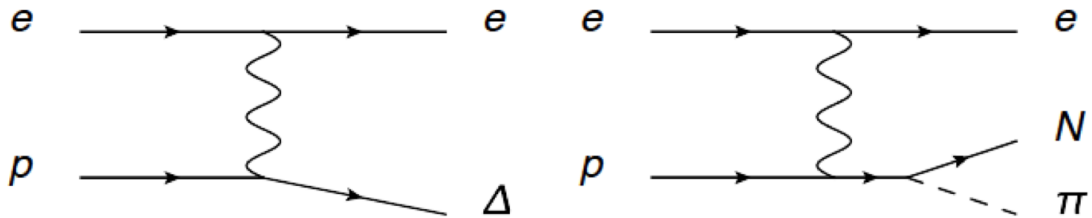


Figure 2.1 Electron-proton  $\rightarrow$  electron- $\Delta$  in  $\Delta$  region, without and with decay of  $\Delta$  in the final state for the one-photon exchange process.

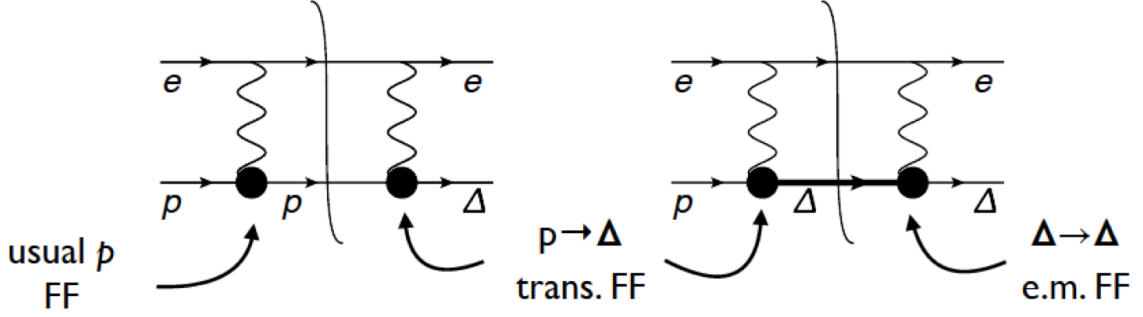


Figure 2.2 BNSSA  $2\gamma \Delta$ .

### 2.1.1 2-photon Exchange

The elastic electron-protons scattering at leading order involves the exchange of a single photon, followed by higher-order processes such as two-photon exchange (as shown in Figures 2.1 and 2.2). Elastic electron-protons scattering in Born approximation is usually approximated as a one-photon exchange process. This approximation is possible due to the small value of the electromagnetic coupling constant  $\alpha \sim 1/137$ . The higher order processes, such as two-photon exchange, are treated as radiative corrections. The two-photon exchange process involves the exchange of two virtual photons with an intermediate hadronic state that includes the ground state and all excited states. The two-photon exchange reactions are used to extract information on the hadron structure such as the form factors of the neutron, pion and heavy nuclei (deuteron and  $^3\text{He}$ ). In the analysis of the form-factor for electron-proton scattering, the contribution of the two-photon exchange amplitude is assumed to be very small [26]. The real part (or dispersive) of this amplitude is obtained by comparing electron-proton and positron-proton scattering cross sections. The calculations of the two-photon amplitude can be divided into two categories: unexcited and excited intermediate proton states. The effects on the elastic electron-proton scattering cross section of the two-photon exchange contribution with an intermediate  $\Delta$  resonance is smaller in magnitude than the nucleon contribution [20].

The discrepancy between Rosenbluth separation and the polarization transfer technique using one-photon exchange approximation are shown in Figure 2.3 (a) [27]. The methods start to deviate from each other above  $Q^2$  of 1  $(\text{GeV}/c)^2$ . After applying the two-photon exchange correction, the discrepancy seems to be resolved between the two methods, as shown in Figure 2.3 (b) [27]. The two-photon exchange calculations are not complete and have not been tested over a wider range of kinematics.

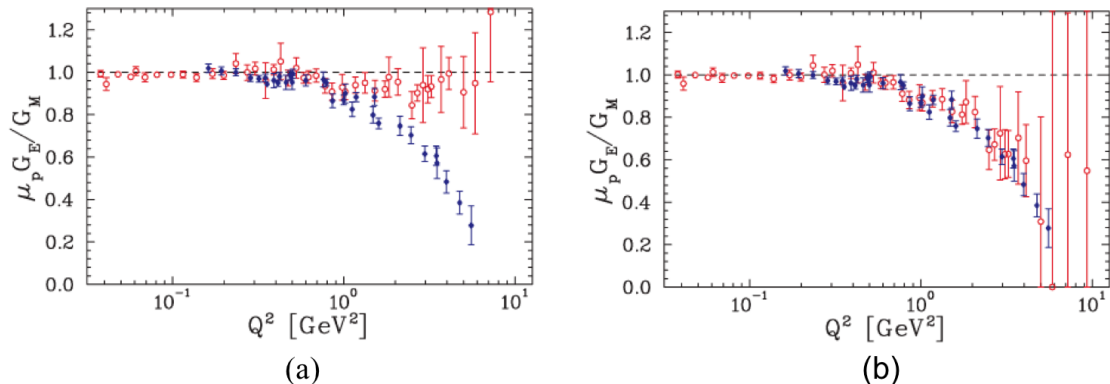


Figure 2.3 Ratio  $\mu_p G_E/G_M$  extracted from the polarization transfer (filled diamonds) and LT measurements (open circles). The figure (a) and (b) shows LT separations without and with the two-photon exchange corrections applied to the cross sections respectively.

Another question naturally arises whether other higher-mass resonances could also have a non-negligible contribution to the two-photon exchange correction like  $\Delta(1232)$  resonance [13]. The effects turn out to be not too sensitive, as shown by Kondratyuk and Blunden [28] by generalizing the calculation to full spectrum of the most important hadron resonances as intermediate states involving spin 1/2 and 3/2 resonances.

## 2.2 Experimental Observation of Beam Spin Asymmetry

The beam spin asymmetries are time-reversal invariant, parity conserving observables which vanish in the Born approximation. The beam spin asymmetry can be extracted by observing only the electron in the final state interaction on the electron side (as shown in Figures 2.1 and 2.2). Since one-photon amplitude is real, only imaginary part of the two-photon amplitude contributes to the beam spin asymmetry. The asymmetry arises due to an electron helicity flip. The asymmetry can be obtained either by polarizing the target perpendicular (transverse) to the incoming unpolarized electron beam, or to the transversely polarized beam on a unpolarized target. The asymmetry in the first case is known as target normal single spin asymmetry ( $A_n$ ) and latter case is called beam normal single spin asymmetry ( $B_n$ ). The measured asymmetry can be expressed as

$$\epsilon_M = \frac{\sigma^\uparrow - \sigma^\downarrow}{\sigma^\uparrow + \sigma^\downarrow} = \frac{\Im \left[ \sum_{spins} (\mathcal{M}^\gamma)^*(Abs\mathcal{M}^{\gamma\gamma}) \right]}{\sum_{spins} |\mathcal{M}^\gamma|^2}, \quad (2.2.1)$$

where  $\sigma^{\uparrow,\downarrow}$  are cross sections with incoming electrons polarized up or down, perpendicular to the scattering plane.  $\Im$  is the imaginary part and  $Abs\mathcal{M}^{\gamma\gamma}$  is a sum over all the possible intermediate states in the two-photon exchange process. The cross section can be parameterized using six invariant amplitudes  $\tilde{G}_E(\nu, Q^2)$ ,  $\tilde{G}_M(\nu, Q^2)$ , and  $\tilde{F}_i(\nu, Q^2)$  and are complex functions of the  $Q^2$  and  $\nu$ . Here  $\nu = \vec{K} \cdot \vec{P}$ , where  $K$  and  $P$  are the average of the incoming and outgoing four-momenta of the electron and proton respectively [29, 30]. In the Born approximation, the complex electromagnetic form factors become the usual Pauli and Sachs form factors of the nucleon,  $\tilde{G}_E(\nu, Q^2) \rightarrow G_E(Q^2)$ ,  $\tilde{G}_M(\nu, Q^2) \rightarrow G_M(Q^2)$ , and  $\tilde{F}_i(\nu, Q^2) \rightarrow 0$ . After Born approximation, using this parameterization, with the virtual photon polarization parameter,

$$\varepsilon = \frac{\nu^2 - M^4\tau(1+\tau)}{\nu^2 + M^4\tau(1+\tau)}, \quad (2.2.2)$$

the beam normal single spin asymmetry can be expressed as [31]

$$B_n = \frac{2m_e}{Q} \sqrt{2\varepsilon(1-\varepsilon)} \sqrt{1 + \frac{1}{\tau}} \left( G_M^2 + \frac{\varepsilon}{\tau} G_E^2 \right)^{-1} \times \left[ -\tau G_M \Im \left( \tilde{F}_3 + \frac{1}{1+\tau} \frac{\nu}{M^2} \tilde{F}_5 \right) - G_E \Im \left( \tilde{F}_4 + \frac{1}{1+\tau} \frac{\nu}{M^2} \tilde{F}_5 \right) \right] + \mathcal{O}(e^4), \quad (2.2.3)$$

whereas target normal spin asymmetry can be written as

$$A_n = \sqrt{\frac{1\varepsilon(1+\varepsilon)}{\tau}} \left( G_M^2 + \frac{\varepsilon}{\tau} G_E^2 \right)^{-1} \times \left[ -G_M \Im \left( \delta \tilde{G}_E + \frac{\nu}{M^2} \tilde{F}_3 \right) + G_E \Im \left( \delta \tilde{G}_M + \frac{2\varepsilon}{1+\varepsilon} \frac{\nu}{M^2} \tilde{F}_3 \right) \right] + \mathcal{O}(e^4). \quad (2.2.4)$$

To polarize an ultra-relativistic particle in the direction normal to its momentum involves a suppression factor  $m/E$ , where  $m$  is the mass and  $E$  is the energy of the particle. The suppression factor for the electron with beam energy in the 1 GeV range is of order  $10^{-4} - 10^{-3}$ . The resulting beam-normal single spin asymmetry is expected to be of order  $10^{-6} - 10^{-5}$ , whereas the target-normal spin asymmetry is of order  $10^{-2}$  [32].

### 2.2.1 Measurement of the Beam Normal Single Spin Asymmetry

The beam normal single spin asymmetry (BNSSA) is measured by scattering transversely polarized electrons off of unpolarized nucleons. The measured asymmetry ( $\epsilon_M$ ) has a sinusoidal dependence about the beam axis

$$\epsilon_M(\phi) = -B_n \vec{S} \cdot \hat{n} = -B_n |\vec{S}| \sin(\phi - \phi_0), \quad (2.2.5)$$

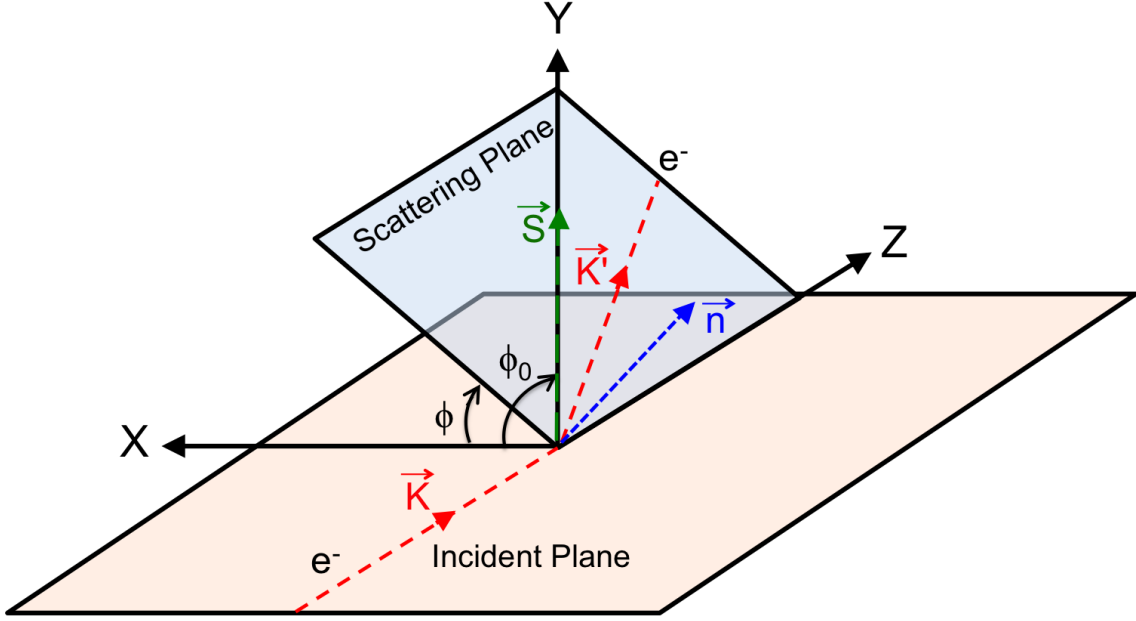


Figure 2.4 The schematic of transverse electron-nucleon scattering reaction. The electron spin is polarized in the vertical transverse direction. The initial (final) momentum of the electron is given by  $\vec{K}$  ( $\vec{K}'$ ).

where  $\vec{S}$  is the electron spin in the transverse direction, and  $\hat{n}$  is the unit vector, normal to the scattering plane.  $\phi$  and  $\phi_0$  are the azimuthal angles of  $\vec{S}$  and the scattering plane respectively (see Figure 2.4). The beam normal single spin asymmetry can be measured and extracted from the asymmetry measured in the detector placing at azimuthal angle  $\phi$ .

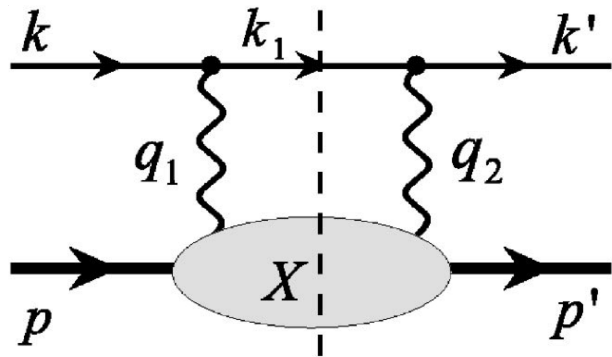


Figure 2.5 The two-photon exchange diagram. The filled blob represents the response of the nucleon to the scattering of the virtual photon [33, 34].

### 2.2.2 Imaginary Part of Two-photon Diagram

The imaginary part of the two-photon exchange amplitude is related to the absorptive part of the doubly virtual Compton scattering (DVCS) tensor on the nucleon, as shown in Figure 2.5 and can be written as [35]

$$Abs\mathcal{M}^{\gamma\gamma} = e^4 \int \frac{|\vec{k}_1|^2 d|\vec{k}_1| d\Omega_{k_1}}{2E_{k_1}(2\pi)^3} \bar{u}(k')\gamma_\mu(\gamma k_1 + m_e)\gamma_\nu u(k) \frac{1}{Q_1^2 Q_2^2} W^{\mu\nu}(w, Q_1^2, Q_2^2) \quad (2.2.6)$$

The inelastic contribution to  $W^{\mu\nu}$  corresponding with the  $\pi N$  intermediate states in the blob of Figure 2.5 using the MAID model (resonance region) [35] is given by

$$W^{\mu\nu}(p', \lambda'_N; p, \lambda_N) = \frac{1}{4\pi^2} \frac{|\vec{p}_\pi|^2}{[|\vec{p}_\pi|(E_\pi + E_n) + E_\pi |\vec{k}_1| \hat{k}_1 \cdot \hat{p}_\pi]} \times \sum_{\lambda_n} \int d\Omega_\pi \bar{u}(p', \lambda'_N) J_{\pi N}^{\dagger\mu} u(p_n, \lambda_n) \times \bar{u}(p_n, \lambda_n) J_{\pi N}^\nu u(p, \lambda_N) \quad (2.2.7)$$

where  $p_\pi = (E_\pi, \vec{p}_\pi)$  and  $p_n = (E_n, \vec{p}_n)$  are the four-momenta of the intermediate pion and nucleon states, respectively, and  $k_1 = -\vec{p}_\pi - \vec{p}_n$ . The integration runs over the polar and azimuthal angles of the intermediate pion, and  $J_{\pi N}^\nu$  and  $J_{\pi N}^{\dagger\mu}$  are the pion electro-production currents, describing the excitation and deexcitation of the  $\pi N$  intermediate state, respectively.  $u$  and  $\bar{u}$  are matrix elements and can be parameterized. The inelastic contribution is dominated by the region of pion production threshold.

### 2.3 The $\gamma^* \Delta\Delta$ Form Factors

The proton electromagnetic form factor is well known. The proton  $\rightarrow \Delta$  electromagnetic transition form factor is also fairly well known. For proton and  $\Delta$  intermediate hadrons, vertices therefore are known except for  $\gamma^* \Delta\Delta$  electromagnetic vertex. The information about  $\gamma^* \Delta\Delta$  form factor has potential to measure charge radius of  $\Delta$  and magnetic moment of  $\Delta$ . Besides there have been many theoretical interest:

- Dyson-Schwinger approach [36]
- Covariant quark model [37]
- Lattice QCD [38]

But the form factor experimentally has never been measured before. No dedicated calculations exists to relate  $\gamma^* \Delta\Delta$  form factors to cross section or asymmetry data.

## 2.4 Model Calculations

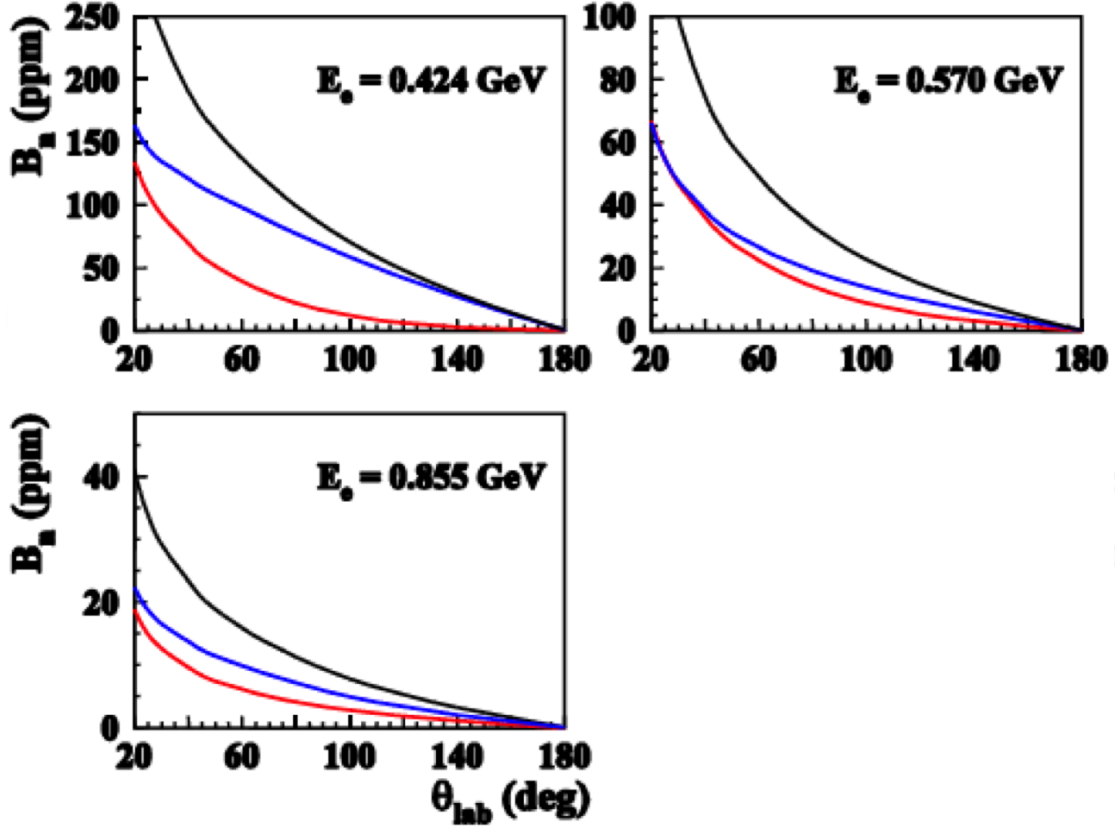


Figure 2.6 Inelastic transverse asymmetry model from Pasquini et al. [39].  $\Delta$  intermediate state is shown in red,  $N$  intermediate state is shown in blue, and total ( $\Delta+N$ ) contribution is shown in black.

The only unpublished model calculation of the beam normal single spin asymmetry in inelastic electron-nucleon scattering was performed by Pasquini & Vanderhaeghen for forward angles and low energies. The BNSSA as a function of the center-of-mass angle,  $\theta_{cm}$  for  $\Delta$  (red) and nucleon (blue) as intermediate states are shown in Figure 2.6. If the intermediate hadronic states are not included in the calculation, the prediction is nearly flat as a function of the  $\theta_{cm}$ . This calculation was performed for lower energy than Q-weak, and an effort to extrapolate this result in to the Q-weak kinematic settings is discussed in later chapter. The beam normal single spin asymmetry are positive and are in the order of few ppm. The large asymmetries in the forward region dominated by quasi-virtual Compton scattering kinematics, where one exchanged photon becomes quasi-real. The asymmetry almost exponentially varies with scattering angle.

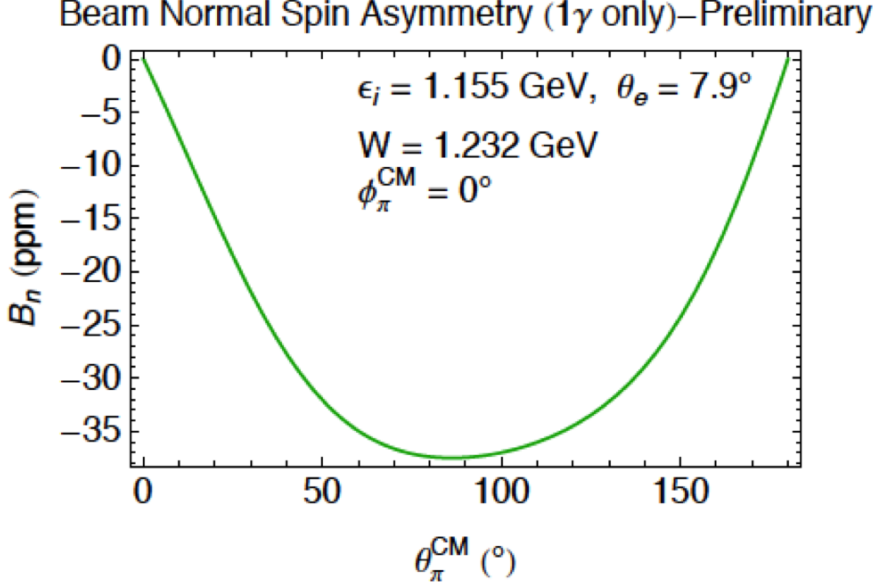


Figure 2.7 Beam normal single spin asymmetry with decay of  $\Delta$  in the final state for one-photon exchange.

There is an ongoing calculation for one-photon exchange in  $\Delta$  region [40], which shows the beam normal spin asymmetry is not zero, although is proportional to  $m_e/Q$ . The asymmetry is proportional to  $\cos\phi_\pi$ , the azimuthal angle of the emerging pion relative to the scattering plane. Considering  $\Delta$  as stable state in  $e+p \rightarrow e+\Delta$ , one can prove the helicity amplitudes are relatively real, and get  $B_n = 0$  [40]. The  $\Delta$  state decays and final state interaction (FSI) gives different phases for different amplitudes. The phases, and whole amplitudes in FSI are known. The multipole amplitudes can be obtained from analyses of other  $e+p \rightarrow e\pi N$  reactions and observing hadronic final state. The variation on  $B_n$  with scattering angle is shown in Figure 2.7 [40] by considering only one-photon exchange.

## 2.5 Goals of the Inelastic Transverse Physics Program

The objective of the Q-weak experiment is to challenge the predictions of the Standard Model in low  $Q^2$  range and search for new physics at the TeV scale through a 4% measurement of the weak charge of the proton via the parity-violating asymmetry ( $\sim 250$  ppb) in elastic  $e+p$  scattering [8]. There is a parity conserving beam normal single spin asymmetry, or transverse asymmetry,  $B_n$  on LH<sub>2</sub> with a  $\sin(\phi)$ -like dependence due to the two-photon exchange. The expected magnitude of  $B_n$  is few ppm which is an order larger than PV asymmetry for the Q-weak. Also  $B_n$  provides

direct access to the imaginary part of the two-photon exchange amplitude. It will be interesting to see the magnitude of  $B_n$  in the  $N \rightarrow \Delta$  region, which has never been measured before.  $B_n$  from electron-nucleon scattering is also a unique tool to study the  $\gamma^* \Delta\Delta$  form factors. This dissertation presents the analysis of the 9% measurement of the beam normal single spin asymmetry in inelastic electron-proton scattering at a  $Q^2$  of 0.0209 ( $GeV/c^2$ )<sup>2</sup>. This measurement will help to improve the theoretical models on the beam normal single spin asymmetry and thereby our understanding of the doubly virtual Compton scattering process.

## SECTION 3

### EXPERIMENTAL SETUP

The Q-weak experiment (E08-016) was performed at Thomas Jefferson National Accelerator Facility (TJNAF) [41] in Newport News, Virginia from January 2011 to May 2012 [8,42,43]. The goal of the Q-weak experiment is to extract the weak charge of the proton by measuring parity violating (PV) asymmetry in elastic electron-proton scattering at low momentum transfer. The Standard Model (SM) predicts this asymmetry to be -230 parts per billion (ppb) and the Q-weak collaboration proposed to measure this asymmetry with 2.1% statistical uncertainty. The Q-weak experiment has highly benefited from technologies developed by previous parity violating experiments such as SAMPLE [44] at the MIT/Bates Linear Accelerator Center, G0 [45] and HAPPEX [46] at JLab. As the Q-weak PV asymmetry and its absolute uncertainty are an order of magnitude smaller than its predecessors, a dedicated design, significant improvement to hardware and software, and additional control of systematic uncertainties were needed to reach the proposed precision goals summarized in Table 3.1. A brief description of the experimental setup will be discussed in this chapter.

Table 3.1 Proposed error budget of the Q-weak experiment [8]. The second and third columns show the relative uncertainty on parity violating asymmetry, and on weak charge of proton respectively. Total uncertainty is the quadrature sum of the statistical and systematic uncertainty.

Source of Error	$\frac{\Delta A_{PV}}{A_{PV}}$	$\frac{\Delta Q_W^p}{Q_W^p}$
Statistics	2.1%	3.2%
Hadronic structure	-	1.5%
Beam polarization	1.0%	1.5%
Absolute $Q^2$	0.5%	1.0%
Backgrounds	0.7%	0.7%
Helicity correlated beam properties	0.5%	0.8%
Total	2.6%	4.2%

### 3.1 Q-weak Kinematics

In two-body elastic electron-proton scattering, an incident electron with energy  $E$  and momentum  $p$  scatters from a stationary proton with mass  $M$ . The electron scatters with energy  $E'$  and momentum  $p_0$  at an angle  $\theta$  with respect to the incident electron as shown in Figure 3.1. The energy

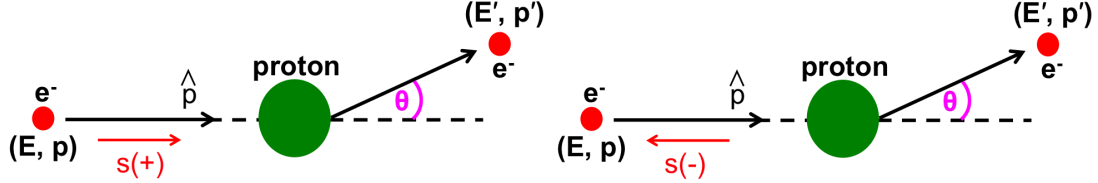


Figure 3.1 Sketch of the elastic electron-proton scattering process.

transfer can be expressed as  $\gamma = E - E'$  and 3-momentum transfer as  $\mathbf{q} = \mathbf{p} - \mathbf{p}'$ . Then the four momentum transfer can be defined as

$$Q^2 = -q^2 = -(\nu^2 - \mathbf{q}^2) \geq 0 \quad (3.1.1)$$

Using energy and momentum conservation for two-body scattering, the scattered energy  $E'$  and  $Q^2$  can be written as

$$E' = \frac{E}{1 + 2\frac{E}{M} \sin^2 \frac{\theta}{2}} \quad (3.1.2)$$

$$Q^2 = \frac{4E^2 \sin^2 \frac{\theta}{2}}{1 + 2\frac{E}{M} \sin^2 \frac{\theta}{2}}. \quad (3.1.3)$$

A dedicated tracking system was used to measure the scattering angle  $\theta$  and  $Q^2$  (more details in Section 3.12). Simulation was used to confirm measurements. A longitudinally polarized electron beam with energy 1.155 GeV was incident on 34.4 cm long liquid hydrogen target ( $\text{LH}_2$ ) where a  $\sim 9000$  A magnetic spectrometer selected out the elastic e-p scattering at  $Q^2 \sim 0.025$   $(\text{GeV}/c)^2$ . A summary of the basic parameters and typical operating conditions for the experiment are shown in Table 3.2. The design parameters of the experiment were chosen to minimize the contributions from the anticipated systematic uncertainties shown in Table 3.1.

## 3.2 Experimental Techniques

The parity-violating asymmetry is defined as the difference over sum of the cross section for two different helicity states (+/-) as shown in Equation 3.2.1. The helicity state of the longitudinally polarized electron beam is flipped between “+” and “-” and scattered off from a fixed un-polarized

Table 3.2 Basic parameters and typical operating conditions of the Q-weak experiment [8, 47, 48].

Parameter	Value
Incident beam energy	1.155 GeV
Beam polarization	89%
Beam current	180 $\mu$ A
LH <sub>2</sub> target thickness	34.4 cm
Cryopower	2.5 kW
Production running time	2544 hours
Nominal scattering angle	7.9°
Scattering angle acceptance	$\pm 3^\circ$
Acceptance	49% of $2\pi$
Solid angle	$\Delta\Omega = 43$ msr
Acceptance averaged $Q^2$	$\langle Q^2 \rangle = 0.025$ (GeV/c) <sup>2</sup>
Acceptance averaged physics asymmetry	$\langle A \rangle = -234$ ppb
Acceptance averaged experimental asymmetry	$\langle A \rangle = -200$ ppb
Luminosity	$2 \times 10^{39}$ s <sup>-1</sup> cm <sup>-2</sup>
Integrated cross section	4.0 $\mu$ b
Integrated rate (all sectors)	6.5 GHz (0.81 GHz per sector)
Full Current Production Running	2544 hours

proton target. The signal from elastically scattered electron for each helicity state is integrated to measure the yield ( $Y^{+/-}$ ). The difference in helicity correlated yield is sensitive to parity violating quantities. The raw asymmetry extracted from helicity correlated yields is defined as

$$A_{\text{raw}} = \frac{Y^+ - Y^-}{Y^+ + Y^-} \propto \frac{\left(\frac{d\sigma}{d\Omega}\right)^+ - \left(\frac{d\sigma}{d\Omega}\right)^-}{\left(\frac{d\sigma}{d\Omega}\right)^+ + \left(\frac{d\sigma}{d\Omega}\right)^-}. \quad (3.2.1)$$

The electron beam polarization was changed pseudo-randomly in a quartet (QRT) pattern of either “+ - - +” or “- + + -” with a helicity reversal rate of 960 Hz. The combination of fast helicity reversal and pseudo-random QRT patterns cancel the slow drifts in yields, and minimizes the target density fluctuations. Any common scale factors between the two helicity states cancel, but any difference does not. Hence Helicity Correlated Beam Asymmetries (HCBAs) in beam parameters like position, angle, energy, and charge can generate false asymmetries in measured asymmetry. Linear regression based on natural beam jitter or driven beam modulation is used to correct for such false asymmetries. The asymmetry is then corrected for the beam polarization, several background contributions, and various experimental biases to obtain the final parity violating asymmetry.

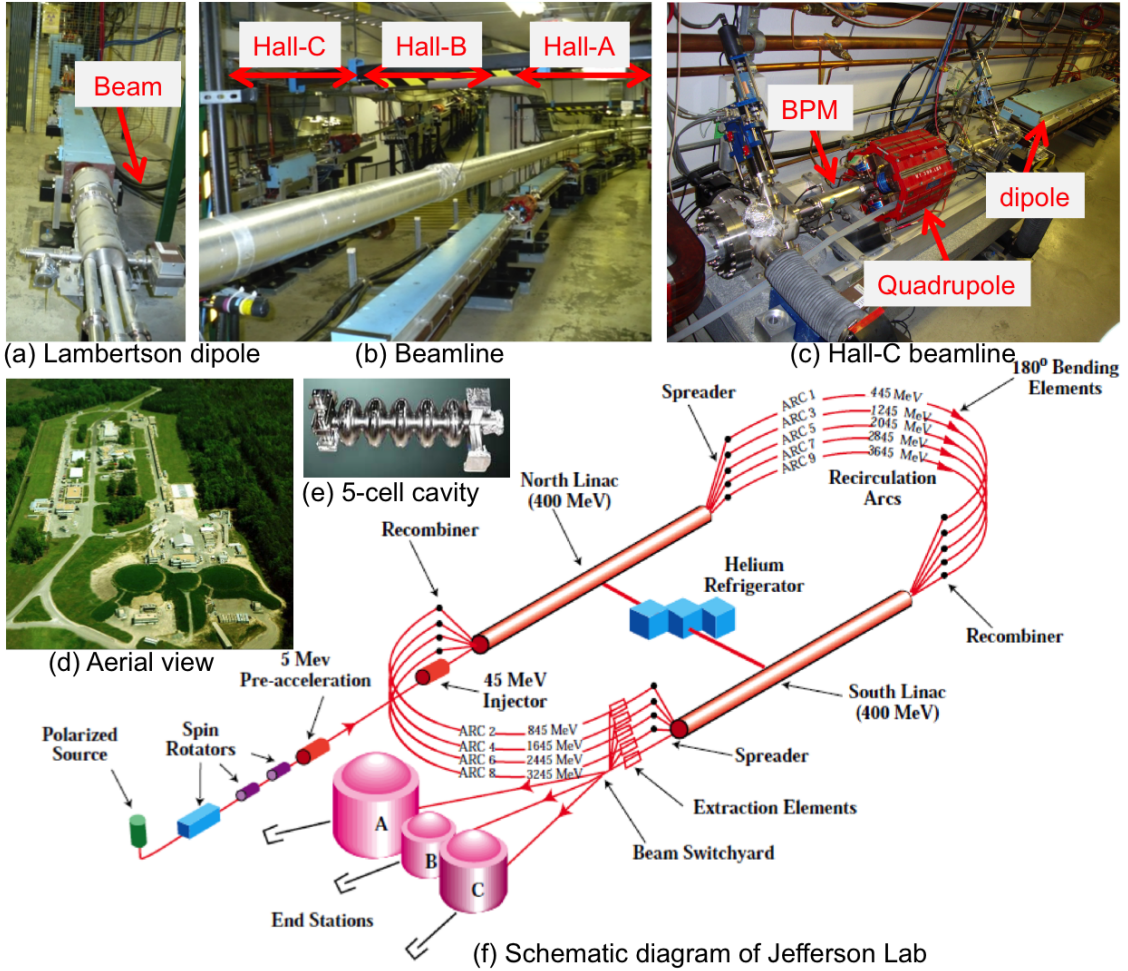


Figure 3.2 Jefferson Lab and its beamline schematic. (a) Dipole at Lambertson region where beam splits for three different experimental halls. (b) Three separate beamlines for three halls. (c) Hall-C beamline before entering in the hall. A typical quadrupole, dipole, and BPM are shown. (d) Aerial view of Jefferson Lab. (e) A JLab made 5-cell accelerating cavity. (f) Schematic diagram of Jefferson Lab. The elliptical region is the electron accelerator. Beam is accelerated by two linear accelerator namely North and South linac in the straight sections. Three existing Halls A, B, C are shown.

### 3.3 TJNAF Overview

The electron accelerator in TJNAF or Jefferson Lab (JLab) is known as the Continuous Electron Beam Accelerator Facility (CEBAF) [49], uses superconducting radio frequency (SRF) technology to accelerate electrons up to 6 GeV and is capable of simultaneous beam delivery to all three experimental halls (A, B and C) at different energies, beam intensities, and orientation of beam polarization. The Q-weak experiment was carried out in the experimental Hall-C during January 2011 to May 2012, although preparation began in 2001. In the future, JLab will upgrade its energy

from 6 GeV to 12 GeV, and a new experimental hall (Hall-D) will be added [50]. A schematic of CEBAF is shown in Figure 3.2 (f). The JLab electron beam starts from a polarized source and end in the beam dump at the end station. The longitudinally polarized beam starts from the source and travels through a series of spin rotators and then accelerated by two linear accelerators and enter the experimental Hall-C. Throughout the beamline, quadrupoles and dipoles were used to focus/defocus the beam and beam position monitors (BPMs), and beam current monitors (BCMs) were used to track the beam at any given point along the beamline. Polarimeters were used to measure the beam polarization before the hall entrance. Inside Hall-C there were various modules of the experimental apparatus like targets, collimators, toroidal magnet, and detectors. This chapter will discuss various key components of the experimental apparatus in following subsections.

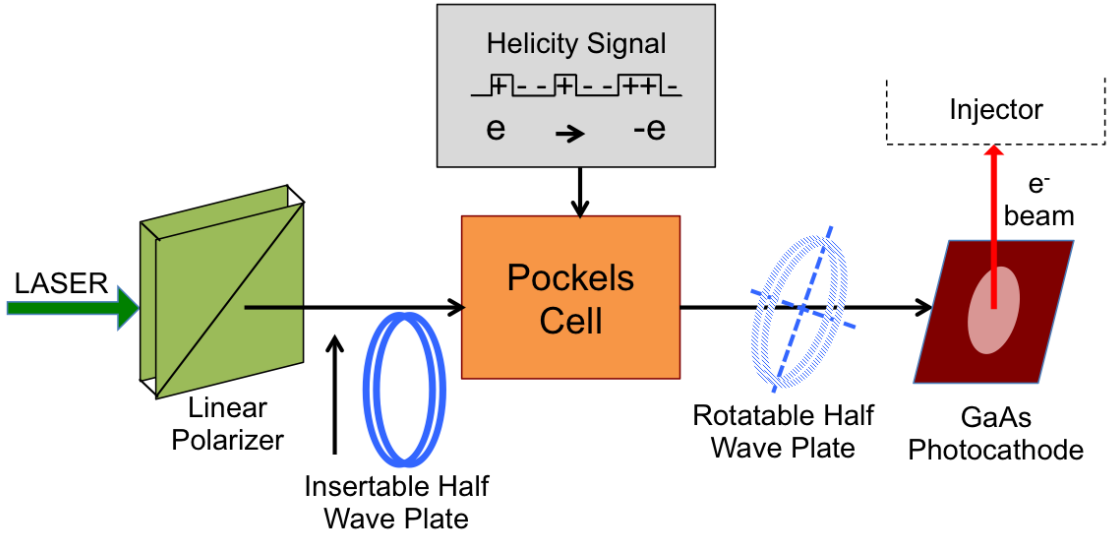


Figure 3.3 Schematic showing the process of producing circularly polarized light. The LASER is circularly polarized before GaAs photocathode using pockels cell.

### 3.3.1 Polarized Source and Helicity Reversal

The production of the electron beam starts with the polarized electron source. Circularly polarized light is used to produce polarized electrons from a strained super-lattice Gallium-Arsenide (GaAs) cathode via the photo-electric effect. This cathode is composed of several layers of material containing GaAs with varying amounts of phosphorus doping, grown on a substrate. Superlattice structure (alternating layers of GaAs and strained GaAs) increased the quantum efficiency (QE), which is the probability of the electron emission per photon [51]. Each experimental hall has a

dedicated laser that emits light at 1560 nm and pulses are  $120^\circ$  out of phase in order to provide beam delivery in all halls simultaneously. To ensure total linear polarization, the light was passed through linear polarizers (shown in Figure 3.3). An insertable half wave plate (IHWP) was used to flip the relative direction of the linearly polarized light without changing electronic helicity signal, which helps to isolate false asymmetry effects. IHWP changes the spin of the electrons by  $180^\circ$ , this provided two independent data sets namely IHWP-IN and IHWP-OUT, that helped remove further helicity correlated beam asymmetries (HCBA). IHWP states were changed at a time interval of eight hours, called slugs. A pockel cell was used to convert linearly polarized light to circularly polarized electrons using induced birefringence. Just after the pockel cells, a rotatable half wave plate (RHWp) was used to rotate the residual linear polarization to circular polarization. This also helps minimize the effect due to the helicity-correlated beam parameters that arise from the residual linear polarization interacting with the photocathode. A more detailed overview of polarized electron beam technology with references to the scientific literature on the subject is available in [52].

A double Wien filter was used to rotate the polarization of the electron beam in order to fine tune and produce fully longitudinally polarized beam during the experiment [53]. A single Wien system can flip the polarization of the beam by  $90^\circ$ . In a double Wien system both Wiens can rotate polarization by  $90^\circ$  which help to cancel systematic false asymmetries. This method also helped to produce fully transversely polarized beam for ancillary and background measurements. A dedicated chapter on transverse polarization measurement will be discussed later.

### 3.4 Accelerator

The length of the accelerator is about 7/8 miles for one complete cycle. A thermionic electron gun is used as the source of electron at the injector to extract electron beam of energy 67 MeV with the standard setup. The electron beam is accelerated by two linear accelerators (linacs), north and south linacs. A series of magnets bends the beam along the arcs which connects the two linacs. The beamlines, transporting the beam to the three halls are shown in the Figure 3.2 (f) by the red lines. Electrons from the injector are sent to the north linac at an energy of 67 MeV. Superconducting niobium RF resonant cavities shown in Figure 3.2 (e) in the north linac section accelerate the electrons, in a standard tune the maximum gain in energy per linac is 600 MeV. There are 20 cryomodules per linac, where each cryomodule consists of 8 cavities with an outer vacuum vessel, thermal radiation shield, magnetic shield, super insulation, and a welded helium vessel [49,54]. The beam then goes through the east arc and into the south linac to accelerate for another 600 MeV

energy gain. This beam can be sent directly to the Beam Switch Yard (BSY) for distribution to the experimental halls (Figure 3.2 (a)) or the beam can be steered along the west arc for another pass through the two linacs for another 1.2 GeV of energy gain. This process can be repeated up to four times. A maximum of five passes through both linacs provide energies from 445 MeV to 5945 MeV. As the beam energies are different in each pass, a different set of magnets are used to steer the beam around the arcs after each pass. One pass beam was used for the Q-weak experiment as the required beam energy was 1.155 GeV.

### 3.5 Beamlne

The beamlines that transport the beam from the accelerator to the experimental halls are shown in Figure 3.2. A two meter long dipole splits the beam for three different halls at Lambertson (Figure 3.2 (a)). Beamlines for each hall (Figure 3.2 (b)) consists of a series of quadrupole and dipole magnets to transport the beam to the target in each hall (shown in Figure 3.2 (c) for Hall-C). Total length of Hall-C beamline from the Lambertson to the beam dump was 196.12 m. The beam position, profile and current were measured at various points along the beamline using BPMs (Figure 3.2 (c)) and BCMs respectively. A part of Hall-C beamline also forms an arc, the bending magnets of the Hall-C arc were used to measure the relative beam energy with a precision of  $\Delta E/E \approx 10^{-4}$  (details in Section 3.6.4). A details sketch of Hall-C beamline elements is provided in APPENDIX ?? and discussed in technical document [55].

### 3.6 Beam Monitoring

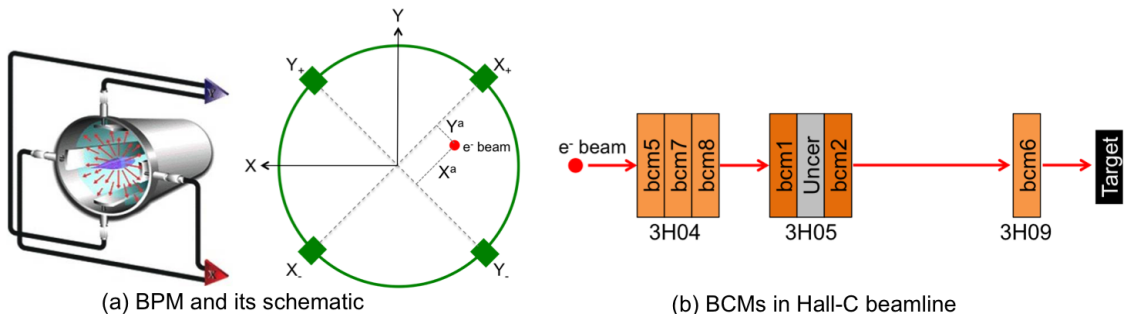


Figure 3.4 Beam position and current monitors. (a) Beam Position Monitors with four antennae rotated by  $45^\circ$  in the plane. Z axis is perpendicular to the plane. (b) Beam Current Monitors and their locations at Hall-C.

### 3.6.1 Beam Position Monitor

The beam position was continuously monitored at many places along the Hall-C beamline and throughout the accelerator by SEE beam position monitors (BPM) during data collection to ensure that the beam was centered on the target. Each beam position monitor consists of a resonant cavity of a fundamental frequency equal to that of the accelerator and the Hall-C beam. The position of the beam is measured using four antennae rotated by  $45^\circ$  in the plane (y axis is in direction opposite to gravity, x is horizontal) perpendicular to beam direction (z-axis) shown in Figure 3.4 (a). Four antennae inductively pick up the fundamental frequency of the beam as it passes through the BPM. Then radio frequency (RF) signal from each antenna (wire) is processed electronically which yields a DC signal proportional to the beam current times the distance between the wire and the beam. DC signals were sent through voltage-to-frequency converters and recorded with scalers that are read out by Experimental Physics Industrial Control System (EPICS), the system used by the accelerator and end stations for slow control and monitoring of accelerator and experiment parameters with the rest of the data from the experiment. The beam position  $X^a$  and  $Y^a$  along the axis of the wires are calculated by a difference over sum of each opposite wire as:

$$X^a = k \frac{(X_+ - X_{\text{offset}+}) - \alpha_X (X_- - X_{\text{offset}-})}{(X_+ - X_{\text{offset}+}) + \alpha_X (X_- - X_{\text{offset}-})} \quad (3.6.1)$$

Where  $X_{\text{offset}+(-)}$  is the offset for the  $X_{+(-)}$  wire,  $k$  is the sensitivity of the BPM at 1497 MHz and  $\alpha_X$  is a measure of the possibly different gain between the  $X_+$  and  $X_-$  antennae [56, 57]. The gain difference  $\alpha_X$  is defined as

$$\alpha_X = \frac{X_+ - X_{\text{offset}+}}{X_- - X_{\text{offset}-}} \quad (3.6.2)$$

The center of gravity of the four antenna signals measures relative changes in the offset of the beam from its ideal trajectory. Same approach is used to compute relative beam position  $Y^a$ . Then the position of the beam in hall co-ordinate system can be written as:

$$\begin{pmatrix} X \\ Y \end{pmatrix} = \frac{1}{\sqrt{2}} \begin{pmatrix} 1 & -1 \\ 1 & 1 \end{pmatrix} \left[ \begin{pmatrix} X^a \\ Y^a \end{pmatrix} - \begin{pmatrix} X_{\text{offset}}^a \\ Y_{\text{offset}}^a \end{pmatrix} \right] \quad (3.6.3)$$

The information from BPM for a event can not be understood as the exact beam position on target for that event, as the signals are not synchronized with the event data itself and also the actual position on target is constantly changing due to the fast raster system. Practically, an average beam

position is calculated using a rolling average of BPM data information over a specified number of previous events depending on the experiment data rate. This average beam position is then corrected for each event using the fast raster signals [58]. Normally average beam position on target is very stable over the period of a single CODA run, it is more practical to simply ignore the event-by-event BPM information and fix the average beam position as a parameter of the analysis, and to use the raster signals to measure the change in beam position relative to the fixed average position. BPMs were calibrated using the super harps in Hall-C beamline [59]. Typically calibrated BPMs has a resolution of 1  $\mu\text{m}$ . Basic details about BPMs can be found in [60].

Six BPMs in the Hall-C beamline over a span of 10 m upstream of the target were used to project the beam path at the target continuously during the experiment. Error averaged postion changes over six BPMs were used to measure the position and angle changes at the target, where BPMs in front of the target were used for the same to verify the result. Detail description about the target BPM can be found in APPENDIX ?? [61, 62] and B. Waidyawansa's thesis [63].

### 3.6.2 Superharp

A more precise and accurate determination of the beam position and profile is obtained using the superharp system. Each superharp consists of a set of two vertical wires and one horizontal wire strung on a moveable frame. These wires can be scanned across a low current beam to measure its profile and absolute position. The signals induced on the wires as they are scanned across the beam are digitized by an analog to digital converter (ADC) and correlated with the wire positions as recorded by an encoder equipped with absolute position readout electronics. Since a harp scan interferes destructively with the electron beam, data taking must be interrupted to perform the measurement. In addition to measuring the beam profile, the superharp system provided a reference coordinate against which the BPMs were calibrated.

### 3.6.3 Beam Current Monitor

Čerenkov detector yields were normalized with beam current monitors to remove charge fluctuation . A series of six beam current monitors (BCMs) were used continuously for relative measurement of the beam current in the Hall-C beamline (as shown in Figure 3.4 (b)). The BCMs were coupled cylindrical stainless steel resonant cavities [64, 65] whcih were used to measure the beam current by measuring resonance of the  $\text{TM}_{010}$  mode at 1497 MHz. This signal then converted to a voltage in a RMS-DC voltage converter and read by TRIUMF made ADCs. This voltage signal also sent

to a 1 MHz voltage to frequency (V-F) converter and scalers for event-mode normalization. In the beginning only available BCMs were 1 and 2 and latter BCMs 5, 6, 7, 8 with low noise digital receiver were added. BCMs were calibrated using a parametric current transformer device called Unser monitor for the high beam current (1-180  $\mu\text{A}$ ) where as for low current (10 nA to 1  $\mu\text{A}$ ) a Faraday cup was used for calibration. The detector yields were normalized with BCM1 and 2 during Run-I and BCM8 during Run-II. Nominal current measured by these BCMs during production running was 180  $\mu\text{A}$ . More details about BCMs used during the Q-weak experiment is discussed in a technical report by Ramesh Subedi [66].

### 3.6.4 Beam Energy

The four momentum transfer squared,  $Q^2$  is approximately proportional to square of absolute energy,  $E^2$  (see Equation 3.1.3), and measured precisely. Energy asymmetry was also measured to remove false asymmetry.

#### 3.6.4.1 Absolute Beam Energy

The Hall-C beamline arc was used as a spectrometer to measure the absolute beam energy [67]. The initial beam energy before scattering was defined as the absolute beam energy. An electron passes through an arc changes its momentum and can be expressed as

$$p = \frac{e}{\Delta\theta} \int B dl \quad (3.6.4)$$

where  $\Delta\theta$  is the change in bending angle through the arc and  $\int B dl$  is the magnetic field integral over the electron path. Three set of supersharp scanners [68] were used to determine the position and the angle by scanning the beam at the beginning, end, and middle of the Hall-C (or 3C<sup>1</sup>) arc. All the active elements (quadrupole, corrector magnets) of the beamline were turned off to avoid any distortion. This procedure is an invasive process and needed dedicated measurements. A typical energy measurement using this method yield energy as  $1160.39 \pm 1.74$  MeV [54].

#### 3.6.4.2 Energy Asymmetry

One of the helicity correlated beam parameter is beam energy asymmetry. Small changes in the energy asymmetry could result into false asymmetry, hence precise measurement of the energy asymmetry was important for Q-weak. In the middle of the 3C arc has the highest dispersion and

---

<sup>1</sup>According to JLab accelerator division coordinate system, 3C symbolize for Hall-C beamline. Similarly 1C and 2C represents Hall-A and Hall-B beamlines respectively.

is represented as 3C12 in JLab accelerator coordinate system. Any change in beam energy could result a big horizontal position change in the 3C12. Then relative energy change at the target can be expressed as

$$\Delta \left( \frac{dE}{E} \right)_{\text{target}} = \frac{1}{M_{15}} \Delta X_{3\text{C}12} - \frac{M_{11}}{M_{15}} \Delta X_{\text{target}} - \frac{M_{12}}{M_{15}} \Delta X'_{\text{target}} \quad (3.6.5)$$

where  $\Delta X_{3\text{C}12}$ ,  $\Delta X_{\text{target}}$ ,  $\Delta X'_{\text{target}}$  are position change at 3C12, position change at target, and angle change at the target respectively. First order beam transport matrix between 3C12 and target  $M_{11}$ ,  $M_{12}$ , and  $M_{15}$  were determined using OptiM [69]. This calculation works for linear models and any residual dispersion at the target or X-Y coupling are not considered in this first order calculation. More details about this model will be discussed in the following chapter. Typical energy asymmetry at the target during the experiment was  $\mathcal{O}(1)$  ppb.

### 3.6.5 Beam Modulation

The e-p scattering rate in first order depends on five beam parameters: horizontal position ( $X$ ), angle ( $X'$ ), vertical position ( $Y$ ), angle ( $Y'$ ), and beam energy ( $E$ ). Changes in these beam parameters when the beam polarization is reversed can create false asymmetries. Although different technique were used to keep helicity-correlated parameter changes as small as possible, must need to correct for such false asymmetries. To do this,  $X$ ,  $X'$ ,  $Y$ ,  $Y'$  were modulated using four air-core dipoles in the Hall C beamline and beam energy was modulated using a superconducting RF cavity. The goal of the beam modulation system was to occasionally induce controlled beam parameter changes  $\Delta X_i$ , measure the resulting detector false asymmetry  $A_{\text{false}}$ , and determine the detector sensitivities  $\partial A / \partial X_i$ . This will allow later correction of beam false asymmetries via

$$A_{\text{false}} = \sum_{i=1}^5 \frac{\partial A}{\partial X_i} \Delta X_i \quad (3.6.6)$$

Even if these corrections prove to be small under ideal running conditions, the modulation system will allow to determine any undesirable changes [70]. A dedicated chapter on beam modulation system will be discussed in following chapter.

### 3.6.6 Halo Monitors

Another important property of the beam is the beam halo which refers to stray electrons that move along with the primary beam but are sufficiently far from the beam center and can contribute

in the background. Beam halo can be generated via space-charge effects from of electrons during bunching, scraping in the beam pipe, or poor vacuum and can be measured using plastic Lucite detector and scintillation counters. An 8 mm square opening and 13 mm diameter hole were used as halo targets. The halo monitors were located immediately downstream of the halo targets and upstream of the  $\text{LH}_2$  target. The beam halo can also be estimated using the main detectors and luminosity monitors which can be normalized using the hole targets.

### 3.6.7 Fast Feed Back

The electron beam at JLab is troubled by the fluctuation in beam position and energy. These fluctuations mostly occur at the power line frequencies of 60, 120, 180 etc. Hz and rooted in the electromagnetic fields generated by the accelerator electronic equipment [71]. These deviations were largely nullified using Fast Feed Back (FFB) system by applying real time corrections targeted at the power line harmonics [72] to the RF verniers along the beamline. The FFB system was implemented by modifying the existing BPM system and integrating it to the algorithm for correction signals. The control system for FFB is EPICS based which provides a graphic interface on Unix workstations connected via Local Area Network (LAN) to a Input/Out Controller (IOC<sup>2</sup>). The FFB system was able to correct the energy fluctuation better than  $10^{-4}$  at power line harmonics up to 720 Hz using a frame rate of 3 kHz [71].

## 3.7 Polarimetry

The most dominant systematic experimental uncertainty for the Q-weak experiment is expected to come from a 1% absolute uncertainty on beam polarization as shown in Table 3.1. In order to achieve this goal two polarimeters, a well tested invasive low current Møller polarimeter and noninvasive relatively new Compton polarimeter, were used to measure the beam polarization.

### 3.7.1 Møller Polarimetry

The Møller polarimeter is used to measure the polarization of the longitudinally polarized electron beam entering Hall-C [73]. To accomplish this goal, the polarimeter measures the spin-dependent asymmetry in the elastic scattering of polarized electrons from polarized electrons i.e.  $e^- + e^- \rightarrow e^- + e^-$  (Møller scattering). This is a pure Quantum Electrodynamics (QED) process and its cross section can be calculated accurately. The target used for the scattering is a thin foil of iron

---

<sup>2</sup>VME bus embedded processor

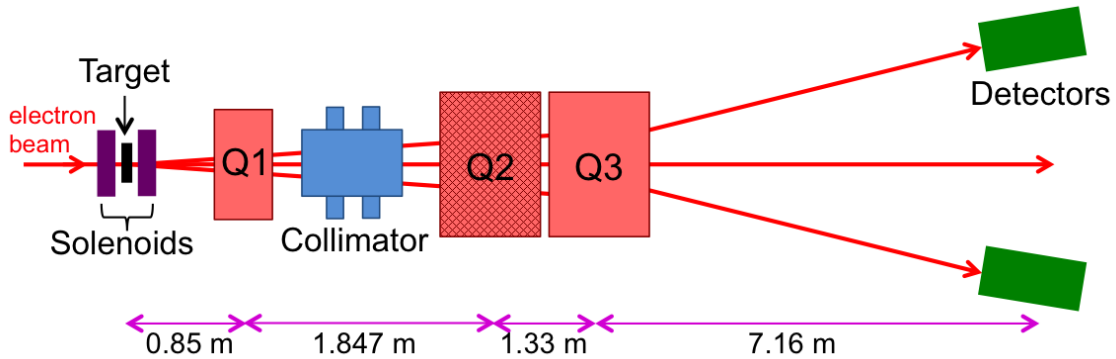


Figure 3.5 Layout of the Hall C Møller polarimeter showing tin foil target, set of superconducting solenoids, quadrupoles (Q2 was off during Q-weak), collimator box, and symmetric detectors.

magnetized by superconducting solenoids with field of  $\sim 4$  T. A set of quadrupole magnets Q1 and Q3 were used (Q2 was off during the experiment<sup>3</sup>) to focus the scattered and recoiled electrons in to the symmetric detectors in coincidence. Then detectors measure the asymmetry and then compute the polarization after correcting for the backgrounds. Figure 3.5 shows the layout of the Hall-C Basel Møller polarimeter. It was designed to operate with currents lower than  $8 \mu\text{A}$  whereas Q-weak production current was  $180 \mu\text{A}$ . During the experiment, Møller measurements were performed invasively at low currents ( $1 \mu\text{A}$ ) three times a week. The typical measured longitudinal polarization using the Møller polarimeter was about 88%. A sample of the Møller result will be shown in later chapters. More elaborated description of the Møller polarimeter can be found in M. Loppacher's thesis [74] and polarization technique used during Q-weak can be found in R. Beminiwattha's [75] thesis.

### 3.7.2 Compton Polarimetry

A new Hall-C Compton polarimeter was installed and used for the Q-weak experiment [76]. This was a noninvasive high current polarimeter and continuously took data during production data taking (with  $\sim 180 \mu\text{A}$ ). The apparatus for the Compton polarimeter includes four dipoles in a chicane, a green laser, an electron detector, and a photon detector as shown in Figure 3.6. The Compton polarimeter use the Compton scattering ( $e^- + \gamma \rightarrow e^- + \gamma$ ) of the incident electron beam with photons from a green laser. The scattered electrons and back-scattered photons provides two independent measurement of the polarization using both electron and photon detector respectively.

<sup>3</sup>some beamline optics survey suggested leakage current in Q2 and will be discussed in details in latter chapter

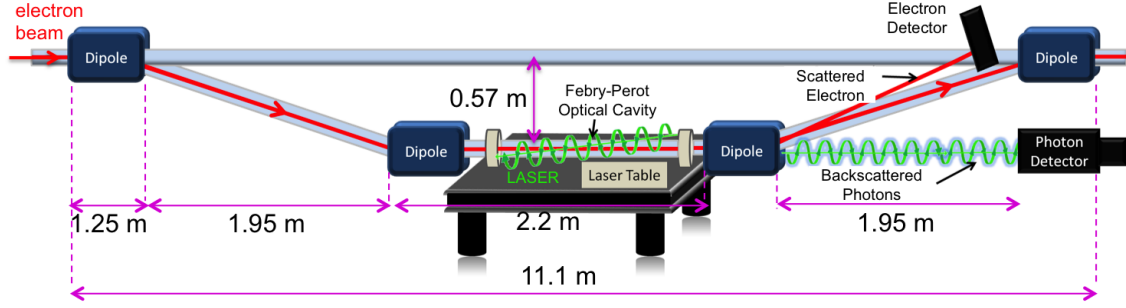


Figure 3.6 Schematic of the Hall-C Compton polarimeter. The incoming electron beam interacts with the green LASER at the straight section of the chicane. The scattered electrons and back-scattered photons are detected by electron detector and photon detector respectively for each helicity (MPS) state.

The dipole chicane were used to move the interaction point away from primary beam in order to detect back-scattered photons in the photon detector. A CsI crystal with photo multiplier tube was used as photon detector. Later in the experiment germanium silicon oxide (GSO), and led-tungstate ( $\text{PbWO}_4$ ) were used instead of CsI in the photon detector. The electron detector consist of radiation hard diamond micro-strips and for the first time used as a tracking device in an experiment. The scattered electrons were detected in a array of 96 diamond strips after third dipole. There were four detector planes, each with  $200 \mu\text{m}$  thick 96 strips, and were controlled by four VME 1495 board. The measured beam polarization using Compton polarimeter was about 87-89%. A sample of Compton result will be shown in later chapters. More detailed description of Compton polarimeter and its electron and photon detector measurements will be discussed by A. Narayan [77] and J. Cornejo [78] respectively in their future theses.

### 3.8 Targets

The Q-weak target system has two main components: a main liquid hydrogen ( $\text{LH}_2$ ) cell for production data taking and a matrix of solid targets used for background measurements and ancillary tests. Solid target ladder was thermally coupled to the bottom of the  $\text{LH}_2$  cell. A schematic of the target system is shown in Figure 3.7.

#### 3.8.1 Liquid Hydrogen Target

A 34.4 cm long liquid hydrogen ( $\text{LH}_2$ ) cell was used as the primary target for the Q-weak experiment [79]. This target can dissipate 2.5 kW of power deposited by the 1.155 GeV,  $180 \mu\text{A}$ ,

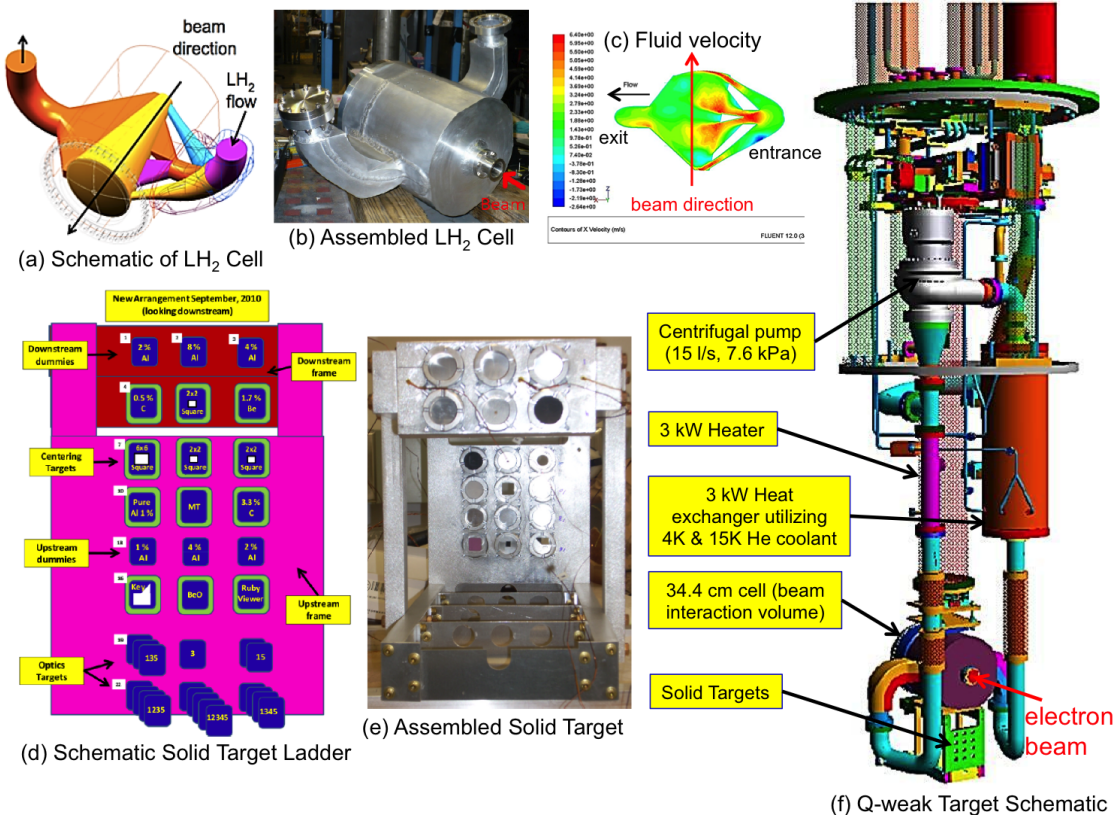


Figure 3.7 Q-weak target system. (a) Canonical shaped Computer Aided Drawing (CAD) model of target cell design. (b) Assembled LH<sub>2</sub> target cell. (c) Simulation of LH<sub>2</sub> velocity contours inside target cell using CFD. (d) Schematic of solid target ladder. (e) Assembled solid target. (f) Full schematic of the target system with key components like main LH<sub>2</sub> target cell, pump, heater, heat exchanger, solid targets are shown.

4 mm × 4 mm rastered electron beam and is the highest powered cryogenic target in the world to date. A unique hybrid cooling system used at JLab is End Station Refrigerator (ESR) for 15 K coolant and the Central Helium Liquefier (CHL) for 4 K coolant were mixed at the heat exchanger (Figure 3.7 (f)). A high power heater was used to replace the heat deposited by the electron beam in case of beam trips. It also helped to stabilize the LH<sub>2</sub> target temperature in conjunction with 15 K and 4 K coolant in a proportional integral derivative (PID) feedback system. The 55 liters of LH<sub>2</sub> was contained within a target cell of thin aluminum (Al) alloy window and was operated under 35 psi pressure at 20 K temperature and with a transverse flow of 1.2 kg/s maintained by modified automobile centrifugal turbo pump at frequency of 30 Hz.

This long canonical shaped (Figure 3.7 (a,b)) cell accommodated required 7.9° scattering angle, helped to achieve the high luminosity and hence the statistical goal. The current mode production

data taking was very sensitive to target density fluctuation as such, the target was designed using Computational Fluid Dynamics (CFD) and simulated using ANSYS [80] (a fluid dynamics simulation code) to minimize noise from density fluctuations and maintain nominal fluid density. The simulation shows the main hot spots were entrance and exit windows of the cell as shown in Figure 3.7 (c). The exit window was 0.02 inch thick aluminum alloy with a 10 inch radius of curvature and a 0.005 inch nipple to minimize backgrounds.

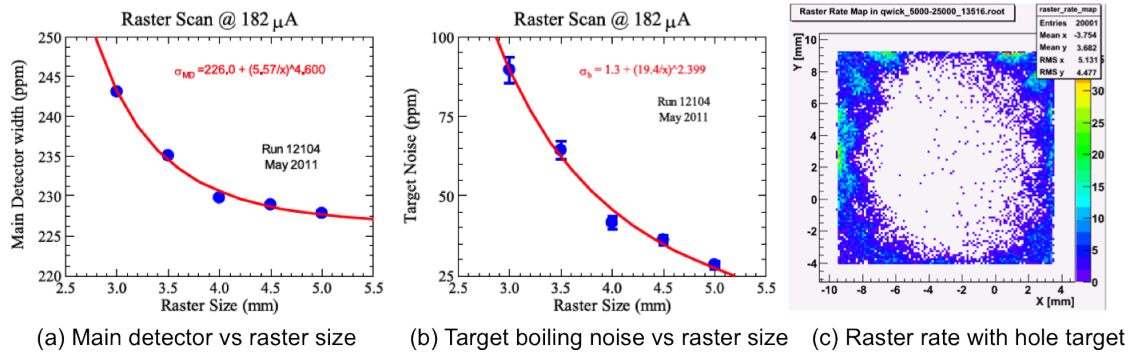


Figure 3.8 Raster studies. (a) Main detector width dependence on raster. (b) Target boiling noise studies at 180  $\mu\text{A}$  [54]. (c) 2d raster rate map with a hole target.

### 3.8.1.1 Raster

The intrinsic size of the electron beam (perpendicular to beam direction) at JLab is  $\sim 2 \mu\text{m}$  and creates localized high power density on the  $\text{LH}_2$  target. This could result in boiling the target. Hence the beam was rastered on the target over an area of 4 mm  $\times$  4 mm by the fast raster system. The raster was designed to have a matching beat frequency with fast helicity flip of 960 Hz. This method assures each integration period has the same complete raster pattern on the target and prevents systematic differences in the beam position between Macro Pulse Signal (MPS). The contribution of target density fluctuation and raster size dependence to the statistical width was measured by using known detector asymmetry widths from statistics and other sources (shown in Figure 3.8 (a)). In typical production running with 180  $\mu\text{A}$ , 4 mm  $\times$  4 mm rastered beam the contribution from target boiling noise was 46 ppm (shown in Figure 3.8 (b)), which is relatively small contribution to the statistical width of  $\sim 200$  ppm.

### 3.8.2 Solid Target

Along with LH<sub>2</sub> target an array of solid targets [81] consist of aluminum (Al) dummy targets, optics targets, and centering targets were used for background and ancillary measurements. The solid target ladder was thermally coupled to the bottom of the LH<sub>2</sub> cell as shown in Figure 3.7 (f). A detailed schematic of solid target matrix looking upstream is shown in Figure 3.7 (d,e). Horizontal and vertical motion controller were used to insert different targets into the beam. Three different Al dummy target thicknesses for both upstream and downstream locations were used to measure the effect of radiative corrections in the measured asymmetry. The optics targets were primarily used for particle origin reconstruction in the tracking measurements. Optics target helped to locate the position of the target ladder in raster rate scan as shown in Figure 3.8 (c).

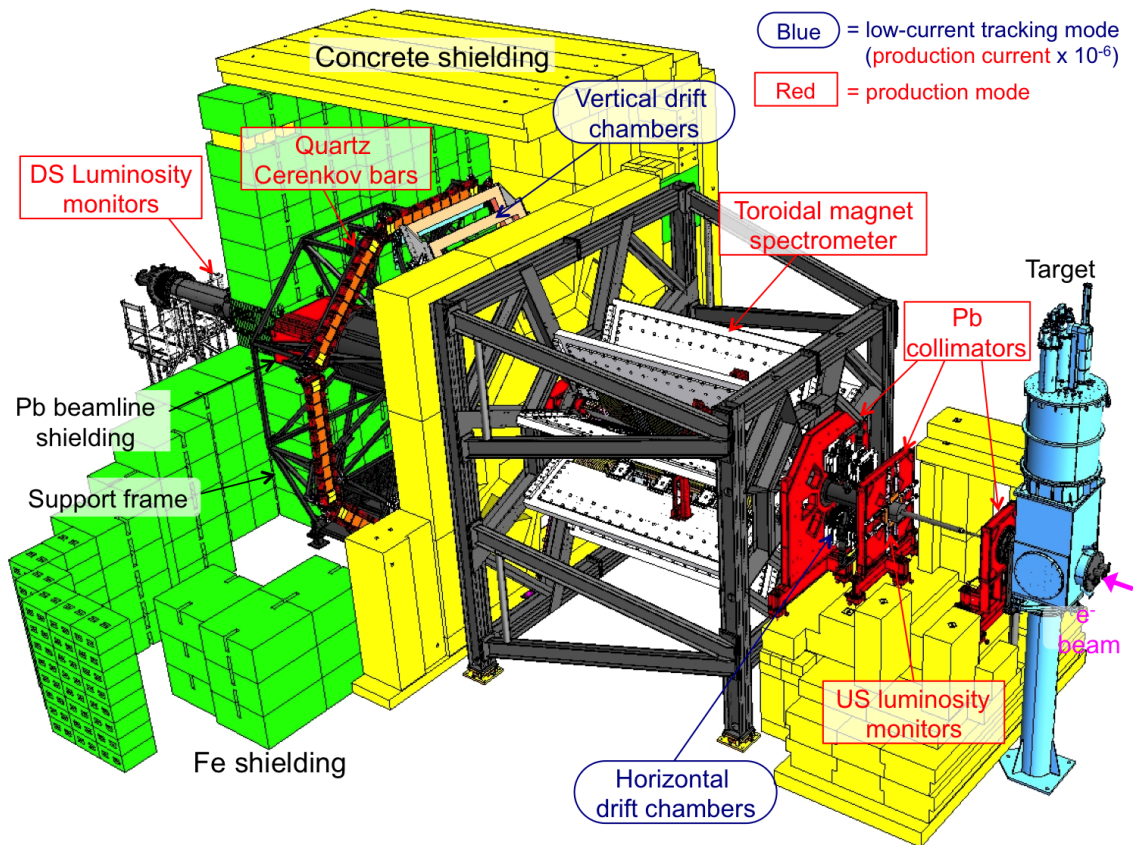


Figure 3.9 Schematic diagram of the Q-weak apparatus. The basic experimental design showing the target, collimators, toroidal magnet coils, and detectors. Elastically scattered electrons focus at the Čerenkov detectors. High current production mode apparatus components are shown in red rectangular boxes and low current tracking mode components are shown in blue elliptical boxes. Beam direction is from right to left.

### 3.9 Collimators and Shielding

A set of three lead collimators were used to define the experiment's angular acceptance and minimize the inelastic and neutral background contribution to the detector. The collimator system is shown in Figures 3.9 and 3.10 (c). The first collimator, a water cooled tungsten plug of inner radius  $\sim 7$  mm, was placed just downstream of the target and was used to reduce the electron scattering from the beamline. The second (or primary) collimator defined the acceptance as 4% of  $\pi$  in  $\theta$  and 49% of  $2\pi$  in  $\phi$ . The angular acceptance of the primary collimator from the upstream end of the target window is  $\theta = 5.8^\circ - 10.2^\circ$  and  $\theta = 6.6^\circ - 11.5^\circ$  from the downstream end. The third collimator was before the Q-weak Toroidal Magnetic Spectrometer (QTor) and further cleaned the electron flux before it reached to QTor magnetic field. Besides these three collimators a 80 cm thick shielding wall of barite-loaded ( $\text{Ba}_2\text{SO}_4$ ) high-density (2.7 g/cm<sup>3</sup>) concrete was used after QTor for addition shielding. A details description of shield wall and collimator system can be found in J. Mammei [30], and K. Myers's [54] theses.

### 3.10 Q-weak Toroidal Magnetic Spectrometer: QTor

The eight fold symmetric torodial magnetic spectrometer used for the Q-weak experiment is known as QTor (shown in Figure 3.10 (a,d)). It has race track shaped water cooled copper (iron free) magnetic coils (shown in Figure 3.10 (e)). The dimensions of the each magnet coil are 2.2 m long along the straight section, 0.235 m of inner radius, and 0.75 m of outer radius. Eight such identical coil packages with  $\Delta\phi \sim 45^\circ$  gaps between them made the QTor structure (relevant coordinate system is shown in Figure 3.10 (b)). The primary objective of QTor magnet was to focus the elastically scattered electron to the main Čerenkov detector in the focal plane of the asymmetry measurement (shown in Figure 3.10 (c)). Neutral particles (neutrons, photons, etc.) remain unchanged. Also QTor did not affect the unscattered beam as there was no field in the geometric center of the magnet. During nominal elastic asymmetry measurement QTor was operated at 8921 A whereas during inelastic ( $N \rightarrow \Delta$ ) asymmetry measurement the operational current was 6700 A. The magnet required a 10 kA power supply at 130 V and produced a field integral  $\int \vec{B} \cdot d\vec{l} = 0.67$  T.m along the central trajectory. P. Wang has more details about the QTor design structure and field map in his master's thesis [82].

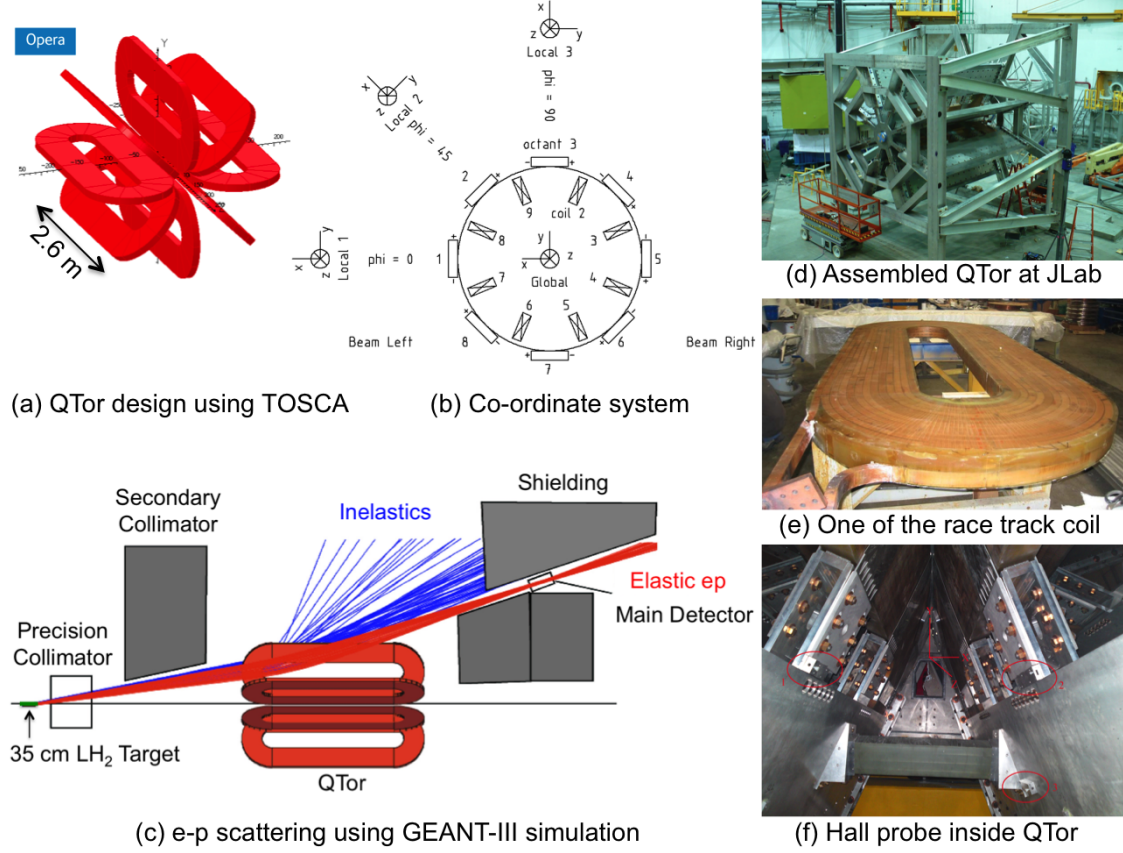


Figure 3.10 Q-weak torodial magnetic spectrometer (QTor). (a) QTor design using TOSCA. (b) Co-ordinate system. (c) e-p scattering using GEANT-III simulation. (d) Assembled QTor at JLab. (e) One of the race track coil. (f) Hall probe inside QTor.

### 3.10.1 Hall Probe

A transverse (LakShore MNT-4E02-VH) hall probe was used to measure the QTor magnetic field in real time. Three hall probe mount panels were designed and attached to the inside wall of QTor as shown in Figure 3.10(f). The probe was inserted inside the mount and attached with a LakeShore 460 3-channel Gaussmeter controller [83] via a 30 m long special magnetically shielded cable (MPEC-100). A VME IOC was then connected with the controller in order to control the system remotely via a CPU (vmec18). EPICS controls were used as a live read back system via the active EPICS channel (Q1HallP). More details about design and functionality of QTor hall probe can be found in [84].

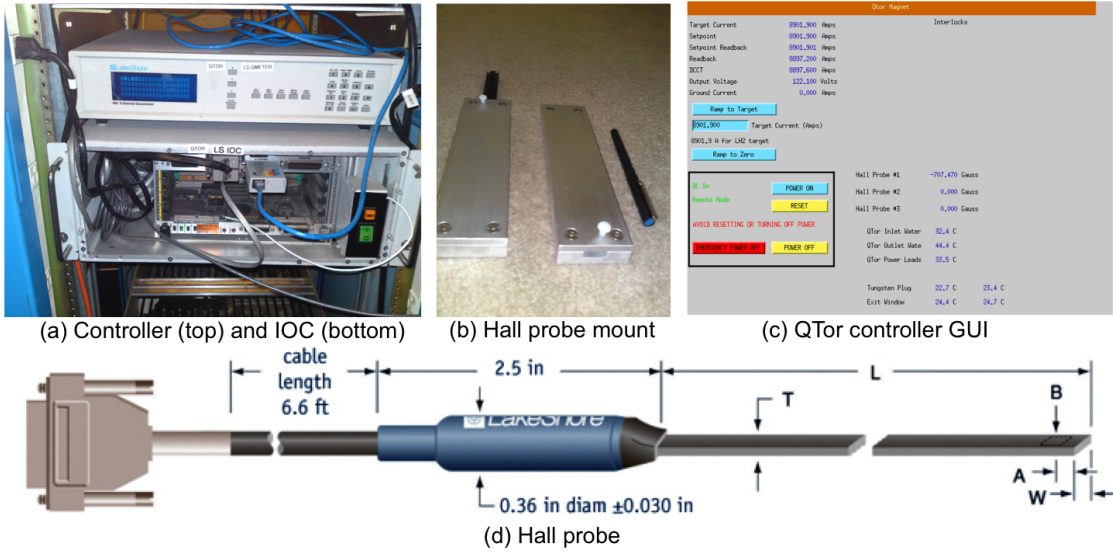


Figure 3.11 QTor controls and hall probe. (a) Lakeshore controller and IOC. (b) Hall probe mount. (c) QTor controller GUI. (d) Hall probe.

### 3.11 Detector System

The Q-weak detector system consists of main Čerenkov detectors and two set of luminosity monitors.

#### 3.11.1 Main Čerenkov Detectors

The Q-weak main detectors are  $200\text{ cm} \times 18\text{ cm} \times 1.25\text{ cm}$  fused silica Čerenkov quartz bars. The QTor magnetic spectrometer focuses elastically scattered electrons into the eight main detector bars azimuthally oriented around the beamline (Figure 3.12 (b,c)). Each detector consists of 100 cm long quartz bar optically coupled together and at each end of the bar, a 5 cm diameter photo-multiplier tube (PMT) also optically glued outside of electron flux (shown in Figure 3.12 (a)). Electrons entering the quartz produce a cone of Čerenkov light that undergoes total internal reflection. Light that reaches the ends of the bars enters the PMTs. The silica was chosen for its radiation hardness and low scintillation. A lead (Pb) pre-radiator was installed in front of the main detectors to improve elastic electron light yield and reduce neutral background. The pre-radiator improved the signal to noise ratio by absorbing soft photon background from primary electron bremsstrahlung and producing low energy electron shower. More details description of the Čerenkov detector development, construction, and installation can be found in P. Wang's thesis [87].

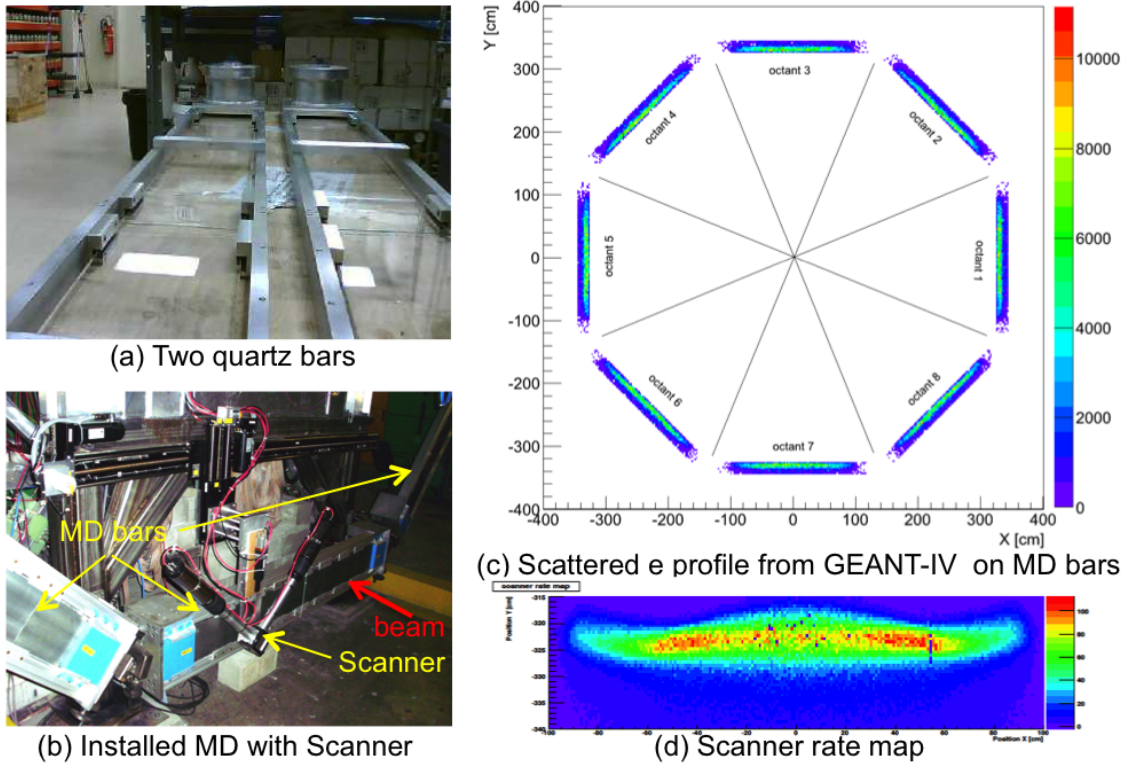


Figure 3.12 Q-weak main Čerenkov detector system. (a) Two quartz bars. (b) Installed main detectors at Hall-C with scanner system. (c) A GEANT-IV simulation showing elastic scattered electron profile on the quartz bars [85]. (d) The measured rate distribution in MD at  $50 \mu\text{A}$  beam current with  $\text{LH}_2$  target using scanner [86].

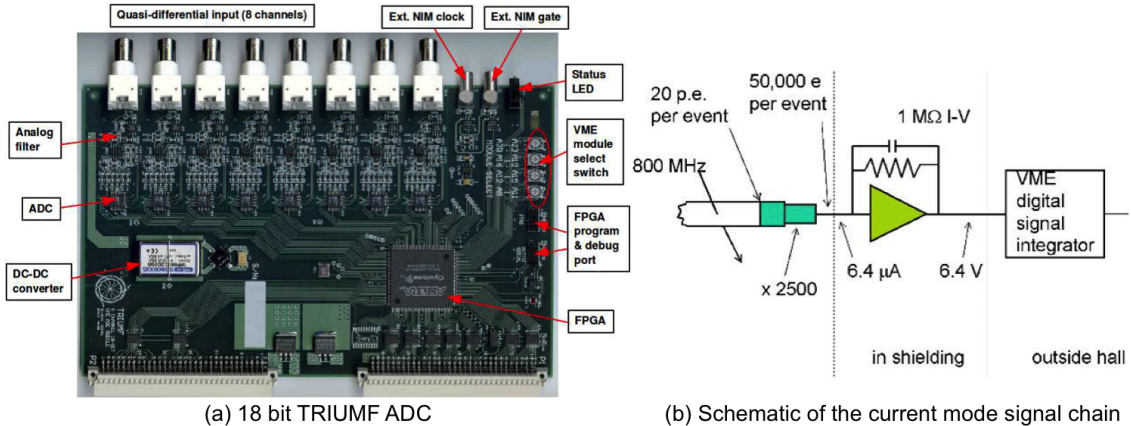


Figure 3.13 Schematic of a TRIUMF made ADC and current mode signal chain.

### 3.11.1.1 Low Noise Electronics

Low noise current-voltage preamplifiers and digitizing integrators were designed and built by TRIUMF [88] to minimize the contribution of electronic noise in the statistical uncertainty. The preamplifiers convert the DC anode current coming from the PMTs to a voltage  $\sim 6$  V signal for nominal production running. This signal is then digitized by 18-bit analog to digital converters (ADCs) at a sampling rate of 500 kHz to integrate at 1 kHz [89]. Each ADC module has eight ADC channels which were synchronized and triggered by the MPS signal from helicity board. A signal with 960 Hz event rate was integrated by summing the samples within the event window and then samples were stored in the channel memory on First-In-First-Out (FIFO) basis to avoid data loss due to delayed read-cycles. Another feature of this module was to produce the sum of the samples over four equal sub-blocks within an event. This sub-block feature of the ADCs was very useful to observe signal variations within an event for diagnostics.

### 3.11.1.2 Focal Plane Scanner

A focal plane scanner was used to measure the beam profile in both high current production running and low current tracking mode in order to test systematic effects like target density change. Two 1 cm  $\times$  1 cm  $\times$  1 cm fused silica quartz radiator overlapped in a “V” shaped and signals were read by individual PMTs in the scanner. This scanner system is then mounted on MD octant 7 (as shown in Figure 3.12 (b)) for beam profile scan. One example of such scan at 50  $\mu$ A beam current with LH<sub>2</sub> target is shown in Figure 3.12 (d). J. Pan has described in details about the construction, schematic and analysis of focal plane scanner in her thesis [86].

## 3.11.2 Luminosity Monitors

The luminosity monitors (lumis), like the main detectors, were based on fused silica Čerenkov radiators and with a light guide flushed with nitrogen gas to minimize corrosion. Two types of azimuthally symmetric luminosity monitors were used as beam diagnostic tools for the Q-weak experiment. The upstream luminosity monitors were located on the front face of the primary collimator 5 m from the target (shown in Figure 3.14 (a)) and the downstream luminosity monitors are located 17 m downstream of the target and very close to the beam dump area (shown in Figure 3.14 (b)). Both lumis were expected to detect electrons from small angle electron-proton and electron-electron scattering with an anticipated null asymmetry (ppb-level asymmetry). Upstream lumis were extremely useful for estimating beamline backgrounds. In some cases the measured asymmetry by the

lumis were not as small as expected and were also time dependent. Examples will be discussed in a later chapter. More detailed description of luminosity monitors and analysis can be found in J. Leacock's thesis [10].

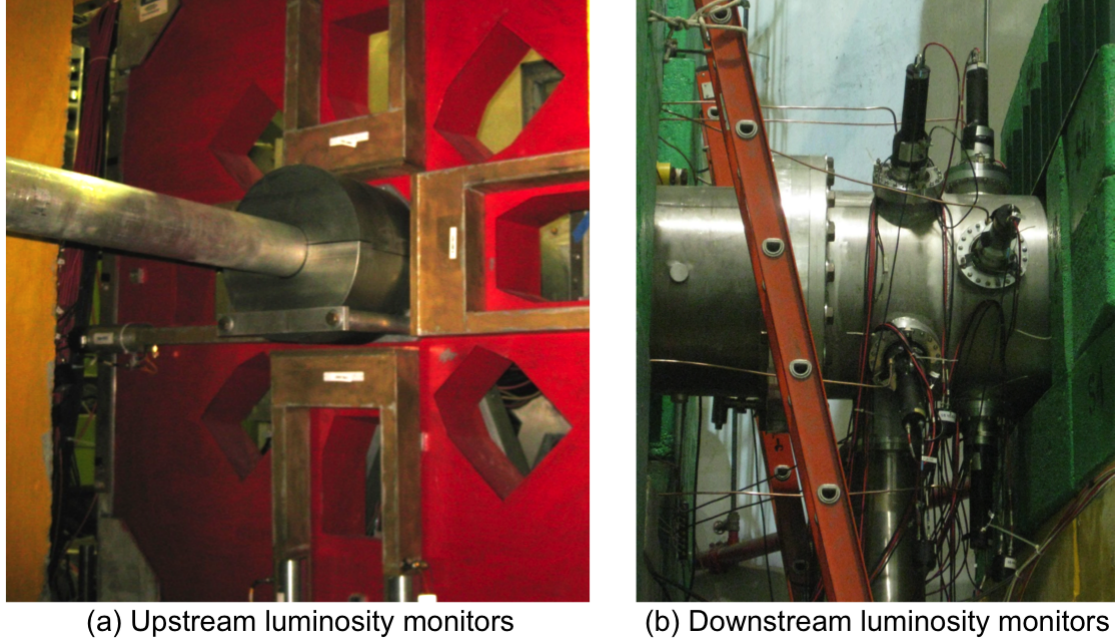


Figure 3.14 Luminosity monitors. (a) Four upstream luminosity monitors installed on the face of the primary collimator. (b) Eight downstream luminosity monitors near beam dump.

### 3.12 Tracking Detector System

The asymmetry of the elastically scattered electron is approximately proportional to the four momentum transfer squared,  $Q^2$  (details in Equation 3.1.3). A tracking system was necessary to measure  $Q^2$  with 0.5% relative uncertainty as proposed by the experiment (shown in Table 3.1). A pair of horizontal drift chambers (HDCs) in region 2 (R2) were used to determine the scattering angle  $\theta$  with an angle resolution of  $\sim 0.6 \mu\text{rad}$  and particle trajectory with a position resolution  $\sim 200 \mu\text{m}$  (as shown in Figure 3.9). Four set of vertical drift chambers (VDCs) and two trigger scintillators were used upstream of the target (shown in Figure 3.9) in region 3 (R3) to measure  $Q^2$  (more details in J. Lackey's thesis [90]). Detector packages in R2 and R3 can be rotated into each MD octant pair using a mechanical rotor to measure any octant dependence. Relation of  $Q^2$  with  $\theta$  is shown in Equation 3.1.3. The tracking system operated at  $\sim 6$  order of magnitude smaller beam

current than parity production current. A details description of tracking system can be found in J. Pan's thesis [86].

### 3.13 Data Acquisition

The Q-weak data acquisition (DAQ) system was based on the CEBAF Online Data Acquisition (CODA) [91, 92] framework designed for experiments at Jefferson Lab. Two independent DAQ configurations were used for the experiment: integration mode for high current production data taking and counting mode for low current tracking measurements. The data taking during integration mode was triggered by the MPS signal from the accelerator with frequency of 960 Hz and trigger scintillators were used as the trigger for the event mode running. A software prescale factor was used to control how often the DAQ was triggered by the specific trigger for each hardware trigger. Several read out controllers (ROCs) were used to install different subsystem electronics. The CODA system used ethernet to communicate with all the ROCs. The Event Builder (EB) system was used to generate complete event from data fragments read from ROCs and the Event Transfer (ET) system provided central access to data events for multiple clients at real-time. The data rate during integration mode was approximately 5.6 MB/s. Data taken in an hour was defined as run and each run was segmented into 1.9 - 2.0 GB data files called runlets. One run has about 9 - 12 runlets. During the entire experiment  $\sim$ 120 TB of raw data were collected. The averaged data such as yields, asymmetries, differences, HWP state, target, regression slopes, flags for data quality were saved to a MySQL database. B. Waidyawansa [63] and R. Beminiwattha [75] provided more technical details on data acquisition in their theses.

### 3.14 Online Displays and Data Monitoring

The collected raw data files were processed to produce CERN ROOT and MySQL structured files for real time data quality monitoring and to store for future analysis. The real time analyzer produced a ROOT file for the first 100,000 events for each one hour production run. This ROOT file was used to generate all the necessary figures and summary tables to monitor the data quality and key physics parameters. Then C++, ROOT, and HTML based analysis structure **qwanalysis** with Hall-C wrapper script **hclog-post** [93] were used to produce HTML files and uploaded automatically to Hall-C electronic log book (HCLOG) for each run. A CODA trigger was used to initiate the analysis process when ROOT file generation for the first 100,000 events was completed. Necessary precautions

and changes were made for the next run based on careful screening of standard acceptable set of parameters for the ongoing run.

One of the key component of the experiment was the target and was necessary to monitor it constantly. A C++ and Virtual Network Computing (VNC) based software was used to monitor the target, and related parameters and to publish the status in the web. A snapshot of the target controls, all the key parameters, temperature from different sensors, cryogenic liquid flow, alarm handler, and cameras that monitors the target were taken every few minutes by the software and uploaded in the website [94]. This system was also used as a backup control system for the target in case of a failure of the computer that controlled the target. The same software, and technique were also used to monitor the beamline optics [95] for each production run by monitoring the BPM responses to the beam modulation signals and will be discussed in the later chapter.

### 3.15 Parity Analysis

To extract the main detector normalized yields for asymmetry calculations, several corrections applied on raw yields as described below.

$$Y^{+/-} = \frac{\frac{(Y_{\text{raw}}^{+/-} - Y_{\text{ped}}) \times g}{N_s}}{I^{+/-}} \quad (3.15.1)$$

where  $Y_{\text{raw}}^{+/-}$  is the raw ADC signal in the “+/-” helicity state,  $Y_{\text{ped}}$  is the measured beam off signal or pedestal (a details pedestal analysis of the entire experiment is discussed in latter chapter),  $g$  is the calibration factor to convert ADC counts per sample to volts,  $N_s$  is the number of  $2 \mu\text{s}$  read-out samples per MPS state, and  $I^{+/-}$  beam is the beam current in the “+/-” helicity state. The pedestals were subtracted from the raw signals to remove the effect from the DC offsets of the electronics chains, dark current due to thermal noise and cosmic rays. In order to sum the two PMT signals for one detector to obtain the detectors yield, or to sum the total 16 PMT signals to obtain the yield for all detectors, the gains of those PMT channels were matched to each other. The main detector yields are normalized to beam current to reduce the dependence on beam intensity fluctuations. Beam stability cut is applied to the raw detector yield to eliminate data taken during a beam trip or unstable beam excursion [75]. Further cuts to the data are made on a runlet-by-runlet basis during data quality checks.

The parity analysis engine processes raw data to extract event and pattern based quantities. Events which pass the event and pattern number checks are grouped into patterns of four events,

known as quartets and the pattern based differences, yields, and asymmetries are computed as shown in Table 3.3. In the final step of the data analysis process, event and pattern based processed data were saved into a set of pre-defined histograms and ROOT trees. Event based yields are saved in the Mps\_Tree and pattern based differences, yields, and asymmetries are saved in the Hel\_Tree. Additionally, event based EPICs values for key components (QTOR current, target position, etc.) are stored in a Slow\_Tree. The running averages, running sums, uncertainties on the running averages and the slow control values are written into the MySQL databases.

Table 3.3 Definition of different variables used in the experiment [63]. The subscripts indicate the event sequence in a quartet pattern defined as 1, 2, 3, 4 with helicity “ $+-+$ ”. The definition of differences, yields, and asymmetries are shown here. Two different ways of combining yields and asymmetries were used in the experiment. The barsum yields are extracted using yields of the left/right PMTs ( $Y_{L/R}$ ) with proper weights ( $W_{L/R}$ ). The yields and asymmetries for each detector bar or for the whole detector were computed using the barsum yields and asymmetries. Another way to combine yields and asymmetries was pmtavg. The yield and asymmetry for each PMT were calculated first and then averaged to get yields and asymmetries for each detector or whole detector.

Quantity	Definition	Comments
differences	$D = \frac{(Y_1^+ + Y_4^+) - (Y_2^- + Y_3^-)}{2}$	BPMs, Combined BPMs, Energy calculator
yields	$Y = \frac{(Y_1^+ + Y_4^+) + (Y_2^- + Y_3^-)}{2}$	All detectors
asymmetry	$A = \frac{(Y_1^+ + Y_4^+) - (Y_2^- + Y_3^-)}{(Y_1^+ + Y_4^+) + (Y_2^- + Y_3^-)}$	PMTs, Lumis, BCMs,BPM effective charge
barsum	$Y_{\text{barsum}} = \frac{W_L Y_L + W_R Y_R}{W_L + W_R}$	$A_{\text{barsum}}$ calculated using yields
pmtavg	$A_{\text{pmtavg}} = \frac{1}{2}(A_L + A_R)$	$A_{L/R}$ is calculated from PMT yields
mdallbars	$Y_{\text{allbars}} = \frac{1}{8} \sum_{i=1} Y_{\text{barsum}}^i$	$A_{\text{allbars}}$ calculated using yields
mdallpmtavg	$Y_{\text{pmtavg}} = \frac{1}{16} \sum_{i=1} (Y_L^i + Y_R^i)$	$A_{\text{pmtavg}}$ calculated using yields

## SECTION 4

### BEAM MODULATION

#### 4.1 Introduction

The e+p scattering rate largely depends on the five beam parameters: horizontal position ( $X$ ), horizontal angle ( $X'$ ), vertical position ( $Y$ ), vertical angle ( $Y'$ ), and energy ( $E$ ). Changes in these beam parameters when the beam polarization is reversed create false asymmetries. Although attempt has been made to keep changes in beam parameters during reversal as small as possible, it is necessary to correct for such false asymmetries. A challenge for the Q-weak experiment was to keep these helicity-correlated parameter differences as small as possible and measure the detector sensitivities. The goal of the beam modulation system is to occasionally induce controlled beam parameter changes  $\Delta T_i$ , measure the resulting detector false asymmetry  $A_{\text{false}}$ , and determine the detector sensitivities  $\frac{\partial A}{\partial T_i}$ . This technique will allow to correct for the beam false asymmetries as shown in Equation 5.1.1. Even if these corrections were small under ideal running conditions, the modulation system described in this chapter will allow to quickly determine if undesirable changes have occurred.

$$A_{\text{false}} = \sum_{i=1}^5 \left( \frac{\partial A}{\partial T_i} \right) \Delta T_i \quad (4.1.1)$$

#### 4.2 Measurement Time vs Modulation Asymmetry

It is assumed that it would be helpful to measure the whole-detector sensitivities to 10% accuracy every few days (provided it can be done using only a small fraction of the beam time and without beam strikes or halo scraping) [96]. Stable sensitivities would yield uncertainties of a few percent by the end of the experiment, which is much better than one would need to regress out the helicity-correlated differences seen in the previous parity violating experiment HAPPEX [97]. However, frequent whole-detector sensitivity measurements might reveal important changes in the beam or the target cell position, the presence of an unmeasured beam parameter, or even a broken glue joint in the main detector. Furthermore, accurate single octant sensitivities (which would be obtained as a by-product) are an essential prerequisite to extract the  $\sin \phi$  and  $\cos \phi$  dependence which are characteristic of residual transverse beam polarization.

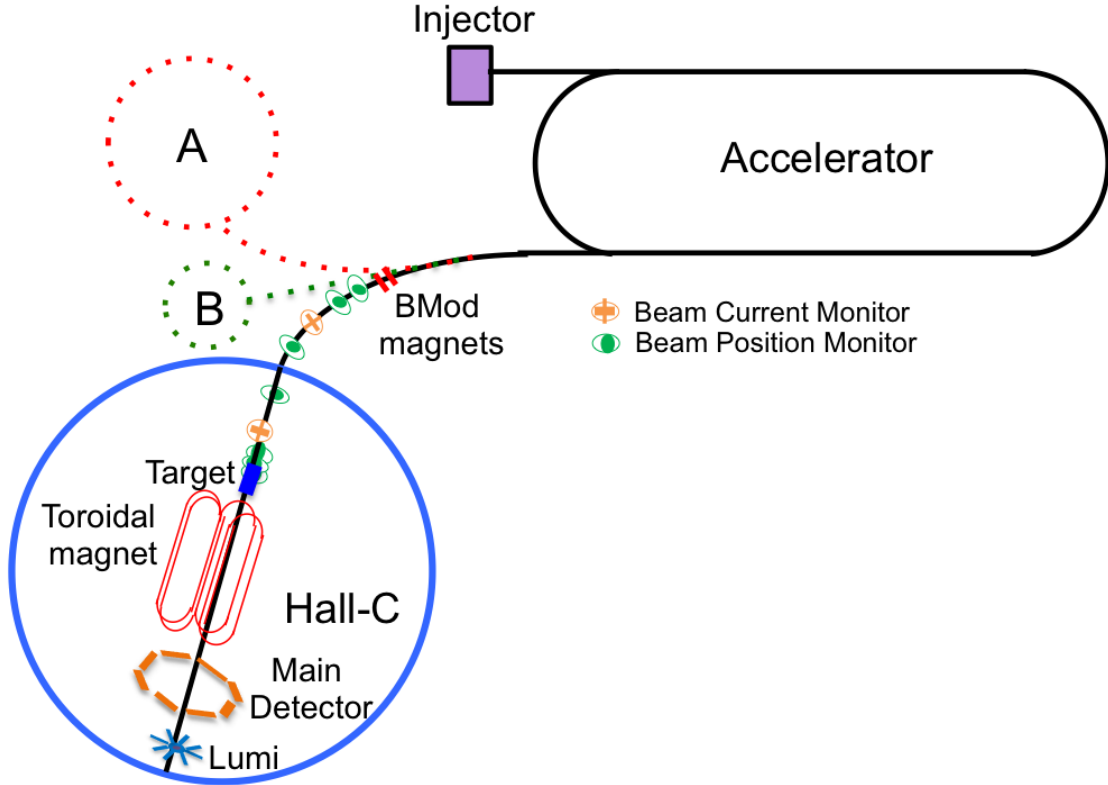


Figure 4.1 Simple schematic cartoon of the accelerator. The beam modulation magnets are shown in Hall-C beamline. The BPMs, BCMs, and other key components of the experiment are shown in the Hall-C beamline.

For the size and duration of the modulations discussed here, the natural beam jitter and the SEE BPM (section 3.6.1) electronic noise of roughly  $5 \mu\text{m}/\sqrt{\text{Hz}}$  will be negligible. If this was not the case, measurement times would become much longer. This means that the uncertainty on the detector sensitivities is dominated by the statistical uncertainty on the detector false asymmetry. At nominal luminosity, the Q-weak experiment has a rate of 800 MHz/octant, hence the whole-detector statistical sensitivity,  $dA$ , is  $12.5 \text{ ppm}/\sqrt{t}(\text{sec})$  or 1 ppm in 156.25 seconds. The clock times needed to measure a single beam sensitivity to 10% are therefore given by

$$t(s) = \frac{1}{\text{DF}} \frac{\left( \frac{12.5 \text{ ppm}}{A(\text{ppm})} \right)^2}{\left( \frac{dA}{A} \right)^2} = \frac{1}{\text{DF}} \left( \frac{12.5 \text{ ppm}}{A(\text{ppm})} \right)^2 (10)^2 \quad (4.2.1)$$

Table A.1 estimates required clock time for a 10% measurement of a single beam sensitivity with different assumptions about the modulation asymmetry and the modulation duty factor. A

Table 4.1 Dead time calculation for beam modulation. The clock time needed to measure detector sensitivity for a single parameter and how it varies with asymmetries are shown here.

Modulation asymmetry [ppm]	Clock time required		
	10% DF [Hours]	1% DF [Hours]	0.1% DF [Hours]
1	43	430	4300
10	0.43	4.3	43

modulation of 10 ppm would permit a measurement of all 5 sensitivities to 10%, require about 1-10 calendar days, and have minimal negative impact on production duty cycle. For fixed uncertainty, smaller amplitudes would require at least quadratic increases in measurement time or duty factor (DF). For fixed measurement time and duty factor, smaller amplitudes would cause at least linear increases in the uncertainties.

### 4.3 Modulation Amplitude

The next important step was to estimate the modulation amplitudes for beam position and angle necessary to achieve  $A_{\text{false}} = 10$  ppm. Detailed simulations on sensitivities have been performed using Geant-3 and is discussed in [98]. The simulated single octant detector sensitivities are dominated by the interaction of e+p elastic scattering with the defining collimator, and are shown in the second column of Table A.2. Except for energy, the whole detector sensitivities were much smaller. They were much more complicated since they were determined by imperfect cancellation of the linear sensitivities due to broken symmetries (coil misalignment, radiator radial positions), plus quadratic sensitivities which depend on beam offsets. It is not unreasonable to disagree as to what expected suppression factor is to be used in going from single octant sensitivities to whole detector sensitivities. Therefore, the relatively conservative cancellation factor was assumed to be 50, which leads to the modulation amplitude for position, angle, and energy to generate 10 ppm whole detector asymmetry and are shown in Table A.2.

The estimated whole detector sensitivities were small. Compared to the Q-weak statistical uncertainty of  $\sim 5$  ppb, the beam parameter corrections resulting from the helicity-correlated differences seen in the previous parity violating experiments [97]  $\mathcal{O}(1 \text{ nm}, 0.1 \text{ nrad}, 0.1 \text{ ppm in energy})$  were negligible. Alternatively, this means the allowable uncertainty in determining the beam sensitivity is 100%, so a system capable of making a 10% measurement on all 5 beam sensitivities every 1-10 days is apparently overkill. The real value of such a beam modulation system may be to detect undesired

Table 4.2 A crude estimate of the modulation amplitudes to generate 10 ppm whole detector asymmetries.

Beam Parameter	Single Octant Sensitivity	Assumed Cancellation	Whole Detector Sensitivity	Modulation Amplitude for 10 ppm
Position	10 ppb/nm	50	0.2 ppb/nm	50 $\mu\text{m}$
Angle	30 ppb/nrad	50	0.6 ppb/nrad	20 $\mu\text{rad}$
Energy	1 ppb/ppb	1	1 ppb/ppb	10 ppm ( $\sim$ 10 keV)

changes in the experiment, or as insurance in case the e+p sensitivities prove to be much larger than anticipated, or for those cases where the sensitivities are known to be much larger e.g., for elastic scattering on  $^9\text{Be}$  or  $^{27}\text{Al}$  window-like targets, inelastic scattering on  $\text{LH}_2$  or  $^{27}\text{Al}$ , or the small angle scattering into the luminosity monitors.

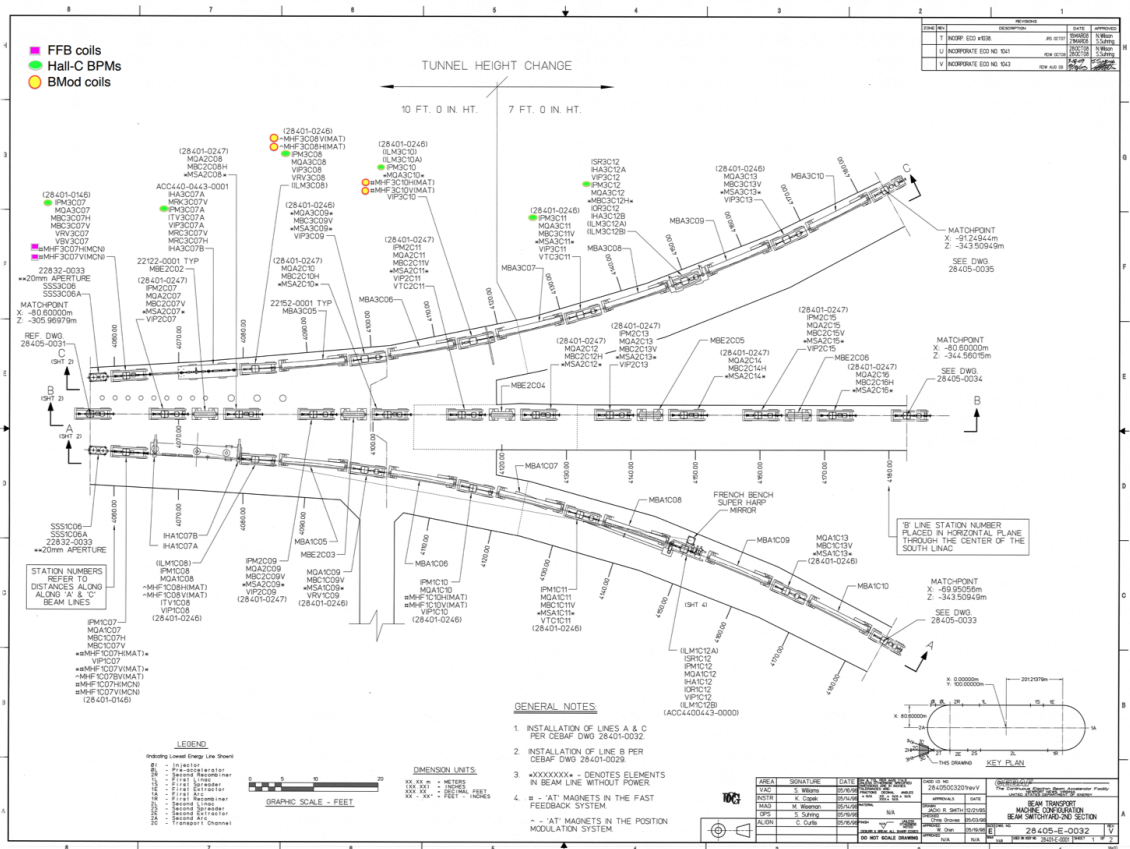


Figure 4.2 Jefferson Lab and its beamline schematic for all three experimental halls using Computer Aided Design (CAD) drawings (informally referred as songsheets at Jefferson Lab) are shown. Beam modulation magnets, fast feed back coils, and BPMs in the Hall-C beamline are labeled separately.

## 4.4 Optics Calculation

A software written by Valery Lebedev for linear and non-linear optics calculations, OptiM [69], and an input deck prepared by Jay Benesch [99] (JLab) were used to simulate the Hall-C beamline (3C). The 3C beamline was substantially modified before Q-weak to accommodate the Compton polarimeter. A schematic view of the Hall-C beamline (songsheet<sup>1</sup>) along with the other halls are shown in Figure 4.2. The goal for the beam modulation system was to achieve robust modulation in  $X$ ,  $X'$ ,  $Y$ ,  $Y'$ , and  $E$  at the target. These modulations do not have to be strictly pure, but they have to be linearly independent so that have solutions for the individual sensitivities. The asymmetries from position modulations were an order of magnitude larger than the corresponding asymmetries from angle modulations for similar sized magnet kicks in the Q-weak and will be discussed in later sections of this chapter. This fact, plus the relatively large statistical noise in the detector asymmetries, plus the certainty of small drifts in the optics, suggested that mixed mode modulation is unlikely to be robust. Running times and uncertainties were also quite difficult to estimate for the mixed mode modulation. Therefore, relatively pure modulations in which  $\sim 90\%$  of the asymmetry arises from the variable of interest was attempted to produce.

### 4.4.1 Simulation using OptiM

The main OptiM deck [100] contain the information about the location, field strength, size, orientation etc. for each component of the Hall-C beamline. The OptiM deck was used to obtain transfer matrices, orbit excursion, beta functions, and simulated trajectories between any two beamline elements in forward or inverse direction.

### 4.4.2 Inverse Beamline

An insightful starting exercise was to start with a pure position or angle deviation at the target and use OptiM to send tracks in the upstream direction which was named as inverse beamline or orbit. Figure 4.3 shows the orbit from the target to the Lambertson (beginning of the 3C line). All 4 panels have the same qualitative features: the beam moves to the right with piece-wise continuous motion, there is a discontinuity at each quadrupole location, and there is at least one zero crossing. The reason this inverse trajectory is so interesting is that, due to time-reversal invariance of electromagnetic interactions, it provides the information about how to perturb a forward beam

---

<sup>1</sup>The CAD drawings were informally referred as songsheets at Jefferson Lab. The CAD annotation is static. Only element names are shown in the drawings.

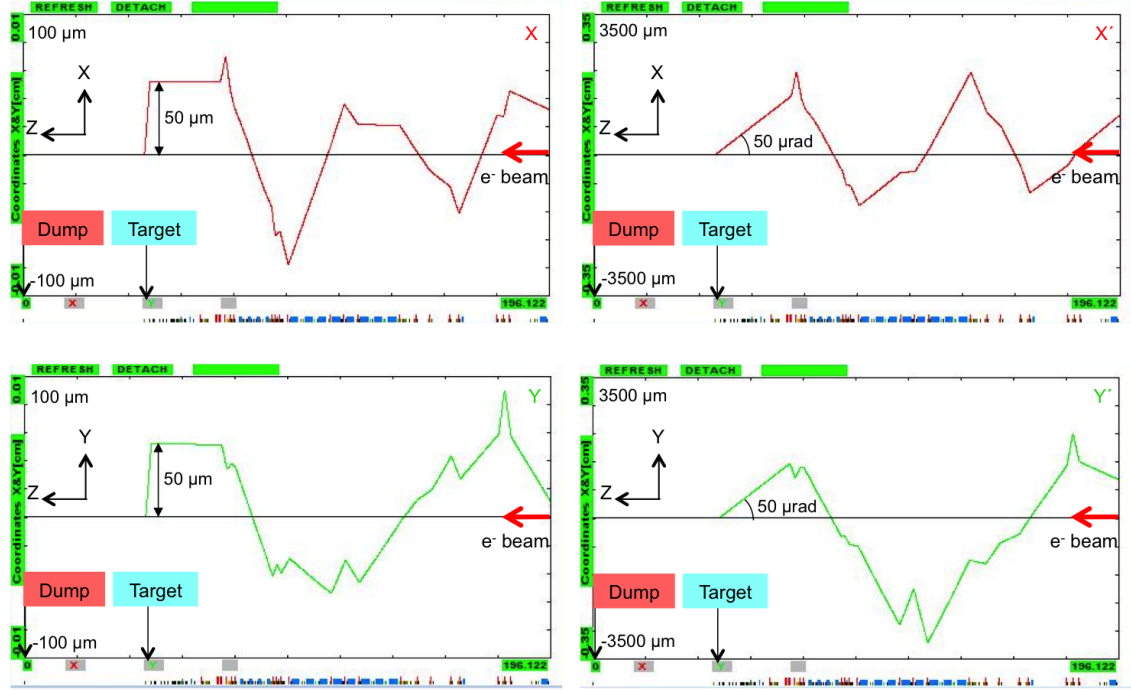


Figure 4.3 Inverse orbit excursions simulation from OptiM. The direction of the beam is from right to left. The tiny blue and red boxes on the horizontal axis at the bottom of the figures are dipoles and quadrupoles, respectively. The location of the target and beam dump are also marked. The orbit excursion for the relatively pure  $X$ ,  $X'$ ,  $Y'$  and  $Y$  motion at the target are shown in the four panels (from top left in clockwise direction).

to obtain a pure position or angle change at the target. As long as the inverse orbit stays inside the beampipe, such a figure is an existence proof that pure modulation at the target is possible with a forward beam.

#### 4.4.3 Forward Beamline with Position or Angle Kicks

The simplest way to perturb an arbitrary forward beam onto the magic trajectory obtained using inverse beamline is to kick the beam with a single small dipole at one of the zero crossings. However, if driving coils were restricted to the first half of the 3C arc, this strategy was not feasible because there was only one zero crossing in that region (corresponding to pure  $X'$  modulation), with no zeros corresponding to  $X$ ,  $Y$ , or  $Y'$  modulation. A better approach was then suggested by Mike Tiefenback [101], similar to that used in the JLab Fast Feedback System (FFB) [71, 72]. As schematically shown in Figure 4.4, pairs of separated coils could be used to take an arbitrary forward ray, offset its position and angle, and re-inject it along the appropriate trajectory to produce

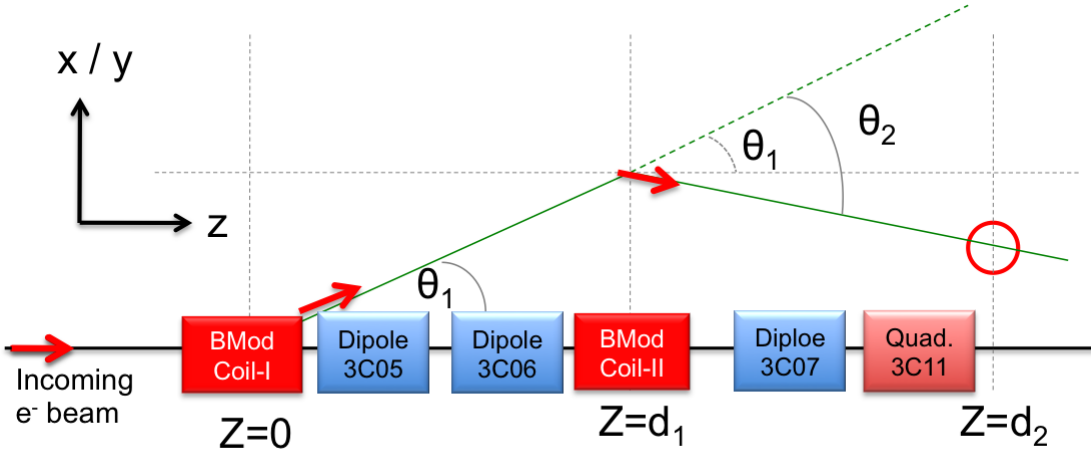


Figure 4.4 A sketch of beam modulation concept. A pair of magnets ( $Z=0$  and  $Z=d_1$ ) with opposite kick were used to match a trajectory at any arbitrary point ( $Z=d_2$ ) in the beamline. There were two big dipoles between the modulation magnets. Using simple algebra  $\theta_1$  and  $\theta_2$  can be expressed in terms of position and angle at the match point. Hence required field integral in the beam modulation magnets can be calculated to generate a particular trajectory (details of the calculation in APPENDIX A).

a pure position or angle change at the target. Detailed OptiM solutions for forward rays are shown in Figure 4.5 for a pair of coils separated by 9.5 m. Note that position modulation of  $\pm 250 \mu\text{m}$  at the target yields orbit deviations of similar magnitude in the beamline, while angle modulation of  $\pm 50 \mu\text{rad}$  at the target yields orbit deviations of up to 3 mm. The size of the latter orbit deviations is large enough to cause some concern about scraping of the beam or halo. (The impact on the Compton polarimeter laser X electron beam lock has not been examined.) Hence the angle kick was reduced by an order of magnitude smaller to match the size of the orbit deviations. This might be a better match to the size of natural beam jitter, but the time required in Table A.2 for a single 10% measurement would increase by at least a factor of 100. The field integrals for that yielded pure modulations at the Q-weak target were calculated using most updated available OptiM deck [100] and are shown in Table 4.3. These field integrals were converted to currents using the measured MAT coil field constant of 330 G-cm/A. This two-coil scheme was very convenient, as any changes in the 3C line was easily simulated for the modulation system by re-tuning the ratio of coil currents without having to move coils.

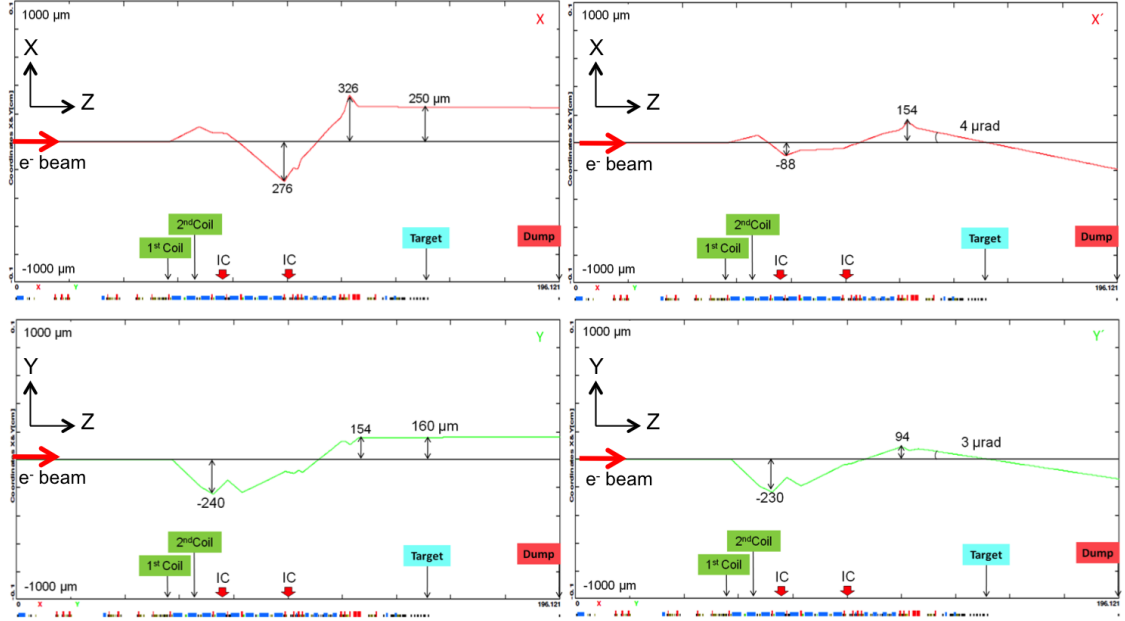


Figure 4.5 Forward orbit excursions simulation from OptiM. Beam moves from left to right. The ting blue and red boxes on the horizontal axis at the bottom of the figures are dipoles and quadrupoles, respectively. Simulated location of the modulation magnets and recommended location for ion chambers are shown in the figures. The forward orbit excursion for the relatively pure  $X$ ,  $X'$ ,  $Y'$  and  $Y$  motion at the target are shown in the four panels (from top left in clockwise direction).

Table 4.3 Required field integrals for the modulation dipole pair to generate relatively pure position and angle at the target from OptiM are shown here. Coil currents to produce such field integrals are calculated. The ratio between coil current in 2nd and 1st coil is defined as tune parameters. The negative tune parameters signifies the out of phase current in the two coils.

Beam Parameter	Amplitude for 10 ppm	$I_1$ [A]	$\int \vec{B} \bullet d\vec{l}_1$ [G-cm]	$I_2$ [A]	$\int \vec{B} \bullet d\vec{l}_2$ [G-cm]	Tune
$X$	$250 \mu\text{m}$	0.159	52.4	-0.372	-122.9	-1.875
$X'$	$4 \mu\text{rad}$	0.554	183.0	-1.872	-618.0	-3.864
$Y$	$160 \mu\text{m}$	-0.242	-80.0	0.060	20.0	-0.367
$Y'$	$3 \mu\text{rad}$	-1.606	-530.0	0.771	254.0	-0.489

#### 4.4.4 Forward Rays with Energy Kick

The beam energy was modulated using a superconducting RF cavity in the South Linac of the accelerator. The effect of a simulated 10 ppm energy kick from OptiM is shown in Figure 4.6. At 3C12, the point of highest dispersion (the middle of the 3C arc), the induced motion is shown by a  $41 \mu\text{m}$  red spike. From a comparison of Figures 4.5 and 4.6, it is pretty clear that energy

changes could not possibly be confused with position or angle changes. Further downstream in the beamline, the small green bump represents the dispersion inside the vertically bending Compton chicane. Because of the lower dispersion, the induced motion in the Compton was only about  $5 \mu\text{m}$ , much smaller than the nominal JLab electron beam rms width. The energy change at the target was identified in terms of change in beam position at 3C12 and at any arbitrary location. A pair of BPMs at the beginning or the end of the 3C arc would seem to be the most natural choice for energy change measurement. Any two  $X$  BPMs on the beamline could be used as long as the magnifications were favorable. But there were advantages to work in terms of target position ( $X_T$ ) and angle ( $X'_T$ ) because: 1) these were the coordinates that were used in the simulations to estimate the beam sensitivities, and 2) there were seven BPMs in the drift region upstream of the target which provided flexibility to determine  $X_T$  and  $X'_T$  with relatively high accuracy [61]. Previous experiments typically used two BPMs in front of the target, thus lacking the above two advantages.

The position or angle at 3C12 in terms of target parameters can be expressed as

$$\overleftrightarrow{X}_{3C12} = \underline{M} \overleftrightarrow{X}_T \quad (4.4.1)$$

Expanding the Eq. 4.4.1

$$\begin{bmatrix} X \\ X' \\ Y \\ Y' \\ \frac{dE}{E} \end{bmatrix}_{3C12} = \begin{bmatrix} M_{11} & M_{12} & M_{13} & M_{14} & M_{15} \\ M_{21} & M_{22} & M_{23} & M_{24} & M_{25} \\ M_{31} & M_{32} & M_{33} & M_{34} & M_{35} \\ M_{41} & M_{42} & M_{43} & M_{44} & M_{45} \\ M_{51} & M_{52} & M_{53} & M_{54} & M_{55} \end{bmatrix} \begin{bmatrix} X \\ X' \\ Y \\ Y' \\ \frac{dE}{E} \end{bmatrix}_T \quad (4.4.2)$$

where the matrix elements were obtained from [100] and can be written as

$$M = \begin{bmatrix} 0.69 & -928 & 0 & 0 & 411 \\ -5 \times 10^{-4} & 2.1 & 0 & 0 & -0.5 \\ 0 & 0 & -0.60 & -3.5 \times 10^4 & -1 \\ 0 & 0 & -6 \times 10^{-4} & -5 & -1 \times 10^{-3} \\ 0 & 0 & 0 & 0 & 1 \end{bmatrix} \quad (4.4.3)$$

Using Eq. 4.4.2 and 4.4.3, the energy change at the target can be written in terms of horizontal position change at 3C12, and horizontal position and angle changes at the target as

$$\Delta \left( \frac{dE}{E} \right)_T = \frac{1}{M_{15}} \Delta X_{3C12} - \frac{M_{11}}{M_{15}} \Delta X_T - \frac{M_{12}}{M_{15}} \Delta X'_T \quad (4.4.4)$$

More detailed calculation about the energy modulation can be found in [102].

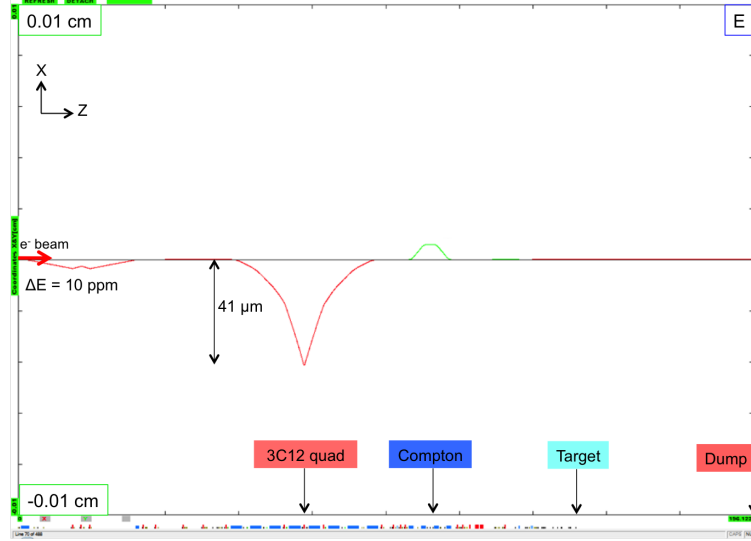


Figure 4.6 Forward orbit excursions simulation for energy modulation from OptiM. Beam moves from left to right. The energy was changed by 10 ppm using a horizontal corrector in the simulation. The pronounced horizontal position (red) change of 41  $\mu\text{m}$  at the middle of the arc is due to the energy change of 10 ppm. A small vertical position (green) bump can be identified at the Compton region.

## 4.5 Beam Modulation Hardware

The hardware of the beam modulation system spans three different regions: BSY service building, accelerator beamline, and Hall-C. In the BSY service building, there were two signal generators controlled by an IOC. The sinusoidal signals from signal generator were sent to power amplifier, and the amplified signals were sent to two pairs of air core coils and one SRF cavity in the beamline. The read-backs from signal generators, power amplifiers, current transducers to measure the coil current, and BPM responses were sent to two sets of ADCs at the Q-weak cage at Hall-C counting house and at BSY service building to monitor the system and to perform further analysis. A trigger from parity violating DAQ in the Hall-C counting house were sent to the IOC at BSY service building to start the process. The schematic diagram of the beam modulation hardware is shown in Figure 4.7.

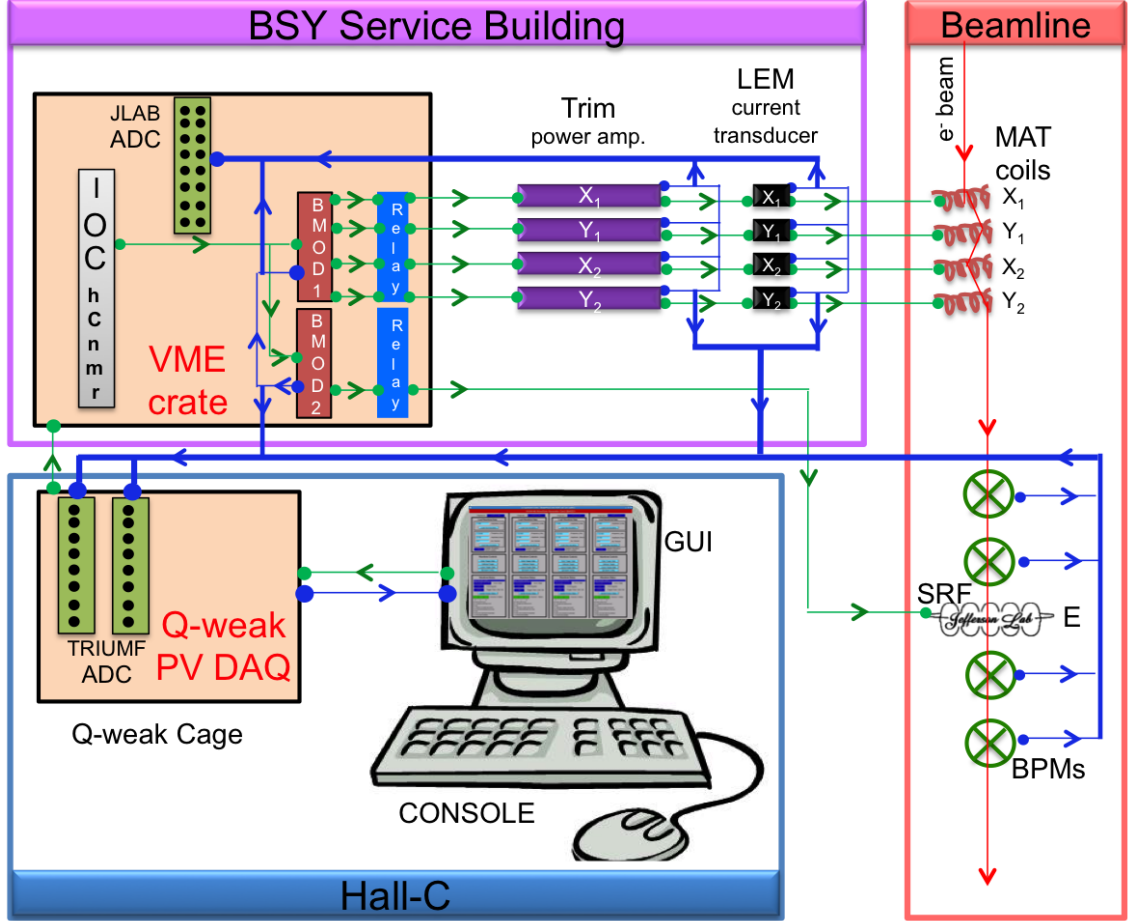


Figure 4.7 Beam modulation hardware sketch. BMod hardware spans three different regions: BSY service building, accelerator beamline, and Hall-C. In BSY service building there were two VME-4145 signal generators controlled by an IOC (iochcnmr). The sinusoidal signals from signal generator were sent to Trim-I power amplifier, and amplified signals were sent to two pairs of MAT coils and one SRF cavity (SL20 vernier) in the beamline. The read-backs from signal generators, power amplifiers, current transducers, BPMs, and cavity were sent to two TRIUMF-made ADCs at Q-weak cage and one JLab-made ADC at BSY service building. The drive or input signals are shown by green and read-backs by blue lines respectively. In order to trigger the process, a signal from parity violating DAQ in the Hall-C counting house were sent to the IOC.

#### 4.5.1 Air-Core Coils

Two pairs of JLab MAT(HF) air-core coils were used to perturb the electron beam for the modulation system as they produced sufficient field integral, were readily available, and were compact enough (10 cm) to be inserted easily in almost anywhere in the beamline. Their properties have been measured and summarized by Sarin Philips in [103]. The MAT coils were calibrated in bench test and the most critical parameters are summarized in Table 4.4. The total impedance of the coil

was related to the frequency ( $f$ ) as  $X_{\text{total}} = 1.6 \Omega + 2\pi f(0.0038 \text{ H})$ . The reduction in field due to the skin effect in a standard stainless steel beampipe was determined to be roughly 10% at 1 KHz, and less than a few percent at nominal frequency of 125 Hz. The skin effect was ignored as the used frequency of the sinusoidal modulation was 125 Hz, which was constrained by the power amplifier (see section 4.5.5).

Table 4.4 Basic properties of the air core MAT coils used for the beam modulation system.

Magnet Parameter	Value
Magnet Constant ( $B/I$ )	33 G/A
$\int \vec{B} \bullet d\vec{l} = (B/I) \times \text{Length}$	(330 G-cm/A)×I
Length	10 cm
Inductance	3.8 mH
Resistance	1.6 Ω

### 4.5.2 IOC

A VME based Input Output Controller (IOC) *hcnmr* at BSY service building was used to operate the beam modulation system. IOC was a chassis containing a processor, various input/output (I/O) modules, and VME modules that provide access to other I/O buses [104]. The IOC used to establish communication with two VME 4145 Signal Generator boards through two patch panels and controlled the drive signal of VME 4145 board via a database access library that works on Unix, vxWorks<sup>2</sup>, and EPICS databases.

### 4.5.3 VME 4145 Signal Generator

Two GE Fanuc Intelligent Platforms' VME-4145 programmable function generator boards [105] were used to drive two pairs of MAT coils (shown in Figure 4.7). The VME-4145 has an analog output board that provides four high-quality analog output channels with 16-bit resolution. Each output has a dedicated Digital-to-Analog Converter (DAC), and can source or sink 10 mA ± 10 V. Each channel has a dedicated 64 Kword<sup>3</sup> waveform buffer. Each buffer may be segmented to provide independent subwaveforms. The unit was capable of downloading an arbitrary bipolar waveform and then replay it. Any arbitrary waveform like square, sine, triangle, and sawtooth may be programmed. Two pairs of MAT coils were driven using sine waveform from the four channels of the first VME-4145 board. Only two channels of the second board were used. One channel was used to drive superconducting

<sup>2</sup>VxWorks is a real-time operating system developed as proprietary software by Wind River Systems of Alameda, California, USA. First released in 1987, VxWorks is designed for use in embedded systems.

<sup>3</sup>KWord is a deprecated word processor and a desktop publishing application, part of the KOffice suite [106].

RF cavity for energy modulation with a sine waveform and the other channel was used to produce a ramp (sawtooth) wave to monitor the phase of the all five drive signals. Each waveform was generated start to finish and then the next was seamlessly started. All of the waveforms were preloaded before waveform generation begins. An external trigger input from Q-weak main DAQ was used to start playback of the waveform. This feature allowed to trigger the drive signal and ramp wave channels to synchronize in phase. The boards were programmed to run in the continuous mode (Type II) which scanned the waveform table, ran for 510 cycles and then halted. The next cycle started again when the boards were triggered from the Q-weak DAQ.

#### 4.5.4 Relay Board

Two sets of JLab-made 16-channel relay output register modules [107] were used to make it easy to keep everything safe and tidy for the modulation system. The board consists of four 16-bit registers used to control 16 relays and read-back status information. The front panel contains indicator LED's for power, heartbeat and relay on/off status. Relay contacts are brought out on a 50-pin D connector. A DC shift of  $\sim 0.015$  V was observed in the sinusoidal drive signal due to the relay boards which seem to have no effect on the driven coils (more details in [108]).

#### 4.5.5 Trim Power Amplifier

Four 1 to 12 A series pass regulator power supplies, known as Trim Card I, were used as power amplifiers to control two pairs of the MAT dipoles for the beam modulation system. The Trim-I was programmable, 200 W, bipolar, power supply and was realized as a single plugin circuit board, approximately with dimensions  $9'' \times 20''$ . A new generation plug-compatible supply Trim-II was being developed to replace the Trim-I by JLab accelerator group [109]. Thirty two Trim cards were housed in card-cages within a single rack (BS04B14) at BSY service building. But only four of those cards were used for the modulation system and the rest were used to power other components in the beamline. The Trim cards consisted of a Motherboard which helped to interconnect all the daughter cards, distribute power to the daughter cards, and house the power amplifier section (shown in Figure 4.10). A 48-pin connector, mounted on the rear apron, was used to engage a mating connector in the card cage where  $\pm 27$  V bulk power, 5 V power, and RS-485 communication were derived. External programming commands and data read-backs were exchanged with the EPICS via a RS-485 data link. The cards had a display module in the front connected to a digital temperature sensor which was used to set warning flags or shutdown the trim card in case of overheating. The

Trim cards setup suffers from a discontinuity when conduction changes from the positive to negative pass bank transistor arm as the output passes through the zero point. This effect was suppressed by the feedback loops, and was problematic for fast ramps or step changes. The drive signal for the modulation was constrained by this phenomena, and instead of square or triangular waves, sinusoidal wave was chosen. Originally, the Trim cards were designed to operate in the DC regime, but managed to amplify up to 250 Hz smooth sine wave linearly. Near the higher frequency and saturation current, the Trim cards locked itself to prevent any potential damage.

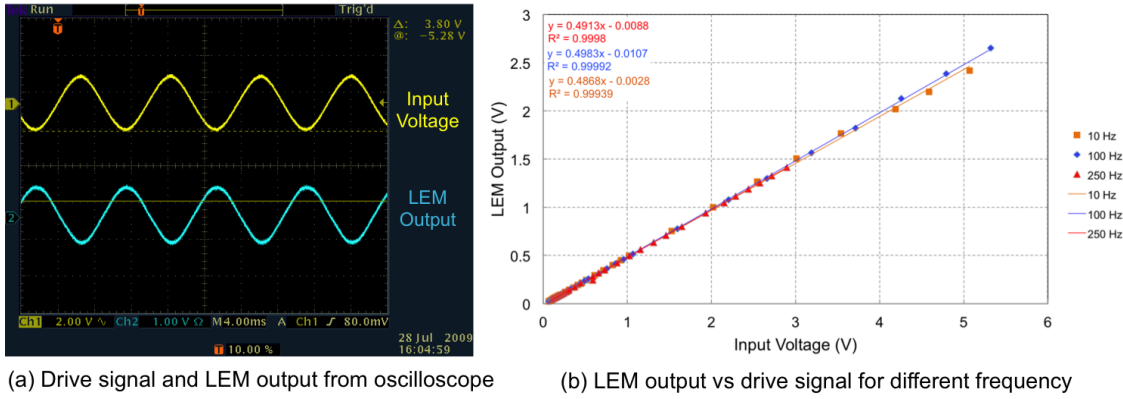


Figure 4.8 LEM current transducer output response (blue) to input sine drive signal (yellow) seen by oscilloscope (left). The output from the LEM was out of phase with the input signal. The figure on the right shows LEM calibration up to 5 V of input signal. The frequency dependence of the input signals were studied up to 250 Hz. The gains of the LEMs were  $\sim 0.5$ .

#### 4.5.6 LEM Current Transducer

Four LEM CT-10T [110] were used to monitor the current through the two pairs of the MAT dipoles. The LEM has two pins for the input current in one side and two power supply pins ( $\pm 15$  V) on the other side along with two pins for output voltages. The LEMs were calibrated up to 5.5 V of input voltage, whereas nominal input operating voltage during the experiment was  $\sim 1$  V. The calibration was performed using a bench top and VME-4145 signal generators. A typical drive signal and its readback signal by a LEM are shown in Figure 4.8 (a) and the variation of LEM output with input drive voltage has been shown in Figure 4.8 (b). There was a  $180^\circ$  phase shift between the input (or Trim) signal and the LEM output signal. The measured gain was  $\sim 0.5$  for all the LEMs. There was no frequency dependence of the gain for the LEMs in the voltage domain 0 - 5 V as shown in Figure 4.8 (b). The LEMs were assembled in an insulated box and installed in the

Hall-C patch panel VME crate in the BSY service building [111] and were connected in series with the MAT dipoles. During the experiment, there was -75 mV, 240 Hz square wave noise injection in the beamline due to the cable connection fault in the LEM chassis. So, LEMs were disconnected during most of the production data taking. They were only turned on for tests and calibration during the commissioning period of the experiment. During preliminary bench test, LEM LA 50-P current transducer [112] was used to monitor the current. LEM LA 50-P used the induction method to measure the current; hence there was no series connection with the coils for the measurements. Use of the induction current transducer has a lesser chance of injecting noise in the system. For future work, one might consider LEM LA 50-P or similar current transducer for precision parity measurements. The LEM current transducers have also helped to calibrate the strength of the magnets during the commissioning tests. More details about LEMs and its calibration are described in [113].

#### 4.5.7 Energy Modulation Hardware

A 125 Hz sinusoidal signal was sent to an energy vernier SL-20 of a cryo-module in South linac of the accelerator to modulate the energy. One of the standard features of the accelerator is the use of Fast Feed Back (FFB) system (Section 3.6.7) to maintain a steady beam position. Unfortunately, the energy FFB system did a perfect job of countering the 125 Hz energy modulation signal. The energy monitor BPM 3C12X saw no response in Figure 4.9 (bottom) for the energy modulation signal (top) when the FFB was on. So, the FFB system had been paused during the energy modulation to avoid any suppression from the FFB system.

#### 4.5.8 ADCs

Two sets of TRIUMF-built 18-bit analog to digital converters (ADCs) were used to study the readback signals from different components of the beam modulation system. Each module had eight ADC channels which were synchronized and triggered by the MPS signal sent by the helicity board. The ramp wave and 5 drive signals ( $X$ ,  $X'$ ,  $Y$ ,  $Y'$ ,  $E$ ) from VME function generator, 4 readback signals from LEM current transducer, 4 readback signals from Trim-II power amplifiers were read by the TRIUMF ADCs (more details in section 3.11.1.1 and [88,89] ).

All the readback channels (above mentioned 14 channels and a readback from SL-20 vernier for energy modulation) were also sent to a 32-channel JLab made ADC module [115] which was used to monitor the peaks of the signals. The ADC had 16-bit resolution and supported up to a 100 kHz

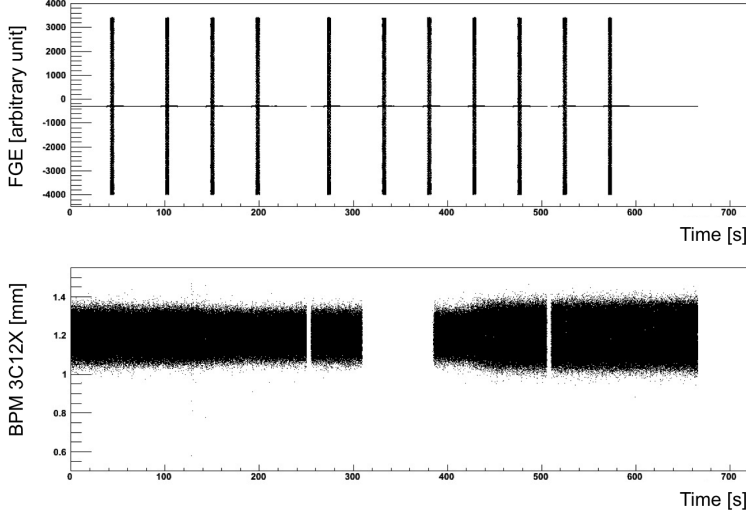


Figure 4.9 The effect of Fast Feed Back (FFB) system on energy modulation [114]. Top panel shows function generator drive signal vs time. Bottom panel shows the response of the BPM 3C12X (which is located in the middle of the arc and supposed to see maximum response for energy modulation) for the same drive signals. No response was observed in the BPM when FFB was on. The missing portions of the BPM response was removed by the software stability cut in order to avoid beam trips.

sample rate. The ADC was configured by 36 16-bit registers and read the analog input data. The data format was configured depending on the selected bipolar or unipolar input range. The analog inputs were fully differential and configured to detect the peak of the input signals. The input connectors for the analog inputs were 50-pin D style connectors. The front panel had indicator LED's for power and heartbeat. The JLab-made peak detection ADC was used as a standalone (independent of Q-weak parity violating data acquisition system) modulation readback system and was installed in the BSY service building.

## 4.6 Hardware Components Calibration and Important Constraints

Extensive bench tests were performed with the beam modulation system so that (except for the absence of long drive cables) it would be possible to predict how the installed system would work. The Trim amplifier was controlled via an analog input from a simple bench-top function generator at the beginning and latter with VME 4145 board. The signal generator produces sine waves of different amplitudes and frequencies as the input voltage to the Trim-II power amplifier. The amplified signal goes to  $\sim 10$  cm long MAT coil through a single LEM current transducer either in phase or out of phase from two coils. The currents through the coils were measured by ammeter.

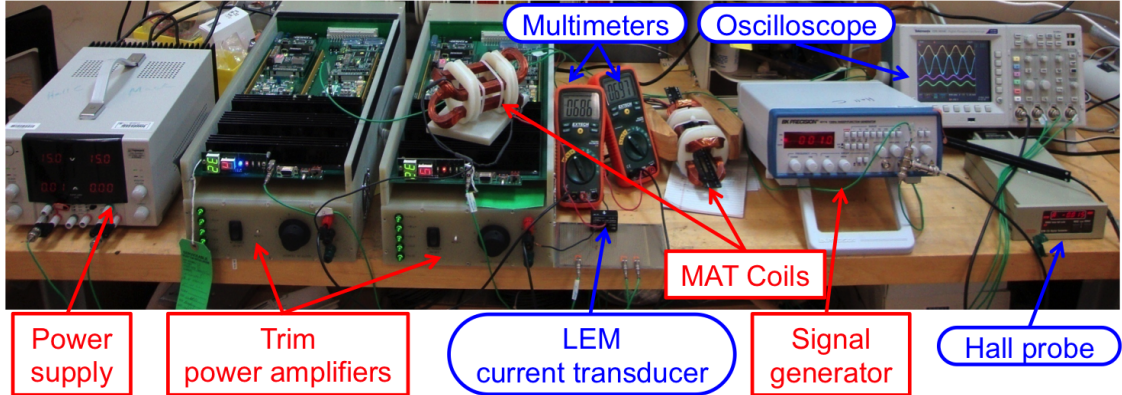


Figure 4.10 Beam modulation hardware bench test setup. It consists of one  $\pm 15$  V power supply, two Trim power amplifiers, pair of assembled MAT coils, and one signal generator. A VME signal generator was also used during the latter part. To see the responses and read-backs, two multimeters, a LEM current transducer, a hall probe, and an oscilloscope were used.

The magnetic fields of the coils were measured by the Tesla meter. All the individual components were tested and calibrated in the bench test. The bench test setup is shown in Figure 4.10.

#### 4.6.1 Coil Positioning

There were significant constraints on where perturbing coils could be located. One absolute requirement was that coils be located upstream of the high dispersion point at 3C12 (the center of the 3C arc) so that modulations in  $X$ ,  $X'$ , and  $E$  could be disentangled. Another highly desirable constraint was that the coils be located downstream of any expected deviations from design optics. Accelerator operations agreed to complete matching in 3C beamline by quadrupole MQA3C08, the beginning of the 3C arc dipole string. Considerations of robustness and purity therefore excluded regions upstream of this point, leaving only the first half of the 3C arc as a potential site for coils. This coil positioning and orbit excursions were simulated using OptiM. Initially, it was attempted to insert both coils into a single  $\sim 1$  m drift, but the angle kicks of interest required excessively high field integrals and the approach did not work. Separating the coils by more than 1 meter required straddling other beamline elements. The coils were mounted between two dipoles (since the orbit inside a dipole is plotted effectively like a drift) with no intervening quadrupoles or active elements between them. The 1st pair of MAT coils, MHF3C08H ( $X_1$ ) and MHF3C08V ( $Y_1$ ), were installed in the drift oD7028, which was located just after quadrupole 3C08 and before the dipole 3C05. The 2nd pair MAT coils, MHF3C10H ( $X_2$ ) and MHF3C10V ( $Y_2$ ), were installed in

the drift 0D7034, which was located between dipoles 3C06 and 3C07. The separation between these two pairs of coils was about  $\sim 9.5$  m. The first coil  $X_1$  was located  $\sim 92.7$  m upstream of the Q-weak target. The  $X_1$  and  $X_2$  coils were pulsed at a time and in opposite phase to produce relatively pure horizontal position or angle changes at the target, for virtually any tune of the beamline as shown in Figure 4.4.

### 4.6.2 Waveform

The Trim power amplifier was unable to drive square or even triangular waveforms in the frequency range of interest. Satisfactory results were obtained only with sinusoidal waveform, which was hence used to drive the magnets. The preferred waveform was to generate at least square-ish modulation (similar to the square helicity reversal) and needed different power amplifier. Due to budget and schedule pressure, existing Trim amplifiers were used.

### 4.6.3 Waveform Phase

A 1 V of sawtooth wave with the same frequency of 125 Hz as sinusoidal drive signal from VME 4145 was used to monitor the phase of the drive signals. The sawtooth ramp wave goes from 0 to 1 V as the phase of the sinusoidal drive signal goes from 0 to  $360^\circ$  (Figure 4.11). The drive signal and ramp wave were triggered together to match and lock the phase. The edges of the ramp wave were not very sharp hence were removed during the analysis to avoid any edge effect. The edges were recreated using a ramp fill method in the software as described in [116].

### 4.6.4 Frequency Range

The frequency of the waveform was tested for the range of 10-500 Hz and nominal 3 A (peak) output. The Trim cards reliably drove sinusoidal waveforms up to 250 Hz. At that frequency, the coil impedance becomes approximately  $X_{\text{total}} = 1.6 \Omega + 2\pi f (0.0038 \text{ H}) = 7.6 \Omega$ , so the amplifier has to provide 22.8 V (peak). The maximum output voltage of the Trim-II amplifier appeared to be approximately  $\pm 27$  V, but it was not strictly bipolar due to the use of NPN diodes for one polarity and PNP diodes for the other. So while one could go a bit higher in frequency than 250 Hz, there would be a rapidly increasing risk of generating asymmetrical sine-like waves (and hence a small DC beam position offset). During production data collection, the nominal drive signal frequency was 125 Hz to stay inside the linear region of the Trim operation. Another criteria for choosing the frequency was to avoid the power line frequencies (60, 120, 180, etc. Hz) suppressed by FFB system.

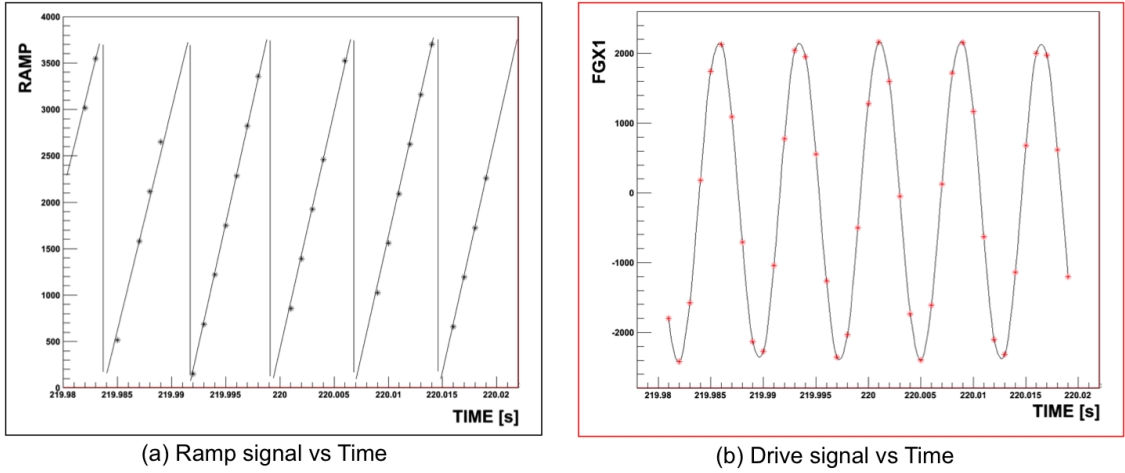


Figure 4.11 Zoomed ramp and drive signal from a beam modulation cycle during a typical production run. (a) Ramp signal vs time. The ramp signal is a sawtooth wave used to track the phase of the other sinusoidal drive signals. (b) Drive signal vs time. The drive signal is a sinusoidal wave with fixed phase.

#### 4.6.5 Maximum Current

With sustained operation, the coils became quite hot to the touch at  $I_{\text{peak}} = 7.07 \text{ A}$  ( $I_{\text{rms}} = 5 \text{ A}$ ). This was significantly above Q-weak's nominal maximum current  $I_{\text{peak}} = 3 \text{ A}$ , but it is worth discussing since future experiments at higher beam energy might try to push the envelope. Although measurements at 1% duty factor would take only 36 seconds per hour, one must assume that a parity violation experiment will eventually take long, dedicated beam modulation runs. Unless cooling fans installed, damage to the enamel-insulated wires or any plastic components could result if  $I_{\text{peak}} = 7.07 \text{ A}$  is significantly exceeded. The “smoke point” of the magnets was not determined, but bear in mind that  $P = I^2R$ , so the temperature would increase rapidly with current above  $I_{\text{peak}} = 7.07 \text{ A}$ . It is hopefully understood that  $I_{\text{peak}} = 7.07 \text{ A}$  refers to the peak current of a sinusoidal waveform, and not to a maximum DC current which would have twice the power dissipation. Constraint on maximum current based on machine protection simulation is discussed in the Section 4.9.

#### 4.6.6 Magnetic Field Calibration of the MAT Coils

The MAT coils were calibrated using a bench test setup, as shown in Figure 4.10. The magnetic field was measured using a GMW Hall Probe. The measured field integral for 10 cm MAT coil was  $\sim 330 \text{ G}\cdot\text{cm}/\text{A}$ . The field was reasonably stable for the span of the coil (Figure 4.12 (a)). There was no current dependence of the field as shown in Figure 4.12 (b). The magnetic field for the MAT coils

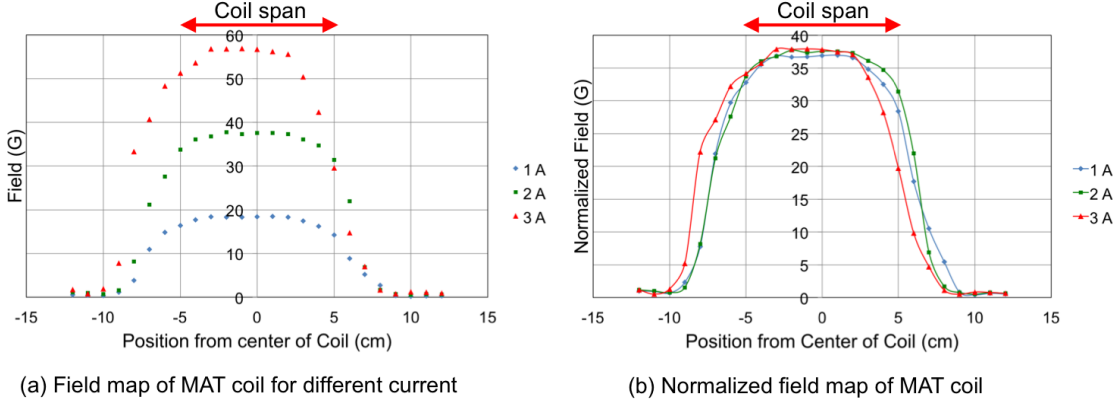


Figure 4.12 Field map of MAT coil for different input coil currents (left). The field was linear in the region of the coil span of 10 cm. The field profile did not change with coil current upto 3 A. The field was normalized with respect to 1 A (right).

falls quite sharply with distance beyond the coil span, hence reduces the possibility of interaction with other active elements in the beamline.

## 4.7 Controls and Software Sketch

A standalone control system for the beam modulation system was designed by Scott Higgins [117–119]. The drive signals of two VME-4145 signal generator boards was controlled via an EPICS database access library that works on Unix and vxWorks. In the control system, the first VME-4145 card was referred as BMOD1 and the second card as BMOD2. Each function generator card has 4 channels and they are named as CHAN0, CHAN1, CHAN2, and CHAN3. All four channels of BMOD1 and CHAN0 and CHAN3 of BMOD2 were used for the modulation system. The EPICS variable for the master switch was BEAMMODSWITCH. A value for BEAMMODSWITCH of 0 was considered as OFF and 1 was ON. This switch allowed operations to control whether or not to allow any beam modulation requests. The off state was entered when the master switch was set to OFF. In the OFF state the Relays to the Trim cards were set to ground. The OFF state was the default state for the system after an IOC reboot. The CONFIG state was entered when the operations toggles the master switch from OFF to ON. Once the board was in the CONFIG state all, the channels in BMOD1 and one channel BMOD2 were allowed to load a sine wave, whereas CHAN0 of BMOD2 was allowed to load ramp wave. The inputs controlling the sine wave were frequency and amplitude. The allowed frequency range was set to be 10-250 Hz, and amplitude was limited to  $\pm 0.3$  A, as discussed in previous sections. A negative amplitude would shift the phase of the sine wave by  $180^\circ/\pi$ . The amplitude output for

ramp wave was between 0 and 1 V. The ramp wave period started at 0 volt and then the slope linearly increased to the amplitude entered. Then the ramp wave was loaded the same way as other drive signals. Before the transitions to the trigger state, it was necessary to enter the number of periods for the sinewave or rampwave to run the system. This setting ranged from 1 to 511. A value of 511 would cause the hardware to run the sinewave or rampwave continuously which was a feature of the hardware. Nominal cycle for the system was set to 510. The trigger state was entered by writing a value of 1 to the EPICS variable **TRIGGER** state.

The sine waves could be initiated by both a hardware and software trigger. The software trigger was a button that is activated by writing a value of “1” to the EPICS variable. This feature was primarily used in testing the system. The hardware trigger was initiated from the Hall-C parity violating DAQ. All of the 8 channels shared the same hardware trigger so any of the channels that were in the **TRIGGER** state would initiate sine wave outputs. It should be noted that if another trigger comes in while the VME-4145 is outputting a sine wave, the output will be interrupted and the card will restart the sine wave from the beginning. There were 2 things that could cause a channel to leave the trigger state: if operations selects Beam Modulation Off with the master switch or the user selects to leave the trigger state. The EPICS variables to leave the trigger state is activated by writing a value of “1”.

If the user entered the trigger state after having previously run a sinewave, the last loaded sine wave would be executed. There was no need to reload the sine wave in the **CONFIG** state if amplitude and frequency were to stay the same. If, however, the user desired to change either the frequency or amplitude, a new sinewave must be loaded. There was a time delay in the reporting of the running of a sinewave from the VME-4145. A sine wave could be triggered and finished before the card reported that it was actively running a sinewave. Therefore there was no deterministic way to see the status of the card generating a wave for a particular channel in real time, at least not by monitoring the VME-4145. An external method was needed. A JLab-made ADC was used to monitor those channels in real time. There was a signal that went back to the hall which showed the output of the VME-4145 function generator. The goal of this signal was to show real time values written to the trim card. In order for the output of the function generator to reach the trim card, a relay needed to be set. The signal going back to the Hall-C of the function generator was between the relay board and the trim card. There were 2 RELAYS for each VME-4145 function generator channel. Both were set for the channel to be connected the trim card. A value of “1” meant the relay was enabled and the function generator was connected to the trim card. A value of “0” meant

the relay was off and the trim card was tied to ground. More details about the modulation control system can be found in technical documents [117, 119].

## 4.8 Modulation Modes

Two possible modulation modes were exercised during the experiment. One mode was with single coil modulation, where all four coils  $X_1$ ,  $X_2$ ,  $Y_1$ , and  $Y_2$  were pulsed individually; this mode was mainly used to calibrate and test the system during commissioning period. The other mode was, in which one pair of coils was pulsed together to achieve relatively pure position and angle at the target, was used as nominal mode for the modulation operation. A pulse with a combination of  $X_1$ , and  $X_2$  was used for horizontal position and angle, and one with a combination of  $Y_1$ , and  $Y_2$  was used for vertical position and angle motion. The energy modulation was the same for both the modes. The motivations for using a pair over a single dipole were greater flexibility in coil positioning, coil positions being independent of beamline optics, and a compact configuration. The nominal current through the MAT dipole for the pair mode is shown in Table 4.3. A unique pattern number was assigned in the software to identify the different modulation modes, and parameters as listed in Table 4.5.

Table 4.5 Different beam modulation modes and related pattern numbers. In single coil mode, just one coil was pulsed and the response was a linear combination of position and angle. In pair of coils, two coils were pulsed at a time to produce relatively pure position or angle.

Mode	Parameter	Coils Pulsed	Pattern Number
Single coil	$X$ and $X'$	$X_1$	1
	$X$ and $X'$	$X_2$	2
	$Y$ and $Y'$	$Y_1$	3
	$Y$ and $Y'$	$Y_2$	4
	$E$	$E$	5
Pair of coils	$X$	$X_1$ and $X_2$	11
	$Y$	$Y_1$ and $Y_2$	12
	$E$	$E$	13
	$X'$	$X_1$ and $X_2$	14
	$Y'$	$Y_1$ and $Y_2$	15

## 4.9 Machine Protection Analysis

A simulation was performed to check the maximum possible excursion in the beamline due to beam modulation magnet kicks. The nominal field integrals for the modulation MAT coils are given

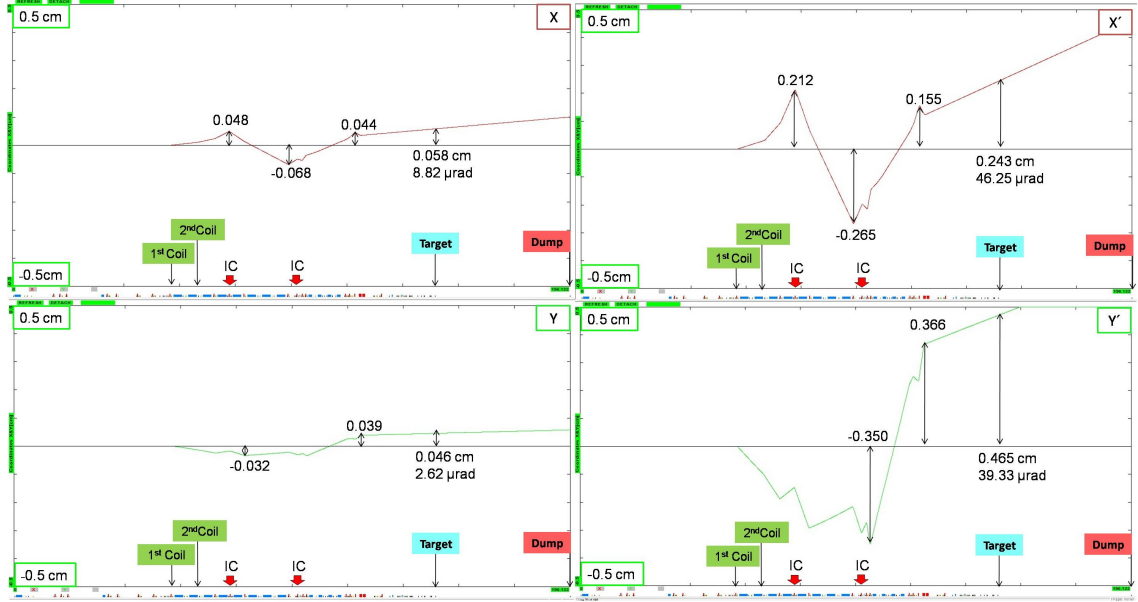


Figure 4.13 Orbit excursions using a pair of coils with incorrect polarity on one of the coil. Beam moves from left to right. Large excursions were observed for angle compared to position. The used field strength to pulse the coils for this simulation was 5 times higher than that used as nominal field strength during the experiment. The location for ion chambers (IC) was recommended based on this study and is shown by the thick arrows at the bottom of the figure.

in Table 4.3 and the corresponding excursions are shown in Figure 4.5. For this simulation, the modulation kicks were increased by increasing the nominal field by 5 times to enhance the effect (these excursions are linearly scaled). The beam excursions with this conditions were 1.3 mm at the upstream of the target and 1.0 mm at the beam dump. The tune parameters in Table 4.3 were negative, which implies the opposite polarity of the magnets. To check the worst possible scenario, the polarity of the magnets was reversed (using the same 5 times of nominal field); the simulated orbits are shown in Figure 4.13. The reversed polarity deviations upstream of the target were 3.6 mm and 6.6 mm at the beam dump. The same simulation with only one coil energized deviations was 2.4 mm upstream of the target and 3.8 mm at the beam dump for  $I_{\max} = 0.6$  A. Considering all of these cases, the maximum obtained excursion was about 4.6 mm at the target for a maximum current of 0.6 A. For angles, the excursions were much larger than position excursion mainly in the regions middle of the arc (around quadrupole 3C12) and end of the arc (around quadrupole 3C17). The deviation at the beam dump was 6.6 mm for  $I_{\max} = 0.6$  A. For protection of the machine, considering all the above cases, the recommended place to install ion chambers (IC) was at the highest beam excursion region of the beamline around 3C12 and 3C17 (as shown in Figure 4.13).

The worst case scenario was found to be the case of incorrect polarity. In order to avoid any mishap, when system was commissioned, a hard coded software limit of  $I_{\max} = 0.3$  A was implemented for the safety of the accelerator. More details about the machine protection analysis can be found in Q-weak internal technical document [120].

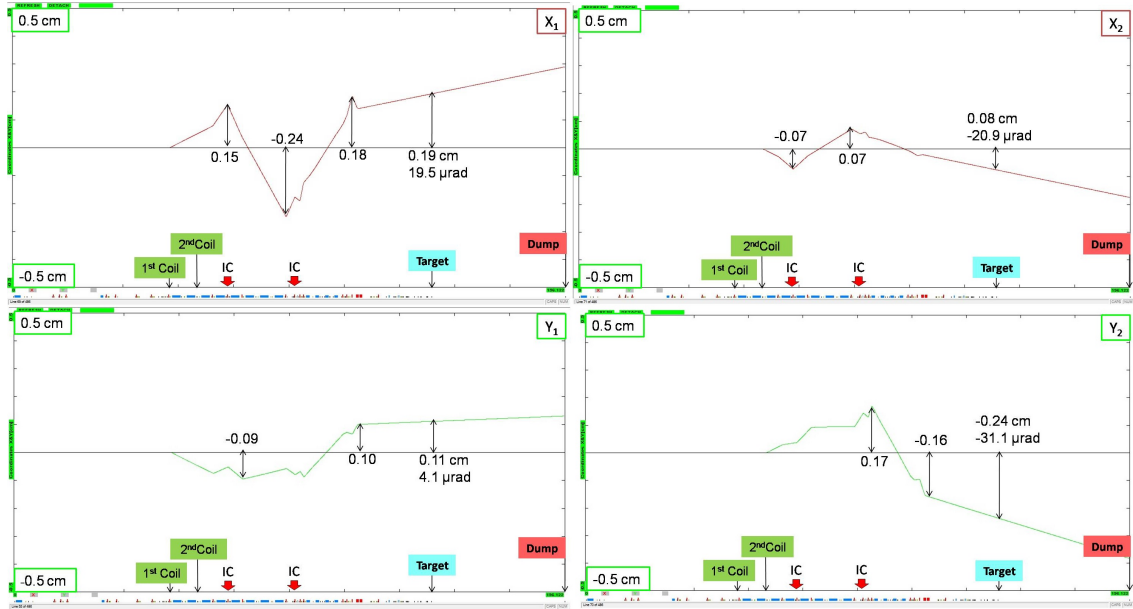


Figure 4.14 Orbit excursions with only one coil energized. Beam moves from left to right. Large excursions were observed for  $X_1$  and  $Y_2$  coils. The maximum current used for all the coils was  $I_{\max} = 0.6$  A. A hard coded restriction of  $I_{\max} = 0.3$  A in the software was set for the safety of the accelerator based on this analysis.

## 4.10 Beam Modulation Cycle

A typical beam modulation cycle vs time during production run is shown in Figure 4.15. A micro cycle ran for 510 cycles with a nominal frequency of 125 Hz for each beam parameter. So the cycle for each parameter was  $\sim 4$  s. One macro cycle consisted of the  $X$ ,  $X'$ ,  $E$ ,  $Y$ ,  $Y'$  cycles and ran for 320 s. Each macro cycle was then continuously repeated. The configuration time between each micro cycle was  $\sim 75$  s. Modulation ran with a duty factor of  $\sim 6\%$ . A zoomed version of the ramp and sinusoidal drive signal from the Figure 4.15 is shown in Figure 4.11.

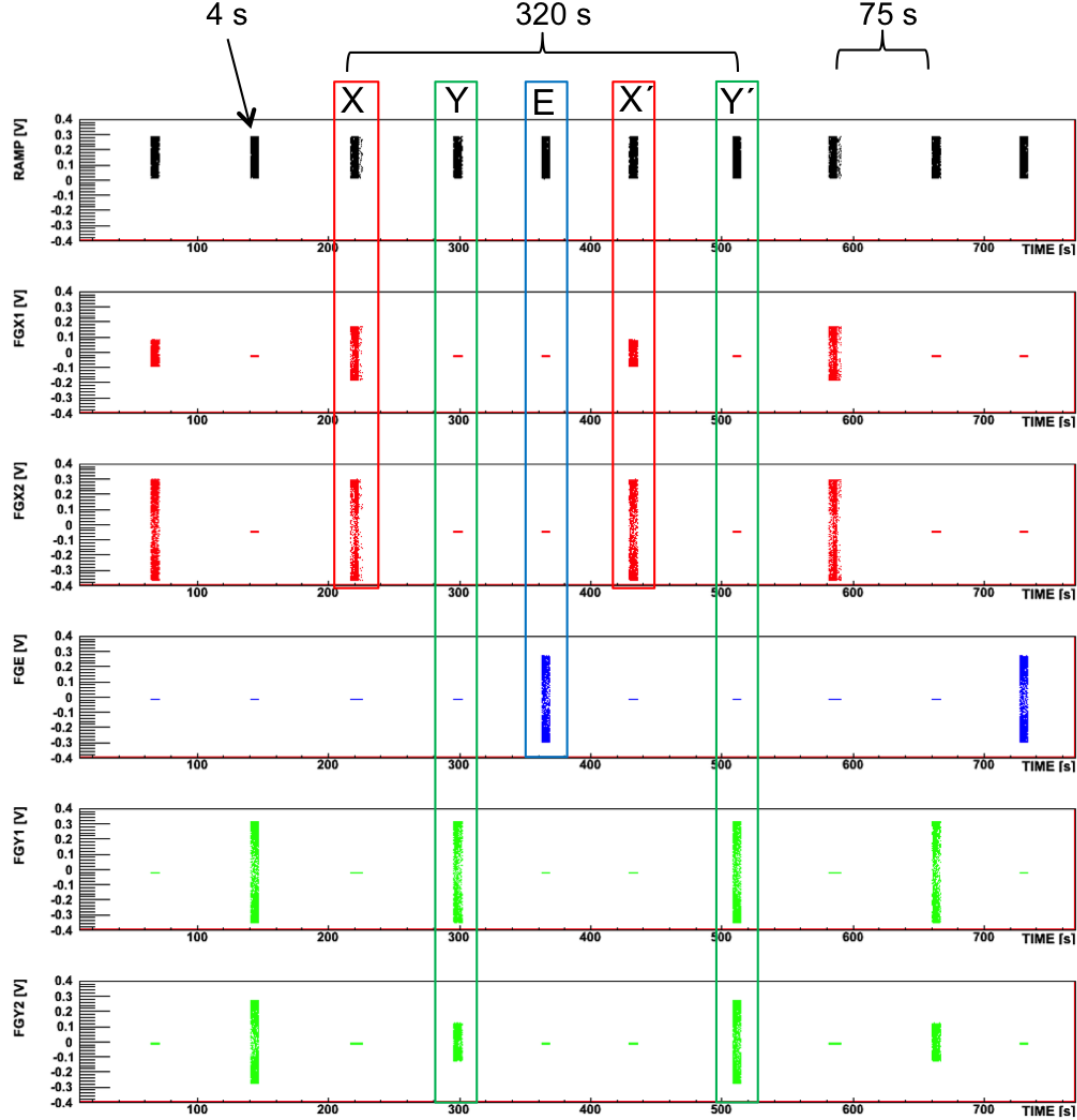


Figure 4.15 Beam modulation cycle during a typical production run. 1st panel shows ramp wave to calibrate sinusoidal signals vs time. 2nd and 3rd panels show sinusoidal drive signals for horizontal position ( $X$ ) and angle ( $X'$ ) modulation vs time. 4th panel shows sinusoidal drive signals for energy ( $E$ ) modulation vs time. 5th and 6th panels show sinusoidal drive signals for vertical position ( $Y$ ) and angle ( $Y'$ ) modulation vs time. The cycle for each parameter is  $\sim 4$  s. One macro cycle consists of the  $X$ ,  $X'$ ,  $E$ ,  $Y$ ,  $Y'$  cycles and ran for 320 s.

#### 4.11 Response to Modulation Signal and Applications

Main detector response to horizontal position ( $X$ ) modulation is shown in Figure 4.16. The detector coordinate is shown in the center of the figure. Detectors 1 and 5 show the maximum response for the  $X$  modulation and are anti correlated to each other. Negligible response has

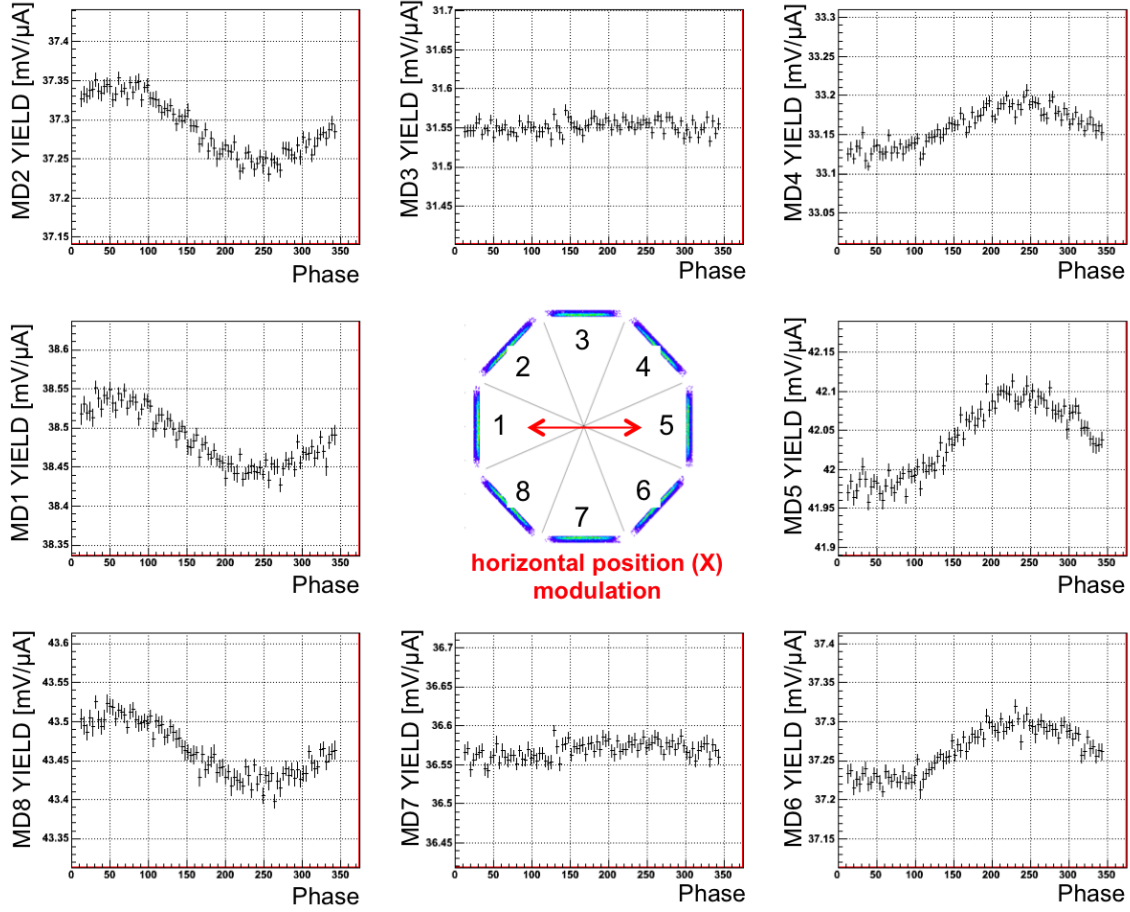


Figure 4.16 Main detector response to  $X$  position modulation. Main detector yields vs modulation phase (ramp wave) plotted for each detector.

been seen in octants 3 and 7. Detector responses correlated with modulation were used to extract sensitivities for the main detector and are discussed in the next chapter.

A typical BPM response to nominal modulation drive signal is a sinusoidal of amplitude  $\sim 200 \mu\text{m}$ , as shown in Figure 4.17. Compared with natural beam jitter, this is an order of magnitude larger and has fewer correlations among the parameters, providing an independent way of measuring sensitivities. Figure 4.17 shows a pair of drive signals for  $X$  modulation in top two panels, whereas the target BPM  $X$  and  $Y$  responses are shown in the bottom two panels. As expected, the BPM  $X$  shows a significant sinusoidal response to the horizontal drive signal but no response in  $Y$ . Besides measuring sensitivities, the BPM response to the modulation signal helped to track any optics change in the Hall-C beamline. The following chapter will discuss the application and products of the beam modulation system.

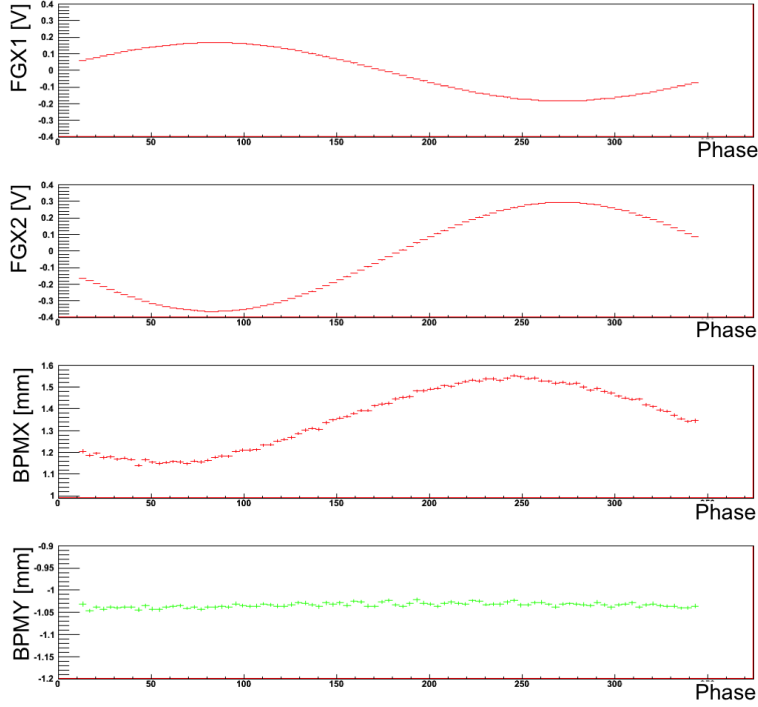


Figure 4.17 Target BPM response to  $X$  position modulation. The signals were plotted vs modulation phase. The drive signals in coils  $X_1$ , and  $X_2$  are shown in top two panels and the corresponding BPM response in  $X$ , and  $Y$  are shown in bottom two panels.

## 4.12 Extension to Other JLab Parity Violation Experiments

The beam modulation system described in this chapter should be useful for other parity violation experiments such as the Moeller experiment at 11 GeV in Hall-A, JLab [121]. Some basic limitations should be kept in mind. First of all, the modulation amplitude of the system described here will scale like  $E_{\text{beam}}$  (GeV)/1.165, hence the amplitudes at 11 GeV will be smaller by an order of magnitude. If the amplitude becomes smaller than the random beam jitter, convergence will be greatly slowed. The air-core coils can be driven harder if the duty factor is limited or if fans are used to cool the coils, but at about 5 A (rms) they become hot enough to risk damaging the enamel coatings on the wires under continuous duty. Secondly, at the frequencies of interest, the coil is an almost purely inductive load, so the voltage needed to drive a given current is nearly proportional to frequency. If one wishes to modulate the beam faster than the 250 Hz system described here, faster, higher voltage power amplifiers than the Trim-II would be needed. Alternatively, larger field integrals could be obtained for a given current by replacing air-core coils with ferrite magnets. Finally, because the

final quadrupole is closer to the target in the Hall-A beamline (1C) line [122], it should be somewhat easier to generate a given angle kick at a given beam energy as compared to the 3C line.

### 4.13 Summary

The beam modulation system presented here was designed for sinusoidal modulation up to 250 Hz which was robust and well-suited for experiments measuring small parity violating asymmetries like the Q-weak experiment. At the cost of 1% of beam time for one parameter, the system was able to measure all sensitivities to 10% accuracy each day. The pairs of coils were tuned to deliver relatively pure positions or angle modulations, making it much less likely that singular matrices are encountered when solving for the sensitivities. The ratio of coil currents was adjusted to incorporate any optics change in the beamline compare to move the coils physically, which made the system independent of the design optic. For 1.165 GeV electron beam, using 125 Hz sinusoidal drive signal, the Trim power amplifier was able to provide the desired beam modulation amplitudes with existing air-core HF (MAT) coils. The modulation system worked quite well for the span of two years during the Q-weak experiment and collected data noninvasively with production running. However, to providing similar amplitudes for the Møller PV experiment at 12 GeV in Hall-A may require an upgrade of the amplifier or magnets.

## SECTION 5

### BEAMLINE OPTICS AND FALSE ASYMMETRIES

#### 5.1 Detector Sensitivities

As described in previous chapter, unwanted helicity correlated changes in the transverse beam positions X (horizontal) and Y (vertical), beam angles X' and Y', and incident energy E on the target give rise to false asymmetries. These HCBAs  $A_{false}(X, Y, X', Y', E)$  can be heavily suppressed with careful tuning at the polarized source and a symmetric detector array. However, the residual effects must be measured and controlled.  $A_{false}$  is determined using the following expression:

$$A_{false} = \sum_{i=1}^5 \left( \frac{\partial A}{\partial T_i} \right) \Delta T_i \quad (5.1.1)$$

Here the slopes  $\partial A / \partial T_i$  are the measured detector sensitivities of the asymmetry  $A_{raw}$  defined in Equation 5.1.1 to changes in the beam parameters  $\Delta T_i$  at the helicity quartet level, and  $\Delta T_i$  is the HC difference of each beam parameter  $\Delta T_i$  measured at the quartet level. The 5 BPMs described in section 3.6.1 were used to continuously measure the HC beam position and angle differences at the target. The measurement of the HC energy difference relied on BPM3C12, as described in Equation 4.4.4 of section 3.6.4.2. The natural jitter of the beam can be and was used to determine the detector sensitivities  $\partial A / \partial T_i$ . However, better decoupling of the 5 sensitivities was achieved by varying the beam parameters in a controlled manner using a beam modulation system built specifically for this purpose. Decoupled position and angle motions were separately produced by varying the current in pairs of air-core magnets placed along the beamline; two pairs in X and two pairs in Y approximately 82 and 93 m upstream of the target.

Typical detector sensitivities for X modulation during an hour long run is shown in Figure 5.1. Detector sensitivities for all beam parameters for few days during Run-I are shown in Figure 5.2. Beam modulation amplitudes at the target, as well as typical monthly results measured for the HC beam properties  $\Delta T_i$  and detector sensitivities  $\partial A / \partial T_i$  during Run-II can be found in Table 5.1. The HCBAs for X, X' are anti-correlated and largely cancel. The same is true for Y & Y'. The uncertainties associated with the monthly HC position (angle) differences  $\Delta T_i$  are 0.07 nm (0.01 nrad) based on the quartet level BPM resolution discussed in Sec. 3.3 of 1 m (0.2 rad) over the  $2 \times 10^8$  quartets in the monthly period shown in Table 5.1.

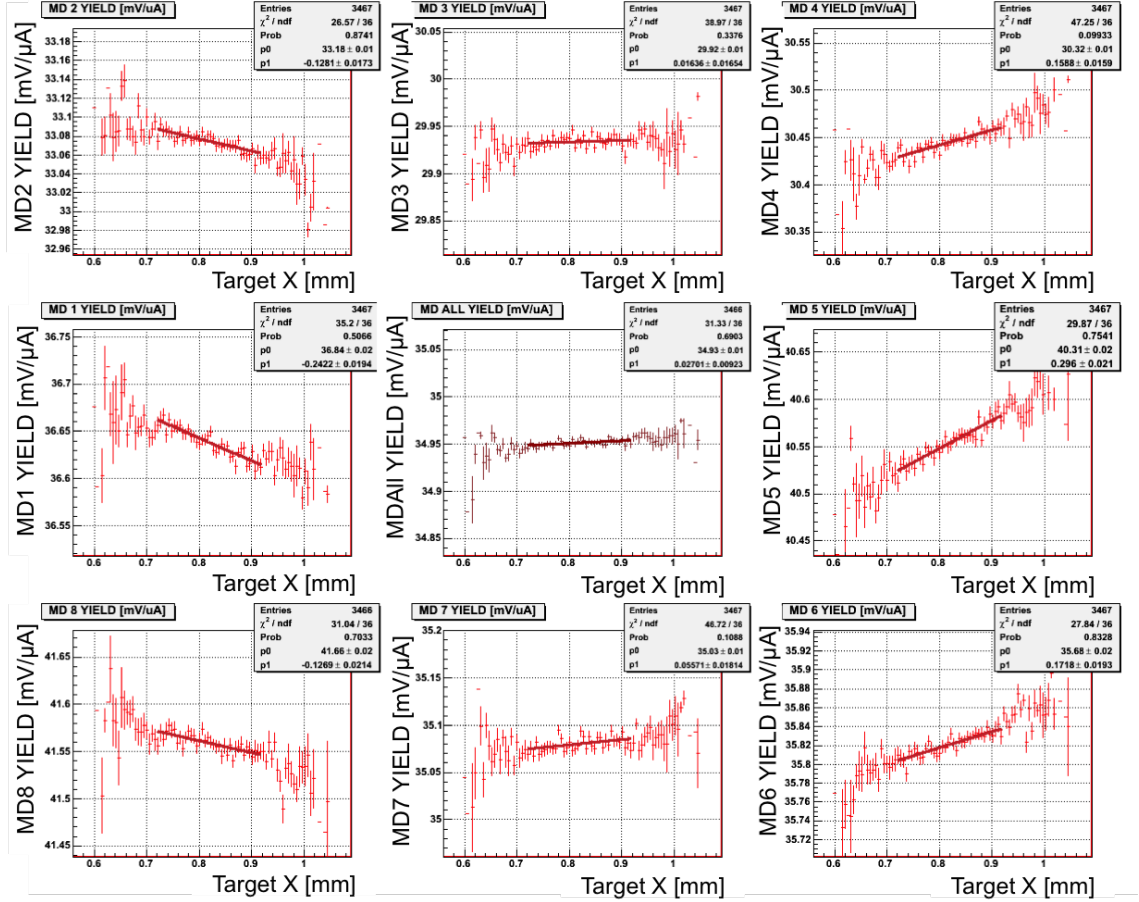


Figure 5.1 Main detector sensitivities with respect to target BPM X position for X Position Modulation.

Table 5.1 Typical amplitudes used for driven beam modulation (column 2). Columns 3 and 4 provide typical average monthly results measured during Run 2 for the helicity correlated beam parameter differences  $\Delta T_i$  and detector sensitivities  $\partial A / \partial T_i$  for the beam parameters i listed in the first column. The total HCBA for this example is only 0.4 ppb. The uncertainties associated with  $\Delta T_i$  and  $\partial A / \partial T_i$  are discussed in the text [123].

Beam Parameter	Modulation Amplitude	Differences [monthly]	Sensitivities [monthly]
X	$\pm 125 \mu\text{m}$	-3.3 nm	-2.11 ppm/ $\mu\text{m}$
Y	$\pm 125 \mu\text{m}$	2.5 nm	0.24 ppm/ $\mu\text{m}$
X'	$\pm 5 \mu\text{rad}$	-0.7 nrad	100.2 ppm/ $\mu\text{rad}$
Y'	$\pm 5 \mu\text{rad}$	0.002 nrad	-0.0 ppm/ $\mu\text{rad}$
E	$\pm 61 \text{ ppm}$ (70 keV)	0.1 nm	-1.56 ppm/ $\mu\text{m}$

Subset of the Run-II production data showing the blinded asymmetry grouped by (monthly) Wien state, and corrected using two different approaches to determine the sensitivities of the appa-

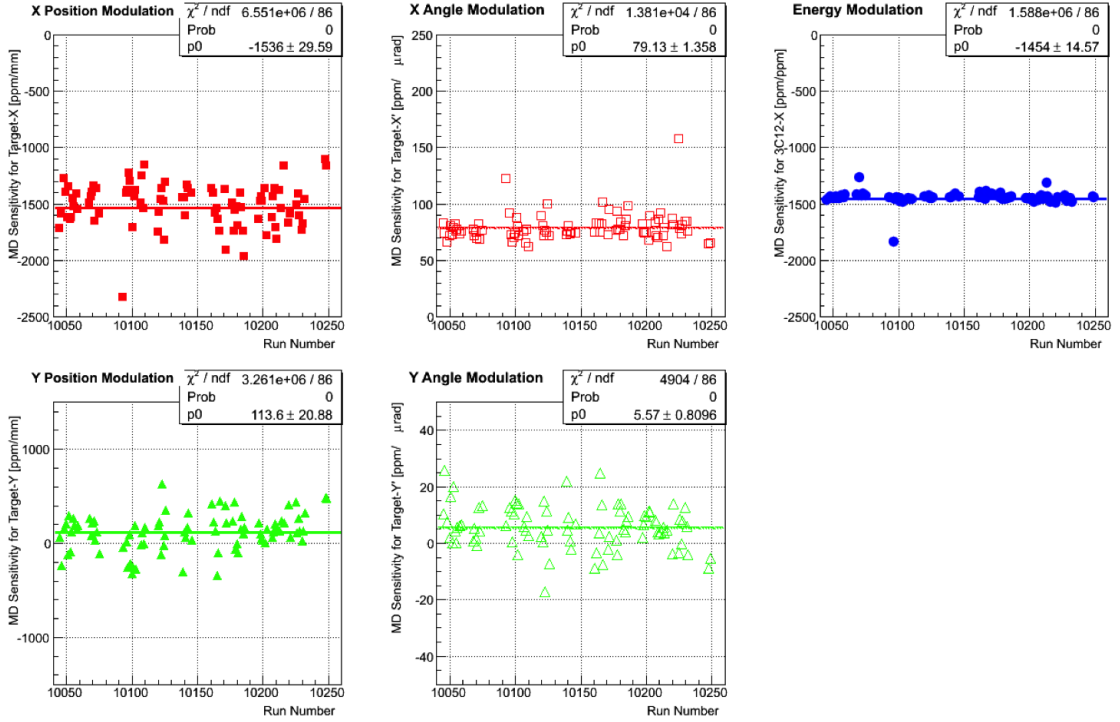


Figure 5.2 Main detector sensitivities for X (solid red square),  $X'$  (empty red square), E (solid blue square), Y (solid green triangle), and  $Y'$  (empty green triangle) are shown.

ratus to HC beam properties. The measured asymmetry without any correction (solid squares) are compared to the asymmetry after correction using the intrinsic random variations in beam properties (Natural motion: upward pointing triangles) and to the asymmetry using the beam modulation (beam modulation: downward pointing triangles). The asymmetries derived using each technique are consistent with each other, and the overall correction for HCBAs is small. The data shown here represent the 80% of the Run-II data for which modulation was available. Run-I provides an additional 1/3 of the total data acquired in the experiment [123].

## 5.2 Beamlne Optics

A typical BPM response to modulation drive signal is shown in Figure 4.17. Response from all 23<sup>1</sup> BPMs in the Hall-C beamline to modulation signal were observed throughout the production data collection. BPM responses in X due to X modulation are shown in the figure. The vertical axis is BPM X-signal for X kick and horizontal axis is ramp-wave (the ramp-wave was used to monitor

<sup>1</sup>There were 24 BPMs in the Hall-C beamline. BPM 3H09B died after Run-I, hence excluded from the analysis.

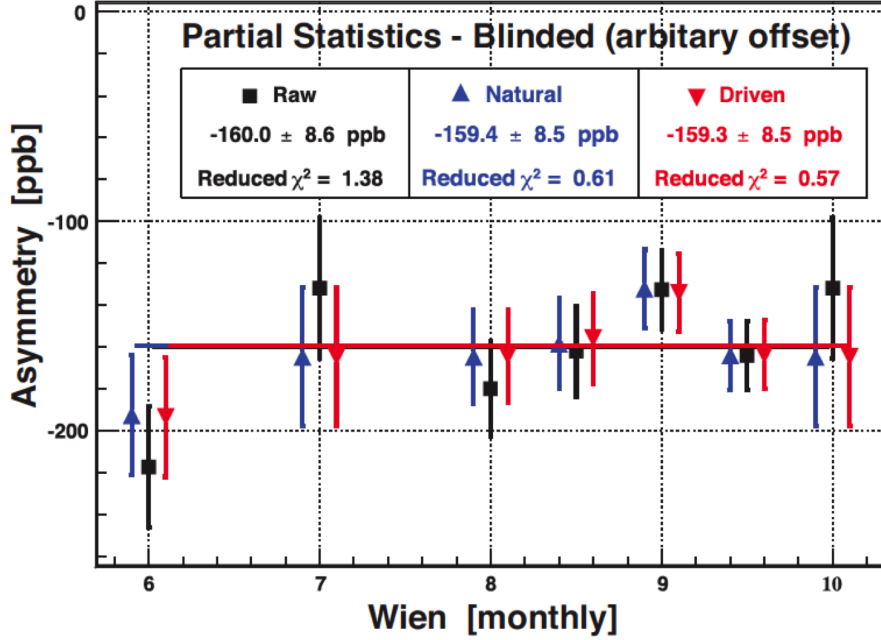


Figure 5.3 Subset of the Run 2 production data showing the blinded asymmetry (in ppb) grouped by (monthly) Wien state, and corrected using two different approaches to determine the sensitivities of the apparatus to HC beam properties that can give rise to false asymmetries. Other needed corrections are not applied to the data in this figure, as discussed in the text. The results without any correction (solid squares) are compared to the results after correction using the intrinsic random variations in beam properties (Natural motion: upward pointing triangles) and to the results using the driven beam motion (Driven motion: downward pointing triangles) discussed in Sec. 3.5 where the sensitivities are derived by actively modulating each property of the beam with a magnitude significantly larger than intrinsically carried by the beam. The asymmetries derived using each technique are consistent with each other, and the overall correction for HCBAs is small. The data shown here represent the 80% of the Run 2 data for which driven motion was available. Run 1 provides an additional 1/3 of the total data acquired in the experiment [123].

the phase of the drive signals). The data is shown in red and fit in dark red. The responses of the BPMs are arranged according to the distance from the target.

Beam position response amplitude of all the BPMs in the Hall-C beamline to X modulation with respect to Z location from the target are shown in Figure 5.5. The location of all the BPMs are shown at the top of the plot by vertical line. All the quadrupoles, dipoles, Compton dipoles, Møller magnets, target, and BMod magnets are shown at the bottom of the plot by vertical lines. Data are shown in solid circle, and simulated points from OptiM are shown in empty square. This figure represent the evolution of the position response amplitude along the Hall-C beamline. The data

matches quite well the simulation. This method of tracking BPM response also helped to find any optics change or hardware failure in the beamline.

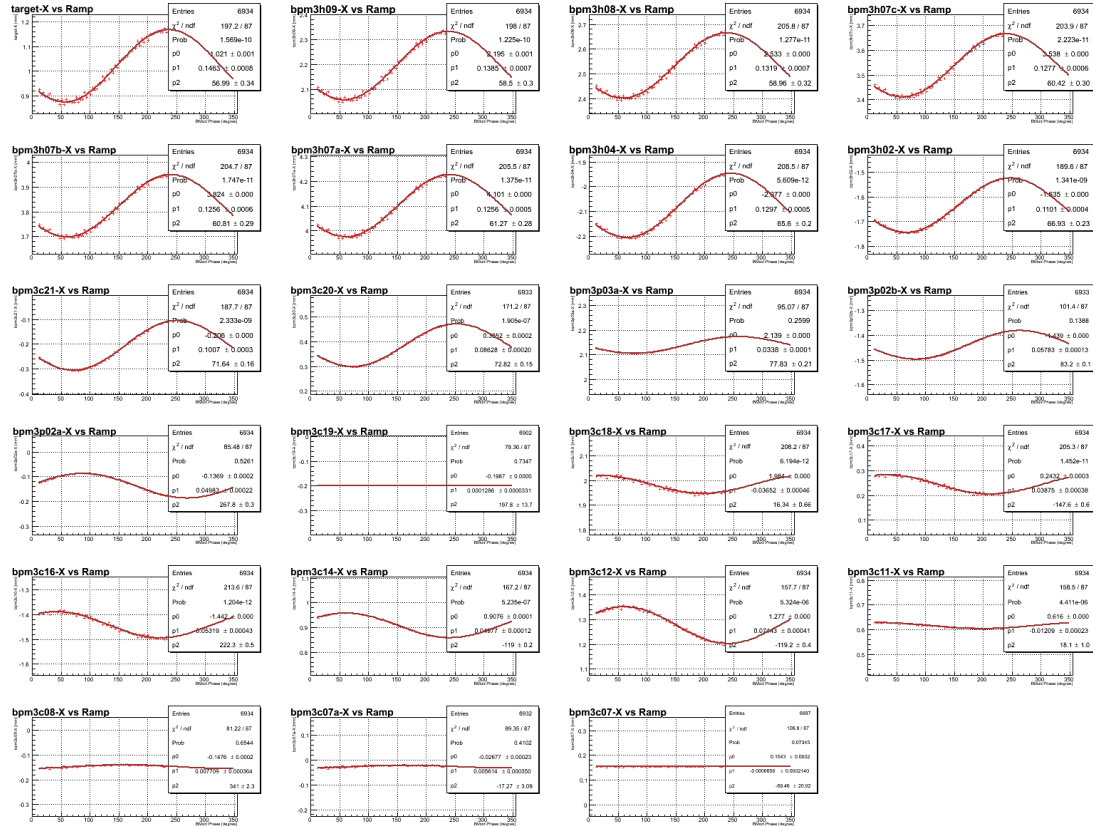


Figure 5.4 Beam position response of all the BPMs in the Hall-C beamline to X modulation. The location of all the BPMs are shown at the top of the plot by vertical line. All the quadrupoles, dipoles, Compton dipoles, Møller magnets, target, and BMod magnets are shown at the bottom of the plot by vertical lines. Data are shown in solid circle, and simulated points from OptiM are shown in empty square.

### 5.2.1 Beam Modulation Tune Parameter Scan

The idea of this analysis is to find a pure angle and position tune at the target for beam modulation system. In order to achieve a pure X and Y position and angle at target scan of the tune parameters was performed by varying the ratio of the drive signals in small steps. The maximum function generator drive signals were set to be 0.444 times of nominal amplitudes (shown in previous chapter Table 4.3) for this test for caution. The tune parameters were changed by changing the current in one coil ( $I_1$ ) in steps of 50%, 25%, 0%, -25% and -50% respectively keeping the other coil

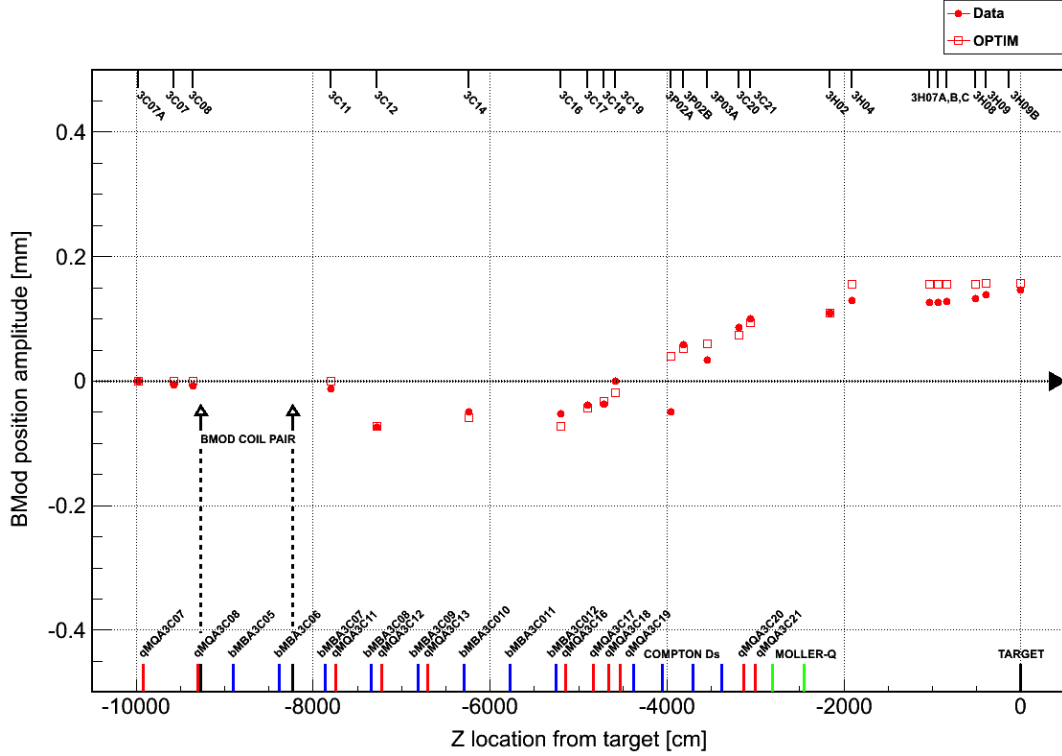


Figure 5.5 Beam position response of all the BPMs in the Hall-C beamline to X modulation. The location of all the BPMs are shown at the top of the plot by vertical line. All the quadrupoles, dipoles, Compton dipoles, Møller magnets, target, and BMod magnets are shown at the bottom of the plot by vertical lines. Data are shown in solid circle, and simulated points from OptiM are shown in empty square.

( $I_1$ ) fixed to achieve a tune that generates pure angle at the target. A pure X- angle tune found to be in between the tune parameters -5.8824(nominal) and -9.0090(53.2%) and Y-angle to be in between -0.500(nominal) and -0.675(35%). The tunes for X and Y positions were already good to produce relatively pure position at the target.

### 5.2.2 Effect of Fast Feed Back on Beam Modulation

The idea of this analysis was to show the effect of Fast Feed Back (FFB) on beam modulation system. The FFB system was designed to suppress any position and energy fluctuation in the energy. So it was important to inspect the effect of FFB system on modulation system. Figure ?? shows the beam position response of all the BPMs in the Hall-C beamline to X modulation for FFB ON and OFF by red empty circle and black empty triangle respectively. The simulated position response from OptiM are also shown in the figure by solid red square. The driven signals were 0.444 times of

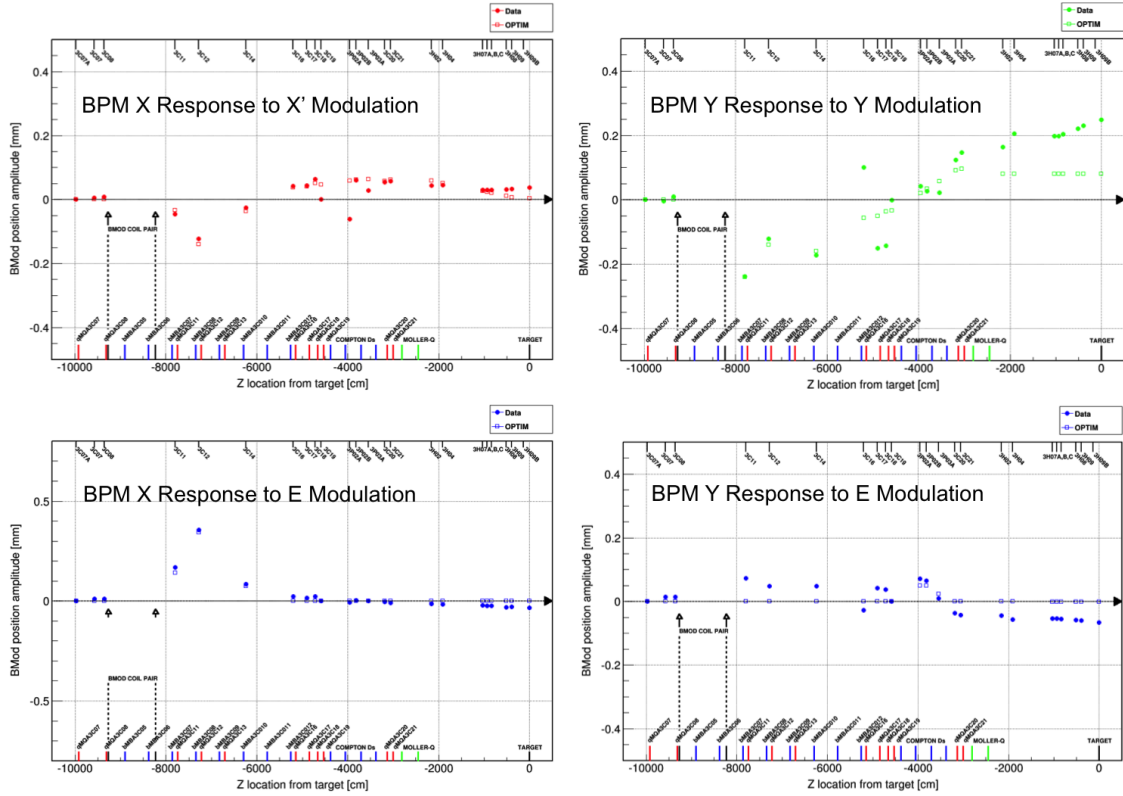


Figure 5.6 Beam position response of all the BPMs in the Hall-C beamline to X modulation. The location of all the BPMs are shown at the top of the plot by vertical line. All the quadrupoles, dipoles, Compton dipoles, Møller magnets, target, and BMod magnets are shown at the bottom of the plot by vertical lines. Data are shown in solid circle, and simulated points from OptiM are shown in empty square.

nominal amplitudes for this test. There were no effects of FFB on BPM responses amplitudes for X, Y and Y' modulation and was very small suppression for X' modulation. So this preliminary study showed no significant position suppression of the BPM responses amplitudes due to FFB system as shown in Figure ???. Although the effect of on the phase of the BPM's along the beamline was not insignificant [124]. The FFB was not paused during position modulation and might be responsible for the phase slip. Originally FFB was paused during Run-I during position modulation, and the energy was locked during energy modulation. In an effort to be less invasive production running FFB was always kept on for position and angle modulations, and number of energy modulation cycles were reduced to half during Run-II. New analysis approach to used to counter the phase slip problem [125]. The position-dependent phase slip was assumed to be a sum of modulation from two different locations and two independent transfer functions from each of the driving locations can be used to decompose the response. The FFB response can be decomposed into a combination of

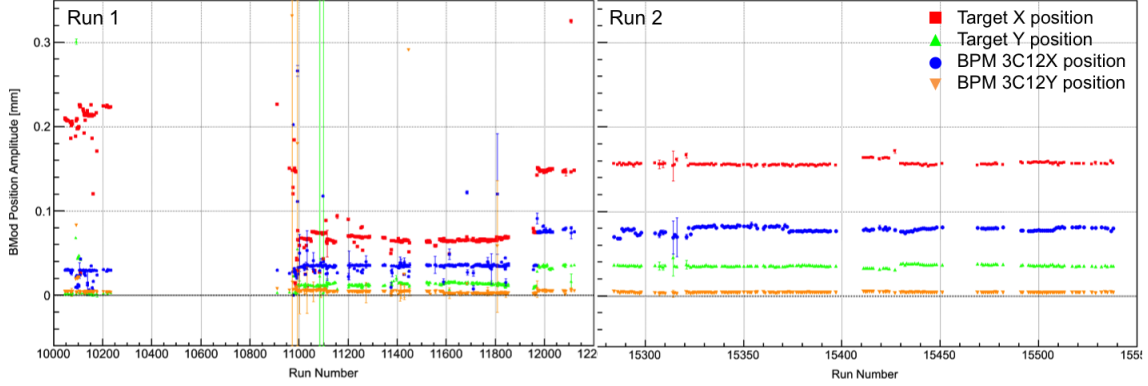


Figure 5.7 Hall-C target BPM responses due to modulation kick using a pair of coil in X. The sinusoidal response of the target BPM of a modulation signal for relatively pure X is fitted and the amplitude of the sinusoidal signal is plotted in vertical axis. The vertical axis is BMod BPM position in cm. The X target position is shown with solid red diamond, Y target position is shown with solid green triangle, BPM 3C12 X position is shown with solid blue square, BPM 3C12 Y position is shown with solid orange circle. For a relatively pure X position motion, we expect largely X target response and very small X angle response. We don't expect any Y position or Y angle response in this case. BPM 3C12X position response is relatively constant and 3C12Y is consistent with zero.

two harmonic functions one sine and one cosine that match phase with the beam modulation signal. The FFB sine response combined with modulation drive sine function become the effective driving signal and FFB cosine response averages to zero amplitude for the sine fit.

### 5.2.3 BPM Sign Corrections

Beam modulation system also helped to track some of the problems in the BPMs in the Hall-C beamline. During Run-I, BPM 3C19X (as shown in Figure ??) and Y showed no response to any modulation drive signals and BPM 3C16Y showed an inverted response to modulation signals (more details in APPENDIX-A.1). After investigation miss connected cables were found for those BPMs and repaired before Run-II. These BPMs did not affect any physics results for Run-I, as they were not used in any asymmetry or regression calculation.

## 5.3 BPM Resolution

It was necessary to extract the BPM resolution from the collected production data. BPMs in front of the target e.g; 3H09B, 3H09, 3H07C, 3H07B, and 3H07A were used for the linear regression and hence important to know their position and angle resolutions.

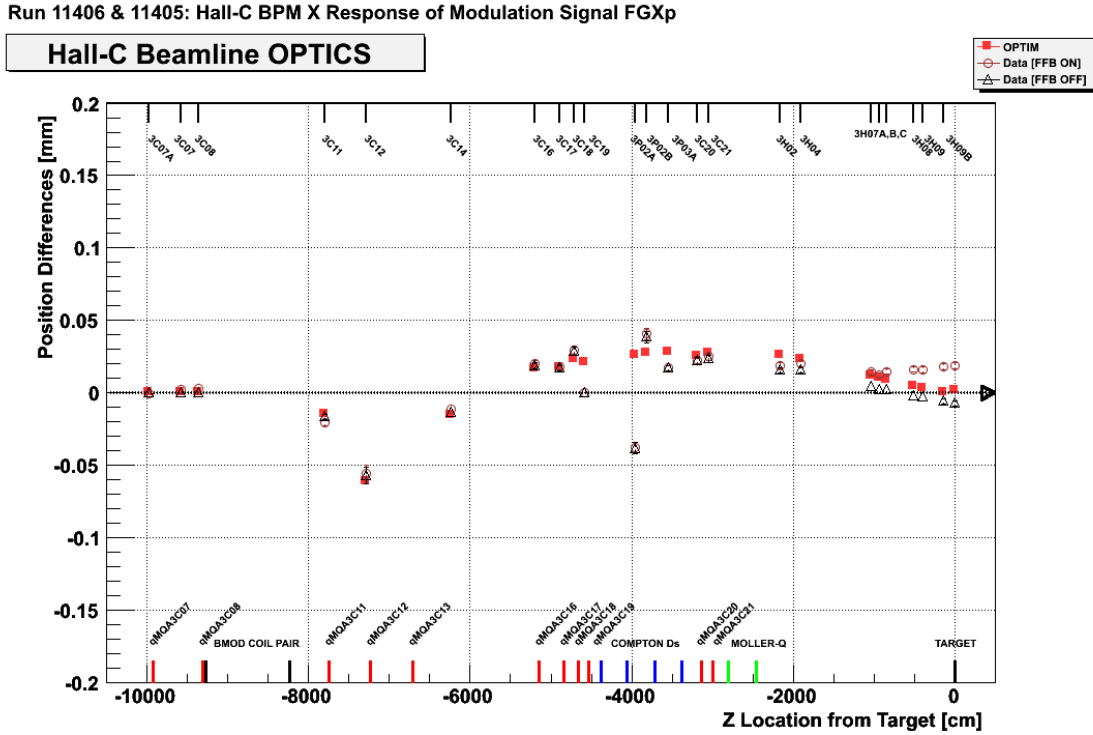


Figure 5.8 Hall-C BPM responses in X due to kick using a pair of coil in X. The vertical axis is BPM X-signal amplitude and horizontal axis is beamline elements. The simulated points from OptiM are shown in solid red square, data with FFB ON are shown in empty red circle and data with FFB OFF are shown in empty black triangle. Almost no effect of FFB on data for X motion. The location of all the BPMs are shown at the top of the plot by vertical line. All the quadrupoles, dipoles, Compton dipoles, Møller magnets, target, and BMod magnets are shown at the bottom of the plot by vertical lines.

### 5.3.1 Position Resolution

The target BPM is a virtual BPM calculated using the BPM in the drift region (more details on virtual target BPM in section 3.6.1 and [63]). The position resolution of the BPM in front of the target were extracted by observing the residual of beam position differences (between two helicity states) on any BPM and the orbit projected from the target and is shown in Equation 5.3.1 and 5.3.2.

$$\text{BPM resolution} \approx \sigma_{\text{Residual}} = \text{diff}_{\text{BPM}} - \text{Orbit Position Differences} \quad (5.3.1)$$

$$\text{Orbit Position Differences} = (Z_{\text{BPM}} - Z_{Tgt})\text{diff}_{TgtSlope} + \text{diff}_{Tgt} \quad (5.3.2)$$

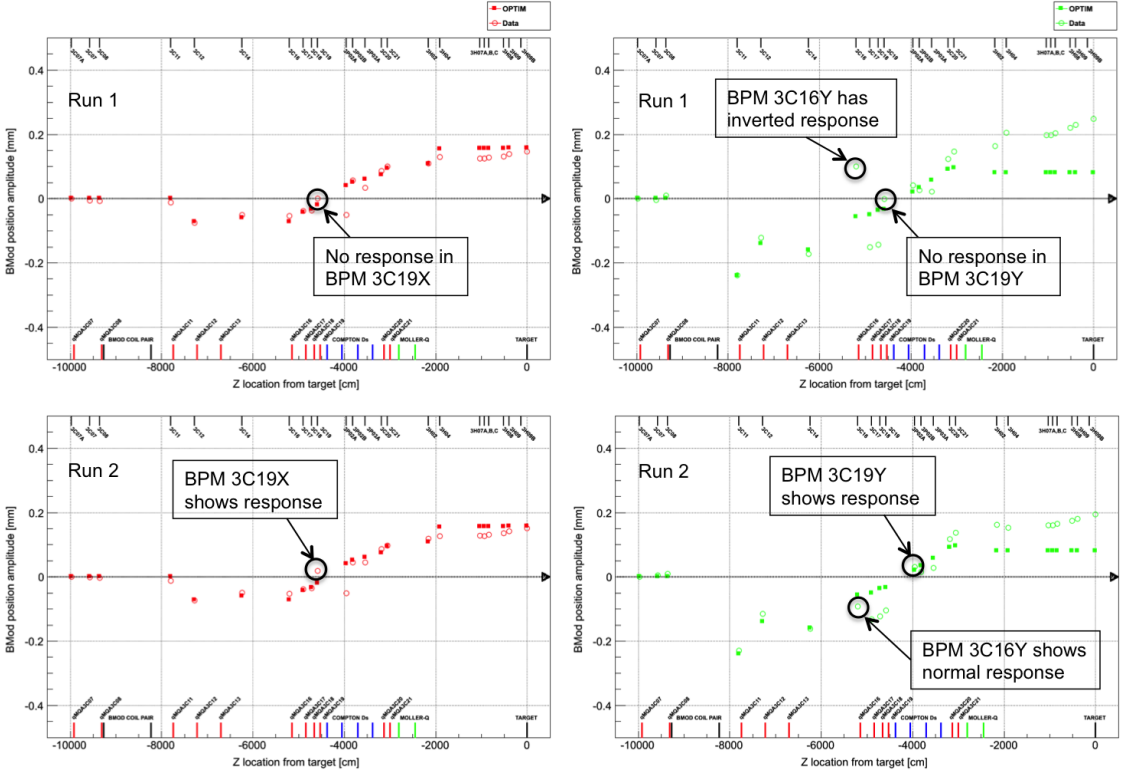


Figure 5.9 Beam position response of all the BPMs in the Hall-C beamline to X modulation. The location of all the BPMs are shown at the top of the plot by vertical line. All the quadrupoles, dipoles, Compton dipoles, Møller magnets, target, and BMod magnets are shown at the bottom of the plot by vertical lines. Data are shown in solid circle, and simulated points from OptiM are shown in empty square.

BPM 3H09B has relatively good resolution but was not available during Run-II. Resolution for 3H04 was poor as shown in Figure 5.10. This inconsistency might be due to noise injected by the existing corrector magnets between BPM 3H04 and 3H07A. BPM 3H08 has a different hardware compare to other BPMs. Hence BPM 3H04 and 3H08 were not included for the target BPM construction. Position resolutions for all the BPMs in front of the target were stable during Wien-0 at fixed current. Y resolution were quite similar to the X resolution. Using selective data samples from the commissioning phase of the experiment the average BPM resolution for Wien-0 is summarized in Table 5.2. An independent study of BPM 3H07B resolution by B. Waidyawansa [126] yields the resolution of  $0.945 \pm 0.003$ , and  $1.060 \pm 0.003$  for X and Y resolution respectively and roughly agrees with this calculation.

HYDROGEN-CELL (Parity, production): HWP-IN Beam Position Differences and Residuals vs Z for Run 9737 from run1\_pass5 Rootfile

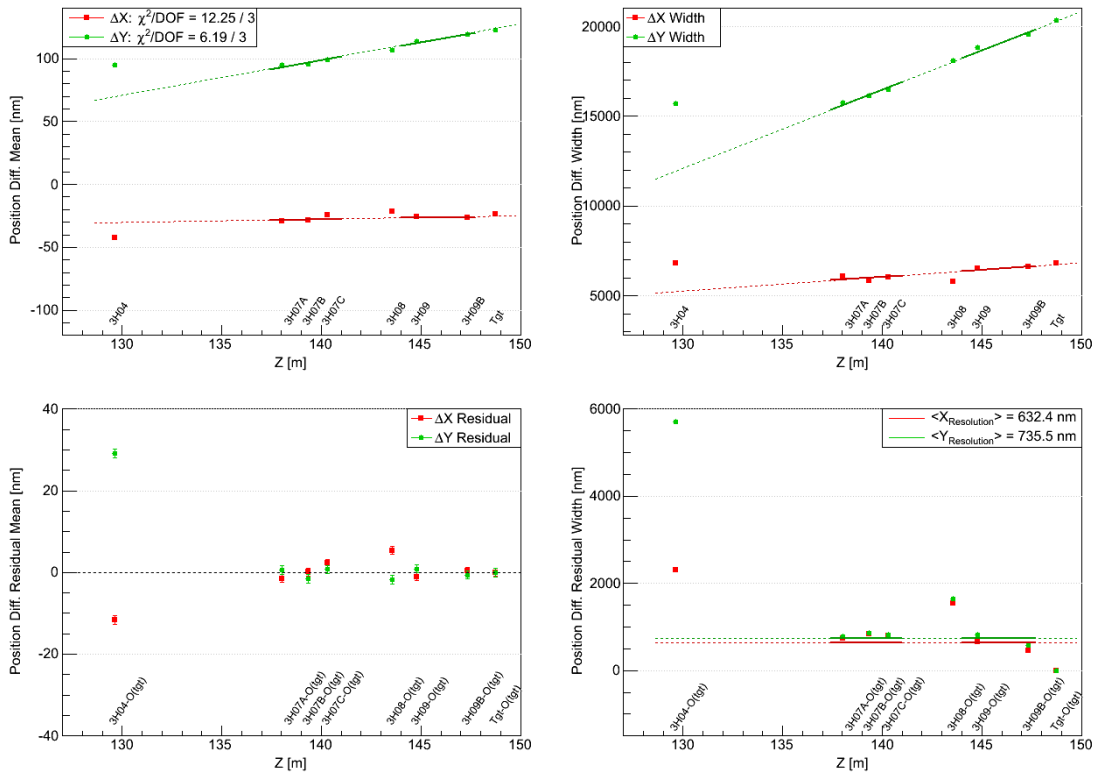


Figure 5.10 BPM position resolution. Beam position differences for a typical one hour production run during Wien0 at beam current of  $145 \mu\text{A}$ . Error weighted pol1 fit are shown by solid line. BPM 3H04, 08 and, Tgt are not in the fit. Fit is extrapolated using dashed line to guide the view.

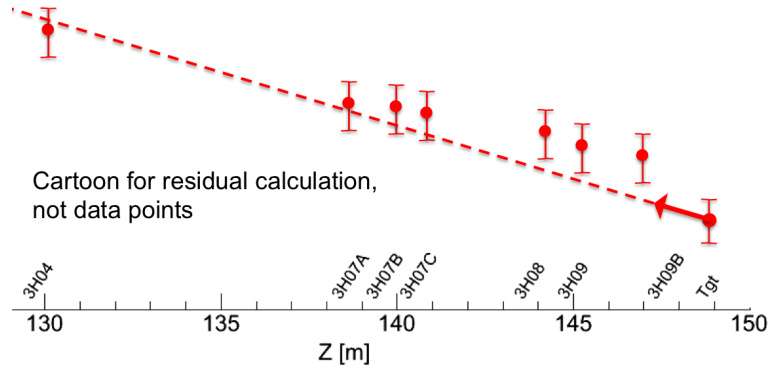
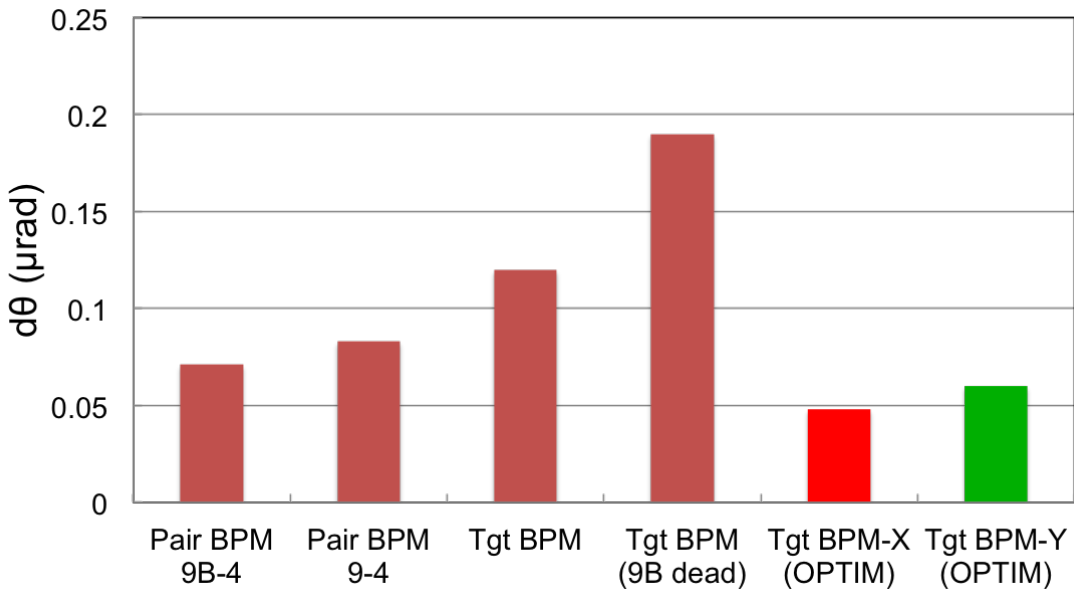


Figure 5.11 BPM resolution cartoon.

Table 5.2 BPM position resolution.

BPM	X Resolution [ $\mu\text{m}$ ]	Y Resolution [ $\mu\text{m}$ ]
9B	0.46	0.57
9	0.67	0.81
7C	0.81	0.83
7B	0.83	0.87
7A	0.74	0.78
4	1.70	3.55
Average (4 excluded)	0.70	0.77

Figure 5.12 Target BPM angle resolution at beam current of 180  $\mu\text{A}$ .

### 5.3.2 Target BPM Angle Resolution

The target BPM angle resolution was simulated using OptiM [69]. In order to estimate target BPM angle resolution a relatively pure position measurement which corresponds to pure angle measurement at target was needed. One such possible position measurement was found to be around Compton region and chosen to be at BPM 3P02A from OptiM simulation. A study of strength sharing between angle and position in the various BPM's along the beamline for Wien-0 shows Compton BPMs (3P02A and B) were insensitive to position on target. Then known BPM position resolution and transport matrices were used to estimate effective angle resolution. Assuming 0.90 (0.96)  $\mu\text{m}$  X(Y)-position resolution estimated target BPM angle resolutions at 180  $\mu\text{A}$  are

$$\text{X-angle resolution} = 0.048 \mu\text{rad} \quad (5.3.3)$$

$$\text{Y-angle resolution} = 0.060 \mu\text{rad} \quad (5.3.4)$$

With the simple model where angle jitter at the target corresponds to pure position at 3P02A (without using transport matrix) also gives similar answer. The simulated target BPM resolution in this analysis is found to be better than the existing calculation with other BPMs. A comparison of the resolution using different BPM pairs are shown in Figure 5.12.

### 5.3.3 Consistency Check of Target Variable

Most commonly used independent variable for the linear regression were target positions and angles. So it was important to check the consistency of the target variable, since it was created using six BPMs in the drift region in the beamline over a span of 10 m upstream of the target (more details about target variable can be found in Section 3.6.1 and in [61, 63]). In order to check the consistency of the variable the BPM differences used for the calculation were projected back to the target as shown in Figure 5.10 (top left). The residuals were shown in the bottom left of the figure. Target BPM itself look fine, it appears that intercept in data base sometimes significantly wrong and made  $\chi^2/\text{DOF}$  worse. As in the regression or any of the Q-weak calculation the intercept was not used hence should not have any problem. A linear fit of the BPMs in front goes through target BPM within 0.03 nm. X position differences errors are usually under estimated and need to know it to assign errors in regression. BPM 3H04 effectively has the wrong units and a scale factor of 0.75 fixes the problem. It is not clear yet how big a problem this is for regression as 3H04 was used in few regression schemes. Beam jitter was stable and Y jitter is larger than X jitter. BPM 3H09B has very good resolution and was only available during Run-I due to hardware failure. Resolution for 3H04 and 8 were high and had different hardware compare to other BPMs. BPM 3H07B resolution was  $\sim 0.9 \mu\text{m}$  and agrees with an independent study [126]. The corrector magnet between 3H04 and 3H07A seems to affect the resolution calculation. Resolution of other BPMs in front of target (in the drift region) seems reasonable.

## 5.4 Helicity Correlated Pedestal Analysis

The Q-weak collaboration proposed to measure the small parity violating asymmetry ( $\sim 250$  ppb) in elastic e+p scattering precisely [8]. The goal of the collaboration is to reduce any false asymmetry from various sources. One such potential source is helicity correlated pedestal differences for different detectors. The beam off detector yield at nominal operation and settings are known as pedestals of that detector. Pedestal can be determined by the preamplifier offset and backgrounds with beam off data.

### 5.4.1 Motivation

A helicity correlated pedestal difference is a detector pedestal that is consistently different between the two helicity states. Any non-zero helicity correlated pedestal differences can cause false asymmetries in the measured parity violating asymmetry. The stability of the detector pedestal in the current mode ( $Y_{ped}$ ) is directly related to the detector yield determination and can affect the detector linearity and asymmetry calculation. Helicity correlated pedestal differences could occur in many possible ways. One such process can be leakage from the pockel cell's high voltage which can change the polarization of the laser light that produces electrons from the photocathode. Main detectors, luminosity monitors and beam charge monitors need to be isolated from this pockel cell voltage flip in order to suppress helicity correlated pedestals. A small mV level leakage can create a huge false asymmetry (as shown in Equation 5.4.2), making this the primary motivation to monitor helicity correlated pedestal differences throughout the experiment.

### 5.4.2 Analysis Procedure and Goal

Typically, 5 minutes of dedicated beam off pedestal runs were taken during production running once a day during Run 1 and once every eight hours during Run 2. There were also  $\sim 1$  hour long beam off pedestal runs taken throughout, whenever there was an opportunity (for details see Appendix A, section D.1). The purpose of these pedestal runs was to minimize nonlinear distortions of asymmetries due to incorrect pedestals in the main detectors in the DC regime and estimate false asymmetry due to leakage current [10, 127]. The goal of this analysis is to survey the helicity correlated pedestal differences and raw pedestal signal for the entire experiment. The mean of the helicity correlated pedestal differences distribution gives an idea about the scale of false asymmetries and its width conveys a sense about the electronic chain noise level. Studying raw pedestal signals

also helps to estimate the detector non-linearity due to wrong pedestals and the rms width of the raw signal provides an impression about the detector resolution.

### 5.4.3 Experimental Method

For a quartet of "+ - - +", measured asymmetry can be expressed as

$$A_M(+--+) = \frac{S_1^+ - S_2^- - S_3^- + S_4^+}{(S_1^+ - P) + (S_2^- - P) + (S_3^- - P) + (S_4^+ - P)}, \quad (5.4.1)$$

where  $S$ 's are the detector signals and  $P$  is the detector pedestal. A typical beam on detector signal size was  $\sim 6$  V. In order to estimate false asymmetry due to helicity correlated differences, consider a  $0.01 \mu\text{V}$  voltage difference between + and - helicity states for the nominal detector signal. Then a false asymmetry due to this voltage difference can be calculated as

$$\frac{0.01 \times 10^{-6} \text{ V}}{6 \text{ V}} = 1.7 \times 10^{-9} = 1.7 \text{ ppb}. \quad (5.4.2)$$

The magnitude of the expected measured asymmetry for the Q-weak experiment is  $\sim 250$  ppb. From the example in Equation 5.4.2 the false asymmetry can be 0.7%. To sense the effect of a wrong raw pedestal signal, consider a typical 120 mV pedestal error in a 6 V signal as an example. Then the potential non-linearity due to this error in the detector can be written as

$$\frac{120 \times 10^{-3} \text{ V}}{6 \text{ V}} = 2\%. \quad (5.4.3)$$

As shown in the above examples, a small leakage in the pockel cell's high voltage and wrong pedestal measurement can create significant false asymmetries in the measured asymmetry and non-linearity in the detector signals. So it was important to survey helicity correlated pedestal difference for the important detectors that can impact the Q-weak measured asymmetry.

### 5.4.4 Results

The main detectors and luminosity monitors are normalized to the charge monitors so it is important that neither have any evidence of helicity correlated pedestal differences. Helicity correlated differences from Hel\_Tree of a typical 5 minutes pedestal run are shown in Figure 5.13. Even with only 5 minutes of data no evidence of any helicity correlated pick ups for combined Čerenkov main detector (MDAllbars), downstream luminosity monitor (DSLumiSum), upstream luminosity moni-

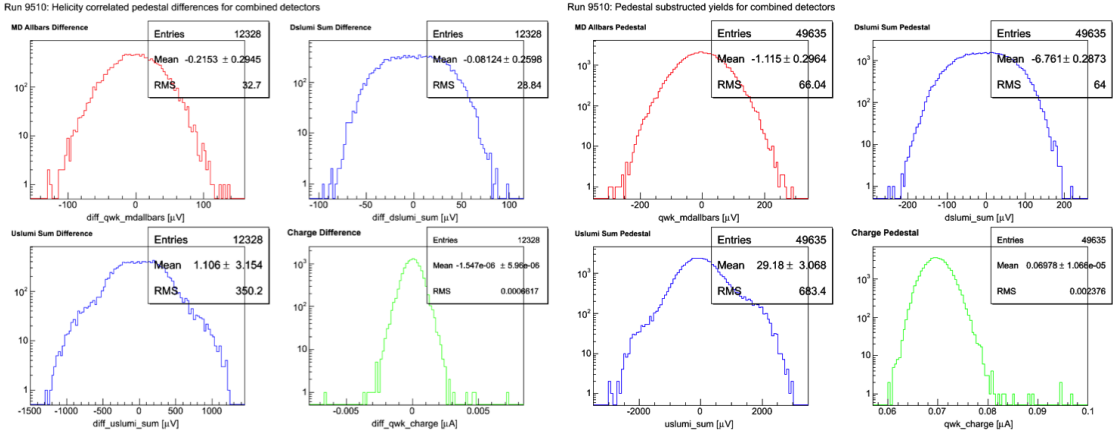


Figure 5.13 A typical beam off pedestal run (run# 9510). Helicity correlated differences for MDAllbars, DSLumiSum, USLumiSum, Charge (clockwise from top left corner) from Hel\_Tree are shown in left panel. Pedestal subtracted signal for MDAllbars, DSLumiSum, USLumiSum, Charge (clockwise from top left corner) from Mps\_Tree are shown in right panel.

tor (USLumiSum), and beam charge monitor (Charge) were seen. The channels surveyed during this analysis are 17 MDs, 9 DSLumis, 9 USLumis, and 9 BCMs (details of the variables are described in Appendix A, section C.2.4). The individual channels of the MDs, DSLumis, USLumis, and BCMs showed no significant pickup. All these channels were investigated individually for each run and then averaged (error weighted) over a Wien<sup>2</sup>. The Wien averaged helicity correlated differences for most important channels for the experiment MDAllbars, DSLumiSum, USLumiSum, and Charge<sup>3</sup> are shown in Figure 5.14.

#### 5.4.4.1 Helicity Correlated Pedestal Signal Pickup

The mean of the pedestal differences from Hel\_Tree in Figure 5.13 represent the helicity correlated pickup by a device. The surveyed result shows the average pickup for MD is  $0.15 \pm 0.52$  ppb for insertable half wave plate (IHWP) IN and  $0.40 \pm 0.50$  ppb for IHWP OUT (shown in Figure 5.14 by colored and black data points respectively). So helicity correlated pedestal differences have negligible contribution ( $\sim 0.2\%$ ) to any false asymmetries in the measured asymmetry. DS Lumi has a similar level of pickup as the MD. US Lumi shows  $\sim 7$  ppb pickup in worst case scenario which can be improved by using a better pedestal subtraction. BCMs have no pickups for the whole experiment.

<sup>2</sup>Experiment has total 11 Wien period. Double Wien filters were rotated to change the electron beam polarization. This help reducing the false asymmetry.

<sup>3</sup>Charge = bcm1 + bcm2 for Run 1 and = bcm8 for Run 2.

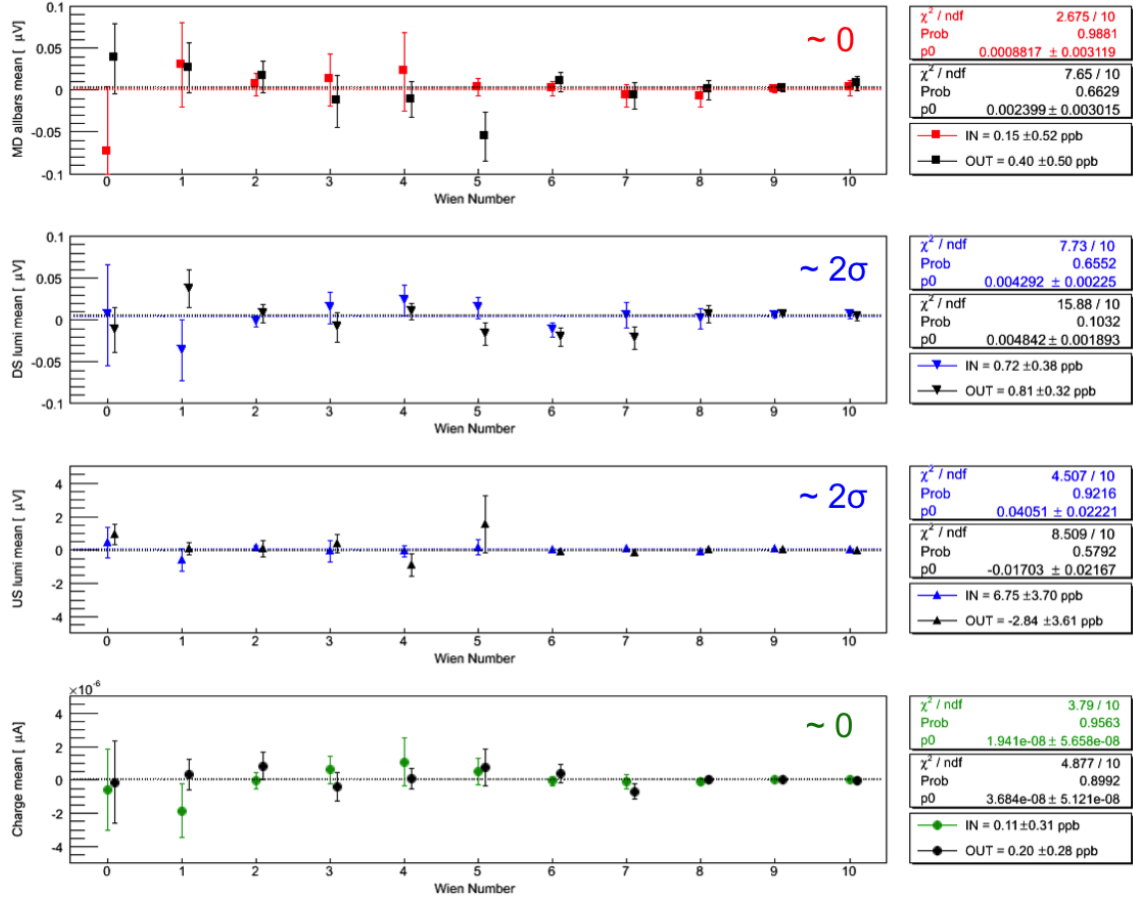


Figure 5.14 The mean of the pedestal differences from Hel\_Tree for MD allbars, DS lumi, US lumi and Charge are shown. Each data point is averaged over a Wien. Two half wave plate states are shown separately.

Overall pickup was much smaller during Run-II (Wien 6 - 10) compared to Run-I (Wien 0 - 5), and Run-0 (Wien 0). The distribution of standard deviations ( $\sigma$ ) for each channel and run is shown in Figure 5.15. The distribution of  $\sigma$  is Gaussian and mean is zero for each channel and run. The few  $\sigma$  from zero pickup for different detectors are within the statistical fluctuation. Mean of the helicity correlated differences for important background detectors (MD9, PMT only, PMT lightguide) were zero within  $\sim 1\sigma$  for each Wien where as for other background detectors pickups were zero within  $\sim 3\sigma$ .

#### 5.4.4.2 Helicity Correlated Pedestal Sensitivities

The helicity correlated pedestal difference width from Hel\_Tree represent the sensitivity of a device to the helicity. It also depicts the measure of electronic noise level for the detectors with low

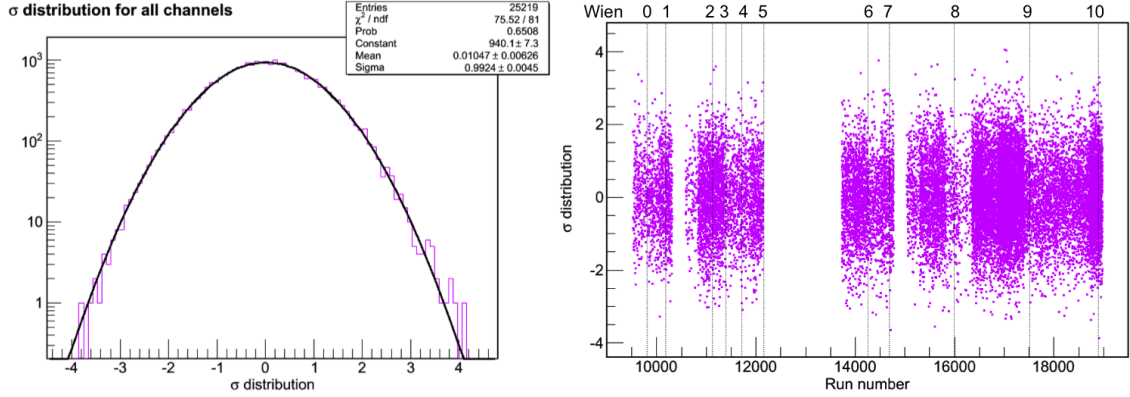


Figure 5.15 Sigma distribution of helicity correlated pedestal differences for all channels and Wien (left). Sigma of helicity correlated pedestal differences vs run number for all the channels are shown (right).

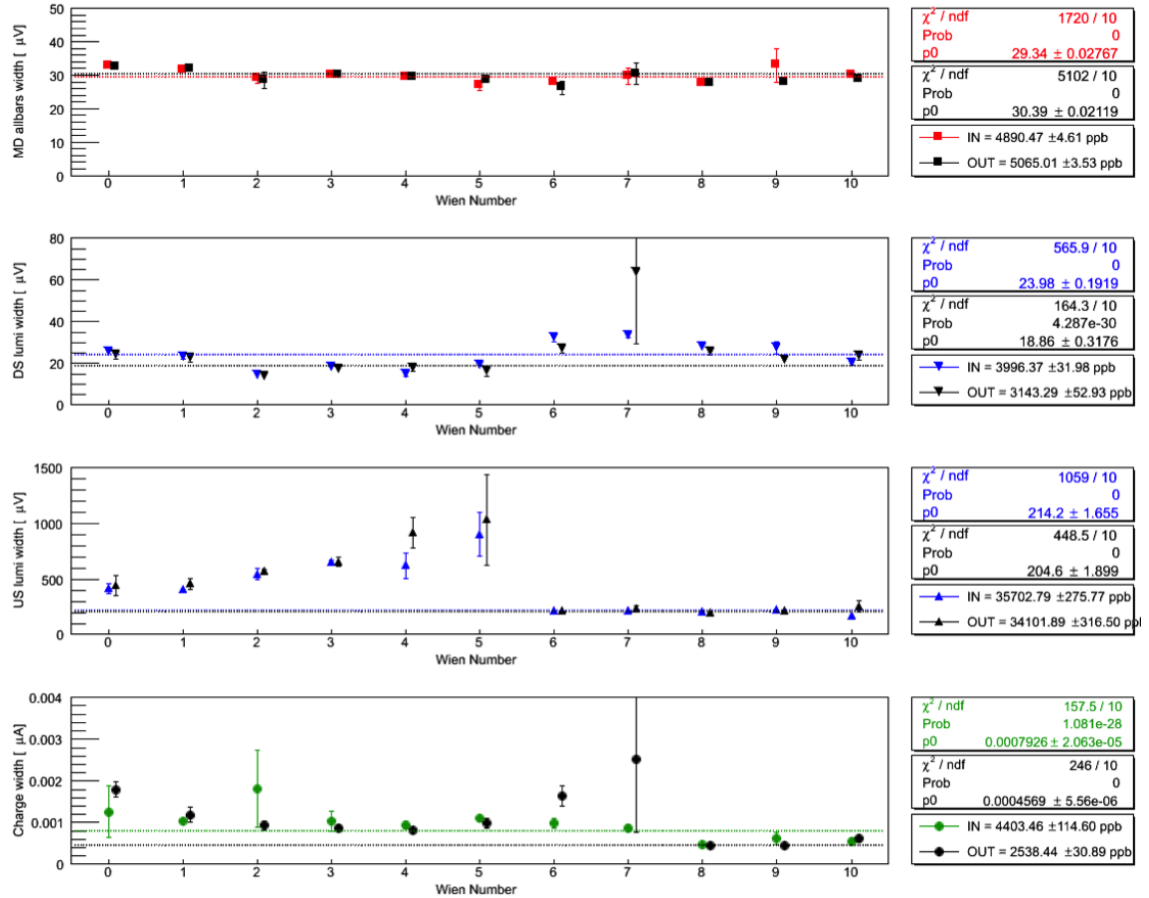


Figure 5.16 The width of the pedestal differences from Hel\_Tree for MDAllbars, DSLumiSum, USLumiSum and Charge are shown.

frequency rejection. The Wien averaged helicity correlated differences width for MDAllbars, DSLumiSum, USLumiSum, and Charge are shown in Figure 5.16. The average noise level of MDAllbars

was 25  $\mu$ V. The MDs and the DSLumis noise levels were acceptable and well behaved throughout the experiment. USLumi electronic noise could have limited the detector's resolution near end of Run-I, but has improved in Run-II after hardware repairs. Background detectors noise levels were reasonably stable during the experiment.

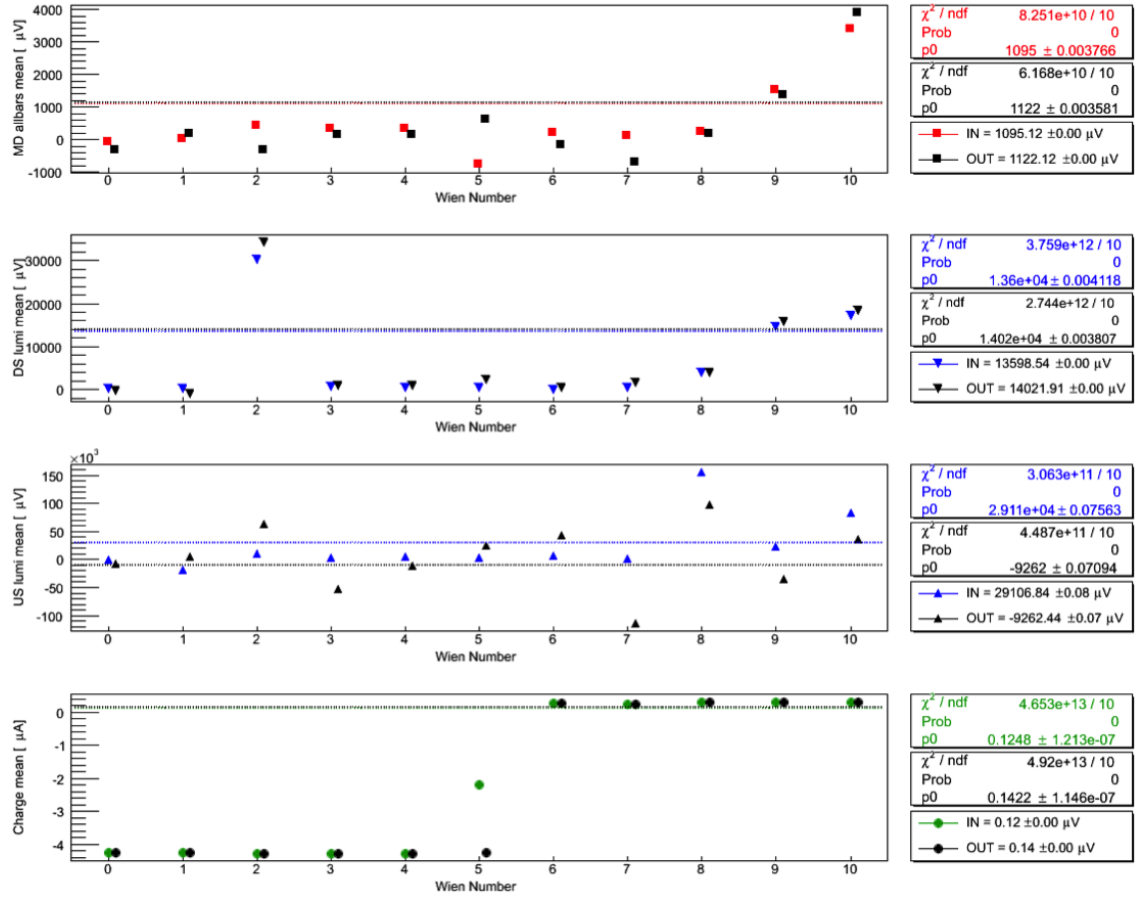


Figure 5.17 The mean of pedestal subtracted signal from Mps\_Tree for MDAllbars, DSLumiSum, USLumiSum and Charge are shown.

#### 5.4.4.3 Stability of Pedestal Subtracted Signal

The mean of pedestal subtracted signal from Mps\_Tree represent the relative change in pedestal signal compared to last pedestal. A wrong pedestal for a detector can cause nonlinearity in the detector system. MD pedestal was good to less than a mV (Figure 5.17). This results a nonlinearity of  $\ll 0.1\%$  for 6 V signals. The detector yields are smaller for Aluminum and N-to- $\Delta$  running compared to normal production running. The signal sizes are  $\sim 30\text{-}40\%$  of 6 V. So the nonlinearity for these cases are higher but still  $< 1\%$ , allowing for smaller yields. DSLumi pedestal was off by at

most 34 mV. The resulting nonlinearity would be < 1% assuming 6 V signals. To support Aluminum running and N-to- $\Delta$  pedestal subtraction should be improved in Wiens 2, 9, 10. USLumi pedestal was off by 100-150 mV in Wiens 7, 8 and could result a nonlinearity of several percent.

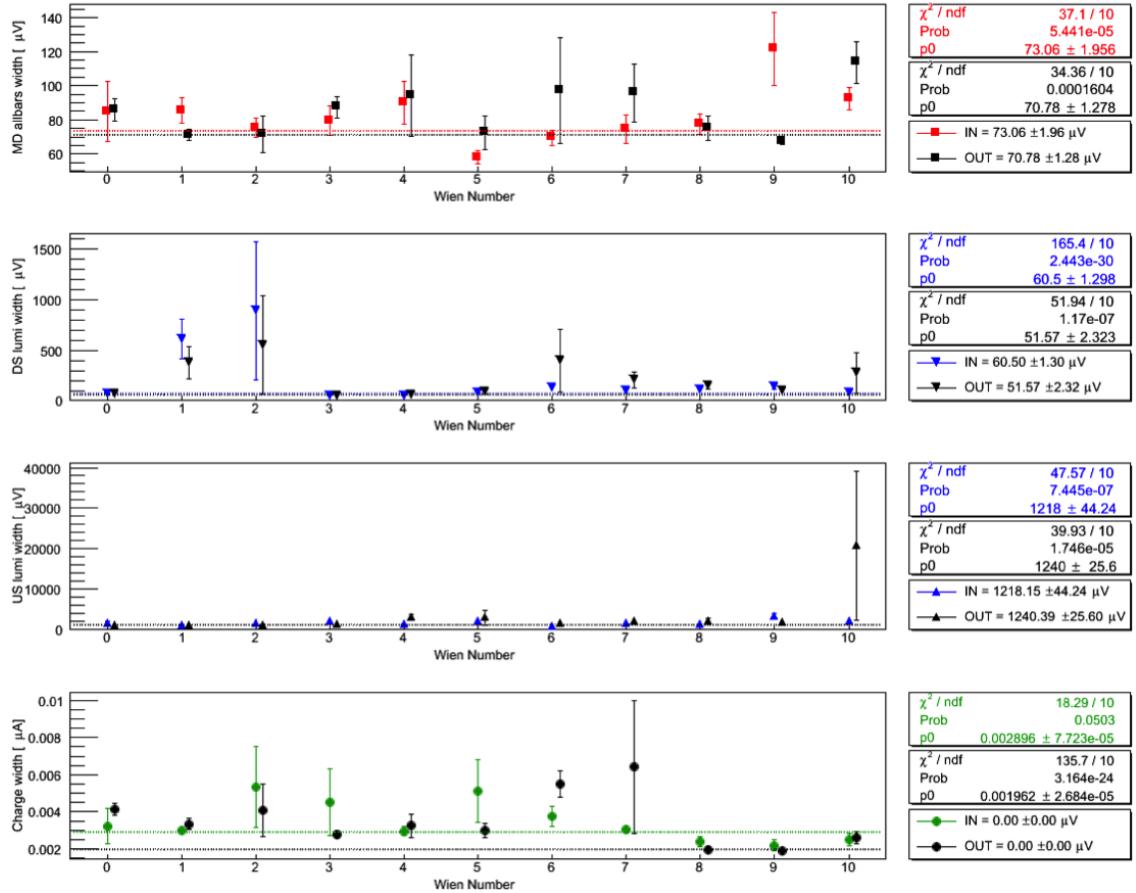


Figure 5.18 The width of pedestal subtracted signal from Mps\_Tree for MDAllbars, DSLumiSum, USLumiSum and Charge are shown.

#### 5.4.4.4 Detector Resolution

The width of pedestal subtracted signal from Mps\_Tree describe the measure of detector resolution. Resolution for MDs and DSLumis were very good ( $\sim 70 \mu\text{V}$ ) and reasonably stable during the experiment (Figure 5.18). USLumis resolution were  $\sim 15$  times worse than MDs and DSLumis but were very stable. The resolution for charge monitors and background detectors (except PMT LED) were steady throughout the experiment.

### 5.4.5 Summary of Helicity Correlated Pedestal Survey

No helicity correlated pickups were seen for most of the detector channels for Q-weak and were at  $\mathcal{O}(1)$  ppb. Electronic noise levels were generally acceptable, though potentially marginal for the USLumi channels near the end of Run-I but improved during Run-II. Nonlinearity for MDs were extremely small. USLumi also had a nonlinearity of few percent. There is a scope for improvement in USLumi pedestal. Nonlinearity could be very large for low-yield production running on Aluminum and N-to- $\Delta$  but still be under 1%. Resolutions for all the detectors were reasonably stable during Q-weak. A summary of helicity correlated pedestal survey all the results discussed are shown in Table 5.3

Table 5.3 Summary of helicity correlated pedestal survey.

Channels	False Asymmetry [ppb]	Sensitivity	Nonlinearity [%]	Electronic Noise
MDAllbars	0.4	30 $\mu\text{V}$	$\ll 0.1$	73 $\mu\text{V}$
DSLumiSum	0.8	24 $\mu\text{V}$	<1.0	61 $\mu\text{V}$
USLumiSum	6.8	214 $\mu\text{V}$	$\sim 1.0$	1240 $\mu\text{V}$
Charge	0.2	0.0079 $\mu\text{A}$	<0.1	0.0029 $\mu\text{A}$

## SECTION 6

### BEAM NORMAL SINGLE SPIN ASYMMETRY

#### 6.1 Introduction

Dedicated measurements of the beam normal single spin asymmetry in inelastic e+p, and e+N scattering near missing mass,  $W$ ,  $\sim 1.2$  GeV were performed during 18 - 20 February 2012 at Hall-C of Jefferson Lab using Q-weak apparatus.

#### 6.2 Experimental Method

The Q-weak setup [8] was used for inelastic transverse measurement. The electron beam polarization was changed from longitudinal to fully horizontal/ vertical polarization using the double Wien filter at the injector (Section 3.3.1). The torodial magnet setting was lowered to 6700 A to focus inelastically scattered electrons onto the main Čerenkov detectors.

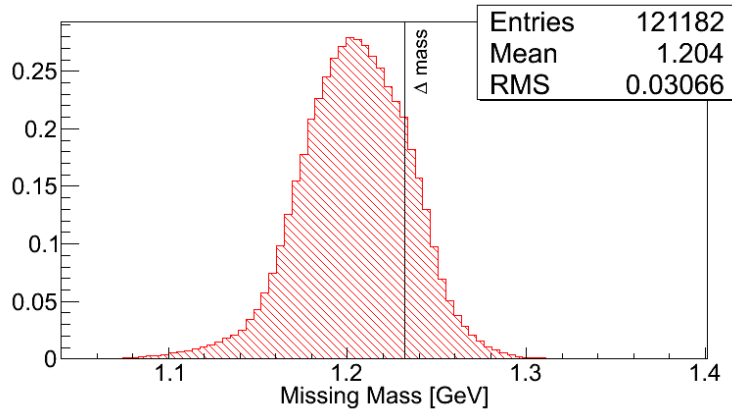


Figure 6.1 Simulated missing mass,  $W$ , distribution at the inelastic QTor setting.

##### 6.2.1 Available Data Set and Condition of Experimental Data Taking

Total collected data after hardware and software quality checks is shown in Table 6.1. The QTor current of 6700 A selects the inelastic events near  $W \sim 1.2$  GeV (Figure 6.1). Data on both sides of the inelastic peak (6000 A and 7300 A) were taken to check simulations of the elastic dilution. Two transverse spin orientations, horizontal and vertical, were used. Data were collected on liquid hydrogen ( $\text{LH}_2$ ) cell, 4% thick downstream aluminum alloy (Al), and a 1.6% thick downstream

carbon foil ( $^{12}\text{C}$ ) with 1.155 GeV beam for both spin orientations (as shown in Table 6.1). Different beam currents ( $I$ ) were used on different targets, as shown in Table 6.1. The beam was rastered on the target over an area of 4 mm  $\times$  4 mm by the fast raster system to minimize the target boiling. The Insertable Half Wave Plate (IHWP) was used to help suppress helicity correlated beam asymmetries and was reversed at intervals of about 2 hours. More information about the condition of data taking is given in APPENDIX-D section D.1.

Table 6.1 Run numbers for transverse N-to- $\Delta$  data set. The runs with vertical transverse polarization are in parentheses, the rest are from horizontal transverse polarization. Data collected in an hour was defined as run. The beam currents for the different targets are shown in second to last row. Total charge in Coulombs is shown in the bottom row.

IHWP	QTor current					
	6000 A		6700 A		7300 A	
	$\text{LH}_2^\dagger$	$\text{LH}_2^\dagger$	$\text{Al}^{\dagger\dagger}$	$^{12}\text{C}$	$\text{LH}_2^\dagger$	$\text{Al}^{\dagger\dagger}$
IN	16152	(16066)	(16067)	16150	16133	16122
	16153	16131	16115	16151	16134	16123
		16132	16116		16135	16124
OUT	16154		(16068)			16120
	16156	(16065)	(16069)	16148	16136	16121
	16157	16129	16117	16149	16137	16161
	16158	16130	16118			
			16119			
Beam current $I$ [ $\mu\text{A}$ ]		180	180	60	75	180
Collected Data [C]		1.5	1.8 (1.9)	0.8(0.4)	0.6	2.0
						0.9

In this dissertation, full analysis of the beam normal single spin asymmetry from inelastic electron-proton scattering on  $\text{LH}_2$  target, indicated by  $\dagger$  in Table 6.1, will be discussed. The transverse asymmetry on Al target, indicated by  $\dagger\dagger$  in the table, was also analyzed as a background correction for the  $\text{LH}_2$  target. The analysis of the remaining data are ongoing and will not be covered in this dissertation.

### 6.3 Extraction of Raw Asymmetries

The single detector asymmetry was obtained by averaging the two PMT asymmetries from each Čerenkov detector. The error weighted average of the asymmetries from runlets,  $\sim$ 5 minute long data samples, was extracted as the average asymmetry for a given data set. To extract the uncorrected raw asymmetry  $A_{\text{raw}}$  from the detectors, the average asymmetry for the two different Insertable Half Wave Plate (IHWP) settings, IN and OUT, were determined separately for each main detector bar.

The asymmetries measured in the IHWP configurations were sign corrected for the extra spin flip and averaged together after checking for the IHWP cancellation of the false asymmetries. The error weighted value of <IN,-OUT> determined the measured raw asymmetry for each bar. These raw asymmetries were then plotted against the detector octant number, which represents the location of the detector in the azimuthal plane ( $\phi = (\text{octant} - 1) \times 45^\circ$ ), and they were fitted using a function of the form in Equation 6.3.1. This analysis will focus on the azimuthal dependence of the detector asymmetries representing the transverse asymmetries.

$$f(\phi) = \begin{cases} \text{Horizontal transverse: } A_M^H \sin(\phi + \phi_0^H) + C^H \\ \text{Vertical transverse: } A_M^V \cos(\phi + \phi_0^V) + C^V \end{cases} \quad (6.3.1)$$

Here,  $\phi$  is the azimuthal angle in the transverse plane to the beam direction.  $\phi = 0$  indicates beam left,  $\phi_0$  is a possible phase offset expected to be consistent with zero.  $A_M$  is the measured asymmetry (amplitude) of the azimuthal modulation generated by BNSSA, and  $C$  is a constant appearing for monopole asymmetries such as the parity violating asymmetry generated by residual longitudinal polarization in the beam. The measured un-regressed raw asymmetries for the horizontal and vertical transverse polarization on LH<sub>2</sub> target are  $A_{\text{raw}}^H = 5.34 \pm 0.53$  ppm and  $A_{\text{raw}}^V = 4.60 \pm 0.81$  ppm respectively.

## 6.4 Asymmetry Correction using Linear Regression

The helicity correlated changes in the electron beam position, angle, and energy change the yield of the electrons in the detector acceptance. This can create false asymmetries in the detector and needs to be corrected before the extraction of the physics asymmetry. A multi variable linear regression [128] is used to remove the beam asymmetries from the raw Čerenkov detector asymmetries as shown in Equation 6.4.1.

$$A_M = A_{\text{raw}} - \sum_{i=1}^6 \left( \frac{\partial A_{\text{raw}}}{\partial T_i} \right) \Delta T_i \quad (6.4.1)$$

Here  $A_M$  is the measured asymmetry after regression, and  $(\partial A_{\text{raw}} / \partial T_i)$  is the detector sensitivity to a helicity-correlated beam parameter  $T_i$  with helicity-correlated differences  $\Delta T_i$ . During this measurement period, the helicity-correlated differences were stable (shown in Figure D.4, and D.5) and are summarized in Figure 6.3 and Table 6.2. The detector sensitivity slopes are calculated with linear regression, which uses natural beam motion during a runlet and considers correlations between

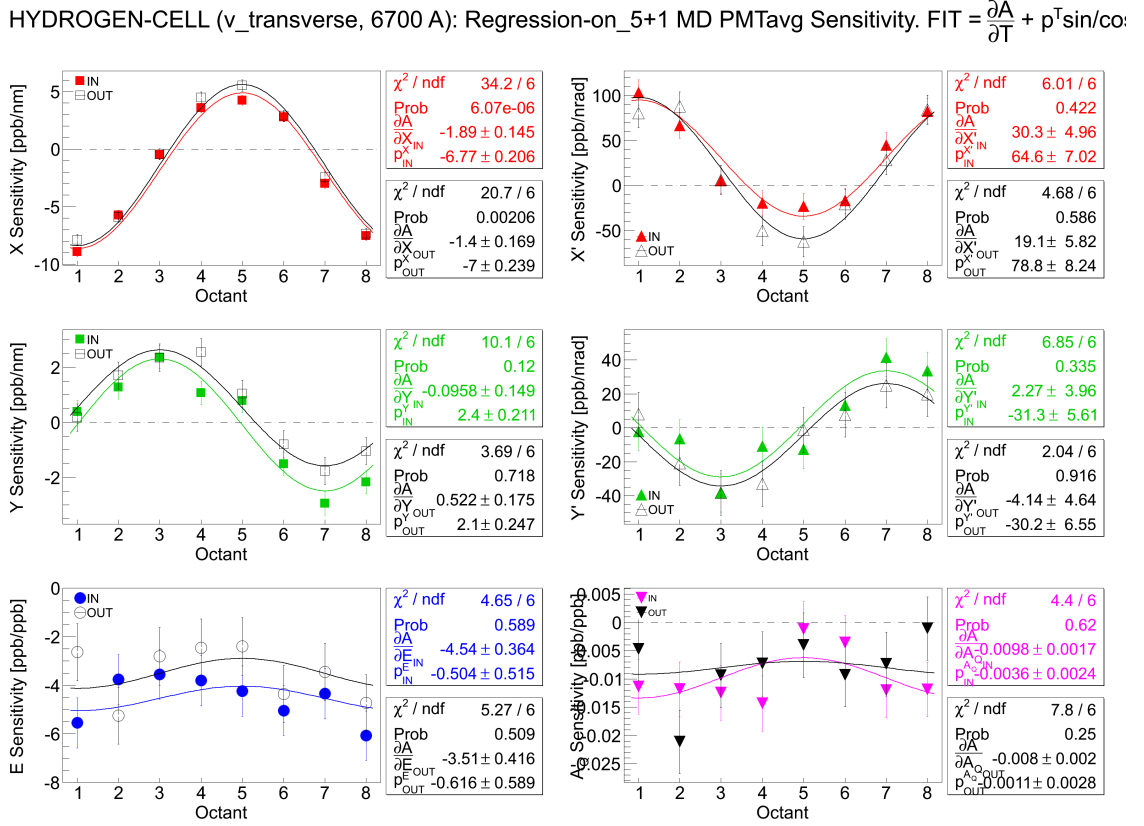


Figure 6.2 Azimuthal dependence of the main detector sensitivities to HCBA for the “5+1” regression scheme in the vertical LH<sub>2</sub> transverse data set are shown here. Sensitivities for beam positions and angles have sinusoidal dependence with octant. No such strong dependence is seen for energy and charge. Two IHWP states are shown separately for each beam parameter. Fit functions used to fit the parameters are shown on the plot. The constant in the fit gives the error weighted average of the sensitivities. See APPENDIX-D, section D.3 for the sensitivities and corrections from full data sets.

different beam parameters. The asymmetries presented in this dissertation are regressed against six (5+1) beam parameters ( $T_i$ ): horizontal position ( $X$ ), horizontal angle ( $X'$ ), vertical position ( $Y$ ), vertical angle ( $Y'$ ), the energy asymmetry ( $A_E$ ), and the charge asymmetry ( $A_Q$ ). The sensitivities of the Čerenkov detectors to different helicity correlated beam parameters have azimuthal dependence, as shown in Figure 6.2 (shown for vertical transverse data only, horizontal transverse can be found in Figure ??). This azimuthal dependence of the position and angle sensitivities are a result of the movement of the scattered electron profile across the octants which changes the effective scattering angle of the detected electrons not specific to the transverse asymmetry measurement. The position and angle sensitivities are anti-correlated. The energy and charge sensitivities are not expected to have any azimuthal dependence since they do not change the acceptance. The size of the applied

correction to the raw asymmetries depends on the size of the helicity-correlated beam parameter differences  $\Delta T_i$  and the sensitivities ( $\partial A_{\text{raw}} / \partial T_i$ ). The size of the corrections were  $\sim 2\text{-}3$  order of magnitude smaller compared to the size of the measured asymmetry and are shown in Figure 6.4 (shown for vertical transverse data only, horizontal transverse can be found in Figure ??). The total applied regression correction (Figure 6.5) is dominated by the  $X$  correction (Figure 6.4 top left). The corrections are summarized in Figure 6.6.

HYDROGEN-CELL (H+V transverse, 6700 A): Regression-on\_5+1 Beam Parameter Differences. No sign flips, or cuts applied.

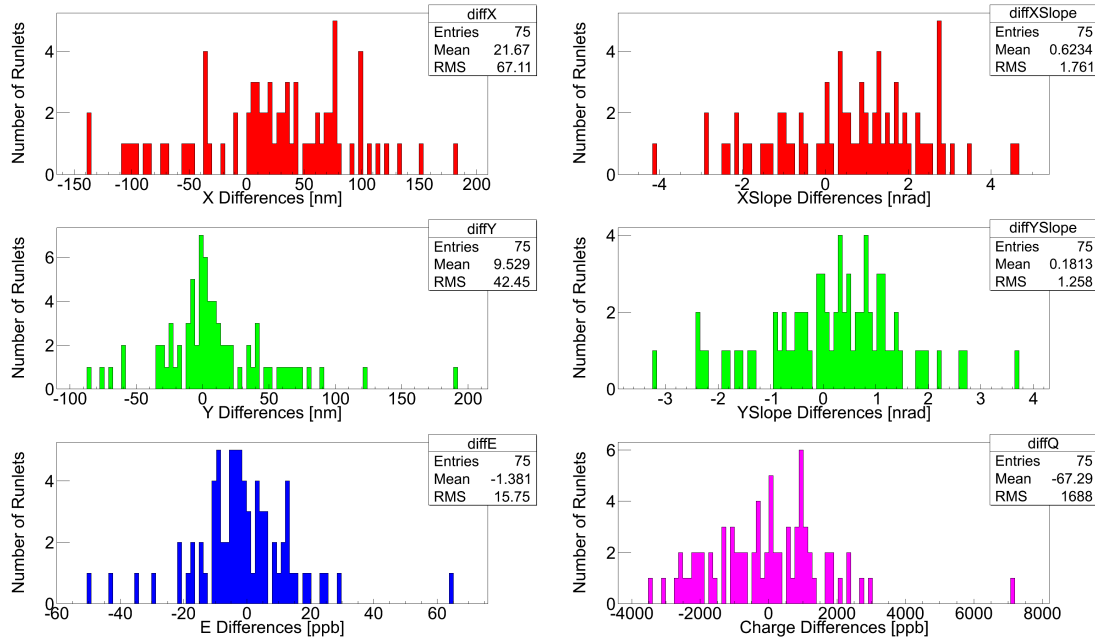


Figure 6.3 Beam parameter differences for the Hydrogen transverse data set.

The regressed (5+1) asymmetries measured using horizontal and vertical transverse polarization beam on  $\text{LH}_2$  target are shown in Figure 6.7. The azimuthal modulating asymmetry flips sign with the insertion of the IHWP as expected. The vertical transverse asymmetry fits may show sign of phase shift between IHWP IN and IHWP OUT settings, but may be explained due to statistical fluctuation. Transverse polarization angle was  $\sim 3\text{-}4^\circ$  off from ideal settings during the measurement, which can not be confirmed with the statistics in hand. The null asymmetry ( $\langle \text{IN} \rangle + \langle \text{OUT} \rangle \rangle / 2$  given by the  $C^{(\text{IN}+\text{OUT})/2}$ ) are compatible with zero within the measurement uncertainties. This indicates the azimuthal modulating component in both IHWP IN and OUT are analogous, and the non-polarization dependent false beam asymmetries were successfully removed by the regression.

The error weighted value of IN-OUT yields the measured regressed asymmetry for each bar. As expected from the azimuthal dependence of the BNSSA, there is a  $90^\circ$  phase offset between the two

Table 6.2 Beam parameter differences for the Hydrogen horizontal and vertical transverse data sets. The X differences are higher compared to Y differences.

Beam parameter differences	IHWP IN	IHWP OUT	$(\langle \text{IN} \rangle + \langle \text{OUT} \rangle)/2$	$(\langle \text{IN} \rangle, -\langle \text{OUT} \rangle)$
Horizontal Transverse				
$\Delta X$ [nm]	$23.8 \pm 2.1$	$20.6 \pm 2.3$	$22.2 \pm 1.6$	$3.6 \pm 1.6$
$\Delta Y$ [nm]	$6.9 \pm 2.1$	$5.6 \pm 2.3$	$6.2 \pm 1.6$	$1.2 \pm 1.6$
$\Delta X'$ [nrad]	$0.7 \pm 0.1$	$0.7 \pm 0.1$	$0.7 \pm 0.1$	$0.1 \pm 0.1$
$\Delta Y'$ [nrad]	$0.2 \pm 0.1$	$-0.3 \pm 0.1$	$-0.0 \pm 0.1$	$0.3 \pm 0.1$
$\Delta E$ [ppb]	$-2.3 \pm 2.1$	$-1.5 \pm 2.3$	$-1.9 \pm 1.6$	$-0.6 \pm 1.6$
$\Delta A_Q$ [ppb]	$8.2 \pm 0.5$	$-237.3 \pm 55.6$	$-114.6 \pm 27.8$	$8.2 \pm 0.5$
Vertical Transverse				
$\Delta X$ [nm]	$15.4 \pm 3.1$	$58.0 \pm 3.7$	$36.7 \pm 2.4$	$-15.2 \pm 2.4$
$\Delta Y$ [nm]	$20.2 \pm 3.1$	$15.4 \pm 3.6$	$17.8 \pm 2.4$	$5.3 \pm 2.4$
$\Delta X'$ [nrad]	$0.6 \pm 0.2$	$1.3 \pm 0.2$	$1.0 \pm 0.1$	$-0.2 \pm 0.1$
$\Delta Y'$ [nrad]	$0.6 \pm 0.2$	$0.9 \pm 0.2$	$0.7 \pm 0.1$	$-0.0 \pm 0.1$
$\Delta E$ [ppb]	$0.5 \pm 3.1$	$-5.4 \pm 3.6$	$-2.4 \pm 2.4$	$2.6 \pm 2.4$
$\Delta A_Q$ [ppb]	$60.1 \pm 0.7$	$158.1 \pm 88.1$	$109.1 \pm 44.1$	$60.1 \pm 0.7$

modulations, as shown in Figure 6.8. The measured regressed asymmetries using horizontal and vertical transverse polarization are extracted as  $A_M^H = 5.34 \pm 0.53$  ppm and  $A_M^V = 4.53 \pm 0.81$  ppm respectively. The combined (error weighted average) regressed asymmetry from horizontal and vertical transverse polarization is given by

$$A_M = 5.095 \pm 0.444 \text{ ppm (stat)}. \quad (6.4.2)$$

This measurement provides a  $\sim 9\%$  statistical measurement of the BNSSA in inelastic e+p scattering (not corrected for backgrounds, polarization or other experimental related systematic uncertainties). Regression has small effect on the extracted measured asymmetries ( $\lesssim 4\%$ ).

#### 6.4.1 Azimuthal Acceptance Correction

The acceptance of a single Q-weak Čerenkov detector is only 49% of an octant (section 3.1), so the reported asymmetry from a detector is an average over  $22^\circ$  azimuthal angle ( $\phi$ ). Each detector bar measures an average asymmetry over a range of  $\phi$  selected by the collimators (details in [63,129]). The effect of averaging cosines for a variable of the form  $y(\phi) = A \cos(\phi + \delta)$  over the azimuthal angle yields

$$AVG[y(\phi)] = \frac{A \int_{\phi_0 - \Delta\phi}^{\phi_0 + \Delta\phi} \cos(\phi + \delta) d\phi}{(\phi_0 + \Delta\phi) - (\phi_0 - \Delta\phi)} = A \cos(\phi_0 + \delta) \times \frac{\sin \Delta\phi}{\Delta\phi}, \quad (6.4.3)$$

HYDROGEN-CELL (v\_transverse, 6700 A): Regression-on\_5+1 MD PMTavg Corrections. FIT =  $C_T + p^T \sin/c$

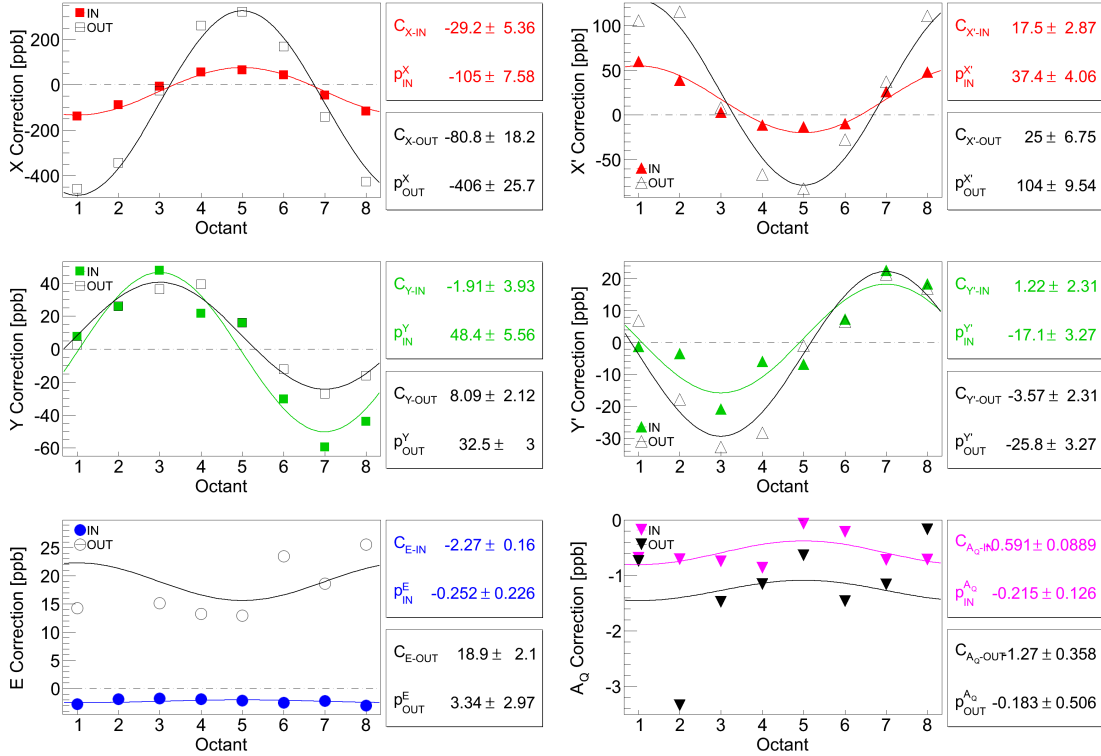


Figure 6.4 Main detector corrections (using sensitivities from “5+1” regression scheme) vs octant for vertical LH<sub>2</sub> transverse data set are shown here. Beam positions and angles have sinusoidal dependence with octant inherited from the sensitivities. No such dependence is seen for energy and charge. Both IHWP states are shown separately for each beam parameter.

HYDROGEN-CELL (v\_transverse, 6700 A): Regression-on\_5+1 MD PMTavg Corrections. FIT =  $C_T + p^T \sin/c$

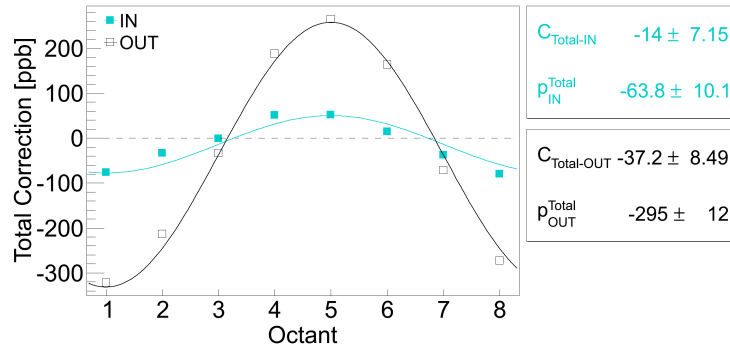


Figure 6.5 Total corrections in “5+1” regression scheme vs octant for vertical LH<sub>2</sub> transverse data set are shown here. The total correction is the sum of all the corrections (with sign) shown in Figure 6.4.

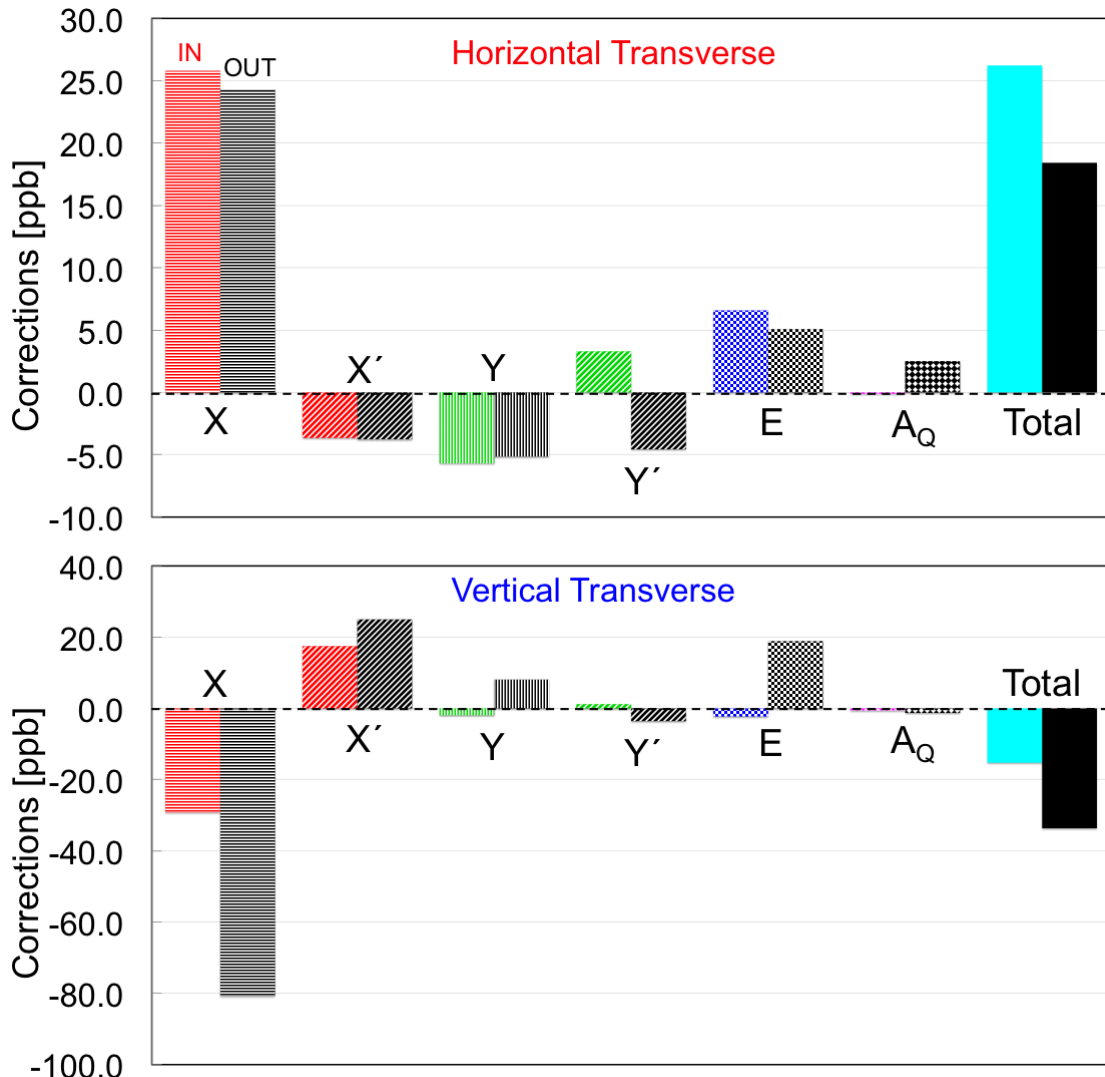


Figure 6.6 Main detector corrections (using sensitivities from “5+1” regression scheme) for horizontal (top) and vertical (bottom) LH<sub>2</sub> transverse data sets are shown here. Both IHWP states are shown separately for each beam parameter. The total correction is the sum of all the corrections (with sign).

where  $\phi_0$  is the nominal azimuthal location of the detector with  $\Delta\phi$  coverage. So the measured asymmetry from each detector needs to be scaled by a factor of  $\frac{\sin \Delta\phi}{\Delta\phi}$  to correct for the acceptance.  $\Delta\phi = 11.025^\circ$  yields the scale factor to be  $\frac{\sin \Delta\phi}{\Delta\phi} = 0.9938$ . The detector acceptance corrected measured asymmetry can be extracted as

$$A_M^{\text{in}} = \frac{A_M}{0.9938} = 5.127 \text{ ppm.} \quad (6.4.4)$$

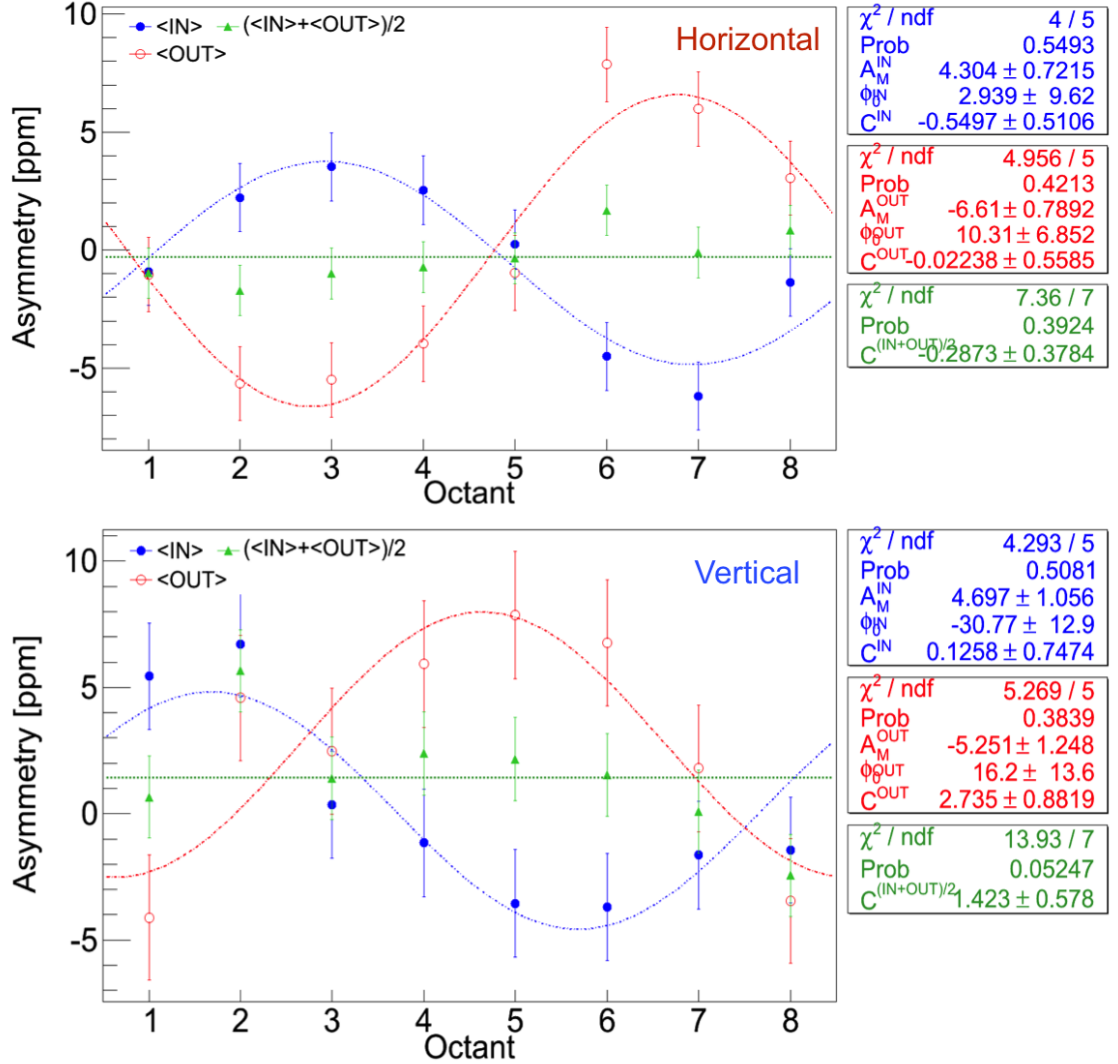


Figure 6.7 Main detector asymmetry for horizontal (top), vertical (bottom) transverse data set. For comparison, asymmetries for IN and OUT data are also shown separately. The regressed asymmetries change sign with the insertion of the IHWP with comparable amplitudes. The  $(\langle \text{IN} \rangle + \langle \text{OUT} \rangle) / 2$  asymmetries of the eight Čerenkov detectors, given by  $C^{(\text{IN+OUT})/2}$  is compatible with zero except in the vertical data set. The extraction of BNSSA depends on the amplitudes in the fits and by comparison of IN and OUT, not the constant term.

A conservative 50% uncertainty was used for  $\Delta\phi$ , which yields a systematic uncertainty of 0.004 in the correction.

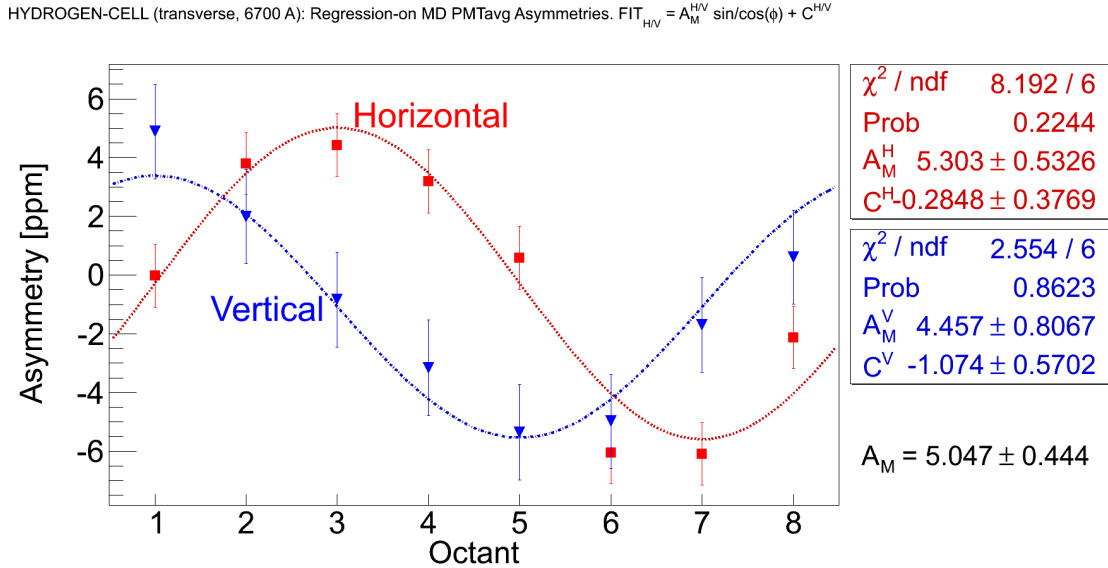


Figure 6.8 Regressed main detector asymmetry for horizontal, vertical transverse polarization are shown with red circle and blue square respectively. Data points for horizontal transverse are  $\sim 4$  hour long measurement, whereas vertical transverse data points are  $\sim 2$  hour long. The fit functions used are  $A_M^H \sin(\phi + \phi_0^H) + C^H$  for horizontal transverse and  $A_M^V \cos(\phi + \phi_0^V) + C^V$  for vertical transverse respectively. Asymmetries in each case shows  $\sim 90^\circ$  phase offset, as expected between horizontal and vertical configurations.

## 6.5 Corrections and Systematic Uncertainties

The dominant uncertainty in the measured asymmetry for this measurement is statistical (9%). A preliminary treatment of the systematic uncertainty performed on the data set is presented in this section.

### 6.5.1 Regression Scheme Dependence

Since the “5+1” linear regression scheme used for this analysis is only one of the many different schemes available, it was worth investigating the scheme dependence. A list of all the independent variables for different regression sets are shown in APPENDIX-???. Ideally, the regression corrections from all the schemes should agree if all equipment is functioning properly and the regression is being done properly. Small differences in the corrections can arise from differences in the noise, resolution, and non-linear response of the monitors. To compare for the systematic studies, a common set of event cuts [75] are applied to all regression schemes to match the quartets used by each scheme. The results are summarized in Table 6.3. The regression scheme dependence uncertainty is defined

Table 6.3 Asymmetries from different regression schemes, along with the raw asymmetry, are shown for horizontal and vertical transverse data sets from Run 2 Pass 5 database. Corrections are small ( $\lesssim 4\%$ ) compared to the amplitude of the measured asymmetry. The schemes without and with charge as regression variable are shown separately. Set 5 and 6 were not available due to failure of BPM 9b during Run 2. Set 9 was ignored for this analysis as it used the upstream luminosity monitor as an independent variable (more details about regression variables are in APPENDIX-??).

Regression scheme	Horizontal		Vertical	
	Asymmetry [ppm]	Correction [ppm]	Asymmetry [ppm]	Correction [ppm]
UnReg	5.339	0.000	4.602	0.000
std	5.343	0.004	4.524	-0.078
set7	5.347	0.007	4.529	-0.073
set11	5.343	0.004	4.524	-0.078
5+1	5.343	0.004	4.525	-0.077
set3	5.343	0.004	4.525	-0.077
set4	5.343	0.004	4.527	-0.076
set8	5.346	0.007	4.531	-0.072
set9	5.343	0.003	4.534	-0.069
set10	5.343	0.003	4.526	-0.077
Max - Min	set8 - set10	0.004	set8 - set11	0.006

as the largest difference between all of the schemes and estimated to be 0.004 ppm for horizontal transverse and 0.006 ppm for vertical transverse data set.

### 6.5.2 Regression Time Dependence

The standard regression algorithm works with 5 minute runlet averaged quantities. The detector sensitivities are averaged over each runlet and corresponding differences are used to correct for the false asymmetry for each quartet in the runlet. There is another systematic uncertainty associated with regression time period that is considered. The effect of using slug, few hours ( $\sim 2$ ), as time period for the regression instead of runlets was determined. The MD error weighted average sensitivities for a slug were calculated and average beam parameter differences for that slug were used to get the corrections, as shown in Equation 6.5.2. These slug averaged corrections were then used to regress asymmetries (Equation 6.5.1).

$$\langle A_{\text{reg}} \rangle_{\text{slug}} = \langle A_{\text{UnReg}} \rangle_{\text{slug}} - \langle C \rangle_{\text{slug}} \quad (6.5.1)$$

$$\langle C \rangle_{\text{slug}} = \sum_{i=1}^6 \left\langle \frac{\partial A}{\partial T_i} \right\rangle_{\text{slug}} \langle \Delta T_i \rangle_{\text{slug}} \quad (6.5.2)$$

where  $T_i$ 's are  $X$ ,  $X'$ ,  $Y$ ,  $Y'$ ,  $A_E$ , and  $A_Q$ . The slug averaged sensitivities and beam parameter differences for the data set are shown in Figure 6.2 (also Figure ?? for horizontal transverse) and Table 6.2 respectively. The impact on regressed asymmetries due to change in the regression averaging time period for horizontal and vertical transverse data set are 0.006 ppm and 0.008 ppm respectively and are assigned as regression time dependence systematic uncertainties. More details in APPENDIX-D section D.6.1.

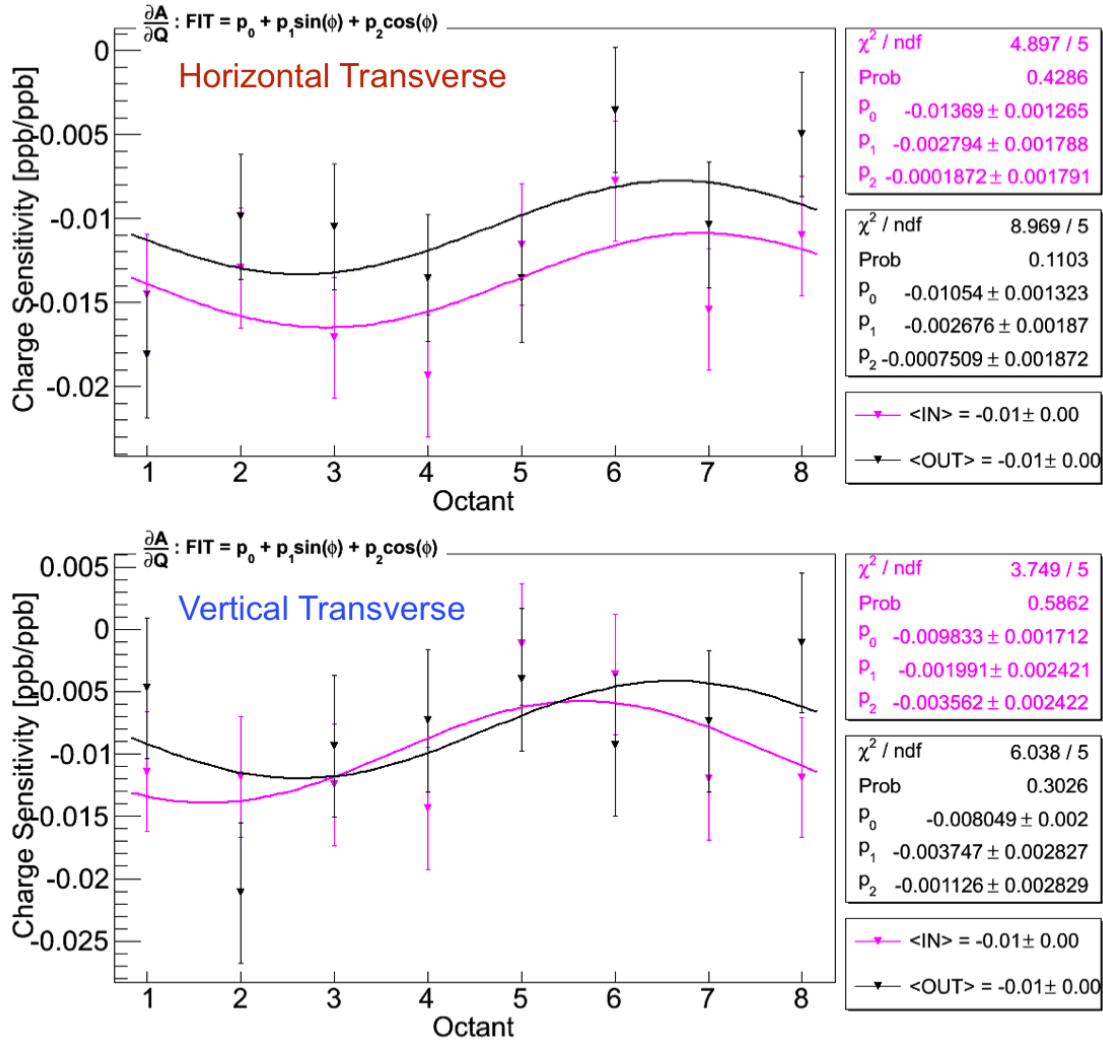


Figure 6.9 Charge sensitivity for horizontal (top) and vertical (bottom) transverse polarization data set. Average charge sensitivities of the measured detector asymmetries extracted from the six parameter (five parameter + charge) regression at beam current 180  $\mu\text{A}$ . Purple (Black) represents the charge sensitivity of the IHWP IN (OUT) data which are consistent with each other. The sensitivities of the eight Čerenkov detectors vary from -0.5% to - 2.0% and are stable within the running period. Average non linearity is -1% for both the cases.

### 6.5.3 Nonlinearity

The Čerenkov detector signals are normalized to the charge and the charge asymmetry is actively suppressed using a charge feedback system. The nonlinearity of the BCM electronics, the main detector electronics, and target density changes can induce nonlinear distortions in the charge asymmetry and hence in the measured asymmetry [130]. This nonlinearity of the system is seen to be non-zero from the non-zero charge sensitivity constant term in the (5+1) regressed detector asymmetries, as shown in Figure 6.9. For both horizontal and vertical polarization data sets, the nonlinearity is found to be -1%. At present, no proper method of handling the measured asymmetry distortion due to nonlinearity is available. The nonlinearity term is multiplied with the measured asymmetry to calculate the false asymmetry [131]. The systematic uncertainties due to nonlinearity for horizontal and vertical transverse measurements are given by 0.053 ppm and 0.045 ppm respectively.

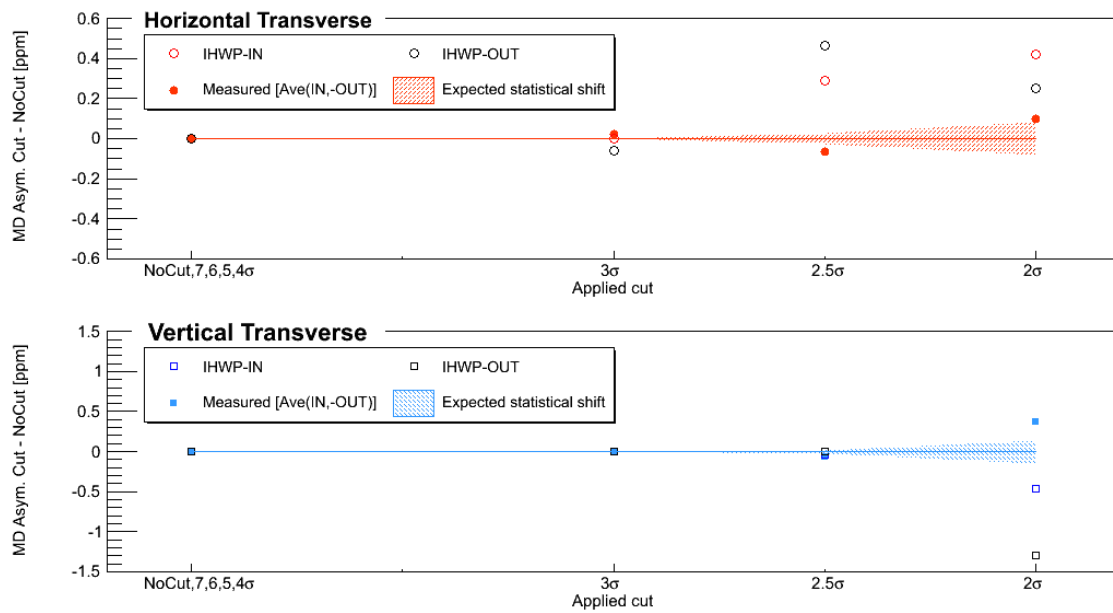


Figure 6.10 Cut dependence study. Shift in the central value of the regressed asymmetry for different cut widths for  $\text{LH}_2$ . The expected statistical shift is shown by the shaded region using the total number of quartets lost when a cut is applied to all parameters.

### 6.5.4 Cut Dependence

The goal of the cut dependence analysis was to assign a systematic uncertainty that comes from shifts in the mean value of the regressed asymmetry beyond statistical fluctuations after applied cuts. If linear regression is working properly, large false asymmetries in runlets with large HCBAs should be removed from the measured asymmetry after linear regression is applied and there should

not be any shift in the mean value of the regressed asymmetry beyond statistical shifts (as shown in Figure 6.10). The point-to-point uncertainty in going from cut  $i$  to cut  $j$  is estimated to be

$$\Delta_{i \rightarrow j}^{\text{pt-to-pt}} = \left( \frac{\sigma_j}{\sqrt{N_j}} - \frac{\sigma_i}{\sqrt{N_i}} \right) \quad (6.5.3)$$

Here the  $\sigma$  is the root mean square (RMS) of each HCBA. Inclusive cuts of 7, 6, 5, 4, 3, 2.5 and  $2\sigma$  are applied to all HCBAs and difference between regressed asymmetry with cut and without cuts are shown in Figure 6.10. The observed shift in the measured asymmetry from these cuts are larger than the expected statistical shift and 2.5  $\sigma$  cuts on the HCBAs were used to assign a systematic uncertainty. The total percentage of quartets lost for cuts with respect to no cut are used to estimate the expected statistical shift, shown as the shaded region in Figure 6.10. Beyond a cut of 2.5  $\sigma$ , most of the data were removed to extract a meaningful asymmetry. This analysis was performed to assign systematic uncertainty only, no data was removed from main data set. Cut dependence for horizontal and vertical transverse data set are found to be  $\sim 0.064$  ppm and  $\sim 0.068$  ppm respectively.

### 6.5.5 Fit Scheme Dependence

A sinusoidal fit to main detector octant asymmetries is used to extract measured transverse asymmetry. So it was important to find the impact of the function on fitted asymmetry. The measured asymmetry was fitted using four different functions, and the solutions are summarized in Table 6.4. The difference in measured asymmetry obtained using standard function  $A_M \sin(\phi + \phi_0) + C$  and rest gives an idea about the fit function dependence of the measured asymmetry. More insightfully, the constant term in the fit function can be thought of as the apparent parity violating asymmetry contamination to the parity conserving transverse asymmetry. The size of  $P_T B_n$  is much larger than  $P_L A_{PV}$  so the latter has significant effect on the transverse measurement. So this PV asymmetry is buried under the fit scheme dependence and give rise to the systematic uncertainties of 0.040 ppm for horizontal and 0.083 ppm for vertical transverse data sets.

### 6.5.6 Summary of Systematic Uncertainties

Summary of systematic uncertainties of the measured inelastic beam normal single spin asymmetry is given in Table 6.5. The systematic studies contain uncertainties related to the extraction of the measured asymmetry such as regression, nonlinearity, cut dependence, and detector acceptance correction. The systematic studies for horizontal and vertical transverse polarization data set were performed separately; these are summarized in Figure 6.11. The statistical uncertainty weighted

Table 6.4 Fit scheme dependence of the measured asymmetry. The fit function was varied to observe the effect on measured regressed asymmetry. The difference in asymmetry between case 1 and rest are shown. Biggest offset comes from the possible phase shift.

	Fit Function	Asymmetry [ppm]	Difference (1-i) [ppm]
Horizontal Transverse			
1	$A_M^H \sin(\phi + \phi_0^H) + C^H$	$5.343 \pm 0.532$	0.000
2	$A_M^H \sin(\phi + \phi_0^H)$	$5.344 \pm 0.532$	0.001
3	$A_M^H \sin(\phi) + C^H$	$5.303 \pm 0.533$	0.040
4	$A_M^H \sin(\phi)$	$5.304 \pm 0.533$	0.039
Vertical Transverse			
1	$A_M^V \cos(\phi + \phi_0^V) + C^V$	$4.525 \pm 0.806$	0.000
2	$A_M^V \cos(\phi + \phi_0^V)$	$4.510 \pm 0.806$	0.015
3	$A_M^V \cos(\phi) + C^V$	$4.458 \pm 0.807$	0.067
4	$A_M^V \cos(\phi)$	$4.442 \pm 0.807$	0.083

average of the systematic uncertainties from horizontal and vertical transverse data sets is used for the total systematic uncertainty. The total uncertainty is the quadrature sum of the statistical and systematic uncertainties. The total uncertainty is dominated by 9% statistical uncertainty compared to 1% systematic uncertainty.

Table 6.5 Summary of uncertainties on measured asymmetry for combined horizontal and vertical data sets. The relative uncertainties are also shown in the table.

Uncertainty from	Contribution to $A_M$ [ppm]	Relative Contribution [%]
Statistics	0.444	8.7
Regression scheme	0.005	0.1
Regression time binning	0.007	0.1
Non-linearity	0.051	1.0
Cuts	0.065	1.3
Fit scheme	0.052	1.0
Detector acceptance correction	0.016	0.3
Systematic only	0.100	2.0
Total	0.455	8.9

## 6.6 Extraction of Physics Asymmetry

The beam normal single spin asymmetry from inelastic e+p scattering is obtained from measured asymmetry using Equation 6.6.1 by accounting for EM radiative corrections, kinematics normalization, polarization, and backgrounds.

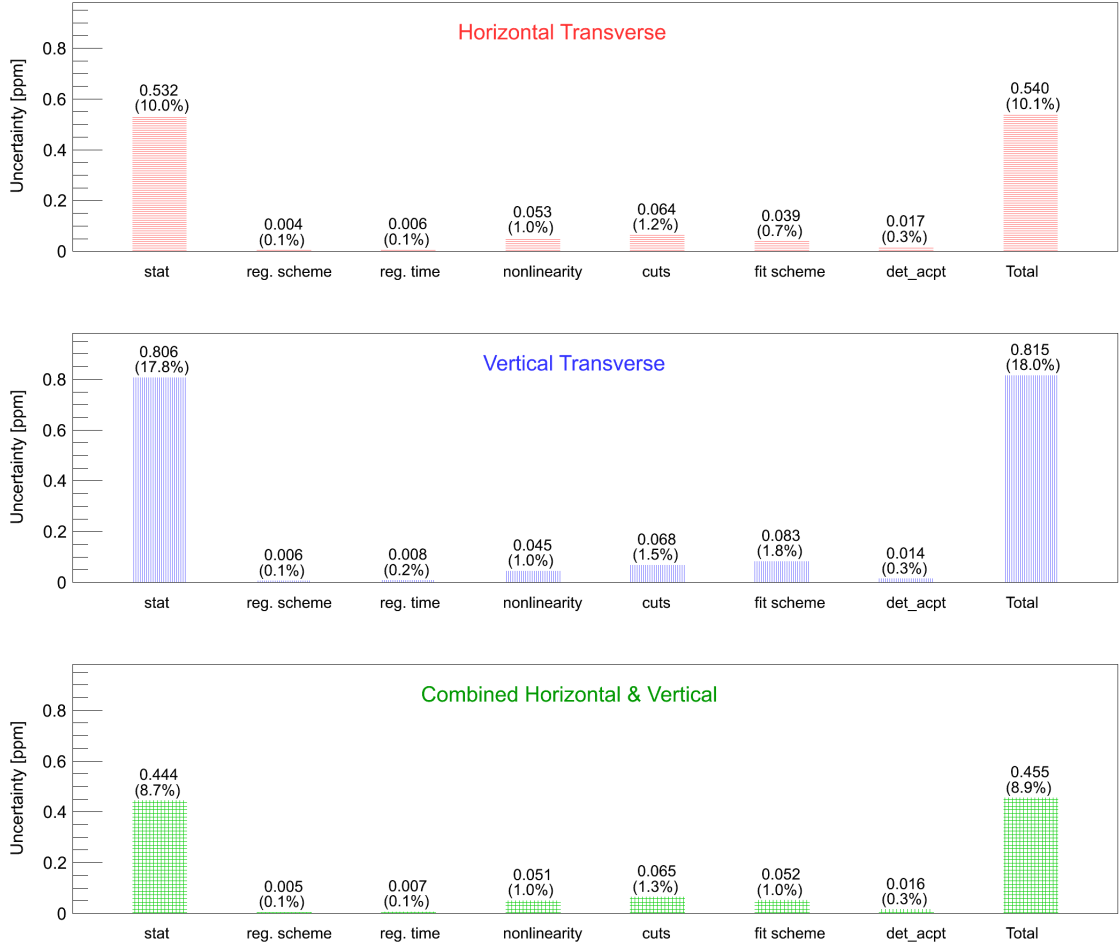


Figure 6.11 Summary of uncertainties on measured asymmetry for horizontal and vertical data set. The relative total uncertainty is dominated by statistical uncertainty compared to systematic uncertainties.

$$B_n = R_{total} \left[ \frac{\left( \frac{A_M^{in}}{P} \right) - \sum_{i=1}^4 A_{bi} f_{bi}}{1 - \sum_{i=1}^4 f_{bi}} \right] \quad (6.6.1)$$

Here  $R_{total}$  is a correction factor for the experimental bias and radiative effects,  $P$  is the beam polarization, and  $A_{bi}$  is  $i^{th}$  background asymmetry with fraction of backgrounds in the total detector acceptance (dilution)  $f_{bi}$ . The corrections to the physics asymmetry and the associated uncertainties are discussed in the following sections.

### 6.6.1 Beam Polarization

The Hall-C Møller polarimeter and the Compton polarimeter were used to measure the beam polarization for the experiment. The photocathode Quantum Efficiency was stable and hence the beam polarization was stable for the period [132]. The Møller polarimeter is only sensitive to longitudinally polarized beam, so measurements performed with the longitudinally polarized beam right after the transverse data taking was used to determine the beam polarization. The Møller runs used for this analysis are 1593 - 1599, carried out on 20th February 2012. Each run is  $\sim 10$  min long. Slug averaged polarizations from this Møller measurement are shown in Table 6.6. The measured beam polarization is  $P = 87.50 \pm 0.28$  (stat)  $\pm 0.74$  (sys)% [133]. Details of systematic studies for the Møller polarization measurement can be found in the Q-weak internal technical document [134].

Table 6.6 Beam polarization using Møller polarimeter for Run 2 transverse data set [134].

IHWP	Polarization [%]	Statistical Uncertainty [%]
Out	87.029	0.398
In	- 87.939	0.387
Total	87.497	0.277

### 6.6.2 Background Corrections

The largest background source in beam normal single spin asymmetry arises from the elastic radiative tail. Small background contributions also come from electrons scattering from aluminum target windows, beamline scattering, and other soft neutral scattering. The analysis of the background asymmetries and their contributions to the BNSSA is described in the following sections.

#### 6.6.2.1 Target Aluminum Windows

One of the important background contributions to the measured asymmetry comes from electrons scattering from the aluminum alloy target windows. Data were taken on the 4% downstream aluminum alloy target to determine the asymmetry and dilution. The measured regressed asymmetry for horizontal and vertical transverse are  $A_M^{H-DSA_l} = 7.892 \pm 1.186$  ppm and  $A_M^{V-DSA_l} = 9.631 \pm 1.768$  ppm [135], as shown in Figure 6.12. Combined (error weighted) regressed aluminum alloy asymmetry is  $A_M^{DSA_l} = 8.432 \pm 0.985$  ppm. This asymmetry is then scaled by a 0.9938 for azimuthal acceptance averaging (already discussed in section 6.4.1), which yields the asymmetry as  $8.484 \pm 0.985$  ppm. The acceptance difference between the upstream and downstream target

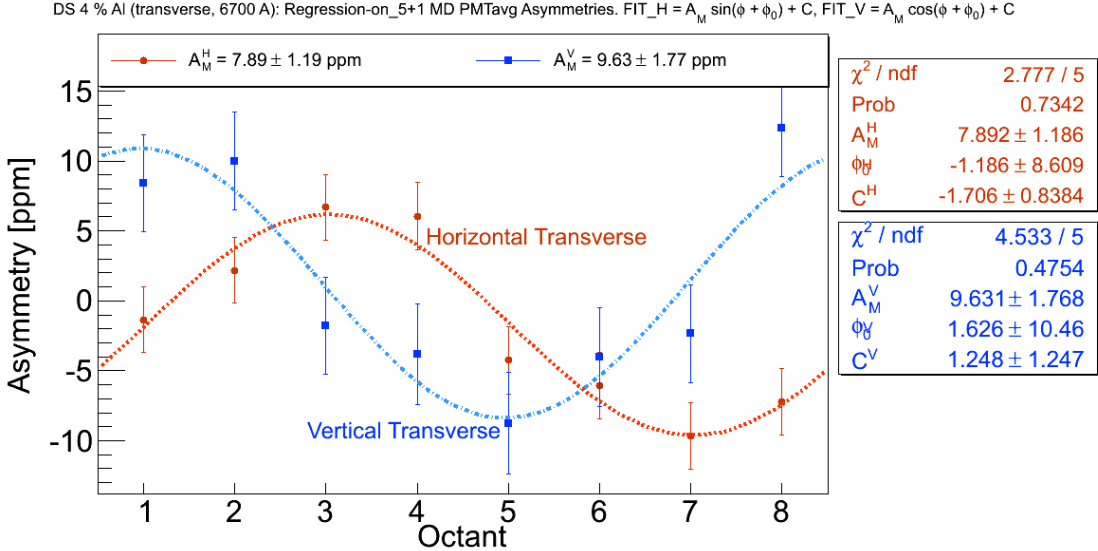


Figure 6.12 Azimuthal dependence of asymmetry from the 4% downstream aluminum target. The uncertainties are statistical only. The octant dependence in either polarization orientation are similar to what was observed for the LH<sub>2</sub>-cell. The asymmetry is larger than the LH<sub>2</sub>-cell asymmetry. The fit functions used for horizontal and vertical transverse data points are  $A_M^H \sin(\phi + \phi_0^H) + C^H$  and  $A_M^V \cos(\phi + \phi_0^V) + C^V$  respectively.

windows need to correct before the background correction. This acceptance difference causes a 20% relative difference between the mean  $Q^2$  of the electrons coming from the upstream window compared to the downstream window, as shown in GEANT4 simulations [54] ( $Q_{USA}^2 = 0.8 \times Q_{DSA}^2$ ). The beam normal single spin asymmetry from nuclei at forward angle scattering asymmetry is proportional to  $\sqrt{Q^2}$  as described in theoretical models [136, 137]. So, asymmetry for upstream aluminum target can be calculated as  $A_M^{USA} = \sqrt{0.8} A_M^{DSA} = 7.589$  ppm. Downstream and upstream aluminum target windows are expected to contribute equally [54] to the aluminum dilution in the main detector asymmetries resulting in an effective aluminum asymmetry of  $A_M^{Al} = (A_M^{DSA} + A_M^{USA})/2 = 8.036$  ppm. An additional systematic uncertainty of  $0.08 \times A_M^{Al}$  is assigned for the system non-linearity (more details in APPENDIX D). The polarization corrected asymmetry for background windows correction is  $A_{b1} = A_M^{Al}/P = 9.185 \pm 1.409$  ppm.

The measured aluminum windows dilution is  $f_{b1} = 0.033 \pm 0.002$  [138]. Dedicated measurements were performed with different pressures of hydrogen gas in the target cell. Using the known pressure of hydrogen gas at different points, the pressure was extrapolated to zero.

The correction to the physics asymmetry from aluminum alloy windows is  $c_{b1} = \kappa P A_{b1} f_{b1} = 1.427$  ppm, where  $\kappa = (R_{total}/P)/(1 - f_{total})$ .

Table 6.7 Measured asymmetry on aluminum target.

Target	Asymmetry [ppm]
DSA1	8.432
USA1	7.589
$\langle \text{DS+US} \rangle$	8.036

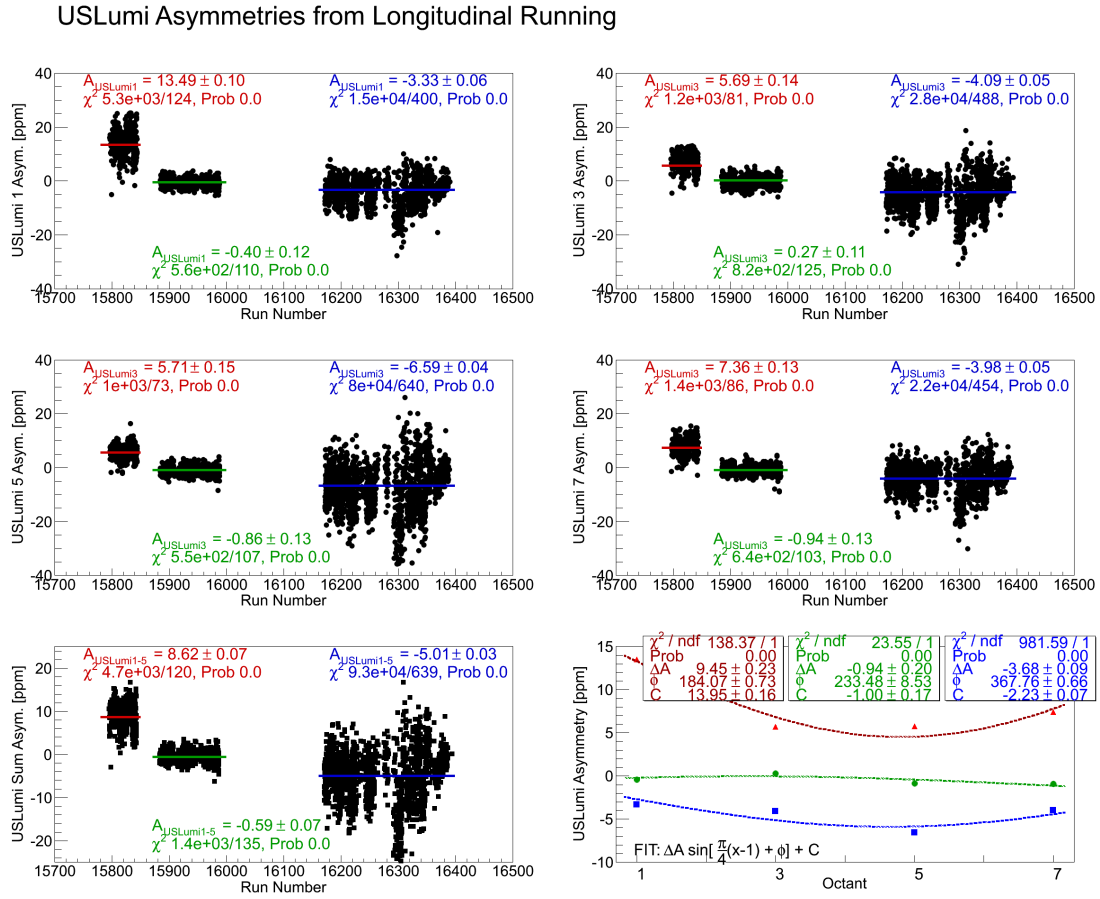


Figure 6.13 Regressed (5+1) USLumi asymmetries longitudinal running for octant 1, 3, 5, and 7 are shown in panel 1-4. USLumi sum asymmetry is shown in panel 5. Each point is a runlet. The average asymmetries vs octant for each time period are shown in panel 6.

### 6.6.2.2 Beamlime Scattering

Another correction accounts for scattering sources in the beam line ( $b2$ ). The asymmetry ( $A_{b2}$ ) was measured, along with its dilution ( $f_{b2}$ ), by blocking two of the eight openings in the first of the three Pb collimators with tungsten. The measured asymmetry in the blocked octants detectors was correlated with different background detectors located outside the acceptance of the main detectors

for scaling during the primary measurement, assuming a constant dilution [139]. The variation of upstream luminosity monitor asymmetry with octant during longitudinal running can provide a good indication of the beamline scattering asymmetry. The maximum variation before and after the transverse data collection period (during longitudinal running)  $\Delta A_{\text{USLumi}} = 3.534 \pm 0.16$  ppm (Figure 6.13) was used to estimate the beamline scattering asymmetry. A very simple postulate was considered: that measured main detector asymmetry has a background with a fixed fraction and an asymmetry that scales linearly with that measured in the background monitors and USLumis. The scale factor was measured directly, correlating the MD asymmetry to background asymmetries, and was estimated to be  $0.0085 \pm 0.0016$  [140] from longitudinal period. The signal drops by an order of magnitude lower for inelastic scattering compared to elastic, whereas beamline background remains similar. Hence an additional factor of 10 was multiplied to incorporate the signal drop. The beamline background does not depend on polarization and is not corrected for it. Then, asymmetry for beam line scattering is given by  $A_{b2} = \Delta A_{\text{USLumi}} \times 0.085 = 0.300 \pm 0.058$  ppm.

The beamline scattering dilution factor for inelastic running is an order of magnitude larger than in the elastic kinematic setting. The total rate at the inelastic peak drops to 10% of the total rate at the elastic peak, whereas the number of events originating in the beamline remains similar. The measured dilution for inelastic beamline scattering is  $0.018 \pm 0.001$  [10, 141]. A 50% uncertainty on the dilution was assigned to allow the sinusoidal modulation specific to the BNSSA. The beamline scattering dilution used for the background correction is  $f_{b2} = 0.018 \pm 0.009$ . The correction to the physics asymmetry due to beam line scattering is  $c_{b2} = \kappa P A_{b2} f_{b2} = 0.025$  ppm.

### 6.6.2.3 Other Neutral Background

An additional correction was applied to include soft neutral backgrounds (*b3*) arising from secondary interactions of scattered electrons in the scattered electron transport line, and was not accounted in the blocked octant studies [142]. This can arise from Møller scattering, e+p elastic scattering, etc. Simulations are in progress [143]. The other neutral background asymmetry could be as large as 5 ppm (size of the transverse asymmetry). To make the sign of the asymmetry uncertain, the asymmetry for other neutral background was assumed to be  $A_{b3} = 0.000 \pm 10.000$  ppm. Here, uncertainty of 100% of the measured transverse asymmetry was assigned to give an upper bound on the neutral background asymmetry.

The neutral background dilution for the inelastic scattering has been measured as  $f_{\text{neutral}} = 0.0520 \pm 0.0040$  (stat)  $\pm 0.0014$  (sys) [144]. The dilution for the other neutral background was obtained by subtracting the blocked octant background from the total neutral background measured

by the main detector and is given by  $f_{b3} = f_{\text{neutral}} - f_{b2} = 0.034 \pm 0.010$ . The correction to the physics asymmetry due to other neutral background is  $c_{b3} = \kappa P A_{b3} f_{b3} = 0.000$  ppm.

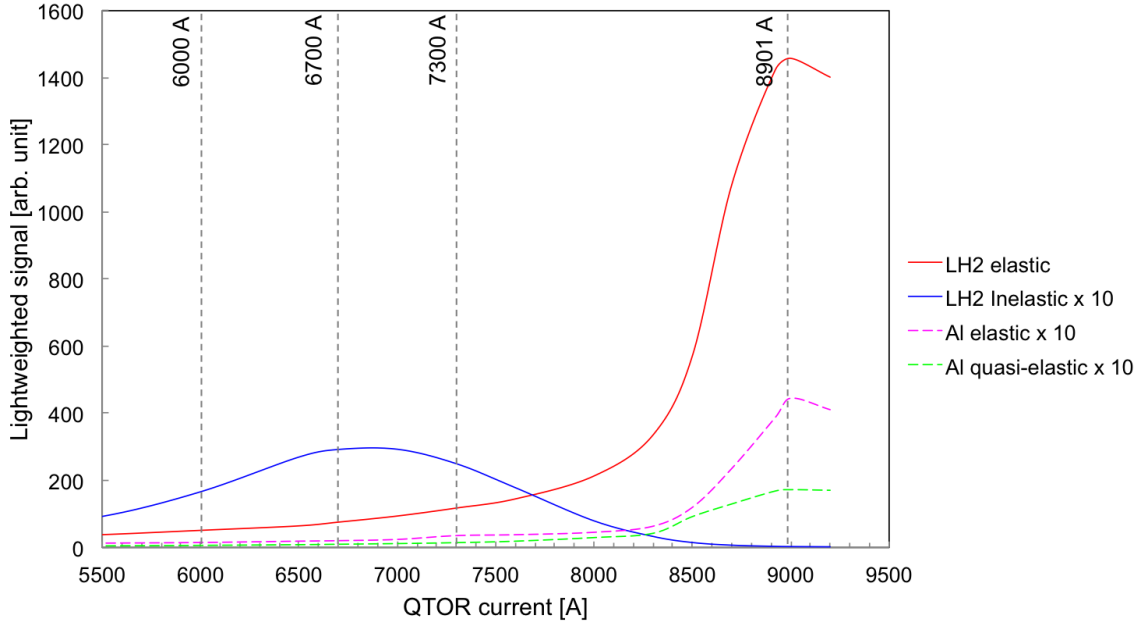


Figure 6.14 Simulation of contributions from elastic and inelastic  $e+p$ , and elastic  $e+Al$  scattering from upstream (US) and downstream (DS) target windows [145]. All but elastic  $e+p$  events have been multiplied by 10 for better visualization.

#### 6.6.2.4 Elastic Radiative Tail

The largest background correction comes from the elastic radiative tail ( $b4$ ). The polarization corrected measured elastic transverse asymmetry was  $A_T^{el} = -5.345 \pm 0.067$  (stat)  $\pm 0.076$  (sys) ppm [146]. The elastic physics asymmetry from the LH<sub>2</sub>-cell is similar in magnitude to the inelastic asymmetry but has the opposite sign. The elastic asymmetry was measured at  $Q_{el}^2 = 0.0250 \pm 0.0006$  (GeV/c)<sup>2</sup> [147] where as inelastic measurement was at  $Q_{in}^2 = 0.0209 \pm 0.0005$  (GeV/c)<sup>2</sup> (shown in Figure 6.17), hence it is necessary to scale it to the inelastic peak. The transverse asymmetry is proportional to  $\sqrt{Q^2}$  [136, 137]. The polarization and  $\sqrt{Q^2}$  corrected elastic asymmetry is given by  $A_{b4} = \sqrt{\frac{Q_{in}^2}{Q_{el}^2}} A_T^{el} = -4.885 \pm 0.093$  ppm.

As  $\sim 70\%$  of the total signal in the inelastic peak was from elastic radiative tail (Figure 6.14), it was important to tackle it carefully. A GEANT simulation was used to extract elastic dilution. Dedicated measurements were taken at both sides of the inelastic peak (at QTor current 6000 A and 7300 A) to check the simulation. A  $\sim 10\%$  discrepancy was observed between current mode data and GEANT simulated signal at the inelastic peak, as shown in Figure 6.15. In order to

incorporate this discrepancy, a 10% systematic uncertainty was assigned to the elastic dilution for this preliminary analysis. A more detailed simulation is ongoing to explore this difference. The signal size for inelastic transverse is  $\sim$ 2-3 times smaller than that of the elastic signal. Although the signal reduces for inelastic, the nonlinearity in the detector remains the same and might be responsible for this discrepancy. The simulated elastic dilution factor is given by  $f_{b4} = 0.701 \pm 0.070$  [145, 148]. The correction to the physics asymmetry due to the elastic radiative tail is  $c_{b4} = \kappa P A_{b4} f_{b4} = -16.129$  ppm.

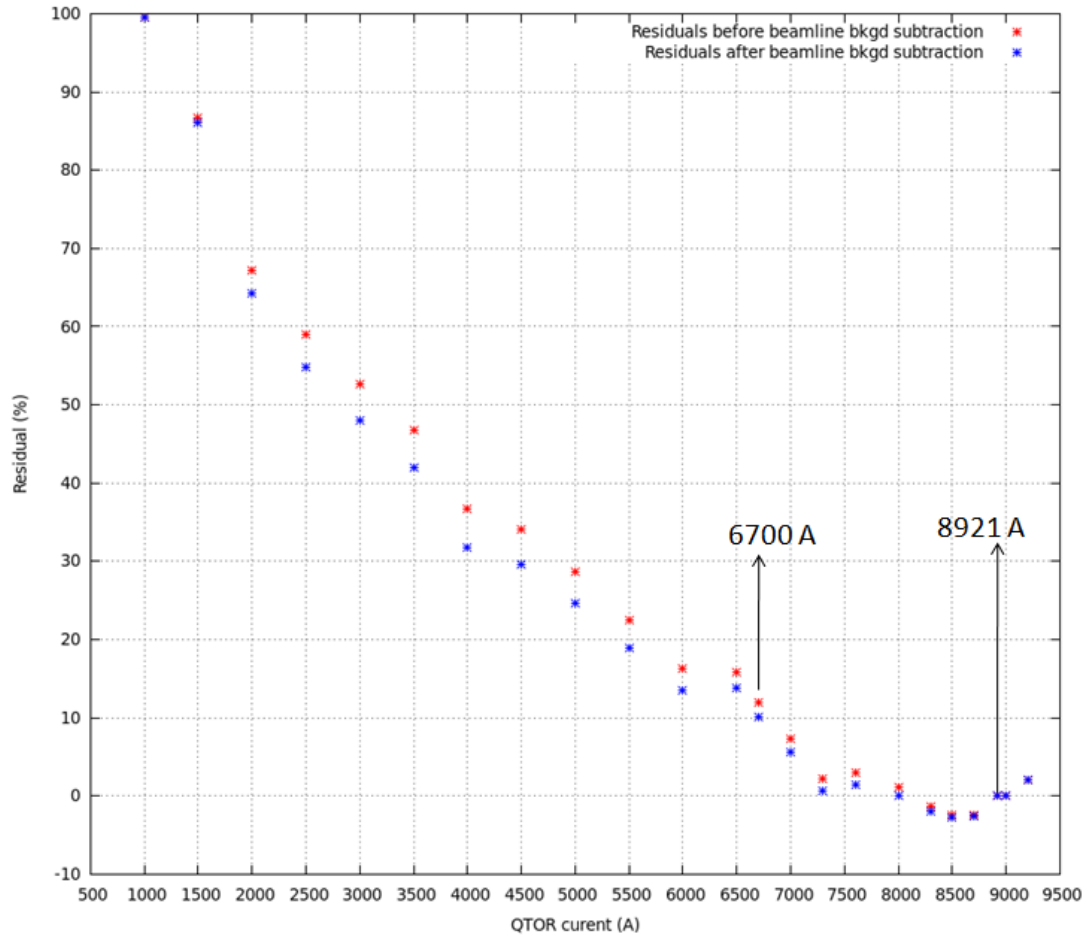


Figure 6.15 The residual of yield using Data and simulation from GEANT 3 [145] are shown in the figure. A  $\sim$ 10% discrepancy was observed at inelastic peak (6700 A) between data and simulation for matching them at elastic peak (8921 A). Beamlime background correction to the yield did not improve the discrepancy.

(HYDROGEN-CELL,6700A) Transverse N-to- Δ Physics Asymmetry vs Elatic Dilution

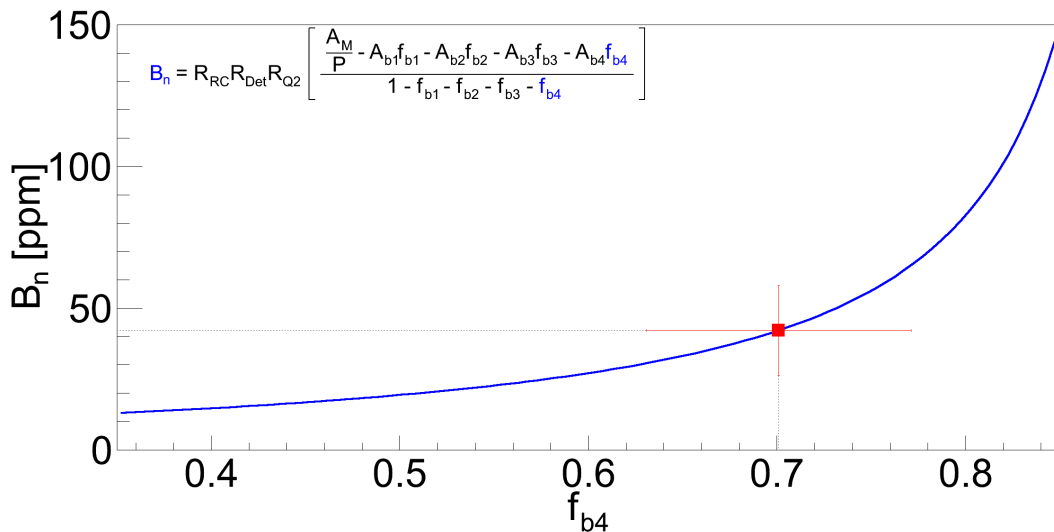


Figure 6.16 The variation of beam normal single spin asymmetry with elastic dilution.

### 6.6.3 Other Corrections

Another set of corrections is used to remove all the experimental bias from the measured asymmetry before extracting BNSSA. The measured asymmetry is corrected for the electromagnetic (EM) radiative corrections, light weighting on the Čerenkov detector, and  $Q^2$  precision. These corrections are considered as independent factors and are applied to the measured asymmetry.

#### 6.6.3.1 Radiative Correction

The energy loss and depolarization of the electrons is a result of electromagnetic (EM) radiation [149]. The measured asymmetry needs to be corrected for these EM radiative effects to obtain the beam normal single spin asymmetry at the effective  $Q^2$  and beam polarization. The deduced radiative correction for elastic e+p scattering from simulations with and without bremsstrahlung, using methods described in Refs. [150, 151], was found to be  $R_{RC} = 1.010 \pm 0.010$  [63]. The same radiative correction was used for this data set as there were no existing simulations available for inelastic e+p scattering. This correction does not have a significant impact in the final asymmetry, hence it was not unreasonable to use the existing elastic simulation result.

### 6.6.3.2 Detector Bias Correction

The correction between light yield and  $Q^2$  across the detector bars affects the measured asymmetry and needs to be accounted for in the final BNSSA extraction. The multiplicative correction factor to be applied to the data is

$$R_{Det} = \frac{A_{\text{no-bias}}^{\text{sim}}}{A_{\text{bias}}^{\text{sim}}} = \sqrt{\frac{(Q^2)_{\text{no-bias}}^{\text{sim}}}{(Q^2)_{\text{bias}}^{\text{sim}}}}. \quad (6.6.2)$$

Here,  $A_{\text{bias}}^{\text{sim}}$  and  $A_{\text{no-bias}}^{\text{sim}}$  are the simulated asymmetries with and without light-collection bias respectively. The detector bias correction used for this analysis is  $R_{Det} = 0.998 \pm 0.002$  and is obtained using transverse simulation results [63, 152].

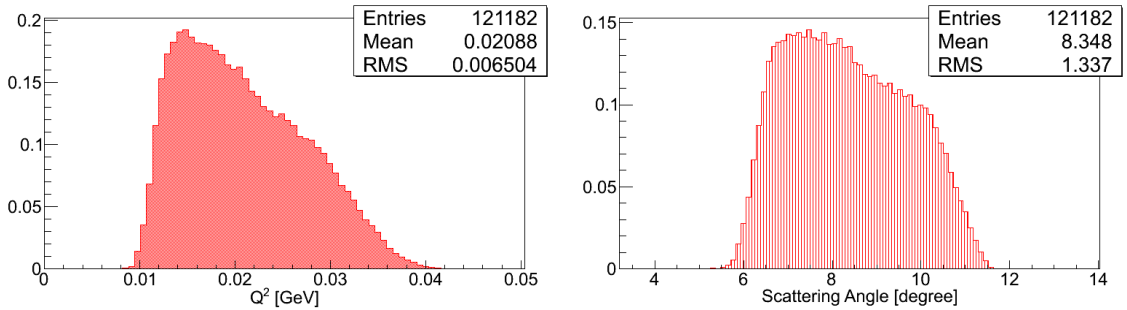


Figure 6.17 The  $Q^2$  from GEANT 3 simulation [153]. The  $Q^2$  was weighted by cross section and did not include any internal bremsstrahlung in the simulation (left panel). The simulated scattering angle is also shown in the right panel.

### 6.6.3.3 $Q^2$ Precision

The  $Q^2$  for inelastic e+p scattering was determined using GEANT 3 simulation and was found to be  $0.0209 \pm 0.0005$  ( $\text{GeV}/c$ ) $^2$  [153], as shown in Figure 6.17. Internal bremsstrahlung was not included in the simulation. The simulation was benchmarked by the tracking mode experimental data to represent the geometry of the experimental setup, collimation, and magnetic spectrometer. The cross section weighted  $Q^2$  was simulated at main detector using the reaction  $e+p \rightarrow e+n+\pi^+$  [153]. The two-body scattering process, and energy and momentum conservation were used to do the calculation. The scattered electron energy, and  $Q^2$  are expressed as

$$\begin{aligned} E' &= \text{RANDOM}() \times (E_{in} - M_e) + M_e \\ Q^2 &= 4EE' \sin^2 \theta, \end{aligned} \quad (6.6.3)$$

where  $E_{in}$  is the incident beam,  $M_e$  is electron mass, and  $\theta$  is scattering angle. It was important to propagate the precision of  $Q^2$  in the final physics asymmetry. Based on theory [154], the transverse beam spin asymmetries  $A_N$  at low  $Q^2$  behave like

$$B_n \approx \sqrt{Q^2} = m\sqrt{Q^2}. \quad (6.6.4)$$

$$dB_n = \pm \frac{1}{2} \frac{m}{\sqrt{Q^2}} dQ^2 = \pm \frac{1}{2} \frac{34.7}{\sqrt{0.02078}} 0.0005 = 0.0601 ppm \quad (6.6.5)$$

Using Equation 6.6.4 on  $Q^2$  and a 5 ppm measured asymmetry, the proportionality constant in the above relation can be calculated as 34.7 ppm/(GeV/c). The estimated uncertainty on the measured asymmetry due to the uncertainty in determining  $Q^2$  is 0.061 ppm (Equation 6.6.5). A correction of  $R_{Q^2} = 1.000 \pm 0.012$  was applied to include the precision in calibrating the central value of  $Q^2$ .

#### 6.6.4 Beam Normal Single Spin Asymmetry

Summary of required quantities to extract the beam normal single spin asymmetry from the transverse data set presented so far using

$$B_n = R_{RC} R_{Det} R_{Q^2} R_\phi \left[ \frac{\left( \frac{\epsilon_{reg}}{P} \right) - A_{Al} f_{Al} - A_{QTor} f_{QTor} - A_{el} f_{el}}{1 - f_{Al} - f_{BB} - f_{QTor} - f_{el}} \right] \quad (6.6.6)$$

is shown in Table 6.8. Equation 6.6.1 has been expanded to obtain Equation 6.6.6. Using all the input values in Equation 6.6.6 gives the beam normal single spin asymmetry in inelastic e+p scattering

$$B_n = 42.27 \pm 2.45 \text{ (stat)} \pm 15.73 \text{ (sys)} ppm \quad (6.6.7)$$

for the effective kinematics of acceptance averaged electron energy  $\langle E \rangle = 1.155 \pm 0.003$  GeV,  $\langle Q^2 \rangle = 0.0209 \pm 0.0005$  (GeV/c)<sup>2</sup> and an average scattering angle  $\langle \theta \rangle = 8.3^\circ$ . The contributions from the different uncertainty sources into the final measurement are summarized in Figure 6.18. The dominant correction to the asymmetry comes from the elastic dilution tail whereas the dominant uncertainty on the measured asymmetry comes from statistics.

Table 6.8 Summary of input quantities to extract the BNSSA. The measured regressed asymmetry is corrected for detector acceptance using the factor provided in the table. The table shows the contributions of normalization factors on  $A_M^{in}$ , then the properly normalized contributions from other sources. Background corrections listed here include only  $R_{total} f_i A_i / (1 - f_{total})$ . Uncertainties in BNSSA due to dilution fraction and background asymmetry uncertainties are noted separately.

Input parameters			
Measured asymmetry ( $A_M^{in}$ )			$5.095 \pm 0.455$ ppm
Beam polarization (P)			$0.875 \pm 0.008$
Detector acceptance correction			0.9938
Background corrections			
Quantity	Asymmetry ( $A_{bi}$ ) [ppm]	Dilution ( $f_{bi}$ )	Correction $c_i = \kappa P A_{bi} f_{bi}$ [ppm]
Target windows (b1)	$9.185 \pm 1.409$	$0.033 \pm 0.002$	1.427
Beamlime scattering (b2)	$0.300 \pm 0.058$	$0.018 \pm 0.009$	0.025
Other neutral bkg. (b3)	$0.000 \pm 10.000$	$0.034 \pm 0.010$	0.000
Elastic asymmetry (b4)	$-4.885 \pm 0.093$	$0.701 \pm 0.070$	-16.129
Other corrections			
Radiative correction ( $R_{RC}$ )	$1.010 \pm 0.004$		
Detector bias ( $R_{Det}$ )	$0.998 \pm 0.001$		
$Q^2$ acceptance ( $R_{Q^2}$ )	$1.000 \pm 0.012$		

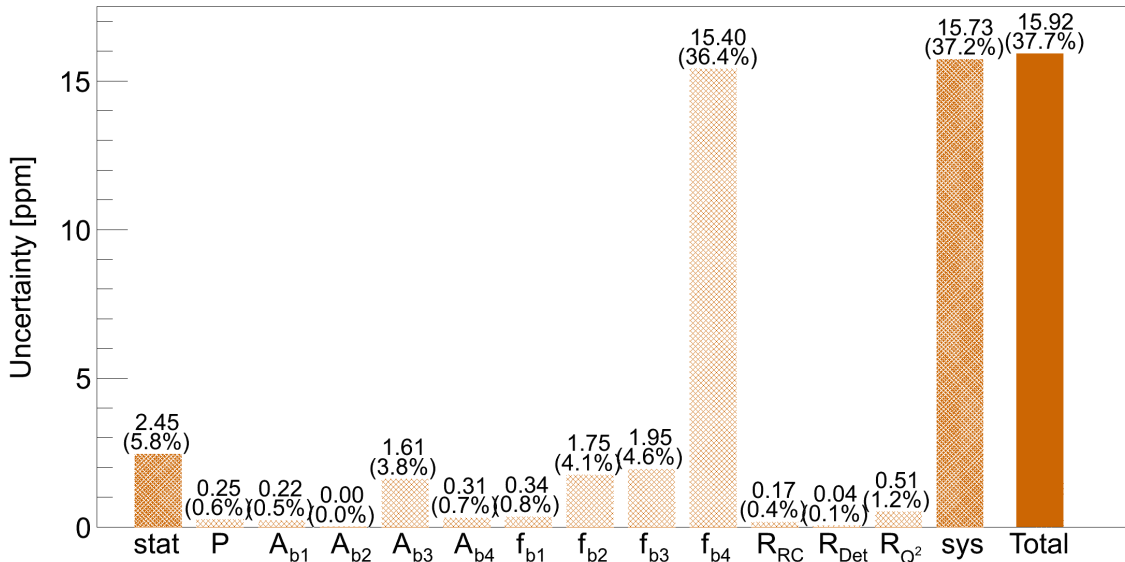


Figure 6.18 Summary of uncertainties in inelastic beam normal single spin asymmetry extraction. Measurement systematic contains the systematic uncertainties related to the extraction of the physics asymmetry such as regression, nonlinearity and acceptance averaging. The uncertainties are in ppm and the corresponding relative uncertainties are shown in parentheses.

## 6.7 Comparison With Model Calculation

No existing model calculation for beam normal single spin asymmetry was available at Q-weak kinematics during this analysis. Pasquini et al. [39] presented beam asymmetry in inelastic electron scattering (as shown in Figure ??) for large scattering angle at energies  $E = 0.424, 0.570, 0.855$  GeV. The BNSSA were calculated separately for  $\Delta$  and  $N$  intermediate states. The total asymmetry was the sum of these two intermediate states. Relatively large asymmetries were observed in the forward region; these are dominated by quasi Virtual Compton Scattering (VCS) kinematics where one exchanged photon becomes quasi-real. These asymmetries are sensitive to  $\gamma^* \Delta\Delta$  form factors and can be a unique tool to study it [38].

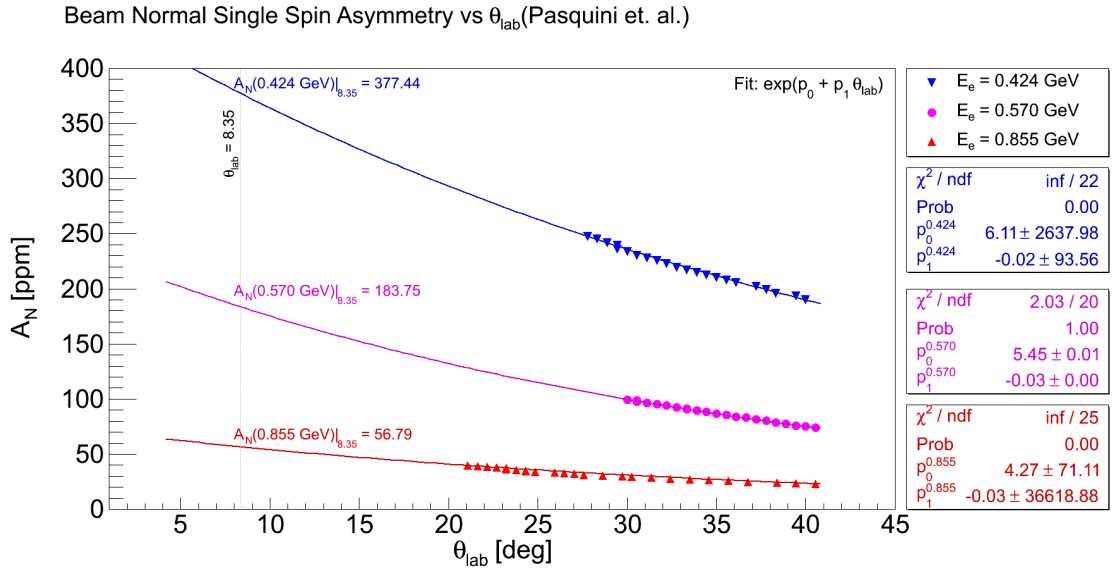


Figure 6.19 BNSSA asymmetry calculation from Pasquini et al. The points are taken from [39]. Then, the calculation is fitted with a function of the form  $f(\theta_{\text{lab}}) = \exp(p_0 + p_1 \theta_{\text{lab}})$  and interpolated to Q-weak  $\theta_{\text{lab}}$  value.

These asymmetries were extrapolated to forward angle down to  $\theta_{\text{lab}} < 5^\circ$  using a suitable fit for all available three energies from [39], as shown in Figure 6.19. The asymmetries were obtained at  $\theta_{\text{lab}} = 8.35^\circ$  for three energies and extrapolated to Q-weak energy  $E = 1.155$  GeV in Figure 6.20. Using this hand waving toy model, the obtained BNSSA is  $B_n[\text{model}] = 12.15$  ppm at Q-weak kinematics. The asymmetry from this analysis,  $B_n[\text{Q - weak}] = 42.27 \pm 15.92$  ppm is also shown in the Figure 6.20. The extrapolation uncertainties are large but cannot be realistically estimated. New calculation are in progress.

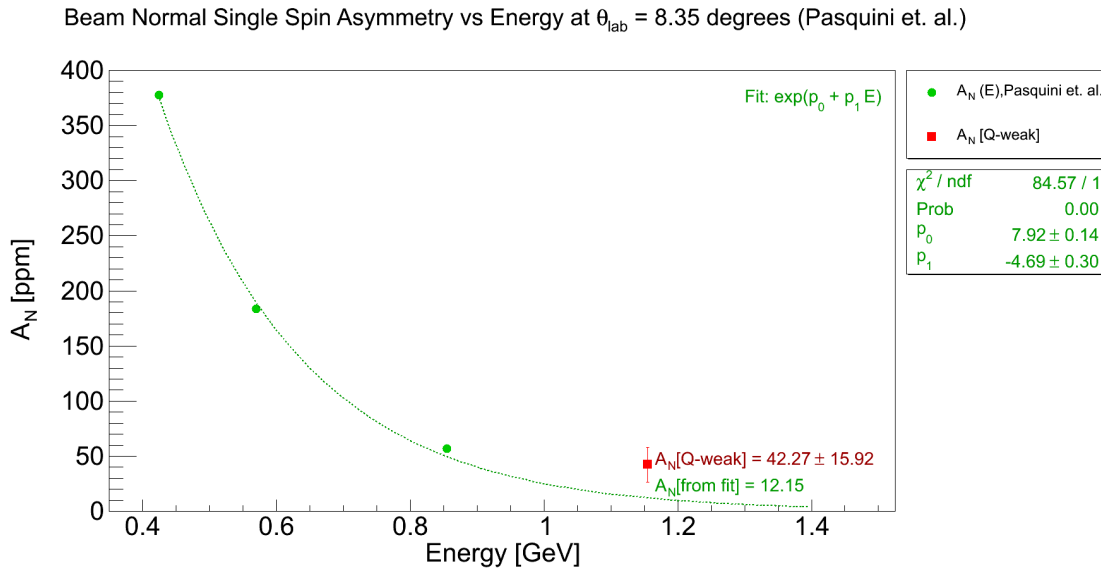


Figure 6.20 BNSSA asymmetry calculation from Pasquini et al. and its extension. The asymmetries from Figure 6.19 at  $\theta_{\text{lab}} = 8.35^\circ$  are plotted here. A fit function of the form  $f(E) = \exp(p_0 + p_1 E)$  is used to extrapolate the asymmetry to the desired Q-weak kinematic region ( $E = 1.155$  GeV).

## 6.8 BNSSA in Nuclear Targets

In this chapter, the inelastic beam normal single spin asymmetry measurements in e-p scattering have been discussed. In addition to the inelastic data from the proton, Q-weak has data on the beam normal single spin asymmetry measurements from several other physics processes. Few of these measurements are the first of their kind and carry interesting physics. The measured regressed (5+1) asymmetries on liquid hydrogen cell, 4% thick downstream aluminum alloy, and a 1.6% thick downstream carbon foil are summarized in Table ???. The relative statistical precision of the measurements are also shown. The analysis of these data is ongoing and expected to test model calculations of beam normal single spin asymmetry.

## 6.9 Conclusion

The Q-weak collaboration has made a 35% relative measurement of the beam normal single spin asymmetry of  $B_n = 42.27 \pm 2.45$  (stat)  $\pm 15.73$  (sys) ppm using transversely polarized 1.155 GeV electrons scattering in-elastically from protons with a  $Q^2$  of 0.0209  $(\text{GeV}/c)^2$ . This is the first measurement of the beam normal single spin asymmetry in inelastic e-p scattering. This measurement

Table 6.9 Measured regressed (5+1) asymmetries in inelastic electron-nucleon scattering for transverse polarized beam. Horizontal and vertical transverse data set are shown separately. The combined (error weighted average) asymmetries are also noted. The inelastic peak is at QTor current 6700 A. The other QTor currents were taken to improve the simulation for elastic radiative tail.

Pol.	Asymmetry [ppm]		
	QTor currents		
	6000 A	6700 A	7300 A
$\text{LH}_2$			
Hor.	$7.198 \pm 0.688 \pm 0.163$	$5.303 \pm 0.533 \pm 0.092$	$0.717 \pm 0.476 \pm 0.252$
Ver.		$4.457 \pm 0.807 \pm 0.117$	
Both	$7.198 \pm 0.688$ (9.5%)	$5.047 \pm 0.444$ (8.7%)	$0.717 \pm 0.476$ (49.3%)
Al			
Hor.		$7.892 \pm 1.186$	$-1.245 \pm 1.087$
Ver.		$9.631 \pm 1.768$	
Both		$8.432 \pm 0.985$ (11.7%)	$-1.245 \pm 1.087$ (87.3%)
$^{12}\text{C}$			
Hor.		$10.190 \pm 1.863$ (18.3%)	

would be an excellent test of theoretical calculations. Unfortunately, at the time of this analysis, there was no existing theoretical calculation or model to compare with the data. Hopefully this thesis will encourage theoreticians to produce new calculations.

## SECTION 7

### DISCUSSION AND CONCLUSIONS

#### **7.1 Summary of Results**

This dissertation presents the highlights of my Ph.D. research work in the context of the Q-weak experiment. This chapter summarizes the results and conclusions presented so far.

#### **7.2 Contribution Towards Q-weak Experiment**

My contributions to the Q-weak experiment towards the measurement of the weak charge of the proton can be summarized under three categories: beam modulation system, beamline optics and false asymmetries, and the beam normal single spin asymmetry measurement in inelastic electron-proton scattering. The experience gained during this experiment will help future precision parity violating measurement at the Jefferson Lab such as the Møller experiment [121].

##### **7.2.1 Beam Modulation**

The electron-proton scattering rate largely depends on the five beam parameters: horizontal position, horizontal angle, vertical position, vertical angle, and energy. Changes in these beam parameters when the beam polarization is reversed create false asymmetries. Although attempt has been made to keep changes in beam parameters during reversal as small as possible, it is necessary to correct for such false asymmetries. To make this correction precisely, a beam modulation system was implemented to induce small position, angle, and energy changes at the target to characterize detector response to the beam jitter. The beam modulation system modulated position and angle using two pairs of air-core dipoles separated by  $\sim 10$  m and pulsing one pair at a time to produce relatively pure position or angle changes at the target. The beam energy was modulated using an SRF cavity. The system has been commissioned using the simulated optics from OptiM [69] and collected data during the experiment. The beam modulation system was designed for sinusoidal modulation up to 250 Hz which was robust and well-suited for experiments measuring small parity violating asymmetries like the Q-weak experiment. At the cost of 1% of beam time for one parameter, the system was able to measure all sensitivities to 10% accuracy each day. The pairs of coils were tuned to deliver relatively pure positions or angle modulations, making it much less likely that singular matrices are encountered when solving for the sensitivities. The ratio of coil currents was

adjusted to incorporate any optics change in the beamline compare to move the coils physically, which made the system independent of the design optic. For 1.165 GeV electron beam, using 125 Hz sinusoidal drive signal, the Trim power amplifier was able to provide the desired beam modulation amplitudes with existing air-core MAT coils. The modulation system worked quite well for the span of two years during the Q-weak experiment and collected data noninvasively with production running. Preliminary detector sensitivities were extracted which helped to reduce the width of the measured asymmetry. The beam modulation system also has proven valuable for tracking changes in the optics, such as dispersion at the target and beam position coupling [155]. The system has also helped to track some of the problems in the BPMs in the Hall-C beamline.

### 7.2.2 Beamline Work

The beam position monitors (BPMs) in front of the target were used for the linear regression and hence was necessary to know their position and angle resolutions. The position resolution of the BPM in front of the target were extracted by observing the residual of beam position differences (between two helicity states) on any BPM and the orbit projected from the virtual target BPM. The concept of the virtual BPM was developed and simulated to determine the position and angle at the target. Using selective data samples from the commissioning phase of the experiment the average BPM resolution was  $0.70 \mu\text{m}$  and  $0.77 \mu\text{m}$  for X and Y respectively. The target BPM angle resolution was simulated using OptiM [69]. A relatively pure position measurement, which corresponds to pure angle measurement at target, was chosen to be at BPM 3P02A from the simulation to extract the angle resolution. Assuming  $0.90$  ( $0.96$ )  $\mu\text{m}$  X(Y)-position resolutions, the estimated target BPM angle resolutions at  $180 \mu\text{A}$  are  $0.048 \mu\text{rad}$ , and  $0.060 \mu\text{rad}$  for  $X'$  and  $Y'$  respectively. A new least square linear regression scheme was developed based on this BPM study.

The helicity correlated pedestals were surveyed to improve the false asymmetry contribution for the entire data set of the experiment. No helicity correlated pickups were seen for most of the detector channels and were at  $\mathcal{O}(1)$  ppb. Electronic noise levels were generally acceptable, though potentially marginal for the upstream luminosity (USLumi) monitor channels near the end of Run-I but improved during Run-II. Nonlinearity for main detectors were extremely small whereas, USLumi had a nonlinearity of few percent. There is a scope for improvement in USLumi pedestal. Nonlinearity could be very large for low-yield production running on aluminum and  $N \rightarrow \Delta$  but still be under 1%. Resolutions for all the detectors were reasonably stable.

### 7.2.3 Beam Normal Single Spin Asymmetry in Inelastic e+p Scattering

The objective of the Q-weak experiment is to challenge the predictions of the Standard Model in low  $Q^2$  range and search for new physics at the TeV scale through a 4% measurement of the weak charge of the proton via the parity-violating asymmetry ( $\sim 250$  ppb) in elastic electron-proton scattering [8]. One of the important correction for the PV asymmetry comes from the residual transverse polarization in the beam. There is a parity conserving beam normal single spin asymmetry or transverse asymmetry ( $B_n$ ) on H<sub>2</sub> with a  $\sin(\phi)$  like dependence due to two-photon exchange. The size of  $B_n$  is few ppm. So, a few percent residual transverse polarization in the beam, in addition to potentially small broken azimuthal symmetries in the detector, might lead to few ppb corrections to the Q-weak data. As part of a program of  $B_n$  background studies, we made the first measurement of  $B_n$  in the N $\rightarrow$  $\Delta$  transition using the Q-weak apparatus.  $B_n$  provides direct access to the imaginary part of the two-photon exchange amplitude. The magnitude of  $B_n$  in the N $\rightarrow$  $\Delta$  transition has never been measured before.  $B_n$  from electron-nucleon scattering is also a unique tool to study the  $\gamma^*\Delta\Delta$  form factors [156].

The Q-weak collaboration has made the first measurement of the beam normal single spin asymmetry as  $B_n = 42.27 \pm 2.45$  (stat)  $\pm 15.73$  (sys) ppm using transversely polarized 1.155 GeV electrons scattering in-elastically from protons with a  $Q^2$  of 0.0209 (GeV/c)<sup>2</sup>. This measurement would be an excellent test of theoretical calculations. In addition to the inelastic data from the proton, Q-weak has data on the  $B_n$  measurements from several other physics processes. The asymmetries were measured on liquid hydrogen cell, 4% thick downstream aluminum alloy, and a 1.6% thick downstream carbon foil. Few of these measurements are the first of their kind and carry interesting physics. The analysis of these data is ongoing and expected to test the theoretical models on beam normal single spin asymmetry and thereby our understanding of the doubly virtual Compton scattering process. Unfortunately, at the time of this analysis, there was no existing theoretical calculation or model to compare with the data. Hopefully this thesis will encourage theoreticians to produce new calculations.

## APPENDICES

## APPENDIX A

### BEAM MODULATION

#### A.1 Beam Modulation

$$dA = \frac{1}{\sqrt{N}} = 1 \times 10^{-6} = 1 \text{ ppm} \quad (\text{A.1.1})$$

$$N = 10^{12} \text{ counts} = Rt \quad (\text{A.1.2})$$

$$t = \frac{N}{R} = \frac{10^{12}}{8 \times 800 \times 10^6 \text{ Hz}} = 156.25 \text{ s} \quad (\text{A.1.3})$$

##### A.1.1 Introduction

The  $Q_{weak}^p$  experiment will measure the parity violating asymmetry ( 234 ppb) in elastic electron-proton scattering to determine the proton's weak charge with 4 % total uncertainty. The e+p scattering rate depends in first order on the five beam parameters at the scattering target: horizontal position ( $X$ ), horizontal angle ( $X'$ ), vertical position ( $Y$ ), vertical angle ( $Y'$ ), and energy ( $E$ ). Small changes in these parameters will create a change in rate which, if beam helicity dependent, would create a false asymmetry. While the source group tries to keep these helicity-correlated parameter changes as small as possible, the goal of our beam modulation group is to occasionally induce controlled beam parameter changes  $dX_i$ , measure the resulting detector false asymmetry  $A_i^{false}$ , and determine the detector sensitivities  $A_i^{false}/dX_i$ . This will allow later correction of beam false asymmetries via  $A_{correction} = i=1,5 (A_i^{false}/dX_i) * X_i$ . Even if these corrections prove to be small under ideal running conditions, the modulation system described here will allow us to quickly determine if undesirable changes have occurred.

##### A.1.2 Measurement Time vs Modulation Asymmetry

We begin with the assumption that it would be helpful to measure the whole-detector sensitivities to 10% accuracy every few days (provided it can be done using only a small fraction of our beam time and without beam strikes or halo scraping). If the sensitivities prove to be stable, this would yield few percent errors by the end of the experiment. This is much better than one would need

to regress out the helicity-correlated differences seen in the last HAPEx Hydrogen run. [ref: A. Acha et al., Precision Measurements of the Nucleon Strange Form Factors at Q2 0.1 GeV2, PRL 98, 032301 (2007)] However, frequent whole-detector sensitivity measurements might reveal important changes in beam or target cell position, the presence of an unmeasured beam parameter, or even a broken glue joint in the main detector. Furthermore, accurate single-octant sensitivities (which would be obtained as a by-product) are an essential prerequisite to extracting the  $\sin \phi$  and  $\cos \phi$  dependences which are symptomatic of residual transverse beam polarization.

For the size and duration of the modulations we discuss below, the natural beam jitter and the SEE BPM electronic noise of roughly 5?m/?Hz will be negligible. (Were this not the case, measurement times would become much longer.) This means the error on the detector sensitivities is dominated by the statistical error on the detector false asymmetry. At nominal luminosity, the  $Q_{weak}^p$  experiment has a rate of 800 MHz /octant, hence the whole-detector statistical sensitivity  $dA = 12.5 \text{ ppm}/?t(\text{sec})$ , or 1 ppm in 156.25 seconds. The clock times needed to measure a single beam sensitivity to 10% are therefore

$$t(s) = \frac{1}{DF} \frac{12.5 \text{ ppm}}{A(\text{ppm})^2} \frac{dA}{A} = \quad (\text{A.1.4})$$

$$t(\text{sec}) = (1/DF)^* (12.5 \text{ ppm}/A(\text{ppm}))2/(dA/A)2 = (1/DF)^* 100 * (12.5 \text{ ppm}/A(\text{ppm}))2 .$$

Table A.1 Dead time calculation for beam modulation. The clock time needed to measure detector sensitivity for a single parameter and how it varies with asymmetries are shown here.

Modulation asymmetry [ppm]	Clock time required		
	10% DF [Hours]	1% DF [Hours]	0.1% DF [Hours]
1	43	430	4300
10	0.43	4.3	43

Table ?? Time estimates for a 10% measurement of a single beam sensitivity with different assumptions about the modulation asymmetry and the modulation duty factor. The green highlighted boxes represent a reasonable range of parameters. For several assumptions about asymmetry and duty factor, required clock times are listed in Table 1. A modulation of 10 ppm would permit a measurement of all 5 sensitivities to 10%, require about 1-10 calendar days, and have minimal negative impact on production duty cycle. For fixed error bar, smaller amplitudes would require at least quadratic increases in measurement time or duty factor. For fixed measurement time and duty factor, smaller amplitudes would cause at least linear increases in the errors.

### A.1.3 Modulation Amplitude

We next estimate how much we will need to modulate the beam position and angle to achieve  $A_{\text{false}} = 10 \text{ ppm}$ . Detailed simulations have been performed by J. Birchall [REF: J. Birchall, "Updated Requirements on Beam Properties for Qweak", Qweak technical note, August 2008, Table 1] . Jim's single octant sensitivities are given in the second column of Table 2, and appear to be dominated by the interaction of e+p elastic scattering with the defining collimator. Except for energy, the whole detector sensitivities are much smaller. They are much more complicated however since they are determined by imperfect cancellation of linear sensitivities due to broken symmetries (coil misalignments, radiator radial positions), plus quadratic sensitivities which depend on beam offsets. Reasonable people might therefore disagree as to what suppression factor we can expect in going from single octant sensitivities to whole detector sensitivities. In Table 2 we assumed the relatively conservative factor of 50 which leads to our estimate for the required modulation amplitudes appear in the last column.

Table A.2 A crude estimate of the modulation amplitudes to generate 10 ppm whole detector asymmetries.

Beam Parameter	Single Octant Sensitivity	Assumed Cancellation	Whole Detector Sensitivity	Modulation Amplitude for 10 ppm
Position	10 ppb/nm	50	0.2 ppb/nm	$50 \mu\text{m}$
Angle	30 ppb/nrad	50	0.6 ppb/nrad	$20 \mu\text{rad}$
Energy	1 ppb/ppb	1	1 ppb/ppb	10 ppm ( $\sim 10 \text{ keV}$ )

Table ?? Crude estimates for the modulation amplitude needed to generate 10 ppm whole detector asymmetries. All values are quoted to one significant figure. One can see from Table 2 that the estimated whole detector sensitivities are small. Compared to the Qweak statistical error bar of 5 ppb, the beam parameter corrections resulting from the O(1nm, 0.1nrad, 0.1ppm in energy) helicity-correlated differences seen in the last HAPPEX Hydrogen run would be negligible. Alternatively, this means the allowable uncertainty in determining the beam sensitivity is 100%, so a system capable of making a 10% measurement on all 5 beam sensitivities every 1-10 days is apparently overkill. The real value of such a beam modulation system may be to detect undesired changes in the experiment, or as insurance in case the e+p sensitivities prove to be much larger than anticipated, or for those cases where the sensitivities are known to be much larger (e.g., for elastic scattering on  $^{9}\text{Be}$  or  $^{27}\text{Al}$  window-like targets, or for the small angle scattering into the luminosity monitors).

## A.2 Optics Calculation

We utilize the OPTIM program written by Valery Lebedev [9] and an input deck prepared by Jay Benesch (JLab). The 3C beamline will be substantially modified before  $Q_{weak}^p$  to accommodate a Compton polarimeter, so the (undocumented) parity infrastructure left over from the G0 experiment would have been toast even if we had planned to retain it. Our goal is to achieve robust modulation in X, X?, Y, Y?, and E at the  $Q_{weak}^p$  target. Strictly speaking, these modulations do not have to be pure, but they have to be linearly independent so that one can solve for the individual sensitivities. However, we'll see below that for similar sized magnet kicks in Qweak, asymmetries from position modulations are an order of magnitude larger than the corresponding asymmetries from angle modulations. This fact, plus the relatively large statistical noise in the detector asymmetries, plus the certainty of small drifts in the optics, suggest to us that "mixed mode" modulation is unlikely to be robust. Running times and uncertainties would also be quite difficult to estimate in the case of mixed mode modulation. Therefore, we will attempt to produce relatively pure modulations in which 90% of the asymmetry arises from the variable of interest. There are significant constraints on where perturbing coils can be located. One absolute requirement is that coils be located upstream of the high dispersion point at 3C12 (the center of the 3C arc) so that modulations in X, X', and E can be disentangled. Another highly desirable constraint is that the coils be located downstream of any expected deviations from design optics. Accelerator operations has agreed to complete matching in our beamline by MQA3C08, the beginning of the 3C arc dipole string. Considerations of robustness and purity therefore exclude regions upstream of this, leaving only only the first half of the 3C arc as a potential site for coils.

### A.2.1 Inverse Beamline

An insightful starting exercise is to start with a pure position or angle deviation at the  $Q_{weak}^p$  target and use OPTIM to send tracks in the upstream direction. We call this the inverse beamline or orbit. Figure 1 shows the result from the target to the Lambertson. All 4 panels have the same qualitative features: the beam moves to the right with piece-wise continuous motion, there is a discontinuity at each quadrupole location, and there is at least one zero crossing. The reason this inverse trajectory is so interesting is that, due to time-reversal invariance of electromagnetic interactions, it tells us how we have to perturb a forward beam to obtain a pure position or angle change at the target. As long as the inverse orbit stays inside the beampipe, such a figure is an existence proof that pure modulation at the target is possible with a forward beam.

### A.2.2 Forward Rays with Position or Angle Kicks

The simplest way to perturb an arbitrary forward beam onto the magic trajectory is to kick it with a single small dipole at one of the zero crossings. However, if our coils are restricted to the first half of the 3C arc, this strategy is not feasible because there is only one zero crossing in that region (corresponding to pure  $X'$  modulation), with no zeros corresponding to  $X$ ,  $Y$ , or  $Y'$  modulation. A better approach was then suggested by Mike Tiefenback, similar to that used in the JLab Fast Feedback System (FFB). As schematically shown in Figure 2, pairs of separated coils could be used to take an arbitrary forward ray, offset its position and angle, and re-inject it along the appropriate trajectory to produce a pure position or angle change at the target. Detailed OPTIM solutions for forward rays are shown in Figure 3 for a pair of coils separated by 9.5 meters. Note that position modulation of  $\pm 50 \mu\text{m}$  at the target yields orbit deviations of similar magnitude in the beamline, while angle modulation of  $\pm 50 \mu\text{rad}$  at the target yields orbit deviations of up to 3 mm. The size of the latter orbit deviations is large enough to cause some concern about scraping of the beam or halo. (The impact on the Compton polarimeter laser x electron beam lock has not been examined.) We could match the size of the orbit deviations by reducing the angle kick an order of magnitude. This might be a better match to size of natural beam jitter, but the time required in Table 1 for a single 10% measurement would increase by at least a factor of 100.

OPTIM-derived field integrals yielding pure modulations at the Qweak target are given in Table 3. These field integrals were converted to currents using the measured HF(MAT) coil field constant of 330 G-cm/Amp. It is conceivable that the 3C beamline design optics will be revised yet again in order to optimize operation of the new Compton polarimeter. Fortunately, in this two-coil scheme, we would be able to simply retune the ratio of coil currents without having to move coils.

### A.2.3 Forward Rays with Energy Kick

The effect of a 10 ppm energy kick is shown in Figure 4. At the point of highest dispersion (the middle of the 3C arc) the induced motion is shown by a  $40 \mu\text{m}$  red spike. From a comparison of Figures 3 and 4, it's pretty clear that energy changes could not possibly be confused with position or angle changes. Further downstream, the small green bump represents the dispersion inside the vertically bending Compton chicane. Because of the lower dispersion, the induced motion in the Compton will only be about  $5 \mu\text{m}$ , much smaller than the nominal JLab electron beam rms width.

### A.3 Beam Modulation Hardware

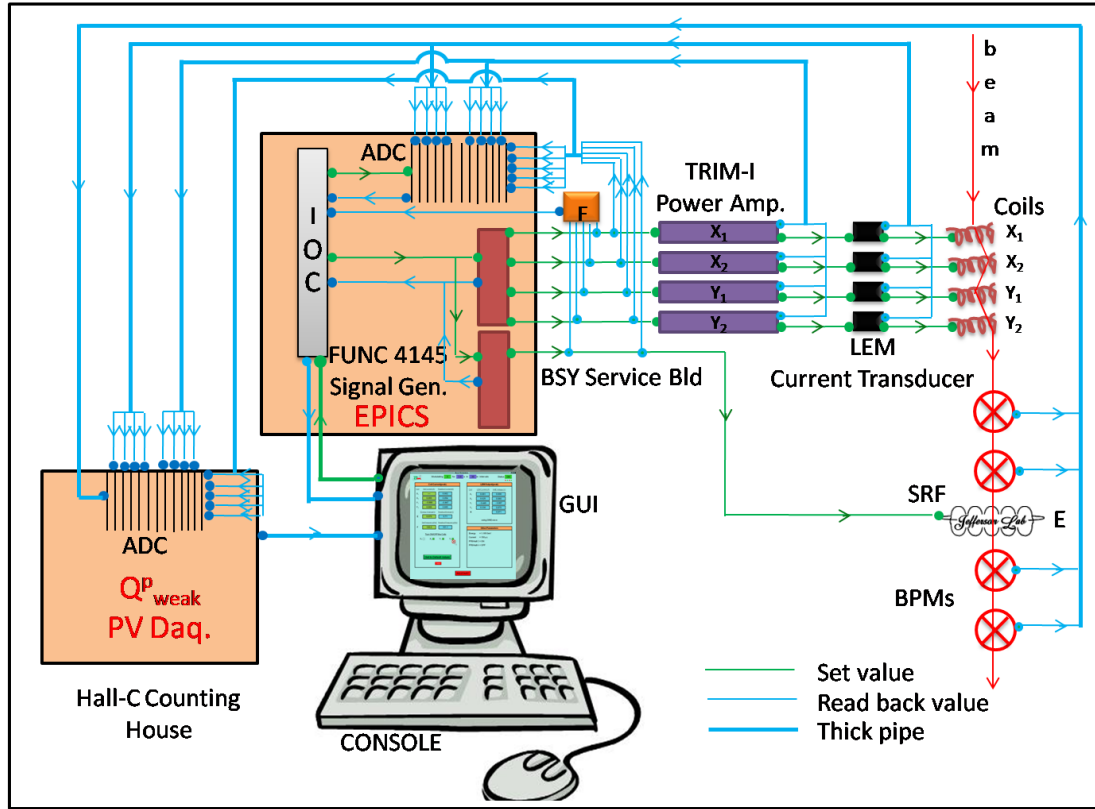


Figure A.1 Beam modulation hardware sketch.

#### A.3.1 Air-Core Coils

We plan to use JLab MAT(HF) air-core coils because they have sufficient field integral, they are readily available due to a recent switch of the FFB system to lower inductance coils, and they are short so can be easily tucked in almost anywhere. Their properties have been measured and summarized in an Excel file by Sarin Philips (JLab). [ref: <http://qweak.jlab.org/doc-public/ShowDocument?docid=979>] The most critical parameters are summarized in Table 4. (For reference, the total impedance is  $X_{tot} = 1.6 \Omega + 2\pi f(0.0038H)$ .) S. Philips also determined the reduction in field due to the skin effect in a standard stainless steel beampipe to be roughly 10% at 1 KHz, and less than a few percent at our nominal frequency of 250 Hz. The amplifiers we plan to use limit us to sinusoidal modulation at 250 Hz, so we will ignore the skin effect henceforth.

### A.3.2 Coil Siting

The nomenclature we use is from the OPTIM deck found in Appendix II. As shown in Figure 5, our 1st coil is in drift oD7028, located just after quadrupole 3C08 and before the dipole 3C05. The 2nd coil will be in drift 0D7031, after dipole 3C06 but before dipole 3C07. The separation is about 9.5 m. Initially, we tried to put both coils into a single 1m drift, but the angle kicks of interest required excessively high field integrals. Separating the coils by more than 1 meter requires straddling an active beam element. We decided to straddle two dipoles with no intervening quadrupoles. Not only does this seem natural in an OPTIM context (since the orbit inside a dipole is plotted effectively like a drift), but it would simplify any trigonometric calculations if we ever have to do any cross-checks.

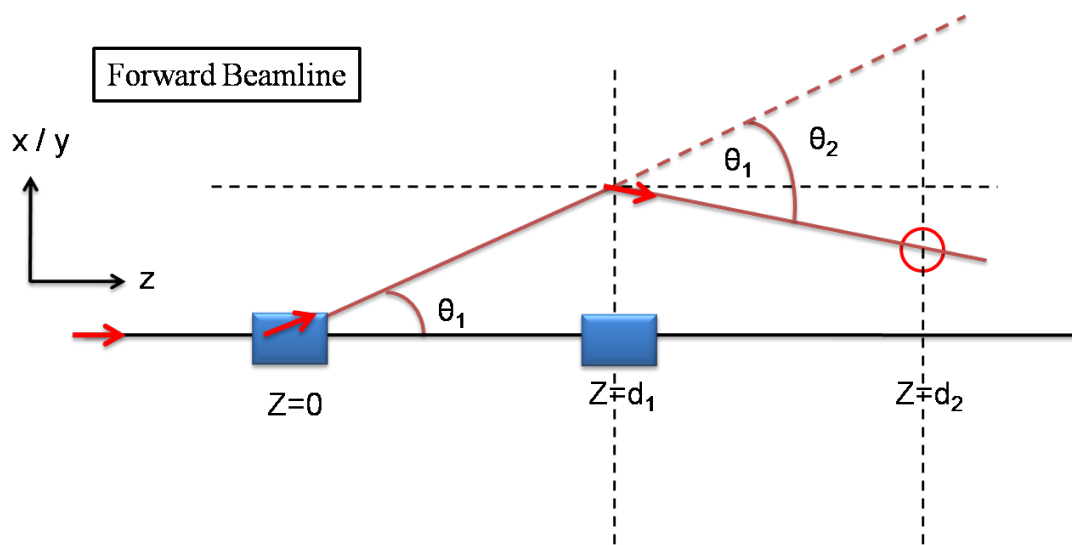


Figure A.2 Beam modulation sketch.

### A.3.3 Energy Modulation Hardware

This procedure uses an energy vernier of a cryo-module in South Linac of the accelerator. Every 1 hour of a production run, the procedure will begin what is called a supercycle for 1 minute. Within each supercycle, modulation coil pair has its current ramped up and down with a proper ratio to each other. The final cycle of the supercycle is the modulation of the energy vernier. Each cycle can be programmed to be about 1minutes. The response of the beam position monitors and detectors can be measured. One of the standard features of the accelerator is the use of Fast Feedback (FFB) to maintain a steady beam position.

Table A.3 Beam modulation bench test.

The Components	Quantity
Signal Generator	1
TRIM-II	2
MAT Coil	2
LEM	1
Ammeter	2
Power Supply	1
Tesla Meter	1

## A.4 Bench Tests

The Signal Generator generates SINE wave of different amplitude and frequency as the input voltage to the TRIM-II which is basically a power amplifier. The amplified signal goes to coil through a single LEM (current transducer) either in phase or out of phase from two coils. The currents through the coils are measured by ammeter. The Magnetic fields of the coils are measured by the Tesla Meter. We have done our measurements with MAT coil of length 10 cm long for several different frequencies. In the next section I am giving a brief of data taking.

We did extensive bench testing with the proposed MAT(HF) coils and the TrimII amplifiers so that (except for the absence of long drive cables) we would be able to predict how the installed system would work. The TrimII amplifier was controlled via an analog input from a simple bench-top function generator (the ???).

## A.5 Waveform

### A.5.1 Waveform

The TrimII amplifier is unable to drive square or even triangular waveforms in the frequency range of interest. Satisfactory results were obtained only with sinusoidal waveforms. We would have preferred being able to generate at least square-ish modulation (similar to the square helicity reversal), but we are under budget and schedule pressure to use the existing TrimII amplifiers.

### A.5.2 Frequency Range

For a test range of 10H-500 Hz and nominal 3A (peak) output, we were able to reliably drive sinusoidal waveforms up to 250 Hz. At that frequency, the coil impedance becomes approximately

$X_{tot} = 1.6 \Omega + 2\pi f(0.0038H) = 7.6 \Omega$  so the amplifier has to provide 22.8 V (peak). The maximum output voltage of the TrimII amplifier appears to be approximately  $\pm 27$  V, but it isn't strictly bipolar due to the use of NPN diodes for one polarity and PNP diodes for the other. So while one could go a bit higher in frequency than 250 Hz, there would be a rapidly increasing risk of generating asymmetrical sine-like waves (and hence a small DC beam position offset).

### A.5.3 Maximum Current

With sustained operation, the coils become quite hot to the touch at  $I_{peak} = 7.07$  A ( $I_{rms} = 5$  A). This is significantly above Qweak's nominal maximum current  $I_{peak} = 3$  A, but it's worth discussing since future experiments at higher beam energy might try to push the envelope. Although measurements at 1% duty factor would take only 36 seconds per hour, one must assume that a parity violation experiment will eventually take long, dedicated beam modulation runs. Unless cooling fans installed, damage to the enamel-insulated wires or any plastic components could result if  $I_{peak} = 7.07$  A is significantly exceeded. We haven't tried to determine the "smoke point", but bear in mind that  $P = R I^2$  so the temperature will increase rapidly with current above  $I_{peak} = 7.07$  A. It is hopefully understood that  $I_{peak} = 7.07$  A refers to the peak current of a sinusoidal waveform, and NOT to a maximum DC current which would have a factor of 2 greater power dissipation!

1. measured the field integral with a GMW Hall Probe
2. monitored the output waveform quality using a LEM current transducer
3. drove two coils simultaneously from our FANUC VME function generator

WHAT DO WE DO ABOUT THE PROBLEM OF EXCESSIVELY SMALL CURRENTS FOR POSITION MODULATION????

## A.6 OBSERVATIONS

The TRIM II is not a linear device. It has frequency dependence. As we are going to higher frequencies starting from 10 Hz to 500 Hz, we are getting higher output voltages across the coils for same input voltage form signal generator with sine wave. As we are going to higher voltages for a fixed frequency, the TRIM II is showing non linearity also. Near the saturation current the TRIM II is getting locked by itself especially with higher frequency. We are getting a phase shift of 180 degrees between the TRIM II output and the LEM current.

## A.7 EXTENSION TO OTHER JLAB PARITY VIOLATION EXPERIMENTS

The system described in this report should be useful for other parity violation experiments such as the Moeller experiment at 11 GeV in Hall A. Some basic limitations should be kept in mind. First of all, the modulation amplitude of the system described here will scale like  $E_{beam}(\text{GeV})/1.165$ , hence the amplitudes at 11 GeV will be smaller by an order of magnitude. If the amplitude becomes smaller than the random beam jitter, convergence will be greatly slowed. The air-core coils can be driven harder if the duty factor is limited or if fans are used, but at about 5A (rms) they become hot enough to risk damaging the enamel coatings on the wires under continuous duty. Secondly, at the frequencies of interest, the coil is an almost purely inductive load, so the voltage needed to drive a given current is nearly proportional to frequency. If we wish to modulate the beam faster than the 250 Hz system described here, faster, higher voltage power amplifiers than the TrimII would be needed. Alternatively, larger field integrals could be obtained for a given current by replacing air-core coils with ferrite magnets. Finally, because the final quadrupole is closer to the target in the 1C line, it should be somewhat easier to generate a given angle kick at a given beam energy as compared to the 3C line.

## A.8 SUMMARY

We have presented a design for sinusoidal modulation up to 250 Hz which is robust and well-suited for experiments measuring small parity violating asymmetries. At the cost of 1% of our beamtime, we will be able to measure all sensitivities to 10% accuracy each day. The pairs of coils can be tuned to deliver relatively pure position or angle modulations, making it much less likely that one will encounter singular matrices when solving for the sensitivities. If the design optics should change for any reason, we can simply change the ratio of coil currents without having to move coils. At 250 Hz and 1.165 GeV, our bench tests confirmed the TrimII power amplifier is able to provide the desired 50?m, 50 ?rad beam modulation amplitudes with existing air-core HF(MAT) coils. However, to provide similar amplitudes for the MoellerPV experiment at 12 GeV in Hall A may require an upgrade of the amplifier or magnets.

### A.8.0.1 Details<sup>1</sup>

Small changes in these parameters will create a change in rate which, if beam helicity dependent, would create a false asymmetry. While the source group tries to keep these helicity-correlated parameter changes as small as possible, the goal of our beam modulation group is to occasionally induce controlled beam parameter changes  $dX_i$ , measure the resulting detector false asymmetry  $A_{\text{false}}$ , and determine the detector sensitivities  $A_{\text{false}}/dX_i$ . This will allow later correction of beam false asymmetries via  $\text{ACORRECTION} = i=1,5$  ( $A_{\text{false}}/dX_i$ )?  $X_i$ . Even if these corrections prove to be small under ideal running conditions, the modulation system described here will allow us to quickly determine if undesirable changes have occurred.

[157]

$$T = \left( \frac{\bar{Y}}{\bar{Y}_{\text{MC}}} \right)_A / \left( \frac{\bar{Y}}{\bar{Y}_{\text{MC}}} \right)_D, \quad (\text{A.8.1})$$

## A.9 Simulation

### A.9.1 OPTIM

We used a software, OPTIM, to do basic calculation for beam modulation. OPTIM is basically computer code for linear and non-linear optics calculations [?]. Main OPTIM deq. file contain all the detailed information about all the beamline elements. It has the information like location of the beamline, field strength, size, orientation etc. One can also get the transfer matrices between any two beamline elements using the software. It also produces simulated trajectories through the beamline from one element to another. We used OPTIM to give us simulated trajectories from beam modulation magnet pair at the beginning of Hall-C beamline to the Q-weak target. We also changed our basis of calculation from beam modulation coil co-ordinate to Q-weak target co-ordinate using OPTIM.

$$\begin{array}{cccc} a_1 & a_2 & \dots & a_n \\ b_1 & \left( \begin{array}{cccc} 1.2 & 3.3 & 5.1 & 2.8 \\ 4.7 & 7.8 & 2.4 & 1.9 \\ \dots & \dots & \dots & \dots \\ 8.0 & 9.9 & 0.9 & 9.99 \end{array} \right) \\ c_1 \\ \dots \\ z_1 \end{array}$$

$3 \times 3$  Matrix:

$$\begin{pmatrix} a & b & c \\ d & e & f \\ g & h & i \end{pmatrix}$$

$3 \times 3$  Determinant:

$$\begin{bmatrix} \lambda - a & -b & -c \\ -d & \lambda - e & -f \\ -g & -h & \lambda - i \end{bmatrix} = \begin{bmatrix} \lambda - a & -b & -c \\ -d & \lambda - e & -f \\ -g & -h & \lambda - i \end{bmatrix} \begin{bmatrix} \lambda - a \\ -d \\ -g \end{bmatrix}$$

Systematic error due to regression schemes dependence is  $\sim 0.0046$  ppm.

Verbatim line.

org~nur

90°

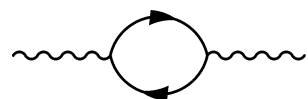


Figure A.3 The caption.

## APPENDIX B

### QTOR

#### B.1 QTOR

QTOR has been used in  $Q_{weak}^p$  experiment for separating elastic and inelastic events.

#### B.2 Hall Probe

The Qtor Hall probes will be hooked up to the same Lakeshore controller that the HMS hall probes used. Nur and I took the VME IOC that was used out of the HMS hut and moved it to the doghouse. We connected IOC to the Lakeshore, and after restoring some boot information on the CPU (vmec18), the EPICS controls appear to still work. For now, we will use the HMS EPICS names, Q1HallP, Q2HallP and Q3HallP. The hall probes can be read from the cdaq machines with the commands:

caget Q1HallP caget Q2HallP caget Q3HallP I will add these to the Qtor GUI I am preparing.

There are EPICS commands to zero the probes:

caput Q1ZeroP caput Q2ZeroP caput Q3ZeroP These will send the command "ZCAL" to the Lakeshore for the specified probe.

Here is the summary for the Ethernet configuration around the doghouse. If you have question, please let me know.

\* Twenty-four Ethernet connections for Qweak

doghouse — T20 Rack — PANEL A — Fiber Optic Slot(FOS) cable # Patch Panel HC01Z04  
 Netgear or hallc-cat2950 1 1 1 FOS 6 2 2 2 FOS 16 3 3 3 FOS 10 4 4 4 FOS 17 5 5 5 FOS 18 6 6 6  
 FOS 19 7 7 7 FOS 20 8 8 8 FOS 5 9-15 9-15 9-15 1-7 (Netgear switch) 16-24 16-24 16-24 available  
 ports on hallc-cat2950 (cisco)

\* Detailed use of T20 Rack Patch Panel #

FOS 1 — Reserved (Boot Power Strip for ROC9) 2 — Reserved (Boot Power Strip for ROC10) 3 — hcreboot13 (Boot Power Strip for others) 4 — hctsv11 (portserver) 5 — IOC for Hall Probe (hctsv11 2002) 6 — qwvme9 (CPU of ROC9) (hctsv11 2008) 7 — qwvme10 (CPU of ROC10) (hctsv11 2007) 8 — qwvme11 (CPU of ROC11) (hctsv11 2006)

Netgear 9 — qwvme9mon (ROC9 crate Power Monitor) 10 — qwvme10mon (ROC10 crate Power Monitor) 11-15 Reserved (connected to the doghouse)

Cisco 16 —— qwscannerctrl (scanner controller unit) 17-22 Reserved (not connected) 23 ——  
a Netgear 4port switch (doghouse, temp?) 24 —— region 3 rotator controller

In addition, I checked the IOC for the Hall probe via the portserver as

[VxWorks Boot]: p boot device : ei processor number : 0 host name : cdaqs3 file name : /KERNELS/vx162 inet on ethernet (e) : 129.57.168.118:fffffc00 host inet (h) : 129.57.168.16 user (u) : cvxwrks flags (f) : 0x20 target name (tn) : vmecl8 startup script (s) : /SCRIPTS/vmec18.boot

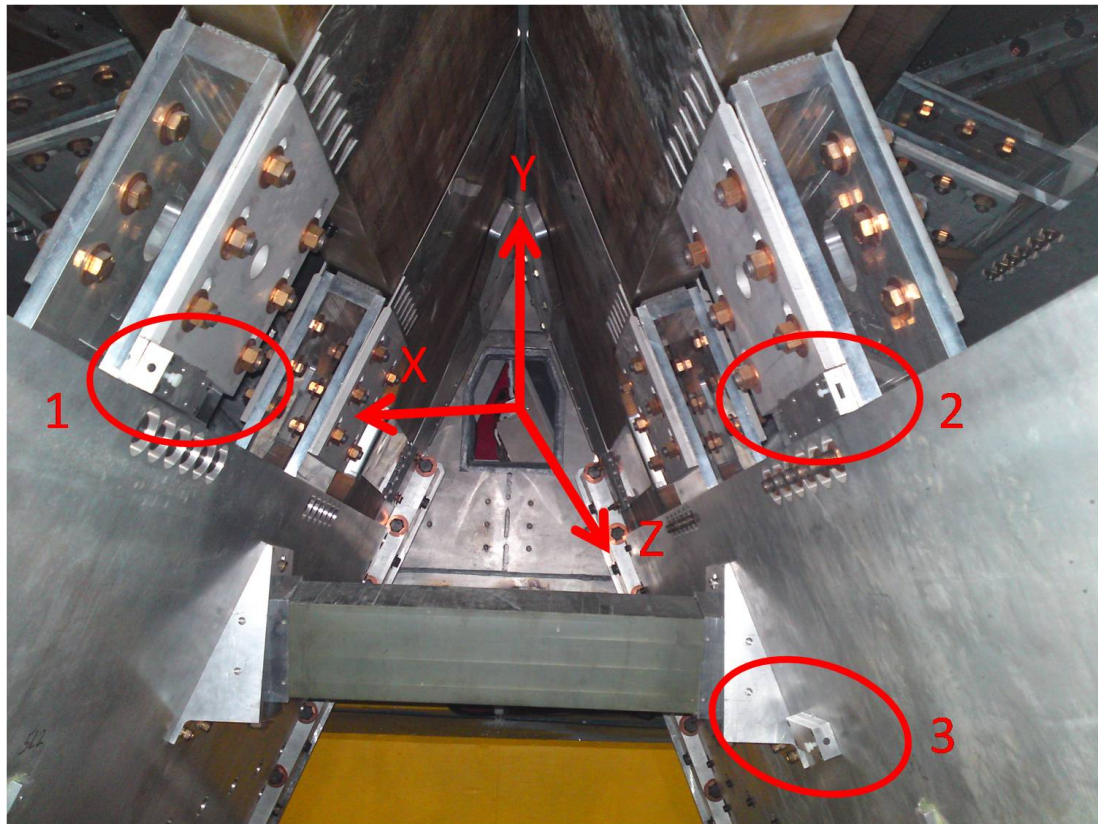


Figure B.1 Q TOR hall probe mounts and their locations are shown here.

### B.3 Q TOR Corrector Magnet

The idea of this analysis is to estimate beam steering due to Q TOR fringe field assuming a field of 4500 Gauss-cm along the beam axis using OPTIM.

Recently we discovered Q TOR steers the forward beam. We tried to examine whether this steering is due to expected Q TOR fringe field along the beam axis, or it indicates misalignment or motion of any Q TOR coils. The steering implies a field integral of 4500 Gauss-cm. See more details

in [1]. In this analysis we tried to predict the effect of QTOR fringe field (4500 Gauss-cm) along the beam axis Using OPTIM simulation.

## B.4 QTOR Corrector Magnet Design

### B.4.1 TOSCA

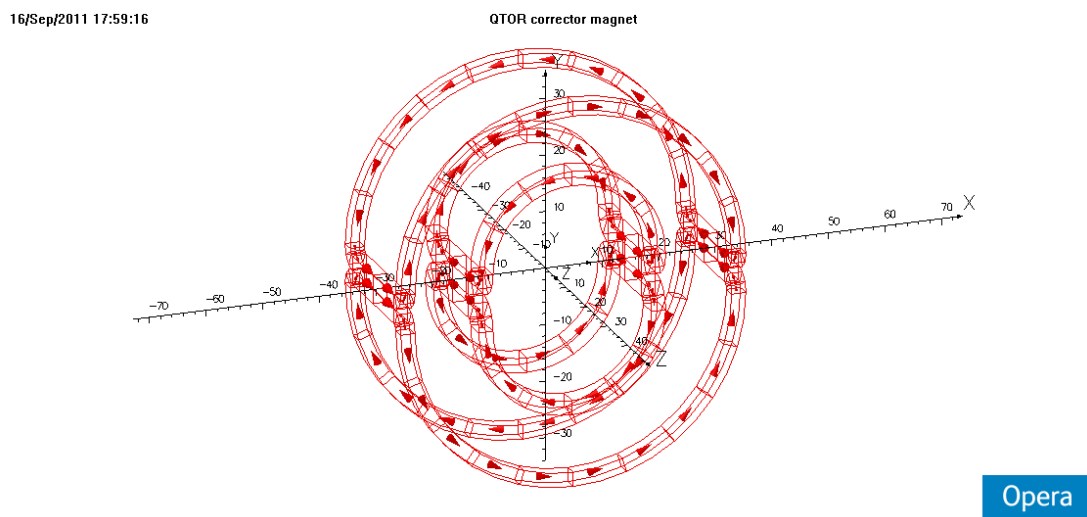


Figure B.2 QTOR corrector magnet design.

We have already seen QTOR steers the forward beam due to fringe field [1, 2]. We have predicted the effect of QTOR fringe field (4250 Gauss-cm) along the beam axis using OPTIM simulation [2] and supported Robs pencil model. In this analysis we want to approach further and want to investigate the different effects of this fringe field on low energy electrons.

\* QTOR and dump viewer in the OPTIM model has been added for this analysis. See details in [2].

\* No microscopic model of the QTOR field symmetry breaking was used. We treated the QTOR region as a 4m long dipole with Rob's suggested field integral, confirming his estimate.

\* Earths magnetic field has not been considered in the model.

Low energy electron scattering due to 4250 G-cm field at QTOR magnet. The points are fitted with polynomial 2. The horizontal axis is shows the different beamline element. The Q-weak target is at zero and beam is coming from left. Different energies are shown in different colors (Colors are chosen according to energy. Convention is Violet 1162 [nominal], Indigo 1000, Blue 750, Green

500, Orange 250 and Red 100 MeV). As expected low energy electrons are deflected much more than high energy electrons.

Motivation: We have already seen QTOR steers the forward beam due to fringe field [1, 2]. We have predicted the effect of QTOR fringe field (4250 Gauss-cm) along the beam axis using OPTIM simulation [2,3]. In this analysis we want to add a corrector magnet in front of QTOR and investigate the effects of this magnet on fringe field on electrons.

Figure 1: Beam trajectory after applying ZERO filed in the corrector magnet in front of QTOR.

Figure 2: Beam trajectory after applying a filed of 4000 G-cm in the corrector magnet in front of QTOR. Its mainly focusing the trajectories at the dump viewer.

Figure 3: Beam trajectory after applying a filed of 4000 G-cm in the corrector magnet in front of QTOR to focus at the dump viewer. Same as Figure 2, just a zoomed in version for better visualization.

Figure 4: Beam trajectory after applying a filed of 4288 G-cm in the corrector magnet in front of QTOR. Its mainly focusing the trajectories at the dump window.

Figure 5: Beam trajectory after applying a filed of 4288 G-cm in the corrector magnet in front of QTOR to focus at the dump window. Same as Figure 4, just a zoomed in version for better visualization.

We have investigated the effects of a magnet in front of QTOR on different energy electrons [4]. In this analysis we want to vary the magnetic field of corrector magnet in front of QTOR and investigate the effects of this field variation on electrons.

Figure 1: Beam trajectory due to different fields in the corrector magnet for a single energy electrons. Then the plot is animated over different beam energies. The beam energy is written on the headings of the plots and different magnetic fields are shown in different colors and symbols are shown in the legend section (right hand side) of the plots.

At the end we may not approach for a magnet in front of QTOR due to its far field effect. Later we may search for a different place (most likely downstream, as we don't have enough space upstream of QTOR) rather than just before QTOR.

Motivation: We found QTOR steers the forward beam most probably due to misalignment of QTOR coils [1]. We have already investigated the effects of a magnet in front of QTOR for primary beam as well as for different energy Moller electrons [2, 3, 4 and 5]. Here we tried to design a magnet we discussed in [4] and [5].

Figure 1: 3D view of QTOR corrector magnet. The current directions for the coils are shown by the arrows.

Figure 2: QTOR corrector magnet along YZ plane. Length along Z-direction (available space for magnet is 25.4 cm) is shown in this figure.

Figure 3: QTOR corrector magnet along XY plane. Magnetic field perpendicular to Z-plane is also shown in a polar patch of radii 40–90 cm.

Figure 4: QTOR corrector magnet field integral along a line in Z- direction (from -50 to +50 cm) at X = 40 cm and Y = 0 cm.

Figure 5: QTOR corrector magnet field integral along a line in Z- direction (from -50 to +50 cm) at X = 0 cm and Y = 40 cm.

Figure 6: QTOR corrector magnet field integral along a line in Z- direction (from -50 to +50 cm) at X = 28.3 cm and Y = 28.3 cm (diagonal).

Figure 7: QTOR corrector magnet field integral along a line in Z- axis (from -50 to +50 cm).

Figure 8: Possible QTOR corrector magnet location. The arrow represents beam direction.

Motivation: We discussed our corrector magnet design in [1]. Here we tried to calculate the power dissipation, voltage drop and temperature rise and other important parameters of the coils.

Motivation: We showed our corrector magnet design in [1]. Here we tried to get an estimate of corrector magnet sensitivity to position or angle using TOSCA.

Motivation: Corrector magnet design has been shown in [1]. We tried to see the profile of magnetic field along the line of collimator opening using TOSCA. [A.9.1](#)

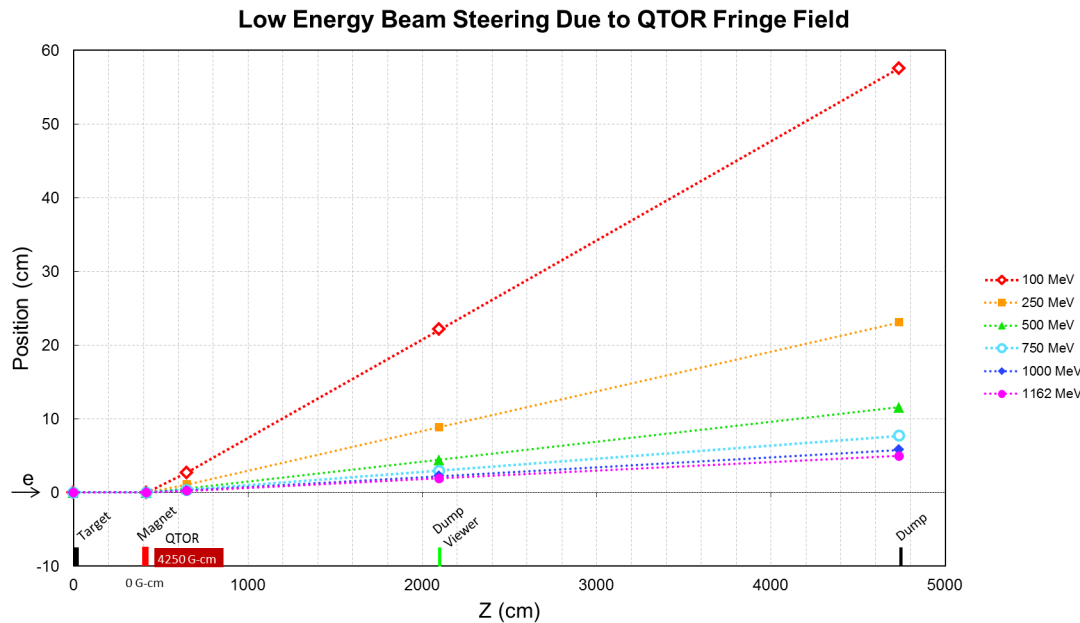


Figure B.3 QTOR qtor allenergy 0Gcm.

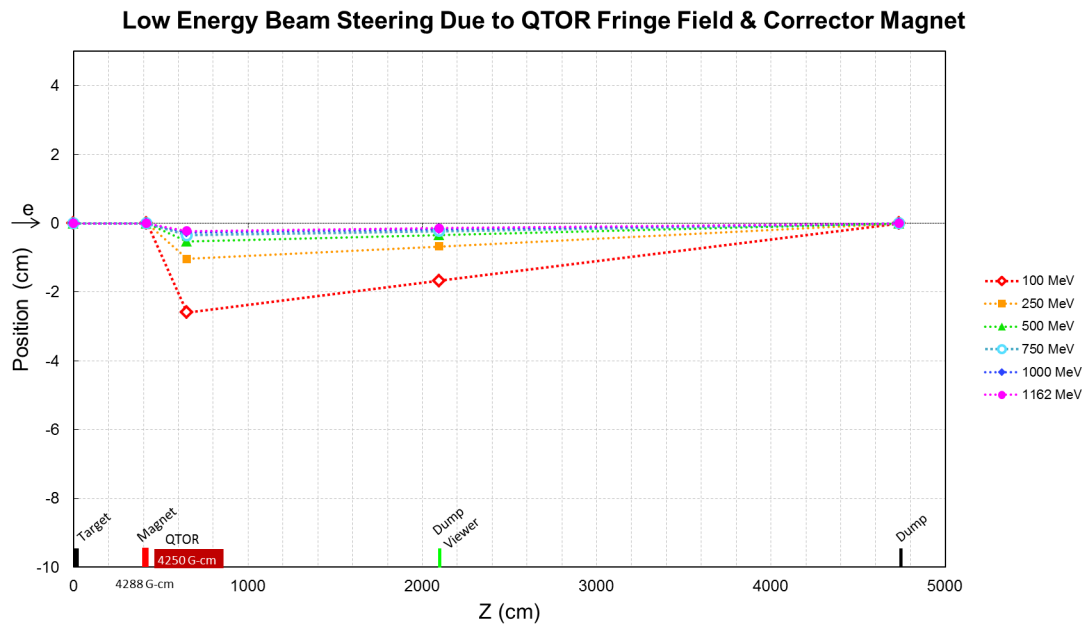


Figure B.4 QTOR all energy 4000Gcm dump.

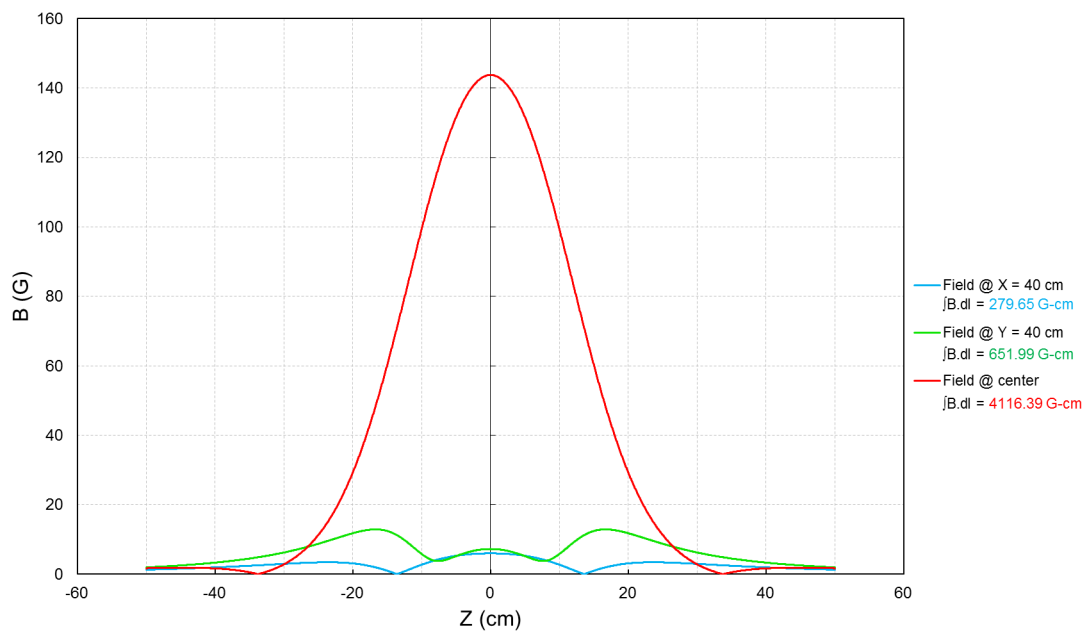


Figure B.5 QTOR qtor corrector field integral.

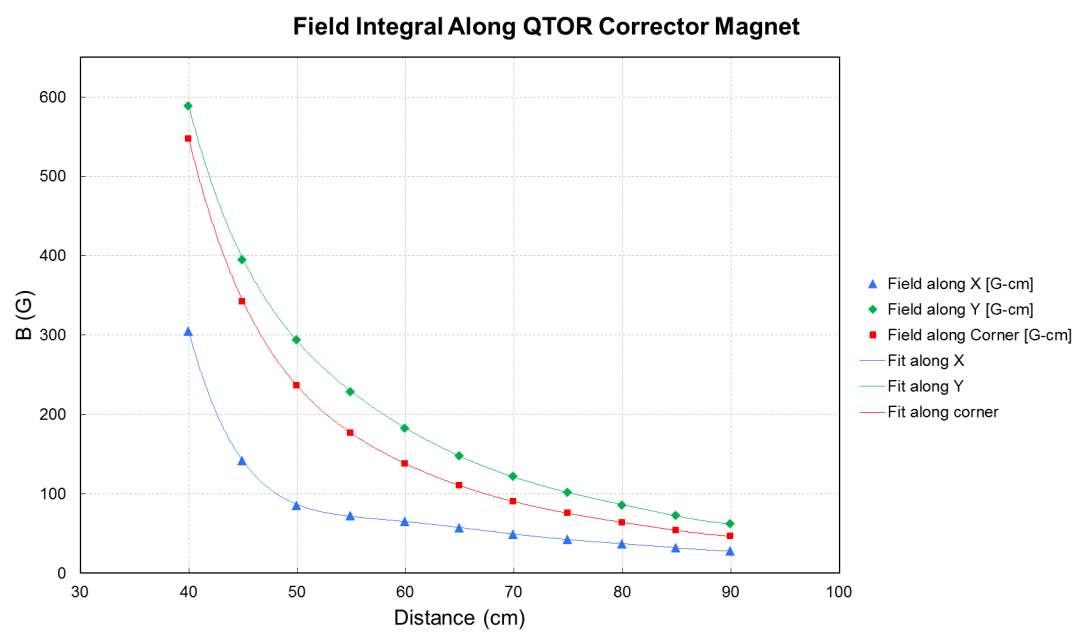


Figure B.6 QTOR qtor corrector field integral variation.

## APPENDIX C

### HELICITY CORRELATED PEDESTAL ANALYSIS

#### C.1 Background Detectors

Helicity correlated differences from Hel\_Tree and pedestal subtracted signals from Mps\_Tree for background detectors are shown here. All other plots for individual channels, and run by run plots grouped by wien can be found in [158].

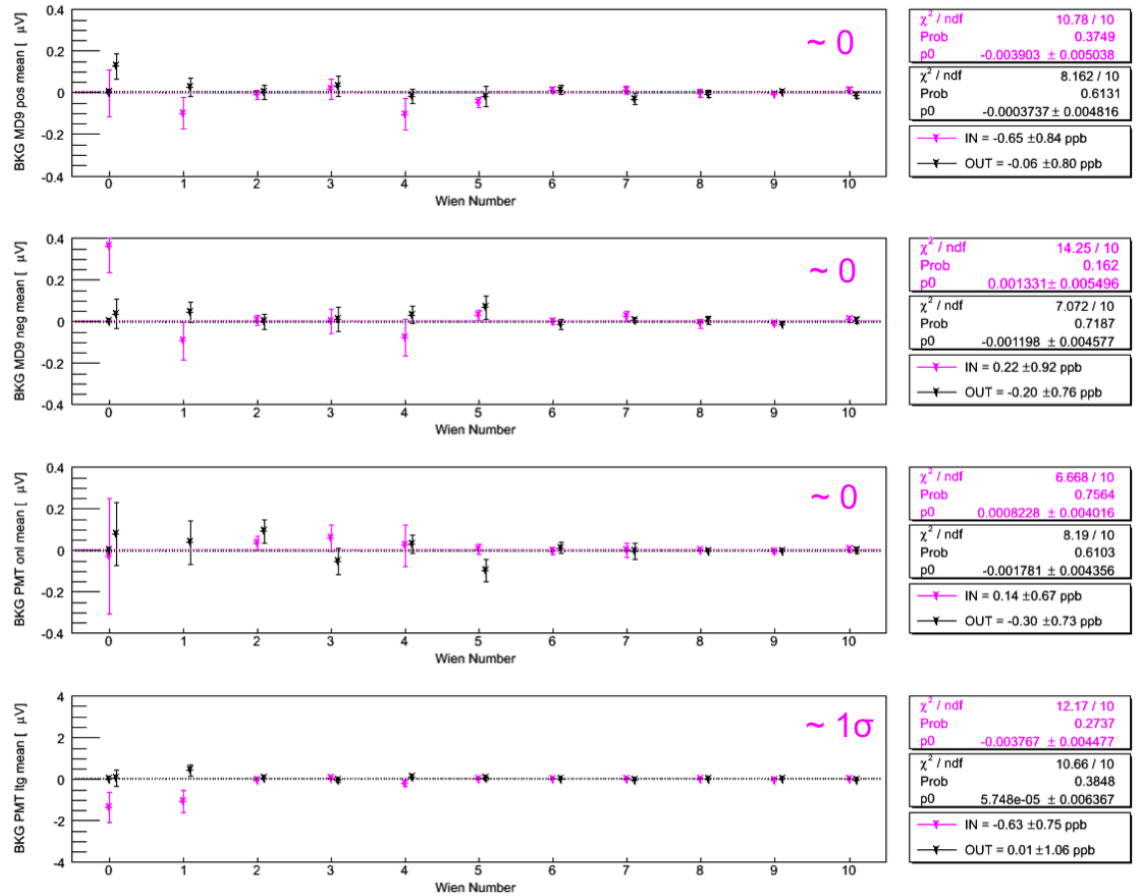


Figure C.1 Mean of the helicity correlated differences for MD9 pos, MD9 neg, PMT onl, and PMT ltg are shown in the figure (top to bottom). Helicity correlated differences for these important background detectors from Hel\_Tree are zero within  $\sim 1\sigma$  for averaged over each wien.

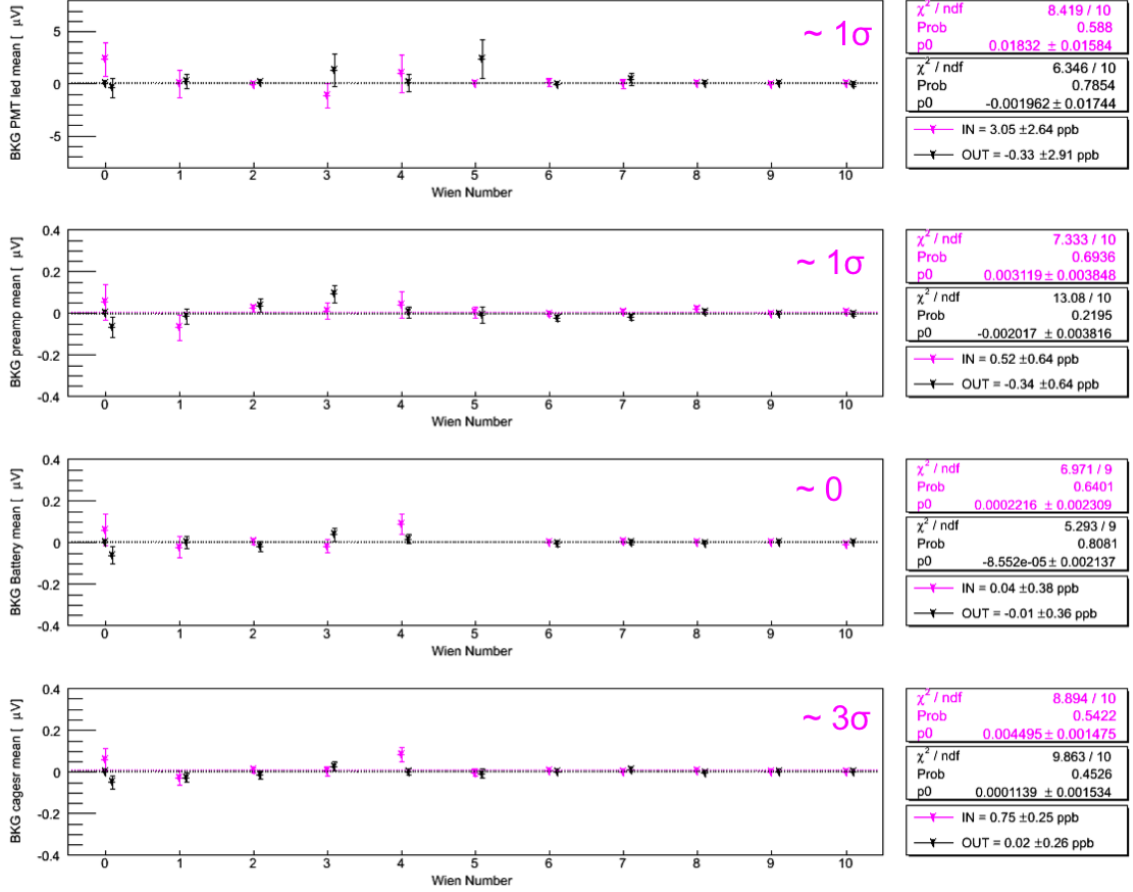


Figure C.2 Mean of the helicity correlated differences for PMT led, preamp, battery, and cages source are shown in the figure (top to bottom). Helicity correlated differences for these important background detectors from Hel\_Tree are zero within  $\sim 3\sigma$  for averaged over each wien.

## C.2 Helicity Corelated Pedestal Analysis

Helicity is the projection of the spin  $\vec{S}$  onto the direction of momentum.

$$\vec{h} = \vec{J} \cdot \hat{p} = \vec{L} \cdot \hat{p} + \vec{S} \cdot \hat{p} = \vec{S} \cdot \hat{p} \quad (\text{C.2.1})$$

### C.2.1 Condition of Experimental Data Taking

- Dedicated pedestal runs: Typically 5 minutes dedicated beam off pedestal run were taken with production running once a day during Run 1 and once a shift during Run 2. There were also  $\sim 1$  hour long beam off pedestal runs taken throughout, whenever there was an opportunity.
- Target - LH2 , Al, No target: Most of the pedestal runs are with LH2 target, but there were significant number of Al pedestal runs. There were few runs without target and while the target was moving.

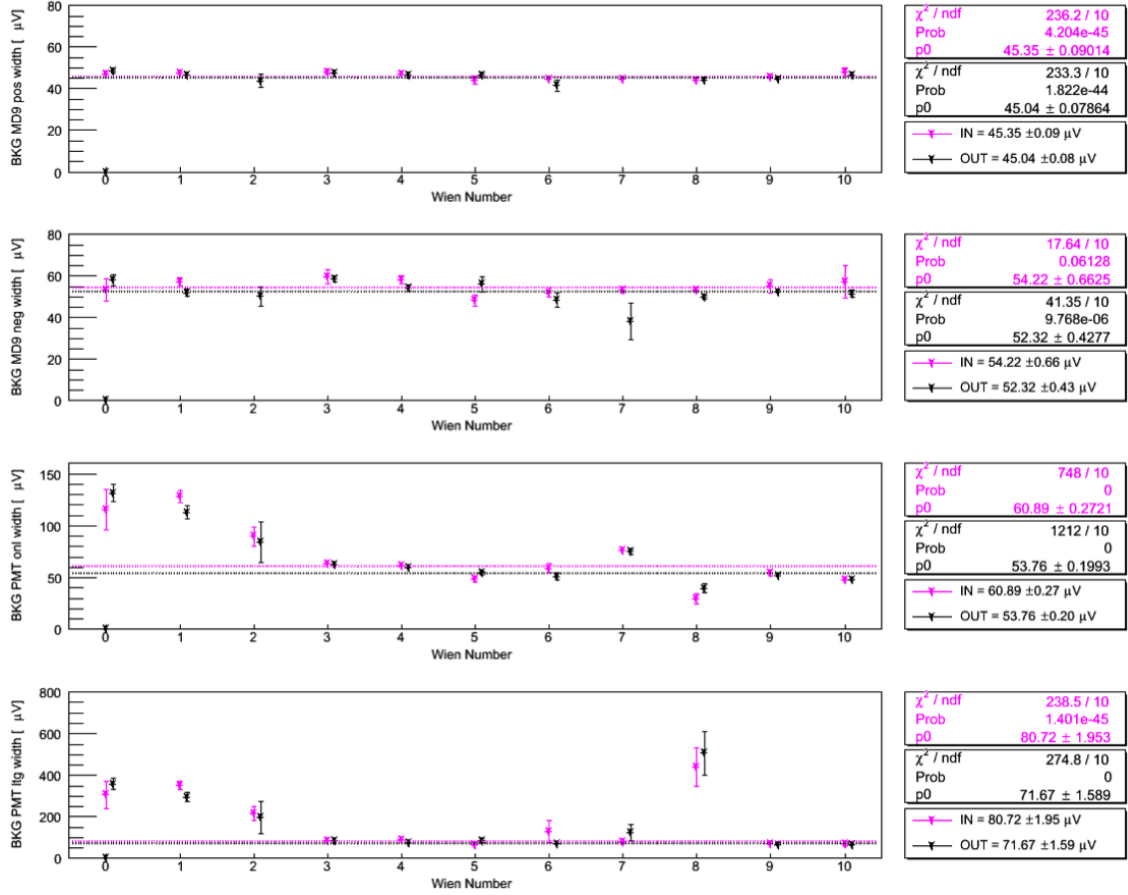


Figure C.3 Width of the helicity correlated differences for MD9 pos, MD9 neg, PMT onl, and PMT ltg are shown in the figure (top to bottom).

- Beam OFF: Only beam off pedestal runs were included in this analysis. There were several runs marked as pedestal in the HCLOG that didn't pass the standard beam current cuts (details in C.2.2), meaning they had some beam and hence were excluded from this analysis. More details has been presented in [159, 160].

### C.2.2 Condition of This Analysis

- Analyzer version: 4024 (12th February 2012 14:06:42).
- Beam current cut (global): -10 to 1  $\mu\text{A}$ .
- Effective charge cut (global) on BPM 3h09 and 3c12: -100000 to 25000.
- Turned OFF normalization: The main detectors and luminosity monitors are normalized to the charge monitors for nominal parity analysis so it is important that neither have any evidence of helicity correlated pedestal differences. Hence, MD and Lumi normalization were turned off during pedestal analysis.
- Hel\_Tree and Mps\_Tree: Helicity correlated differences were taken from Hel\_Tree and raw pedestal signal from Mps\_Tree.

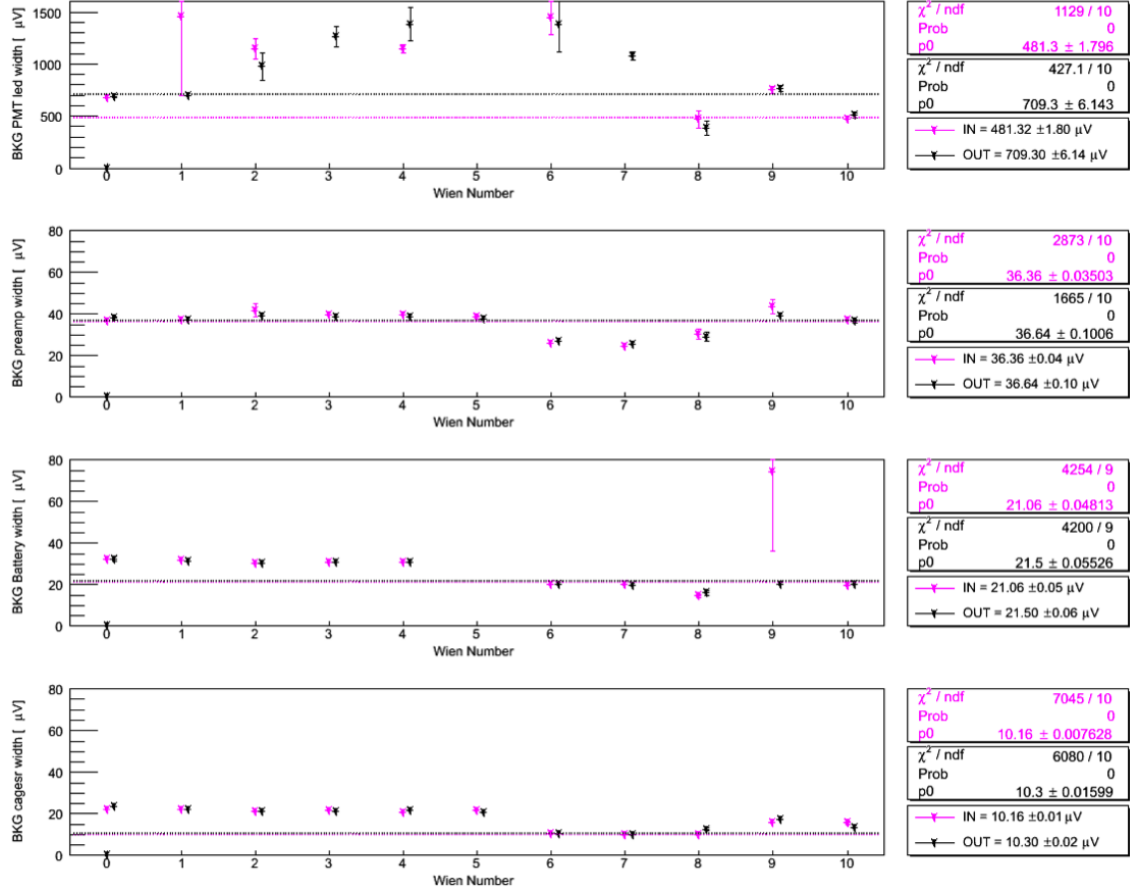


Figure C.4 Width of the helicity correlated differences for PMT led, preamp, battery, and cages source are shown in the figure (top to bottom).

- Turned OFF Data Base update.
- Turned OFF blinding factor for this analysis keeping the integrity of the experiment. [161]

### C.2.3 Configuration

The following command has been used for this analysis using standard Q-weak analyzer.

`qparity -r 18974 -c pedestal_ifarm.conf` (C.2.2)

here 18974 is run number and pedestal\_ifarm.conf is configuration file and has following configurations:

```
chainfiles = yes
single-output-file = yes
```

```

detectors = detectors_pedestal.map
codofile-stem = QwRun_
codofile-ext = log
QwMainCerenkovDetector.normalize = no
QwLumi.normalize = no
rootfile-stem = Qweak_Hel_Ped_Ana_
enable-differences = yes
disable-histos = yes
blinder.force-target-out = yes
disable-slow-tree = yes
disable-burst-tree = yes
disable-by-type = QwScanner
disable-by-type = QwBeamMod
enable-tree-trim = yes
QwDatabase.accesslevel = OFF

```

## C.2.4 List of Variables

The list of variables included in this analysis are shown below. The variables are used are diff\_qwk\_VARIABLE\_NAME from Hel\_Tree of standard Q-weak rootfiles.

### C.2.4.1 Main Cerenkov Detector(17)

mdallbars, md1pos, md2pos, md3pos, md4pos, md5pos, md6pos, md7pos, md8pos, md1neg,  
md2neg, md3neg, md4neg, md5neg, md6neg, md7neg, md8neg.

### C.2.4.2 Downstream Luminosity Detector(9)

dslumi\_sum, dslumi1, dslumi2, dslumi3, dslumi4, dslumi5, dslumi6, dslumi7, dslumi8.

### C.2.4.3 Upstream Luminosity Detector(9)

uslumi\_sum, uslumi1pos, uslumi3pos, uslumi5pos, uslumi7pos, uslumi1neg, uslumi3neg, uslumi5neg,  
uslumi7neg.

#### C.2.4.4 Beam Current Monitor(9)

charge<sup>1</sup>, bcm1, bcm2, bcm5, bcm6, bcm7, bcm8, bcmgl1, bcmgl2.

### C.2.5 List of Runs

List of dedicated pedestal runs included in this analysis are shown in this chapter. The data taken during time period from 31st January 2011 to 17th May 2012.

#### C.2.5.1 Wien 0

9593 9546 9539 9510 9483 9469 9456 9436 9407 9394 9354 9353 9352 9314 9303 9288 9205 9131  
9129 9098 9095 9067 9028 9027 9026

#### C.2.5.2 Wien 1

10182 10168 10150 10133 10105 10092 10087 10083 10082 10077 10066 10060 10026 9979 9972  
9970

#### C.2.5.3 Wien 2

11123 11106 11089 11067 11066 11053 11050 11049 11032 10997 10974 10969 10954 10953 10945  
10920 10916 10902 10892 10891 10890 10889 10887 10886 10822 10805 10802 10799 10797 10782  
10781 10743 10730 10720 10716 10711 10708 10705 10702 10699 10288 10287 10252 10239 10229  
10201

#### C.2.5.4 Wien 3

11380 11343 11304 11289 11285 11274 11264 11255 11246 11238 11229 11215 11211 11206 11189  
11177 11166 11164 11160 11146 11131

#### C.2.5.5 Wien 4

11691 11690 11670 11668 11661 11648 11633 11608 11585 11574 11555 11529 11444 11422

---

<sup>1</sup>charge = bcm1+bcm2 for Run-I and = bcm8 for most of Run-II.

**C.2.5.6 Wien 5**

11715 11712 11691 11690 11670 11668 11661 11648 11633 11608 11585 11574 11555 11529 11444  
 11422 11380 11343 11304 11289 11285 11274 11264 11255 11246 11238 11229 11215 11211 11206  
 11189 11177 11166 11164 11160 11146 11131 11130 11123

**C.2.5.7 Wien 6**

14209 14206 14205 14147 14125 14124 14120 14102 14091 14064 14063 14062 14061 14060 14059  
 14058 14057 14041 14040 14039 14038 14037 14036 14035 14034 14025 13987 13986 13971 13969  
 13968 13967 13966 13928 13927 13926 13925 13924 13914 13895 13888 13886 13859 13858

**C.2.5.8 Wien 7**

14683 14675 14674 14669 14631 14595 14568 14567 14564 14561 14552 14530 14529 14528 14527  
 14524 14466 14464 14452 14449 14440 14430 14384 14326 14325 14324 14322 14308

**C.2.5.9 Wien 8**

15980 15919 15913 15904 15888 15887 15877 15876 15817 15797 15766 15746 15708 15706 15699  
 15694 15676 15660 15659 15658 15657 15656 15645 15639 15638 15637 15624 15623 15618 15599  
 15591 15515 15514 15493 15488 15487 15420 15418 15417 15401 15400 15396 15395 15362 15359  
 15349 15338 15337 15321 15313 15311 15227 15247 15228 15214 15213 15176 15169

**C.2.5.10 Wien 9**

16207 16259 16329 16330 16368 16374 16387 16388 16391 16394 16395 16397 16398 16399 16400  
 16403 16404 16407 16420 16424 16425 16428 16446 16449 16454 16460 16465 16517 16518 16519  
 16520 16521 16522 16523 16581 16582 16583 16593 16595 16598 16606 16616 16619 16620 16626  
 16642 16643 16644 16719 16721 16736 16738 16739 16740 16742 16743 16764 16785 16797 16799  
 16810 16813 16814 16815 16816 16817 16818 16819 16830 16890 16907 16908 16909 16910 16911  
 16915 16921 16926 16934 16945 16950 16966 16967 16981 16988 16989 17000 17001 17002 17003  
 17004 17005 17006 17007 17018 17020 17021 17022 17023 17024 17028 17042 17043 17044 17045  
 17046 17047 17048 17049 17050 17051 17052 17093 17094 17095 17096 17097 17098 17099 17102  
 17103 17104 17105 17106 17107 17108 17109 17110 17144 17145 17146 17160 17165 17167 17173  
 17174 17190 17193 17194 17195 17200 17204 17222 17257 17284 17310 17332 17333 17346 17347  
 17348 17349 17350 17351 17352 17353 17354 17355 17356 17357 17358 17359 17360 17361 17362

17363 17364 17365 17366 17367 17368 17369 17374 17375 17399 17414 17460 17462 17464 17467  
17469 17470 17631 17633 17634 17635 17636 17646 17650 17677 17682 17696 17708 17711 17715  
17718 17723 17753 17801 17868 17869 17870 17890 17891 17957 17958 18001 18002 18003 18005  
18028 18031 18043 18045 18069 18103 18115 18137 18150 18155 18160 18170 18179 18192 18206  
18227 18230 18237 18259 18281 18288 18321 18327 18330 18373 18419 18422 18447 18448

#### C.2.5.11 Wien 10

18587 18588 18589 18590 18606 18611 18612 18644 18676 18677 18678 18679 18680 18681 18682  
18683 18684 18685 18713 18719 18724 18727 18730 18733 18736 18739 18742 18743 18801 18815  
18818 18831 18832 18847 18848 18851 18852 18855 18856 18863 18864 18865 18868 18869 18870  
18871 18872 18874 18875 18876 18877 18878 18879 18880 18881 18885 18899 18900 18902 18909  
18910 18928 18930 18935 18942 18944 18951 18952 18953 18972 18973 18974

## APPENDIX D

### BEAM NORMAL SINGLE SPIN ASYMMETRY IN INELASTIC E-P SCATTERING

#### D.1 Condition of Experimental Data Taking

Run Conditions:

- Transverse N-to- $\Delta$  production runs: Typically one hour dedicated transverse run were taken with production running condition during Run-II.
- Target -  $LH_2$ , 4% DS Al, Carbon: Most of the production runs are with  $LH_2$  target, but there were significant number of Aluminum and few Carbon runs. The existing data set are shown in Figure ??
- Beam current:
  - For  $LH_2$ : 180  $\mu$ A.
  - For 4% DS Al: 60  $\mu$ A.
  - For Carbon :75  $\mu$ A.
- QTor current settings: 6000, 6700 $^\dagger$ , 7300 A.
- Beam raster dimension: 4x4 mm $^2$ .
- Beam energy: 1.155 GeV.

Analysis Conditions:

- From run2\_pass5 data base.
- Standard data base cuts: Only declared GOOD data, no additional cuts applied.
- Regressed with on\_5+1, set3, set4, set7, set8, set9, set10 and set11 schemes. (md9 regression failed for  $LH_2$  horizontal transverse)

This analysis includes:

- Data taken: 16th February 2012 - 20th February 2012
- Preliminary main detector asymmetries, sensitivities, yields, position, angle, energy, differences. charge asymmetries.

## D.2 Uncertainty in Physics Asymmetries

$$(dA_{PHYS}^{in})_{A_M^{in}} = R_{RC} R_{Det} R_{Bin} R_{Q^2} \frac{dA_M^{in}}{P} \left[ \frac{1}{1 - f_{b1} - f_{b2} - f_{b3} - f_{b4}} \right] \quad (\text{D.2.1})$$

$$(dA_{PHYS}^{in})_P = R_{RC} R_{Det} R_{Bin} R_{Q^2} \frac{A_M^{in}}{P} \frac{dP}{P} \left[ \frac{1}{1 - f_{b1} - f_{b2} - f_{b3} - f_{b4}} \right] \quad (\text{D.2.2})$$

$$(dA_{PHYS}^{in})_{A_{b1}} = R_{RC} R_{Det} R_{Bin} R_{Q^2} \left[ \frac{-dA_{b1}f_{b1}}{1 - f_{b1} - f_{b2} - f_{b3} - f_{b4}} \right] \quad (\text{D.2.3})$$

$$(dA_{PHYS}^{in})_{A_{b2}} = R_{RC} R_{Det} R_{Bin} R_{Q^2} \left[ \frac{-dA_{b2}f_{b2}}{1 - f_{b1} - f_{b2} - f_{b3} - f_{b4}} \right] \quad (\text{D.2.4})$$

$$(dA_{PHYS}^{in})_{A_{b3}} = R_{RC} R_{Det} R_{Bin} R_{Q^2} \left[ \frac{-dA_{b3}f_{b3}}{1 - f_{b1} - f_{b2} - f_{b3} - f_{b4}} \right] \quad (\text{D.2.5})$$

$$(dA_{PHYS}^{in})_{A_{b4}} = R_{RC} R_{Det} R_{Bin} R_{Q^2} \left[ \frac{-dA_{b4}f_{b4}}{1 - f_{b1} - f_{b2} - f_{b3} - f_{b4}} \right] \quad (\text{D.2.6})$$

$$(dA_{PHYS}^{in})_{f_{b1}} = R_{RC} R_{Det} R_{Bin} R_{Q^2} df_{b1} \left[ \frac{\frac{A_M^{in}}{P} - A_{b1}(1 - f_{b2} - f_{b3} - f_{b4}) - A_{b2}f_{b2} - A_{b3}f_{b3} - A_{b4}f_{b4}}{(1 - f_{b1} - f_{b2} - f_{b3} - f_{b4})^2} \right] \quad (\text{D.2.7})$$

$$(dA_{PHYS}^{in})_{f_{b2}} = R_{RC} R_{Det} R_{Bin} R_{Q^2} df_{b2} \left[ \frac{\frac{A_M^{in}}{P} - A_{b1}f_{b1} - A_{b2}(1 - f_{b1} - f_{b3} - f_{b4}) - A_{b3}f_{b3} - A_{b4}f_{b4}}{(1 - f_{b1} - f_{b2} - f_{b3} - f_{b4})^2} \right] \quad (\text{D.2.8})$$

$$(dA_{PHYS}^{in})_{f_{b3}} = R_{RC} R_{Det} R_{Bin} R_{Q^2} df_{b3} \left[ \frac{\frac{A_M^{in}}{P} - A_{b1}f_{b1} - A_{b2}f_{b2} - A_{b3}(1 - f_{b1} - f_{b2} - f_{b4}) - A_{b4}f_{b4}}{(1 - f_{b1} - f_{b2} - f_{b3} - f_{b4})^2} \right] \quad (\text{D.2.9})$$

$$(dA_{PHYS}^{in})_{f_{b4}} = R_{RC} R_{Det} R_{Bin} R_{Q^2} df_{b4} \left[ \frac{\frac{A_M^{in}}{P} - A_{b1}f_{b1} - A_{b2}f_{b2} - A_{b3}f_{b3} - A_{b4}(1 - f_{b1} - f_{b2} - f_{b3})}{(1 - f_{b1} - f_{b2} - f_{b3} - f_{b4})^2} \right] \quad (\text{D.2.10})$$

Table D.1 Systematic error table.

Error from	Uncertainty [ppm]	Relative uncertainty [%]
$A_M^{in}$	2.36	5.9
P	0.26	0.7
$A_{b1}$	0.17	0.4
$A_{b2}$	0.55	1.4
$A_{b3}$	0.02	0.1
$A_{b4}$	0.47	1.2
$f_{b1}$	0.30	0.7
$f_{b2}$	0.13	0.3
$f_{b3}$	1.70	4.3
$f_{b4}$	13.96	35.2
$R_{RC}$	0.00	0.0
$R_{Det}$	0.00	0.0
$R_{Bin}$	0.00	0.0
$R_{Q^2}$	1.19	3.0
Total	14.33	36.1

### D.3 Corrections

### D.4 Barsum vs PMTavg Asymmetries

Different ways to calculate the asymmetries. In case of barsum asymmetries we match gain of PMTs and then sum their yields and form asymmetries, whereas PMTavg asymmetries were formed as individual PMT asymmetries and then averaged. PMTavg and barsum asymmetries are shown in section 5.4.4 and ?? respectively.

Table D.2 Barsum and PMTavg asymmetries.

Asymmetries	Barsum [ppm]	PMTavg [ppm]	Difference [ppm]
$A_M^H$	5.34291	5.34293	0.00002
$A_M^V$	4.52568	4.52522	0.00046

Barsum and PMTavg asymmetries match within  $\sim 0.0005$  ppm.

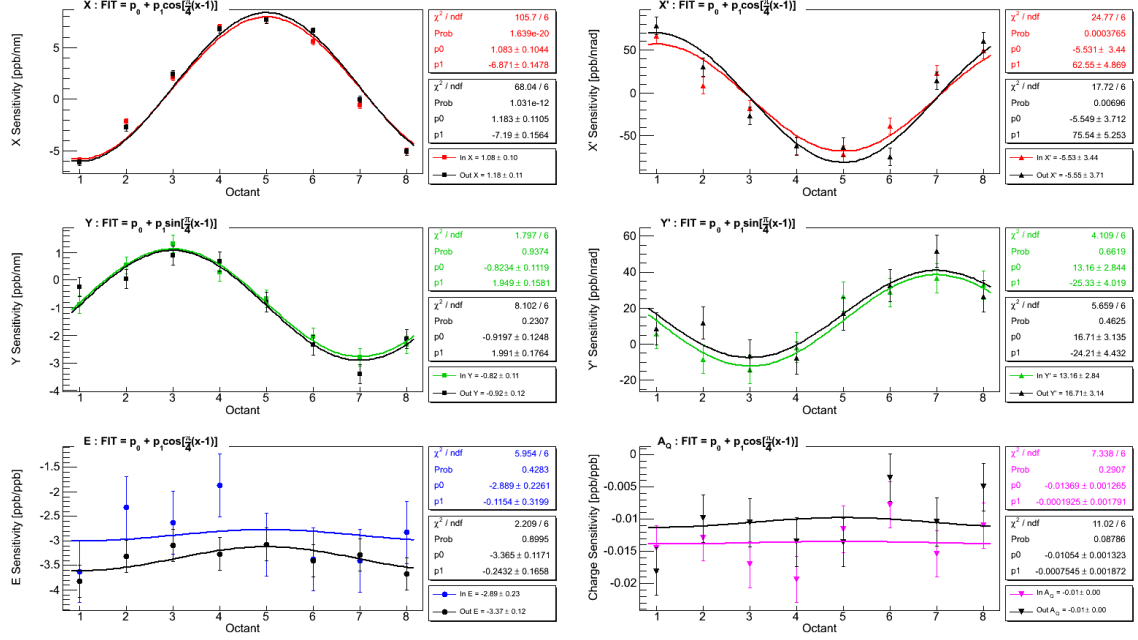


Figure D.1 Main detector octant sensitivities with respect to 5+1 regression scheme for horizontal transverse data set are shown here. Azimuthal dependence of the detector sensitivities to HCBA in the horizontal LH<sub>2</sub> transverse data set. Beam positions and angles have sinusoidal dependence with octant. No such dependence is seen for energy and charge. Two IHWP states are shown separately for each beam parameter. Fit functions used are also shown on the plot. The constant in the fit gives the error weighted average sensitivities. See APPENDIX-D, section D.3 for the sensitivities and corrections from all data sets.

Table D.3 MD Sensitivities for X and Y.

Detector	$\frac{\partial A}{\partial X}$ [ppb/nm]		$\frac{\partial A}{\partial Y}$ [ppb/nm]	
	HWP-IN	HWP-OUT	HWP-IN	HWP-OUT
MD1	-5.91±0.29	-6.13±0.31	-0.88±0.29	-0.25±0.35
MD2	-2.16±0.29	-2.74±0.31	0.53±0.29	0.04±0.35
MD3	2.10±0.29	2.44±0.31	1.32±0.29	0.89±0.35
MD4	6.98±0.30	6.74±0.32	0.29±0.30	0.67±0.36
MD5	7.66±0.30	7.66±0.32	-0.67±0.30	-0.80±0.36
MD6	5.57±0.29	6.58±0.31	-2.05±0.30	-2.35±0.35
MD7	-0.58±0.30	-0.01±0.31	-2.79±0.30	-3.41±0.35
MD8	-4.98±0.29	-5.08±0.31	-2.34±0.29	-2.14±0.35

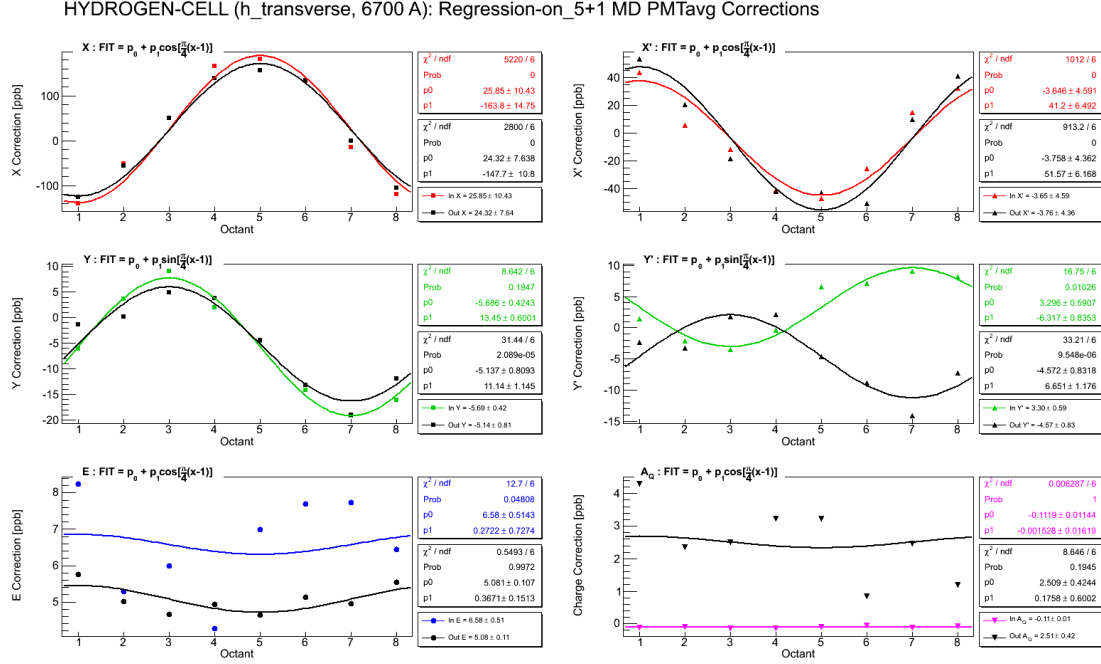


Figure D.2 Main detector correction vs octant using to 5+1 regression scheme and differences for horizontal transverse data set are shown here. Azimuthal dependence of the corrections in the horizontal LH<sub>2</sub> transverse data set. Beam positions and angles have sinusoidal dependence with octant. No such dependence is seen for energy and charge. Two IHWP states are shown separately for each beam parameter.

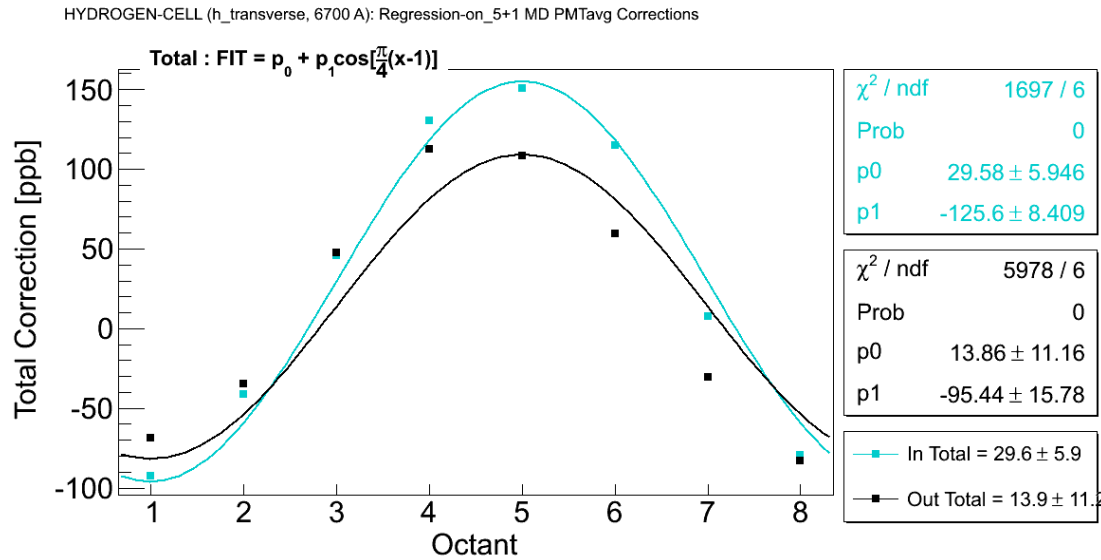


Figure D.3 Total correction vs octant using to 5+1 regression scheme and differences for horizontal transverse data set are shown here.

HYDROGEN-CELL (h\_transverse, 6700 A): Regression-on\_5+1 Beam Parameter Differences.

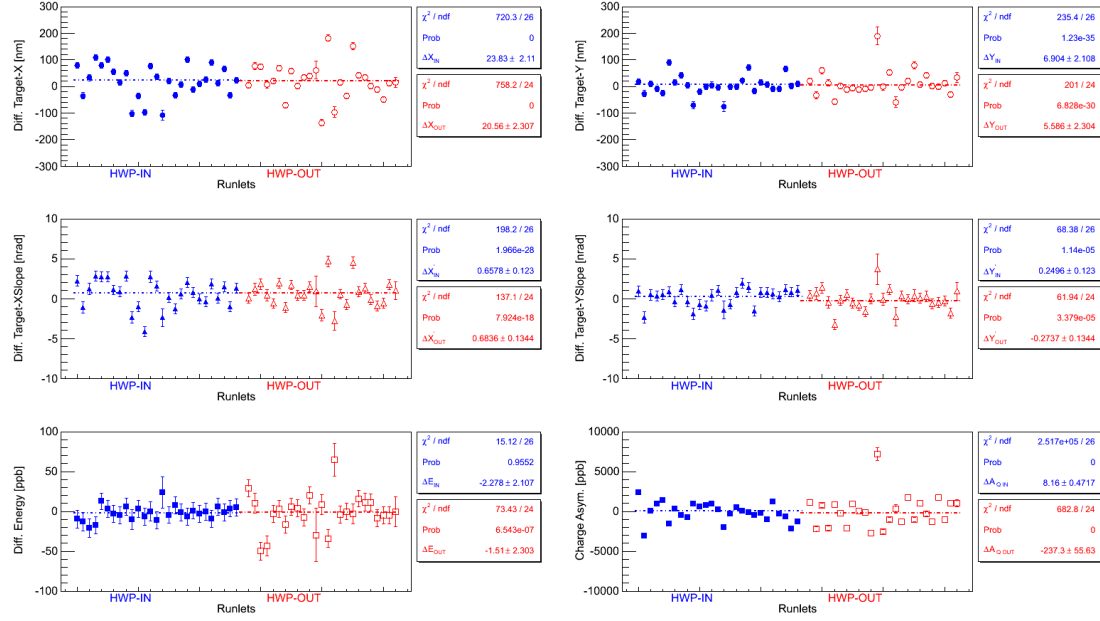


Figure D.4 Beam position differences for horizontal transverse data set.

HYDROGEN-CELL (v\_transverse, 6700 A): Regression-on\_5+1 Beam Parameter Differences.

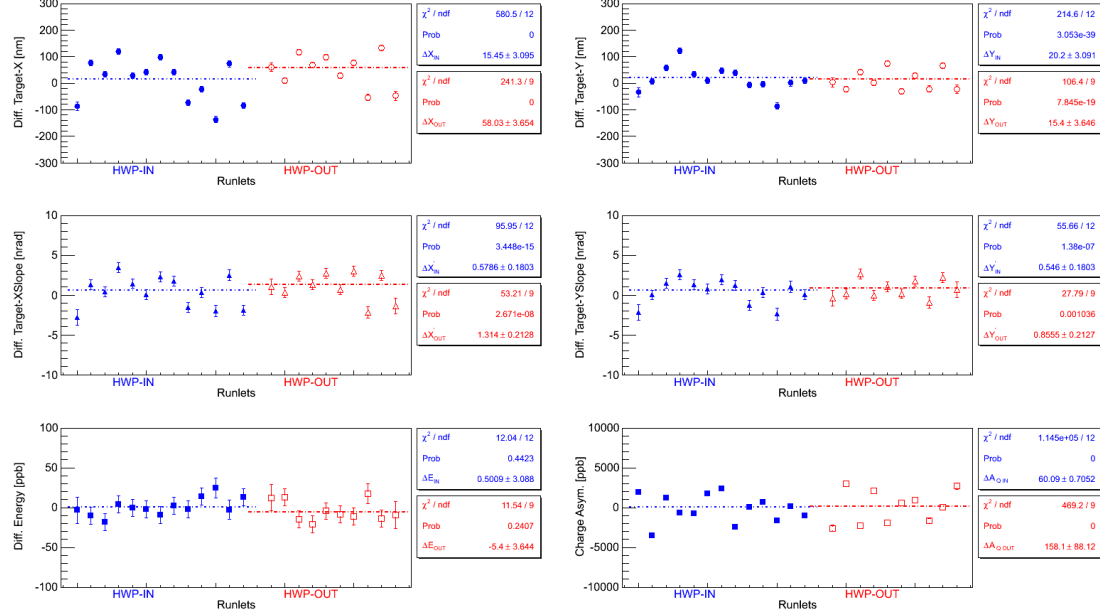


Figure D.5 Beam position differences for vertical transverse data set.

Table D.4 MD Sensitivities for  $X'$  and  $Y'$ .

Detector	$\frac{\partial A}{\partial X'}$ [ppb/nrad]		$\frac{\partial A}{\partial Y'}$ [ppb/nrad]	
	HWP-IN	HWP-OUT	HWP-IN	HWP-OUT
MD1	66.31±9.71	78.33±10.48	5.54±8.03	8.56±8.85
MD2	8.61±9.67	30.13±10.44	-8.33±8.00	11.81±8.82
MD3	-18.33±9.71	-26.87±10.50	-14.08±8.032	-6.59±8.87
MD4	-62.14±9.83	-61.88±10.58	-1.82±8.13	-7.78±8.94
MD5	-71.83±9.82	-63.13±10.60	26.31±8.12	16.87±8.95
MD6	-38.80±9.71	-74.72±10.48	28.69±8.03	32.50±8.85
MD7	22.40±9.76	14.19±10.53	36.49±8.068	51.75±8.90
MD8	49.43±9.62	59.98±10.39	32.82±7.96	26.52±8.78

Table D.5 MD Sensitivities for E and  $A^Q$ .

Detector	$\frac{\partial A}{\partial E}$ [ppb/ppb]		$\frac{\partial A}{\partial A_Q}$ [ppb/ppb]	
	HWP-IN	HWP-OUT	HWP-IN	HWP-OUT
MD1	-3.62±0.64	-3.82±0.33	-0.0146±0.0036	-0.0181±0.0037
MD2	-2.32±0.64	-3.32±0.33	-0.0129±0.0036	-0.0099±0.0037
MD3	-2.63±0.64	-3.09±0.33	-0.0171±0.0036	-0.0105±0.0037
MD4	-1.87±0.65	-3.27±0.33	-0.0194±0.0036	-0.0135±0.0038
MD5	-3.07±0.65	-3.07±0.33	-0.0116±0.0036	-0.0136±0.0038
MD6	-3.38±0.64	-3.40±0.33	-0.0078±0.0036	-0.0036±0.0037
MD7	-3.40±0.64	-3.28±0.33	-0.0154±0.0036	-0.0104±0.0038
MD8	-2.83±0.63	-3.67±0.33	-0.0110±0.0035	-0.0050±0.0037

Table D.6 Regression scheme dependence of measured main detector transverse asymmetry from Run 2 Pass 5 for vertical transverse polarization.

Regression scheme	$A_M$ [ppm]	$\phi_0$ [degree]	C [ppm]	$\chi^2/\text{DOF}$	Prob.
UnReg	4.602 ± 0.807	-9.660 ± 10.042	-1.078 ± 0.571	0.316	0.904
std	4.524 ± 0.806	-9.945 ± 10.211	-1.073 ± 0.570	0.323	0.899
5+1	4.525 ± 0.806	-10.016 ± 10.208	-1.069 ± 0.570	0.321	0.900
set3	4.525 ± 0.806	-10.016 ± 10.208	-1.069 ± 0.570	0.321	0.900
set4	4.527 ± 0.806	-10.017 ± 10.205	-1.068 ± 0.570	0.322	0.900
set7	4.529 ± 0.806	-9.899 ± 10.199	-1.069 ± 0.570	0.320	0.901
set8	4.531 ± 0.806	-9.969 ± 10.196	-1.065 ± 0.570	0.319	0.902
set9	<del>4.534 ± 0.806</del>	<del>-9.872 ± 10.185</del>	<del>-1.612 ± 0.570</del>	<del>0.317</del>	<del>0.903</del>
set10	4.526 ± 0.806	-10.013 ± 10.208	-1.069 ± 0.570	0.321	0.900
set11	4.524 ± 0.806	-9.945 ± 10.211	-1.073 ± 0.570	0.323	0.899

## D.5 Detector Sensitivities

## D.6 Regression Scheme Dependence

### D.6.1 Regression Time Dependence

### D.6.2 Cut Dependence

Table D.7 Regression scheme dependence of measured main detector transverse asymmetry from Run-II Pass5 for horizontal transverse polarization.

Regression scheme	$A_M$ [ppm]	$\phi_0$ [degree]	C [ppm]	$\chi^2/\text{DOF}$	Prob.
UnReg	$5.339 \pm 0.533$	$6.826 \pm 5.729$	$-0.287 \pm 0.377$	1.320	0.252
std	$5.343 \pm 0.533$	$7.089 \pm 5.720$	$-0.289 \pm 0.377$	1.333	0.247
5+1	$5.343 \pm 0.532$	$7.081 \pm 5.720$	$-0.289 \pm 0.377$	1.332	0.247
set3	$5.343 \pm 0.532$	$7.081 \pm 5.720$	$-0.289 \pm 0.377$	1.332	0.247
set4	$5.343 \pm 0.532$	$7.088 \pm 5.720$	$-0.289 \pm 0.377$	1.332	0.247
set7	$5.347 \pm 0.533$	$7.007 \pm 5.716$	$-0.288 \pm 0.377$	1.334	0.246
set8	$5.346 \pm 0.532$	$6.999 \pm 5.716$	$-0.288 \pm 0.377$	1.334	0.246
set9	$5.343 \pm 0.532$	$7.154 \pm 5.719$	$-0.376 \pm 0.377$	1.343	0.243
set10	$5.343 \pm 0.532$	$7.085 \pm 5.720$	$-0.289 \pm 0.377$	1.332	0.247
set11	$5.343 \pm 0.533$	$7.089 \pm 5.720$	$-0.289 \pm 0.377$	1.333	0.247

Table D.8 Correction on measured main detector transverse asymmetry from Run-II Pass5 due to regression scheme dependence.

Regression scheme	Vertical Correction [ppm]	Horizontal Correction [ppm]
std	0.078	0.004
5+1	0.077	0.004
set3	0.077	0.004
set4	0.076	0.004
set7	0.073	0.007
set8	0.072	0.007
set9	0.069	0.003
set10	0.077	0.003
set11	0.078	0.004
Max-Min	0.006	0.004

Table D.9 Regression time dependence.

Polarization	Runlet based $A_M^{\text{runlet}}$ [ppm]	Slug based $A_M^{\text{slug}}$ [ppm]	$A_M^{\text{runlet}} - A_M^{\text{slug}}$ [ppm]
Horizontal	5.3432	5.3492	0.0060
Vertical	4.5252	4.5171	0.0081

Table D.10 Cut dependence.

Cut	Horizontal		Vertical	
	Allowed Statistical Shift [ppm]	$A_M^H$ Cut - NoCut [ppm]	Allowed Statistical Shift [ppm]	$A_M^V$ Cut - NoCut [ppm]
7,6,5,4 $\sigma$	0.000	0.000	0.000	0.000
3 $\sigma$	0.001	0.024	0.000	0.000
2.5 $\sigma$	0.026	-0.064	0.021	-0.068
2 $\sigma$	0.082	0.107	0.142	0.367

HYDROGEN-CELL (6700 A): MD Regressed (on\_5+1) Asymmetry. Cut Dependence for Individual Parameters. Horizontal Transverse.

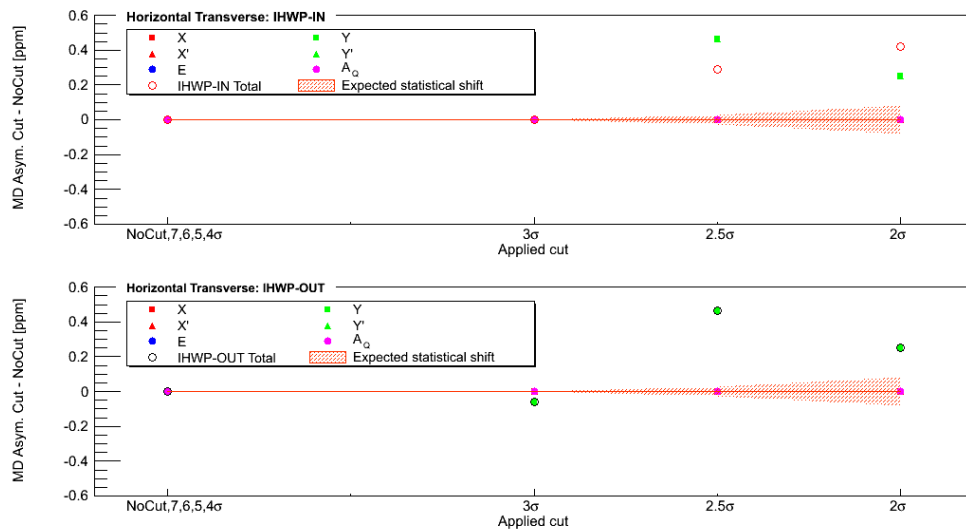


Figure D.6 Cut dependence for horizontal transverse.

HYDROGEN-CELL (6700 A): MD Regressed (on\_5+1) Asymmetry. Cut Dependence for Individual Parameters. Vertical Transverse.

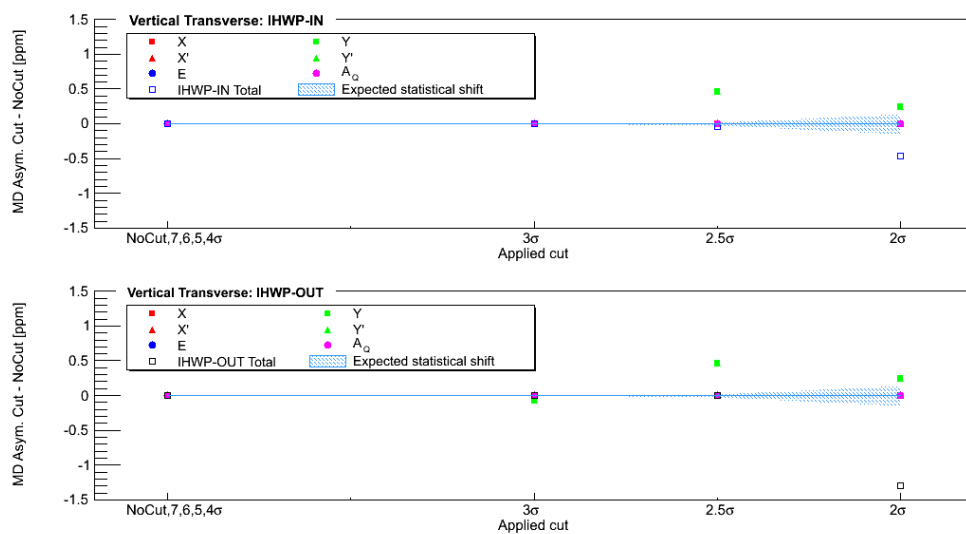


Figure D.7 Cut dependence for vertical transverse.

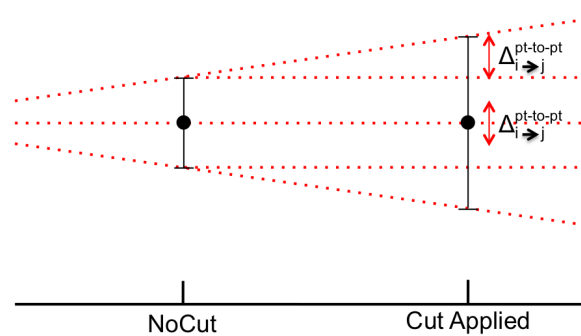


Figure D.8 Cut dependence cartoon.

## APPENDIX E

### MISCELLANEOUS

#### E.1 Target BPM Angle Resolution

The objective is to estimate the effective target angle resolution using a position measurement at a upstream BPM. \* Ideally want to find a model location where angle jitter at the target corresponds to pure position at the upstream BPM. \* With known BPM position resolution, effective target angle resolution can be estimated.

Target angle resolution using 3P02A is better than the angle resolution we have now.

Incorporating BPM 3P02A into a regression scheme might be a good idea.

Note: A study of strength sharing between angle and position in the various BPM's along the beamline (similar to Don's study at ELOG 856) for wien0 (two runs from each slug) seems to show Compton BPMs (3P02A & B) were insensitive to position on target.

OPTIM confirms that the Compton region should have appropriate optics for UVA?`s angle-sensitive BPM (i.e. angle jitter at the target is transformed to position jitter at the BPM).

\* With X (Y) BPM position resolution of 0.90 (0.96) ?m, the effective target angle resolution is estimated to be 0.048 (0.060) ?rad. This is better than the angle resolution we have now, so we encourage UVA?`s strategy of incorporating this BPM into a regression scheme.

## REFERENCES

- [1] Francis Halzen and Alan D. Martin. *Quarks and Leptons: An Introductory Course in Modern Particle Physics*. John Wiley and Sons, Inc., 1st edition, January 1984. (Cited on page 1.)
- [2] C.Y. Prescott, W.B. Atwood, R.L.A. Cottrell, H. DeStaebler, Edward L. Garwin, A. Gonidec, R.H. Miller, L.S. Rochester, T. Sato, D.J. Sherden, C.K. Sinclair, S. Stein, R.E. Taylor, J.E. Clendenin, V.W. Hughes, N. Sasao, K.P. Schler, M.G. Borghini, K. Lbelsmeyer, and W. Jentschke. Parity non-conservation in inelastic electron scattering. *Physics Letters B*, 77(3):347 – 352, 1978. (Cited on page 1.)
- [3] F.J. Hasert, S. Kabe, W. Krenz, J. Von Krogh, D. Lanske, J. Morfin, K. Schultze, H. Weerts, G.H. Bertrand-Coremans, J. Sacton, W. Van Doninck, P. Vilain, U. Camerini, D.C. Cundy, R. Baldi, I. Danilchenko, W.F. Fry, D. Haidt, S. Natali, P. Musset, B. Osculati, R. Palmer, J.B.M. Pattison, D.H. Perkins, A. Pullia, A. Rousset, W. Venus, H. Wachsmuth, V. Brisson, B. Degrange, M. Haguenauer, L. Kluberg, U. Nguyen-Khac, P. Petiau, E. Belotti, S. Bonetti, D. Cavalli, C. Conta, E. Fiorini, M. Rollier, B. Aubert, D. Blum, L.M. Chouinet, P. Heusse, A. Lagarrigue, A.M. Lutz, A. Orkin-Lecourtois, J.P. Vialle, F.W. Bullock, M.J. Esten, T.W. Jones, J. McKenzie, A.G. Michette, G. Myatt, and W.G. Scott. Observation of neutrino-like interactions without muon or electron in the gargamelle neutrino experiment. *Physics Letters B*, 46(1):138 – 140, 1973. (Cited on page 1.)
- [4] F.J. Hasert, H. Faissner, W. Krenz, J. Von Krogh, D. Lanske, J. Morfin, K. Schultze, H. Weerts, G.H. Bertrand-Coremans, J. Lemonne, J. Sacton, W. Van Doninck, P. Vilain, C. Baltay, D.C. Cundy, D. Haidt, M. Jaffre, P. Musset, A. Pullia, S. Natali, J.B.M. Pattison, D.H. Perkins, A. Rousset, W. Venus, H.W. Wachsmuth, V. Brisson, B. Degrange, M. Haguenauer, L. Kluberg, U. Nguyen-Khac, P. Petiau, E. Bellotti, S. Bonetti, D. Cavalli, C. Conta, E. Fiorini, M. Rollier, B. Aubert, L.M. Chouinet, P. Heusse, A. Lagarrigue, A.M. Lutz, J.P. Vialle, F.W. Bullock, M.J. Esten, T. Jones, J. McKenzie, A.G. Michette, G. Myatt, J. Pinfold, and W.G. Scott. Search for elastic muon-neutrino electron scattering. *Physics Letters B*, 46(1):121 – 124, 1973. (Cited on page 1.)
- [5] F.J. Hasert, S. Kabe, W. Krenz, J. Von Krogh, D. Lanske, J. Morfin, K. Schultze, H. Weerts, G. Bertrand-Coremans, J. Sacton, W. Van Doninck, P. Vilain, R. Baldi, U. Camerini, D.C. Cundy, I. Danilchenko, W.F. Fry, D. Haidt, S. Natali, P. Musset, B. Osculati, R. Palmer,

- J.B.M. Pattison, D.H. Perkins, A. Pullia, A. Rousset, W. Venus, H. Wachsmuth, V. Brisson, B. Degrange, M. Haguenauer, L. Kluberg, U. Nguyen-Khac, P. Petiau, E. Bellotti, S. Bonetti, D. Cavalli, C. Conta, E. Fiorini, M. Rollier, B. Aubert, D. Blum, L.M. Chouinet, P. Heusse, A. Lagarrigue, A.M. Lutz, A. Orkin-Lecourtois, J.P. Vialle, F.W. Bullock, M.J. Esten, T.W. Jones, J. McKenzie, A.G. Michette, G. Myatt, and W.G. Scott. Observation of neutrino-like interactions without muon or electron in the gargamelle neutrino experiment. *Nuclear Physics B*, 73(1):1 – 22, 1974. (Cited on page 1.)
- [6] MissMJ. Standard model of elementary particles. (free to use, original file created by user) Own work by uploader, PBS NOVA, Fermilab, Office of Science, United States Department of Energy, Particle Data Group. Licensed under Creative Commons Attribution 3.0 via Wikimedia Commons -[http://commons.wikimedia.org/wiki/File:Standard\\_Model\\_of\\_Elementary\\_Particles.svg#mediaviewer/File:Standard\\_Model\\_of\\_Elementary\\_Particles.svg](http://commons.wikimedia.org/wiki/File:Standard_Model_of_Elementary_Particles.svg#mediaviewer/File:Standard_Model_of_Elementary_Particles.svg), 2014. (Cited on page 2.)
- [7] G. W. Bennett, B. Bousquet, H. N. Brown, G. Bunce, R. M. Carey, P. Cushman, G. T. Danby, P. T. Debevec, M. Deile, H. Deng, S. K. Dhawan, V. P. Druzhinin, L. Duong, F. J. M. Farley, G. V. Fedotovich, F. E. Gray, D. Grigoriev, M. Grosse-Perdekamp, A. Grossmann, M. F. Hare, D. W. Hertzog, X. Huang, V. W. Hughes, M. Iwasaki, K. Jungmann, D. Kawall, and B. I. Khazin. Measurement of the negative muon anomalous magnetic moment to 0.7 ppm. *Phys. Rev. Lett.*, 92(16):161802, Apr 2004. (Cited on page 1.)
- [8] Q weak Collaboration. The Q-weak Experiment: "A Search for New Physics at the TeV Scale via a Measurement of the Proton's Weak Charge". Technical Report E05-008 Jeopardy proposal, December 2007. (Cited on pages 4, 5, 17, 19, 21, 86, 94, and 125.)
- [9] E. Klempert. Baryon resonances and strong QCD. 2002. (Cited on page 7.)
- [10] John Leacock. *Measuring the Weak Charge of the Proton and the Hadronic Parity Violation of the  $N \rightarrow \Delta$  Transition*. PhD thesis, Virginia Polytechnic Institute & State University, Blacksburg, VA 24061-0002, USA, October 2012. (Cited on pages 7, 41, 86, and 113.)
- [11] Nimai C. Mukhopadhyay, M.J. Ramsey-Musolf, Steven J. Pollock, Jn Lu, and H.-W. Hammer. Parity-violating excitation of the  $\delta(1232)$ : hadron structure and new physics. *Nuclear Physics A*, 633(3):481 – 518, 1998. (Cited on page 8.)

- [12] Shi-Lin Zhu, C. M. Maekawa, G. Sacco, B. R. Holstein, and M. J. Ramsey-Musolf. Electroweak radiative corrections to parity-violating electroexcitation of the  $\delta$ . *Phys. Rev. D*, 65:033001, Dec 2001. (Cited on page 8.)
- [13] J. Arrington, P.G. Blunden, and W. Melnitchouk. Review of two-photon exchange in electron scattering. *Progress in Particle and Nuclear Physics*, 66(4):782 – 833, 2011. (Cited on pages 8 and 12.)
- [14] M. K. Jones, K. A. Aniol, F. T. Baker, J. Berthot, P. Y. Bertin, W. Bertozzi, A. Besson, L. Bimbot, W. U. Boeglin, E. J. Brash, D. Brown, J. R. Calarco, L. S. Cardman, C.-C. Chang, J.-P. Chen, E. Chudakov, S. Churchwell, E. Cisbani, D. S. Dale, R. De Leo, A. Deur, B. Diederich, J. J. Domingo, M. B. Epstein, L. A. Ewell, K. G. Fissum, A. Fleck, H. Fonvieille, S. Frullani, J. Gao, F. Garibaldi, A. Gasparian, G. Gerstner, S. Gilad, R. Gilman, A. Glamazdin, C. Glashausser, J. Gomez, V. Gorbenko, A. Green, J.-O. Hansen, C. R. Howell, G. M. Huber, M. Iodice, C. W. de Jager, S. Jaminion, X. Jiang, W. Kahl, J. J. Kelly, M. Khayat, L. H. Kramer, G. Kumbartzki, M. Kuss, E. Lakuriki, G. Lavessière, J. J. LeRose, M. Liang, R. A. Lindgren, N. Liyanage, G. J. Lolos, R. Macri, R. Madey, S. Malov, D. J. Margaziotis, P. Markowitz, K. McCormick, J. I. McIntyre, R. L. J. van der Meer, R. Michaels, B. D. Milbrath, J. Y. Mougey, S. K. Nanda, E. A. J. M. Offermann, Z. Papandreou, C. F. Perdrisat, G. G. Petratos, N. M. Piskunov, R. I. Pomatsalyuk, D. L. Prout, V. Punjabi, G. Quéméner, R. D. Ransome, B. A. Raue, Y. Roblin, R. Roche, G. Rutledge, P. M. Rutt, A. Saha, T. Saito, A. J. Sarty, T. P. Smith, P. Sorokin, S. Strauch, R. Suleiman, K. Takahashi, J. A. Templon, L. Todor, P. E. Ulmer, G. M. Urciuoli, P. Vernin, B. Vlahovic, H. Voskanyan, K. Wijesooriya, B. B. Wojtsekhowski, R. J. Woo, F. Xiong, G. D. Zainea, and Z.-L. Zhou.  $g_{EP}/g_{MP}$  ratio by polarization transfer in e(pol.) p -> e p(pol.). *Phys. Rev. Lett.*, 84:1398–1402, Feb 2000. (Cited on pages 8 and 10.)
- [15] O. Gayou, K. A. Aniol, T. Averett, F. Benmokhtar, W. Bertozzi, L. Bimbot, E. J. Brash, J. R. Calarco, C. Cavata, Z. Chai, C.-C. Chang, T. Chang, J.-P. Chen, E. Chudakov, R. De Leo, S. Dieterich, R. Endres, M. B. Epstein, S. Escoffier, K. G. Fissum, H. Fonvieille, S. Frullani, J. Gao, F. Garibaldi, S. Gilad, R. Gilman, A. Glamazdin, C. Glashausser, J. Gomez, V. Gorbenko, J.-O. Hansen, D. W. Higinbotham, G. M. Huber, M. Iodice, C. W. de Jager, X. Jiang, M. K. Jones, J. J. Kelly, M. Khandaker, A. Kozlov, K. M. Kramer, G. Kumbartzki, J. J. LeRose, D. Lhuillier, R. A. Lindgren, N. Liyanage, G. J. Lolos, D. J. Margaziotis, F. Marie, P. Markowitz, K. McCormick, R. Michaels, B. D. Milbrath, S. K. Nanda, D. Neyret, Z. Papan-

- dreou, L. Pentchev, C. F. Perdrisat, N. M. Piskunov, V. Punjabi, T. Pussieux, G. Quéméner, R. D. Ransome, B. A. Raue, R. Roché, M. Rvachev, A. Saha, C. Salgado, S. Širca, I. Sitnik, S. Strauch, L. Todor, E. Tomasi-Gustafsson, G. M. Urciuoli, H. Voskanyan, K. Wijesooriya, B. B. Wojtsekhowski, X. Zheng, and L. Zhu. Measurement of  $G_{E_p}/G_{M_p}$  in e(pol)p->ep(pol) to  $q^2 = 5.6\text{gev}^2$ . *Phys. Rev. Lett.*, 88:092301, Feb 2002. (Cited on pages 8 and 10.)
- [16] L. Andivahis, P. E. Bosted, A. Lung, L. M. Stuart, J. Alster, R. G. Arnold, C. C. Chang, F. S. Dietrich, W. Dodge, R. Gearhart, J. Gomez, K. A. Griffioen, R. S. Hicks, C. E. Hyde-Wright, C. Keppel, S. E. Kuhn, J. Lichtenstadt, R. A. Miskimen, G. A. Peterson, G. G. Petratos, S. E. Rock, S. Rokni, W. K. Sakumoto, M. Spengos, K. Swartz, Z. Szalata, and L. H. Tao. Measurements of the electric and magnetic form factors of the proton from  $q^2=1.75$  to  $8.83(\text{gev}/c)^2$ . *Phys. Rev. D*, 50:5491–5517, Nov 1994. (Cited on pages 8 and 10.)
- [17] M. E. Christy, A. Ahmidouch, C. S. Armstrong, J. Arrington, R. Asaturyan, S. Avery, O. K. Baker, D. H. Beck, H. P. Blok, C. W. Bochna, W. Boeglin, P. Bosted, M. Bouwhuis, H. Breuer, D. S. Brown, A. Bruell, R. D. Carlini, N. S. Chant, A. Cochran, L. Cole, S. Danagoulian, D. B. Day, J. Dunne, D. Dutta, R. Ent, H. C. Fenker, B. Fox, L. Gan, H. Gao, K. Garrow, D. Gaskell, A. Gasparian, D. F. Geesaman, P. L. J. Guèye, M. Harvey, R. J. Holt, X. Jiang, C. E. Keppel, E. Kinney, Y. Liang, W. Lorenzon, A. Lung, P. Markowitz, J. W. Martin, K. McIlhany, D. McKee, D. Meekins, M. A. Miller, R. G. Milner, J. H. Mitchell, H. Mkrtchyan, B. A. Mueller, A. Nathan, G. Niculescu, I. Niculescu, T. G. O'Neill, V. Papavassiliou, S. F. Pate, R. B. Piercy, D. Potterveld, R. D. Ransome, J. Reinhold, E. Rollinde, P. Roos, A. J. Sarty, R. Sawafta, E. C. Schulte, E. Segbefia, C. Smith, S. Stepanyan, S. Strauch, V. Tadevosyan, L. Tang, R. Tieulent, A. Uzzle, W. F. Vulcan, S. A. Wood, F. Xiong, L. Yuan, M. Zeier, B. Zihlmann, and V. Ziskin. Measurements of electron-proton elastic cross sections for  $0.4 < Q^2 < 5.5 (\text{GeV}/c)^2$ . *Phys. Rev. C*, 70:015206, Jul 2004. (Cited on page 8.)
- [18] J. Arrington. New measurement of G(E) / G(M) for the proton. 2003. (Cited on page 8.)
- [19] P. A. M. Guichon and M. Vanderhaeghen. How to reconcile the rosenbluth and the polarization transfer methods in the measurement of the proton form factors. *Phys. Rev. Lett.*, 91:142303, Oct 2003. (Cited on page 8.)
- [20] S. Kondratyuk, P. G. Blunden, W. Melnitchouk, and J. A. Tjon.  $\delta$  resonance contribution to two-photon exchange in electron-proton scattering. *Phys. Rev. Lett.*, 95:172503, Oct 2005. (Cited on pages 10 and 11.)

- [21] R. C. Walker, B. W. Filippone, J. Jourdan, R. Milner, R. McKeown, D. Potterveld, L. Andivahis, R. Arnold, D. Benton, P. Bosted, G. deChambrier, A. Lung, S. E. Rock, Z. M. Szalata, A. Para, F. Dietrich, K. Van Bibber, J. Button-Shafer, B. Debebe, R. S. Hicks, S. Dasu, P. de Barbaro, A. Bodek, H. Harada, M. W. Krasny, K. Lang, E. M. Riordan, R. Gearhart, L. W. Whitlow, and J. Alster. Measurements of the proton elastic form factors for  $1 \leq Q^2 \leq 3$  (gev/c) $^2$  at slac. *Phys. Rev. D*, 49:5671–5689, Jun 1994. (Cited on page 10.)
- [22] I. A. Qattan, J. Arrington, R. E. Segel, X. Zheng, K. Aniol, O. K. Baker, R. Beams, E. J. Brash, J. Calarco, A. Camsonne, J.-P. Chen, M. E. Christy, D. Dutta, R. Ent, S. Frullani, D. Gaskell, O. Gayou, R. Gilman, C. Glashausser, K. Hafidi, J.-O. Hansen, D. W. Higinbotham, W. Hinton, R. J. Holt, G. M. Huber, H. Ibrahim, L. Jisonna, M. K. Jones, C. E. Keppel, E. Kinney, G. J. Kumbartzki, A. Lung, D. J. Margaziotis, K. McCormick, D. Meekins, R. Michaels, P. Monaghan, P. Moussiegt, L. Pentchev, C. Perdrisat, V. Punjabi, R. Ransome, J. Reinhold, B. Reitz, A. Saha, A. Sarty, E. C. Schulte, K. Slifer, P. Solvignon, V. Sulkosky, K. Wijesooriya, and B. Zeidman. Precision rosenbluth measurement of the proton elastic form factors. *Phys. Rev. Lett.*, 94:142301, Apr 2005. (Cited on page 10.)
- [23] P. G. Blunden, W. Melnitchouk, and J. A. Tjon. Two-photon exchange and elastic electron-proton scattering. *Phys. Rev. Lett.*, 91:142304, Oct 2003. (Cited on page 10.)
- [24] S. Kondratyuk, P.G. Blunden, W. Melnitchouk, and J.A. Tjon. Two-photon exchange in elastic and inelastic electron-proton scattering. *AIP Conf.Proc.*, 842:336–338, 2006. (Cited on page 10.)
- [25] Megh Raj Niroula. *Beyond the Born Approximation: a Precise Comparison of e+p and e-p Elastic Scattering in the CEBAF Large Acceptance Spectrometer (CLAS)*. PhD thesis, Old Dominion University, VA, May 2010. (Cited on page 10.)
- [26] Gary K. Greenhut. Two-photon exchange in electron-proton scattering. *Phys. Rev.*, 184:1860–1867, Aug 1969. (Cited on page 11.)
- [27] J. Arrington, W. Melnitchouk, and J. A. Tjon. Global analysis of proton elastic form factor data with two-photon exchange corrections. *Phys. Rev. C*, 76:035205, Sep 2007. (Cited on page 11.)

- [28] S. Kondratyuk and P. G. Blunden. Contribution of spin 1/2 and 3/2 resonances to two-photon exchange effects in elastic electron-proton scattering. *Phys. Rev. C*, 75:038201, Mar 2007. (Cited on page 12.)
- [29] M. Gorchtein, P.A.M. Guichon, and M. Vanderhaeghen. Normal spin asymmetries in elastic electron-proton scattering. *Nuclear Physics A*, 755(0):273 – 276, 2005. Proceedings of the 10th International Conference on the Structure of Baryons. (Cited on page 13.)
- [30] Juliette Mammei. *Parity-Violating Elastic Electron Nucleon Scattering: Measurement of the Strange Quark Content of the Nucleon and Towards a Measurement of the Weak Charge of the Proton*. PhD thesis, Virginia Polytechnic Institute & State University, Blacksburg, VA 24061-0002, USA, April 2010. (Cited on pages 13 and 36.)
- [31] M Gorchtein, P.A.M Guichon, and M Vanderhaeghen. Beam normal spin asymmetry in elastic lepton-nucleon scattering. *Nuclear Physics A*, 741(0):234 – 248, 2004. (Cited on page 13.)
- [32] Carl E. Carlson and Marc Vanderhaeghen. Two-photon physics in hadronic processes. *Annual Review of Nuclear and Particle Science*, 57(1):171–204, 2007. (Cited on page 13.)
- [33] B. Pasquini and M. Vanderhaeghen. Resonance estimates for single spin asymmetries in elastic electron-nucleon scattering. *Phys. Rev. C*, 70:045206, Oct 2004. (Cited on page 14.)
- [34] B. Pasquini and M. Vanderhaeghen. Single spin asymmetries in elastic electron-nucleon scattering. *Eur Phys J*, 24:29–32, 2005. (Cited on page 14.)
- [35] M. Gorchtein. Beam normal spin asymmetry in the quasireal compton scattering approximation. *Phys. Rev. C*, 73:055201, May 2006. (Cited on page 15.)
- [36] Jorge Segovia, Chen Chen, IanC. Clot, CraigD. Roberts, SebastianM. Schmidt, and Shaolong Wan. Elastic and transition form factors of the delta(1232). *Few-Body Systems*, 55(1):1–33, 2014. (Cited on page 15.)
- [37] G. Ramalho, M. T. Peña, and A. Stadler. Shape of the  $\delta$  baryon in a covariant spectator quark model. *Phys. Rev. D*, 86:093022, Nov 2012. (Cited on page 15.)
- [38] Constantia Alexandrou, Tomasz Korzec, Giannis Koutsou, Cdric Lorc, John W. Negele, Vladimir Pascalutsa, Antonios Tsapalis, and Marc Vanderhaeghen. Quark transverse charge densities in the from lattice {QCD}. *Nuclear Physics A*, 825(1-2):115 – 144, 2009. (Cited on pages 15 and 120.)

- [39] Barbara Pasquini. Two-Photon Physics: Theory. MAMI and Beyond: <http://wwwkph.kph.uni-mainz.de/T//MAMIandBeyond/02%20Dienstag/08%20Pasquini.pdf>, April 2009. (Cited on pages 16 and 120.)
- [40] Carl Carlson. BSA.NΔ@Qweak. <https://qweak.jlab.org/doc-private>ShowDocument?docid=2060>, August 2014. (Cited on page 17.)
- [41] Thomas Jefferson National Accelerator Facility. <http://www.jlab.org/>. (Cited on page 19.)
- [42] Q weak Collaboration. The Q-Weak Experiment: A search for New Physics at the TeV Scale via a Measurement of the Proton's Weak Charge. Technical Report E02-020 proposal, December 2001. (Cited on page 19.)
- [43] Q weak Collaboration. The Q-weak Experiment: "A Search for New Physics at the TeV Scale via a Measurement of the Proton's Weak Charge". Technical Report E05-008 Jeopardy proposal, December 2004. (Cited on page 19.)
- [44] E.J. Beise, M.L. Pitt, and D.T. Spayde. The sample experiment and weak nucleon structure. *Progress in Particle and Nuclear Physics*, 54(1):289 – 350, 2005. (Cited on page 19.)
- [45] D. S. Armstrong, J. Arvieux, R. Asaturyan, T. Averett, S. L. Bailey, G. Batigne, D. H. Beck, E. J. Beise, J. Benesch, L. Bimbot, J. Birchall, A. Biselli, P. Bosted, E. Boukobza, H. Breuer, R. Carlini, R. Carr, N. Chant, Y.-C. Chao, S. Chatopadhyay, R. Clark, S. Covrig, A. Cowley, D. Dale, C. Davis, W. Falk, J. M. Finn, T. Forest, G. Franklin, C. Furget, D. Gaskell, J. Grames, K. A. Griffioen, K. Grimm, B. Guillon, H. Guler, L. Hannelius, R. Hasty, A. Hawthorne Allen, T. Horn, K. Johnston, M. Jones, P. Kammel, R. Kazimi, P. M. King, A. Kolarkar, E. Korkmaz, W. Korsch, S. Kox, J. Kuhn, J. Lachniet, L. Lee, J. Lenoble, E. Litard, J. Liu, B. Loupias, A. Lung, G. A. MacLachlan, D. Marchand, J. W. Martin, K. W. McFarlane, D. W. McKee, R. D. McKeown, F. Merchez, H. Mkrtchyan, B. Moffit, M. Morlet, I. Nakagawa, K. Nakahara, M. Nakos, R. Neveling, S. Niccolai, S. Ong, S. Page, V. Papavassiliou, S. F. Pate, S. K. Phillips, M. L. Pitt, M. Poelker, T. A. Porcelli, G. Quéméner, B. Quinn, W. D. Ramsay, A. W. Rauf, J.-S. Real, J. Roche, P. Roos, G. A. Rutledge, J. Secrest, N. Simicevic, G. R. Smith, D. T. Spayde, S. Stepanyan, M. Stutzman, V. Sulaksky, V. Tadevosyan, R. Tieulent, J. van de Wiele, W. van Oers, E. Voutier, W. Vulcan, G. Warren, S. P. Wells, S. E. Williamson, S. A. Wood, C. Yan, J. Yun, and V. Zeps. Strange-quark contributions to parity-violating asymmetries in the forward g0 electron-proton scattering experiment. *Phys. Rev. Lett.*, 95:092001, Aug 2005. (Cited on page 19.)

- [46] K. A. Aniol, D. S. Armstrong, T. Averett, H. Benaoum, P. Y. Bertin, E. Burtin, J. Cahoon, G. D. Cates, C. C. Chang, Y.-C. Chao, J.-P. Chen, Seonho Choi, E. Chudakov, B. Craver, F. Cusanno, P. Decowski, D. Deepa, C. Ferdi, R. J. Feuerbach, J. M. Finn, S. Frullani, K. Fuoti, F. Garibaldi, R. Gilman, A. Glamazdin, V. Gorbenko, J. M. Grames, J. Hansknecht, D. W. Higinbotham, R. Holmes, T. Holmstrom, T. B. Humensky, H. Ibrahim, C. W. de Jager, X. Jiang, L. J. Kaufman, A. Kelleher, A. Kolarkar, S. Kowalski, K. S. Kumar, D. Lambert, P. LaViolette, J. LeRose, D. Lhuillier, N. Liyanage, D. J. Margaziotis, M. Mazouz, K. McCormick, D. G. Meekins, Z.-E. Meziani, R. Michaels, B. Moffit, P. Monaghan, C. Munoz-Camacho, S. Nanda, V. Nelyubin, D. Neyret, K. D. Paschke, M. Poelker, R. Poletsalyuk, Y. Qiang, B. Reitz, J. Roche, A. Saha, J. Singh, R. Snyder, P. A. Souder, R. Subedi, R. Suleiman, V. Sulkosky, W. A. Tobias, G. M. Urciuoli, A. Vacheret, E. Voutier, K. Wang, R. Wilson, B. Wojtsekhowski, and X. Zheng. Parity-violating electron scattering from  ${}^4\text{He}$  and the strange electric form factor of the nucleon. *Phys. Rev. Lett.*, 96:022003, Jan 2006. (Cited on page 19.)
- [47] D. Androic et al. First Determination of the Weak Charge of the Proton. 2013. (Cited on page 21.)
- [48] Nuruzzaman. Qweak: First direct measurement of the weak charge of the proton. *EPJ Web of Conferences*, 71:00100, 2014. (Cited on page 21.)
- [49] C. W. Leemann, D. R. Douglas, and G. A. Krafft. "The Continuous Electron Beam Accelerator Facility: CEBAF at the Jefferson Laboratory". Annual review of nuclear and particle science, vol. 51, no. 1, pp. 413-450, 2001. (Cited on pages 22 and 24.)
- [50] 12 GeV Upgrade: Future Science at Jefferson Lab. <http://www.jlab.org/12GeV/index.html>. (Cited on page 23.)
- [51] B. Poelker. Q-weak e-Source Issues. Q-weak Collaboration Meeting, Q-weak- DocDB1436: <https://qweak.jlab.org/doc-private>ShowDocument?docid=1436>, June 2011. (Cited on page 23.)
- [52] C. Hernandez-Garcia, P. G. O'Shea, and M. L. Stutzman. *Electron sources for accelerators*. Physics Today, February 2008. (Cited on page 24.)

- [53] J. Grames, P. Adderley, J. Benesch, J. Clark, J. Hansknecht, R. Kazimi, D. Machie, M. Poelker, M. Stutzman, R. Suleiman, and Y. Zhang. Two wien filter spin flipper. *Particle Accelerator Conference Proceedings*, page 862, 2011. (Cited on page 24.)
- [54] Kathrine Myers. *The First Determination of the Proton's Weak Charge Through Parity-Violating Asymmetry Measurements in Elastic e+p and e+Al Scattering*. PhD thesis, The George Washington University, Washington, DC 20052, USA, May 2012. (Cited on pages 24, 28, 34, 36, and 111.)
- [55] Nuruzzaman and *et. all.* List of Beam Components & Critical BPMs. Technical Report Qweak-DocDB-1203, Feb 2010. (Cited on page 25.)
- [56] Sarah Phillips. *Measurement of the Strange Quark Contribution to the Vector Structure of the Proton*. PhD thesis, College of William and Mary, Virginia, Nov 2007. (Cited on page 26.)
- [57] G. Krafft and A. Hofler. How the Linac Beam Position Monitors Work. CEBAF Technical Note CEBAF-TN-93-004, 1993. (Cited on page 26.)
- [58] Andrew James Ruehe Puckett. *Recoil Polarization Measurements of the Proton Electromagnetic Form Factor Ratio to High Momentum Transfer*. PhD thesis, Massachusetts Institute of Technology, MA, Feb 2010. (Cited on page 27.)
- [59] M. Hauger, A. Honegger, J. Jourdan, G. Kubon, T. Petitjean, D. Rohe, I. Sick, G. Warren, H. Whrle, J. Zhao, R. Ent, J. Mitchell, D. Crabb, A. Tobias, M. Zeier, and B. Zihlmann. A high-precision polarimeter. *Nuclear Instruments and Methods in Physics Research Section A: Accelerators, Spectrometers, Detectors and Associated Equipment*, 462(3):382 – 392, 2001. (Cited on page 27.)
- [60] Paul Gueye. Status of the actual beam position monitors in the Hall C beamline. CEBAF Technical Note Unpublished internal document, December 1995. (Cited on page 27.)
- [61] Nuruzzaman and *et. all.* Position and Angle Determination at the  $Q_{\text{weak}}^p$  Target for Beam Modulation. Technical Report Qweak-DocDB-1208, March 2010. Used as a reference for how the position and angle determination at the target for beam modulation in the  $Q_{\text{weak}}^p$  experiment. (Cited on pages 27, 53, and 85.)
- [62] William R. Leo. *Techniques for Nuclear and Particle Physics Experiments: A How-to Approach*. Springer, Berlin, second revised edition, February 1994. (Cited on page 27.)

- [63] Buddhini Waidyawansa. *A 3% Measurement of the Beam Normal Single Spin Asymmetry in Forward Angle Elastic Electron-Proton Scattering using the Qweak Setup*. PhD thesis, Ohio University, Athens OH 45701, USA, August 2013. (Cited on pages 27, 42, 44, 81, 85, 99, 116, and 117.)
- [64] Benjamin Micheal Patrick Clasie. *Measurement of Nuclear Transparency from  $A(e, e'\pi^+)$  Reactions*. PhD thesis, Massachusetts Institute of Technology, MA, Aug 2006. (Cited on page 27.)
- [65] Nuruzzaman. Effective Kaon-Nucleon Cross Section from Nuclear Transparency Measured in the  $A(ee'K^+)$  Reaction. Master's thesis, Mississippi State University, MS, Aug 2010. (Cited on page 27.)
- [66] Ramesh Subedi. Summary report on the BCMs for QWEAK. Technical Report Qweak-DocDB-1777, January 2013. (Cited on page 28.)
- [67] C. Yan, R. Carlini, and D. Neuffer. Beam energy measurement using the Hall C beamline. *Conf.Proc.*, C930517:2136–2138, 1993. (Cited on page 28.)
- [68] C. Yan, P. Adderley, D. Barker, J. Beaufait, K. Capek, R. Carlini, J. Dahlberg, E. Feldl, K. Jordan, B. Kross, W. Oren, R. Wojcik, and J. VanDyke. Superharp- a wire scanner with absolute position readout for beam energy measurement at {CEBAF}. *Nuclear Instruments and Methods in Physics Research Section A: Accelerators, Spectrometers, Detectors and Associated Equipment*, 365(2?3):261 – 267, 1995. (Cited on page 28.)
- [69] Valery Lebedev. OPTIM: Computer code for linear and non-linear optics calculations. <http://www-bdnew.fnal.gov/pbar/organizationalchart/lebedev/OptiM/optim.htm>, June 2007. (Cited on pages 29, 49, 84, 123, and 124.)
- [70] Nuruzzaman and *et. all.* Beam Modulation in the 3C Line for the  $Q_{weak}^p$  Experiment. Hall-C Technical Note Qweak-DocDB-XXXX, Jun 2009. Beam Modulation write up for  $Q_{weak}^p$  experiment. (Cited on page 29.)
- [71] V. Lebedev R. Dickson. Fast Feedback System for Energy and Beam Stabilization. Technical Report JLAB-ACE-99-10, Jefferson Lab, Newport News, VA, 1999. (Cited on pages 30 and 50.)
- [72] B. Bevins. A Distributed Feedback System for Rapid Stabilazation of Arbitrary Process Variables. Technical Report JLAB-ACE-01-09, Jefferson Lab, Newport News, VA. (Cited on pages 30 and 50.)

- [73] M. Hauger, A. Honegger, J. Jourdan, G. Kubon, T. Petitjean, D. Rohe, I. Sick, G. Warren, H. Whrle, J. Zhao, R. Ent, J. Mitchell, D. Crabb, A. Tobias, M. Zeier, and B. Zihlmann. A high-precision polarimeter. *Nuclear Instruments and Methods in Physics Research Section A: Accelerators, Spectrometers, Detectors and Associated Equipment*, 462(3):382 – 392, 2001. (Cited on page 30.)
- [74] Matthias Loppacher. *Moller polarimeter for CEBAF Hall-C*. PhD thesis, University of Basel, Basel, April 1996. (Cited on page 31.)
- [75] Rakitha Beminiwattha. *A Measurement of the Weak Charge of the Proton through Parity Violating Electron Scattering using the Qweak Apparatus: A 21% Result*. PhD thesis, Ohio University, Athens OH 45701, USA, August 2013. (Cited on pages 31, 42, 43, and 103.)
- [76] A. Narayan. Precision Compton Polarimetry During the Qweak Experiment. DNP 2012 Conference, Q-weak-DocDB1732: <https://qweak.jlab.org/doc-private>ShowDocument?docid=1732>, October 2012. (Cited on page 31.)
- [77] Amrendra Narayan. *Electron Detector in Compton polarimeter for CEBAF Hall-C*. PhD thesis, Mississippi State University, Mississippi State, MS, April 2013. (Cited on page 32.)
- [78] Juan Carlos Cornejo. *Photon Detector in Compton polarimeter for CEBAF Hall-C*. PhD thesis, College of William and Mary, Williamsburg, VA, USA, April 2014. (Cited on page 32.)
- [79] Gregory Smith, Silviu Covrig, and Jim Dunne. "Qweak Liquid Hydrogen Target: Preliminary Design & Safety Document". Technical Report Qweak-DocDB-1041, August 2009. (Cited on page 32.)
- [80] ANSYS: A fluid dynamics simulation code. <http://www.ansys.com/>. (Cited on page 34.)
- [81] Gregory Smith. "Optics Target". Technical Report Qweak-DocDB-1144, December 2009. (Cited on page 35.)
- [82] Peiqing Wang. Magnetic Field Simulation and Mapping for the  $Q_{Weak}^p$  Experiment. Master's thesis, University of Manitoba, Winnipeg, Manitoba, Canada, 2009. (Cited on page 36.)
- [83] Lake Shore Cryotronics Inc., 575 McCorkle Boulevard, Westerville, OH 43082. *Gaussmeter Hall Probes*. (Cited on page 37.)
- [84] Nuruzzaman. Hall Probe Mount Design for QTOR. Technical Report Qweak-DocDB-1244, May 2010. (Cited on page 37.)

- [85] Peiqing Wang. Simulated elastic flux images on main bars. ELOG-Analysis-588: <https://qweak.jlab.org/elog/Analysis+&+Simulation/588>, May 2012. (Cited on page 39.)
- [86] Jie Pan. *Towards a Precision Measurement of Parity-Violating e-p Elastic Scattering at Low Momentum Transfer*. PhD thesis, University of Manitoba, Winnipeg, Manitoba, Canada, June 2012. (Cited on pages 39, 40, and 42.)
- [87] Peiqing Wang. *A Measurement Of The Protons Weak Charge Using An Integration Cerenkov Detector System*. PhD thesis, University of Manitoba, Winnipeg, Manitoba, Canada, June 2011. (Cited on page 38.)
- [88] TRIUMF: Canada's national laboratory for particle and nuclear physics. <http://www.triumf.ca/>. (Cited on pages 40 and 59.)
- [89] B. Roberts and H. Hui. *VME QWEAK 8 Channel 18-bit ADC*. TRIUMF, rev 1 edition, November 2007. (Cited on pages 40 and 59.)
- [90] John Lackey. *The First Direct Measurement of the Weak Charge of the Proton*. PhD thesis, College of William and Mary, Williamsburg, VA, USA, October 2011. (Cited on page 41.)
- [91] Jlab DAQ Group. CEBAF Online Data Acquisition. [https://coda.jlab.org/wiki/index.php/Main\\_Page](https://coda.jlab.org/wiki/index.php/Main_Page). (Cited on page 42.)
- [92] P. Banta, J. Chen, W.G. Heyes, E. Jastrzembski, C. Timmer, et al. The Front end readout control software for the CODA data acquisition toolkit. 1997. (Cited on page 42.)
- [93] Brad Sawatzky. Private communication, 2009-2011. (Cited on page 42.)
- [94] Nuruzzaman and Greg Smith. Hall-C Target Status Page. <https://hallcweb.jlab.org/poltar/>. (Cited on page 43.)
- [95] Nuruzzaman. Beam Modulation Website: Hall-C Beamline Optics. <https://hallcweb.jlab.org/qweak/bmod/>. (Cited on page 43.)
- [96] Dave Mack. Private communication, 2009-2013. (Cited on page 45.)
- [97] A. Acha, K. A. Aniol, D. S. Armstrong, J. Arrington, T. Averett, S. L. Bailey, J. Barber, A. Beck, H. Benaoum, J. Benesch, P. Y. Bertin, P. Bosted, F. Butaru, E. Burtin, G. D. Cates, Y.-C. Chao, J.-P. Chen, E. Chudakov, E. Cisbani, B. Craver, F. Cusanno, R. De Leo, P. Decowski, A. Deur, R. J. Feuerbach, J. M. Finn, S. Frullani, S. A. Fuchs, K. Fuoti, R. Gilman,

- L. E. Glesener, K. Grimm, J. M. Grames, J. O. Hansen, J. Hansknecht, D. W. Higinbotham, R. Holmes, T. Holmstrom, H. Ibrahim, C. W. de Jager, X. Jiang, J. Katich, L. J. Kaufman, A. Kelleher, P. M. King, A. Kolarkar, S. Kowalski, E. Kuchina, K. S. Kumar, L. Lagamba, P. LaViolette, J. LeRose, R. A. Lindgren, D. Lhuillier, N. Liyanage, D. J. Margaziotis, P. Markowitz, D. G. Meekins, Z.-E. Meziani, R. Michaels, B. Moffit, S. Nanda, V. Nelyubin, K. Otis, K. D. Paschke, S. K. Phillips, M. Poelker, R. Pomatsalyuk, M. Potokar, Y. Prok, A. Puckett, X. Qian, Y. Qiang, B. Reitz, J. Roche, A. Saha, B. Sawatzky, J. Singh, K. Slifer, S. Sirca, R. Snyder, P. Solvignon, P. A. Souder, M. L. Stutzman, R. Subedi, R. Suleiman, V. Sulkosky, W. A. Tobias, P. E. Ulmer, G. M. Urciuoli, K. Wang, A. Whitbeck, R. Wilson, B. Wojtsekhowski, H. Yao, Y. Ye, X. Zhan, X. Zheng, S. Zhou, and V. Ziskin. Precision measurements of the nucleon strange form factors at  $Q^2 \sim (\text{gev})^2$ . *Phys. Rev. Lett.*, 98:032301, Jan 2007. (Cited on pages 45 and 47.)
- [98] James Birchall. Updated Requirements on Beam Properties for Qweak, August 2008. Technical Report Qweak-DocDB-818, August 2008. (Cited on page 47.)
- [99] Jay Benesch. Private communication, 2009-2013. (Cited on page 49.)
- [100] Jay Benesch and Nuruzzaman. OptiM Deck for Beam Modulation in Hall-C beamline. Q-weak-DocDB1367: <https://qweak.jlab.org/doc-private>ShowDocument?docid=1367>, May 2011. (Cited on pages 49, 51, and 53.)
- [101] Michael Tiefenback. Private communication, 2009. (Cited on page 50.)
- [102] Nuruzzaman and *et. all.* How Beam Energy will be Identified in  $Q_{\text{weak}}^p$ . Technical Report Qweak-DocDB-1149, January 2010. Used as a reference for how the beam enegy will be identified in the  $Q_{\text{weak}}^p$  experiment. (Cited on page 54.)
- [103] Sarin Philip. JLab MAT (or HF) coil characteristics. DocDB-979: <http://qweak.jlab.org/doc-public>ShowDocument?docid=979>, June 2009. (Cited on page 55.)
- [104] Martin R. Kraimer. Experimental Physics and Industrial Control System (EPICS): Input / Output Controller (IOC) Application Developer's Guide. Technical Report APS Release 3.11.6, May 1994. (Cited on page 56.)
- [105] GE Fanuc. *VME-4145 4-Channel 16-bit Arbitrary Waveform Generator Board with Autocalibration*, first edition edition, June 2008. (Cited on page 56.)

- [106] KWord is an intuitive word processor and desktop publisher application. With it, you can create informative and attractive documents with pleasure and ease. <http://www.kde.org/applications/office/kword/>. (Cited on page 56.)
- [107] Chad Seaton. VME 16-Channel Relay Output Register. Technical Report Qweak-DocDB-XXXX, May 2009. (Cited on page 57.)
- [108] Nuruzzaman. An Update on Beam Modulation for the Q-weak Experiment. Q-weak Collaboration Meeting, Q-weak-DocDB1312: <https://qweak.jlab.org/doc-private>ShowDocument?docid=1312>, September 2010. (Cited on page 57.)
- [109] T. Allison, S. Higgins, E. Martin, W. Merz, and S. Philip. Jefferson lab's trim card ii. In *Particle Accelerator Conference, 2005. PAC 2005. Proceedings of the*, pages 3670–3672, May 2005. (Cited on page 57.)
- [110] LEM, West Lancashire Investment Centre, Skelmersdale, WN8 9TG, England. *Current Transducer CT 5..25-T*, 2006-2014. (Cited on page 58.)
- [111] Sarin Philip. Private communication, 2009-2010. (Cited on page 59.)
- [112] LEM, West Lancashire Investment Centre, Skelmersdale, WN8 9TG, England. *Current Transducer LA 55-P/SP1*, 2006-2014. (Cited on page 59.)
- [113] Nuruzzaman. LEM Current Transducer for the Beam Modulation System. Technical Report Qweak-DocDB-XXXX, February 2014. (Cited on page 59.)
- [114] David Armstrong. BMod energy modulation: indeed, needs FFB paused. HCLOG-249809: [https://hallcweb.jlab.org/hclog/1201\\_archive/120124094154.html](https://hallcweb.jlab.org/hclog/1201_archive/120124094154.html), January 2012. (Cited on page 60.)
- [115] Chad Seaton. VME 32-Channel ADC Module. Technical Report Qweak-DocDB-XXXX, May 2010. (Cited on page 59.)
- [116] Donald Jones. Ramp fill procedure documentation. ELOG-Analysis-948: <https://qweak.jlab.org/elog/Analysis++Simulation/948>, July 2013. (Cited on page 62.)
- [117] Nuruzzaman, Scott Higgins, Dave Mack, and Josh Hoskins. Beam Modulation Controls and Software Sketch for the Q-weak Experiment. Technical Report Qweak-DocDB-XXXX, May 2010. (Cited on pages 64 and 66.)

- [118] Scott Higgins. Private communication, 2009-2010. (Cited on page 64.)
- [119] Nuruzzaman and *et. all.* Beam Modulation GUI proposal. Technical Report Qweak-DocDB-1140, December 2009. Submitted to accelerator division of JLab and was used as a reference for control system of Beam Modulation in the  $Q_{weak}^p$  experiment. (Cited on pages 64 and 66.)
- [120] Nuruzzaman and *et. all.* Machine Protection Analysis of the Beam Modulation System for the  $Q_{weak}^p$  Experiment. Technical Report Qweak-DocDB-1207, March 2010. This analysis shows the worst case possibilities we can have during the experiment for Beam Modulation in  $Q_{weak}^p$  experiment. (Cited on page 68.)
- [121] K. Kumar *et al.* The MOLLER Experiment: Measurement Of Lepton Lepton Elastic Reactions. <http://hallaweb.jlab.org/collab/PAC/PAC37/C12-09-005-Moller.pdf>, December 2010. (Cited on pages 71 and 123.)
- [122] Nuruzzaman. Hall-A Beamline elements using Pass1 beam. MSU-ELOG-296: <http://urvashi.ph.msstate.edu:8080/mepgroup/296>, November 2012. (Cited on page 72.)
- [123] D. Androic, D. S. Armstrong, A. Asaturyan, T. Averett, J. Balewski, J. Beaufait, R. S. Beminiwattha, J. Benesch, F. Benmokhtar, J. Birchall, R. D. Carlini, G. D. Cates, J. C. Cornejo, S. Covrig, M. M. Dalton, C. A. Davis, W. Deconinck, J. Diefenbach, J. F. Dowd, J. A. Dunne, D. Dutta, W. S. Duvall, M. Elaasar, W. R. Falk, J. M. Finn, T. Forest, D. Gaskell, M. T. W. Gericke, J. Grames, V. M. Gray, K. Grimm, F. Guo, J. R. Hoskins, K. Johnston, D. Jones, M. Jones, R. Jones, M. Kargiantoulakis, P. M. King, E. Korkmaz, S. Kowalski, J. Leacock, J. Leckey, A. R. Lee, J. H. Lee, L. Lee, S. MacEwan, D. Mack, J. A. Magee, R. Mahurin, J. Mammei, J. W. Martin, M. J. McHugh, D. Meekins, J. Mei, R. Michaels, A. Micherdzinska, A. Mkrtchyan, H. Mkrtchyan, N. Morgan, K. E. Myers, A. Narayan, L. Z. Ndakum, V. Nelyubin, Nuruzzaman, W. T. H. van Oers, A. K. Opper, S. A. Page, J. Pan, K. D. Paschke, S. K. Phillips, M. L. Pitt, M. Poelker, J. F. Rajotte, W. D. Ramsay, J. Roche, B. Sawatzky, T. Seva, M. H. Shabestari, R. Silwal, N. Simicevic, G. R. Smith, P. Solvignon, D. T. Spayde, A. Subedi, R. Subedi, R. Suleiman, V. Tadevosyan, W. A. Tobias, V. Tvaskis, B. Waidyawansa, P. Wang, S. P. Wells, S. A. Wood, S. Yang, R. D. Young, and S. Zhamkochyan. The  $q_{weak}$  experimental apparatus. XXX(X):XX – XX, 2014. (Cited on pages 74, 75, and 76.)
- [124] Josh Hoskins. Effects of fitting BPM response with fixed phase. ELOG-Analysis-690: <https://qweak.jlab.org/elog/Analysis++Simulation/690>, August 2012. (Cited on page 79.)

- [125] Kent Paschke. Beam Modulation response with FFB interference. ELOG-Analysis-695: <https://qweak.jlab.org/elog/Analysis++Simulation/695>, August 2012. (Cited on page 79.)
- [126] Buddhini Waidyawansa. Beam Position and Angle Determination in Qweak. Technical Report Qweak-DocDB-1772, December 2012. (Cited on pages 82 and 85.)
- [127] John Leacock. Helicity Correlated Pedestal Differences for April 2011 from Qweak Run I. Technical report, VT, VA, Nov 2011. (Cited on page 86.)
- [128] P. Pébay. Formulas for robust, One-Pass Parallel Computation of Covariances and Arbitrary-Order Statistical Moments. Sandia Report SAND2008-6212, Sandia National Laboratories, 2008. (Cited on page 96.)
- [129] Jim Birchall. Effect of averaging over azimuthal angle. ELOG-Analysis-373: <https://qweak.jlab.org/elog/Analysis++Simulation/373>, June 2011. (Cited on page 99.)
- [130] Dave Mack. BCM Normalization Issues Part II: Calibrations and Linearity. Q-weak-DocDB1369: <https://qweak.jlab.org/doc-private>ShowDocument?docid=1369>, March 2011. (Cited on page 106.)
- [131] Dave Mack. Non-linearity Specification for the Qweak Detector Chain. Technical Report Qweak-DocDB-172, November 2004. (Cited on page 106.)
- [132] Joshua Magee. Private communication, 2014. (Cited on page 110.)
- [133] Nuruzzaman. Beam Polarization from Moller Polarimeter for Transverse Run-II Dataset. ELOG-Ancillary-91: <https://qweak.jlab.org/elog/Ancillary/91>, April 2014. (Cited on page 110.)
- [134] Joshua Magee. The Qweak Run 2 Moller Polarimetry Analysis. Technical Report Qweak-DocDB-1955, January 2014. (Cited on page 110.)
- [135] Nuruzzaman. Transverse Asymmetries for N-to-Delta in Nuclear Targets. ELOG-Ancillary-43: <https://qweak.jlab.org/elog/Ancillary/43>, July 2013. (Cited on page 110.)
- [136] E. D. Cooper and C. J. Horowitz. Vector analyzing power in elastic electron-nucleus scattering. *Phys. Rev. C*, 72:034602, Sep 2005. (Cited on pages 111 and 114.)
- [137] M. Gorchtein and C. J. Horowitz. Analyzing power in elastic scattering of electrons off a spin-0 target. *Phys. Rev. C*, 77:044606, Apr 2008. (Cited on pages 111 and 114.)

- [138] Josh Magee. Aluminum Status Qweak Collaboration Meeting. Hall C collaboration meeting, Q-weak-DocDB1891: <https://qweak.jlab.org/doc-private>ShowDocument?docid=1819>, April 2013. (Cited on page 111.)
- [139] Kent Paschke. Proposed Wien0 neutral beamline background correction. ELOG-Analysis-782: <https://qweak.jlab.org/elog/Analysis++Simulation/782>, October 2012. (Cited on page 113.)
- [140] Manolis Kargiantoulakis. Beamline Backgrounds Update. ELOG-Analysis-1191: <https://qweak.jlab.org/elog/Analysis++Simulation/1191>, July 2014. (Cited on page 113.)
- [141] Dave Mack. Wien0 Beamline Background Dilution Central Value and Uncertainty. ELOG-Analysis-784: <https://qweak.jlab.org/elog/Analysis++Simulation/784>, October 2012. (Cited on page 113.)
- [142] Dave Mack. Input file for Wien 0 elastic e+p asymmetry corrections (v11 frozen modulo unblinding). ELOG-Analysis-714: <https://qweak.jlab.org/elog/Analysis++Simulation/714>, September 2012. (Cited on page 113.)
- [143] Martin McHugh. Neutral Background Analysis. <https://qweak.jlab.org/doc-private>ShowDocument?docid=2072>, September 2014. (Cited on page 113.)
- [144] Rakitha S Beminiwattha. Main Detector Neutral Background Contribution. Technical Report Qweak-DocDB-1549, July 2012. (Cited on page 113.)
- [145] Adesh Subedi. Simulation of QTor scans using QWGEANT3. ELOG-Analysis-837: <https://qweak.jlab.org/elog/Analysis++Simulation/837>, December 2012. (Cited on pages 114 and 115.)
- [146] Buddhini Waidyawansa. Qweak Transverse Asymmetry Measurements. Hall C collaboration meeting, Q-weak-DocDB1961: <https://qweak.jlab.org/doc-private>ShowDocument?docid=1961>, February 2014. (Cited on page 114.)
- [147] D. Androic, D. S. Armstrong, A. Asaturyan, T. Averett, J. Balewski, J. Beaufait, R. S. Beminiwattha, J. Benesch, F. Benmokhtar, J. Birchall, R. D. Carlini, G. D. Cates, J. C. Cornejo, S. Covrig, M. M. Dalton, C. A. Davis, W. Deconinck, J. Diefenbach, J. F. Dowd, J. A. Dunne, D. Dutta, W. S. Duvall, M. Elaasar, W. R. Falk, J. M. Finn, T. Forest, D. Gaskell, M. T. W. Gericke, J. Grames, V. M. Gray, K. Grimm, F. Guo, J. R. Hoskins, K. Johnston, D. Jones,

- M. Jones, R. Jones, M. Kargiantoulakis, P. M. King, E. Korkmaz, S. Kowalski, J. Leacock, J. Leckey, A. R. Lee, J. H. Lee, L. Lee, S. MacEwan, D. Mack, J. A. Magee, R. Mahurin, J. Mammei, J. W. Martin, M. J. McHugh, D. Meekins, J. Mei, R. Michaels, A. Micherdzinska, A. Mkrtchyan, H. Mkrtchyan, N. Morgan, K. E. Myers, A. Narayan, L. Z. Ndakum, V. Nelyubin, Nuruzzaman, W. T. H. van Oers, A. K. Opper, S. A. Page, J. Pan, K. D. Paschke, S. K. Phillips, M. L. Pitt, M. Poelker, J. F. Rajotte, W. D. Ramsay, J. Roche, B. Sawatzky, T. Seva, M. H. Shabestari, R. Silwal, N. Simicevic, G. R. Smith, P. Solvignon, D. T. Spayde, A. Subedi, R. Subedi, R. Suleiman, V. Tadevosyan, W. A. Tobias, V. Tvaskis, B. Waidyawansa, P. Wang, S. P. Wells, S. A. Wood, S. Yang, R. D. Young, and S. Zhamkochyan. First determination of the weak charge of the proton. *Phys. Rev. Lett.*, 111:141803, Oct 2013. (Cited on page 114.)
- [148] Nuruzzaman. Comparison of H<sub>2</sub> Dilutions from Geant-III, IV, and Data at the Inelastic Peak. ELOG-Ancillary-59: <https://qweak.jlab.org/elog/Ancillary/59>, December 2013. (Cited on page 115.)
- [149] Haakon Olsen and L. C. Maximon. Photon and electron polarization in high-energy bremsstrahlung and pair production with screening. *Phys. Rev.*, 114:887–904, May 1959. (Cited on page 116.)
- [150] K. A. Aniol, D. S. Armstrong, M. Baylac, E. Burtin, J. Calarco, G. D. Cates, C. Cavata, J.-P. Chen, E. Chudakov, D. Dale, C. W. de Jager, A. Deur, P. Djawotho, M. B. Epstein, S. Escoffier, L. Ewell, N. Falletto, J. M. Finn, K. Fissum, A. Fleck, B. Frois, J. Gao, F. Garibaldi, A. Gasparian, G. M. Gerstner, R. Gilman, A. Glamazdin, J. Gomez, V. Gorbenko, O. Hansen, F. Hersman, R. Holmes, M. Holtrop, B. Humensky, S. Incerti, J. Jardillier, M. K. Jones, J. Jorda, C. Jutier, W. Kahl, D. H. Kim, M. S. Kim, K. Kramer, K. S. Kumar, M. Kuss, J. LeRose, M. Leuschner, D. Lhuillier, N. Liyanage, R. Lourie, R. Madey, D. J. Margaziotis, F. Marie, J. Martino, P. Mastromarino, K. McCormick, J. McIntyre, Z.-E. Meziani, R. Michaels, G. W. Miller, D. Neyret, C. Perdrisat, G. G. Petratos, R. Pomatsalyuk, J. S. Price, D. Prout, V. Punjabi, T. Pussieux, G. Quéméner, G. Rutledge, P. M. Rutt, A. Saha, P. A. Souder, M. Spradlin, R. Suleiman, J. Thompson, L. Todor, P. E. Ulmer, B. Vlahovic, K. Wijesooriya, R. Wilson, and B. Wojtsekowski. Measurement of the neutral weak form factors of the proton. *Phys. Rev. Lett.*, 82:1096–1100, Feb 1999. (Cited on page 116.)
- [151] K. A. Aniol, D. S. Armstrong, T. Averett, M. Baylac, E. Burtin, J. Calarco, G. D. Cates, C. Cavata, Z. Chai, C. C. Chang, J.-P. Chen, E. Chudakov, E. Cisbani, M. Coman, D. Dale,

- A. Deur, P. Djawotho, M. B. Epstein, S. Escoffier, L. Ewell, N. Falletto, J. M. Finn, K. Fissum, A. Fleck, B. Frois, S. Frullani, J. Gao, F. Garibaldi, A. Gasparian, G. M. Gerstner, R. Gilman, A. Glamazdin, J. Gomez, V. Gorbenko, O. Hansen, F. Hersman, D. W. Higinbotham, R. Holmes, M. Holtrop, T. B. Humensky, S. Incerti, M. Iodice, C. W. de Jager, J. Jardillier, X. Jiang, M. K. Jones, J. Jorda, C. Jutier, W. Kahl, J. J. Kelly, D. H. Kim, M.-J. Kim, M. S. Kim, I. Kominis, E. Kooijman, K. Kramer, K. S. Kumar, M. Kuss, J. LeRose, R. De Leo, M. Leuschner, D. Lhuillier, M. Liang, N. Liyanage, R. Lourie, R. Madey, S. Malov, D. J. Margaziotis, F. Marie, P. Markowitz, J. Martino, P. Mastromarino, K. McCormick, J. McIntyre, Z.-E. Meziani, R. Michaels, B. Milbrath, G. W. Miller, J. Mitchell, L. Morand, D. Neyret, C. Pedrisat, G. G. Petratos, R. Pomatsalyuk, J. S. Price, D. Prout, V. Punjabi, T. Pussieux, G. Quéméner, R. D. Ransome, D. Relyea, Y. Roblin, J. Roche, G. A. Rutledge, P. M. Rutt, M. Rvachev, F. Sabatie, A. Saha, P. A. Souder, M. Spradlin, S. Strauch, R. Suleiman, J. Templon, T. Teresawa, J. Thompson, R. Tieulent, L. Todor, B. T. Tonguc, P. E. Ulmer, G. M. Urciuoli, B. Vlahovic, K. Wijesooriya, R. Wilson, B. Wojtsekowski, R. Woo, W. Xu, I. Younus, and C. Zhang. Parity-violating electroweak asymmetry in  $\vec{e}p$  scattering. *Phys. Rev. C*, 69:065501, Jun 2004. (Cited on page 116.)
- [152] Peiqing Wang. Simulated octant-by-octant event rate, scattering angle and momentum transfer. ELOG-Analysis-589: <https://qweak.jlab.org/elog/Analysis+&+Simulation/589>, May 2012. (Cited on page 117.)
- [153] Nuruzzaman.  $Q^2$  for transverse N-to-Delta from GEANT-III. ELOG-Ancillary-44: <https://qweak.jlab.org/elog/Ancillary/44>, July 2013. (Cited on page 117.)
- [154] Andrei V. Afanasev and N.P. Merenkov. Collinear photon exchange in the beam normal polarization asymmetry of elastic electron?proton scattering. *Physics Letters B*, 599(1?2):48 – 54, 2004. (Cited on page 118.)
- [155] Nuruzzaman and Qweak Collaboration. Beam modulation system for the q-weak experiment at jefferson lab. *AIP Conference Proceedings*, 1560(1):240–242, 2013. (Cited on page 124.)
- [156] Constantia Alexandrou, Tomasz Korzec, Giannis Koutsou, Cedric Lorce, John W. Negele, et al. Quark transverse charge densities in the  $\Delta(1232)$  from lattice QCD. *Nucl.Phys.*, A825:115–144, 2009. (Cited on page 125.)
- [157] A. S. Carroll, I. H. Chiang, T. F. Kycia, K. K. Li, M. D. Marx, D. C. Rahm, W. F. Baker, D. P. Eartly, G. Giacomelli, A. M. Jonckheere, P. F. M. Koehler, P. O. Mazur, R. Rubinstein,

- and O. Fackler. Total cross sections of  $\pi$ ,  $k$ , p and on protons and deuterons between 200 and 370 (gev/c). *Phys. Lett. B.*, 80(4-5):423 – 427, 1979. (Cited on page 137.)
- [158] Nuruzzaman. Survey of Helicity Correlated Pedestal Differences for the Full Q-weak Data Set. Technical Report Qweak-DocDB-XXXX, June 2012. (Cited on page 147.)
- [159] Nuruzzaman. Q-weak Physics Meeting: Helicity Correlated Pedestal Differences for Wien 0 - 9. Q-weak Physics Meeting, Q-weak-DocDB1608: <https://qweak.jlab.org/doc-private>ShowDocument?docid=1608>, March 2012. (Cited on page 149.)
- [160] Nuruzzaman. Q-weak Physics Meeting: Pedestal Survey for the Q-weak Experiment. Q-weak Physics Meeting, Q-weak-DocDB1608: <https://qweak.jlab.org/doc-private>ShowDocument?docid=1678>, June 2012. (Cited on page 149.)
- [161] Private communication with Paul King. [pking@jlab.org](mailto:pking@jlab.org). (Cited on page 150.)

## Curriculum Vita

12000 Jefferson Ave, Suite 16, Newport News, VA 23606. (757) 952-6686. [nur@jlab.org](mailto:nur@jlab.org). [userweb.jlab.org/~nur](http://userweb.jlab.org/~nur)

### Education

Ph. D.	Hampton University, Hampton, VA, USA.	August, 2014
M. S.	Mississippi State University, Mississippi State, MS, USA.	August, 2010
M. Sc.	Indian Institute of Technology Roorkee, Uttarakhand, India.	May, 2007
B. Sc.	University of Kalyani, West Bengal, India.	May, 2005

### Professional Experience

Participated in the  $Q_{weak}^p$ (E02-020), PVDIS(E08-011), HKS(E05-115), HAPPEX-III(E05-109), d2n(E06-014), SANE(E07-003) and GEp-III(E04-108) experiments at Jefferson Lab, Newport News, VA

### Honors and Awards

- Received Junior Scientist Travel Award from Jefferson Science Associates (JSA) for the following conferences: International Conference on New Frontiers in Physics (ICNFP) 2013 at Kolymbari, Crete, Greece; Eleventh Conference on the Intersections of Particle and Nuclear Physics (CIPANP) 2012 at St. Petersburg, Florida, USA; 4th Canada-America-Mexico Graduate Students Physics Conference (CAM) 2009 at Acapulco, Guerrero, Mexico.
- Served as the Chairman for the Particle Physics I session in the 4th Canada- America- Mexico Graduate Students Physics Conference on October 22-24, 2009 at Acapulco, Guerrero, Mexico
- Received Merit-cum-means Scholarship from IIT Roorkee during M.Sc in 2005.
- Cleared entrance exam for IIT (JAM) in 2005 with all India rank 154.
- Selected for integrated Ph.D. at Indian School of Mines (ISM) in 2005 with all India rank 1.

### Selected Publications and Presentations

1. I. Korover *et al.* Approaching the nucleon-nucleon short-range repulsive core via the  ${}^4\text{He}(e,e' p\text{N})$  triple coincidence reaction. [arXiv:1401.6138](https://arxiv.org/abs/1401.6138) / To be published.
2. D. Wang *et al.* New Measurement of Parity Violation in Electron-Quark Scattering. *Nature* **506** (2014) 7486, 67-70.
3. D. Androic *et al.* First Determination of the Weak Charge of the Proton. *Phys. Rev. Lett.* **111**, 141803 (2013).
4. D. Wang *et al.* Measurement of the Parity-Violating Asymmetry in Electron-Deuteron Scattering in the Nucleon Resonance Region. *Phys.Rev.Lett.* **111** (2013) 082501.
5. X. Qiu *et al.* Direct Measurements of the Lifetime of Heavy Hypernuclei. [arXiv:1212.1133](https://arxiv.org/abs/1212.1133) / To be published.
6. S. Abrahamyan *et al.* New Measurements of the Transverse Beam Asymmetry for Elastic Electron Scattering from Selected Nuclei. *Phys.Rev.Lett.* **109** (2012) 192501.
7. S. Abrahamyan *et al.* Measurement of the Neutron Radius of  ${}^{208}\text{Pb}$  Through Parity-Violation in Electron Scattering. *Phys.Rev.Lett.* **108** (2012) 112502.
8. W. Luo *et al.* Polarization components in  $\pi^0$  photoproduction at photon energies up to 5.6 GeV. *Phys.Rev.Lett.* **108** (2012) 222004.
9. Z. Ahmed *et al.* New Precision Limit on the Strange Vector Form Factors of the Proton. *Phys.Rev.Lett.* **108** (2012) 102001.
10. Nuruzzaman *et al.* Nuclear transparency and effective kaon-nucleon cross section from the  $A(e, e' K^+)$  reaction. *Phys. Rev. C* **84**, 015210(2011).
11. M. Meziane *et al.* Search for effects beyond the Born approximation in polarization transfer observables in ep elastic scattering. *Phys. Rev. Lett.* **106**, 132501(2011).
12. A. J. R. Puckett *et al.* Recoil Polarization Measurements of the Proton Electromagnetic Form Factor Ratio to  $Q^2 = 8.5$  GeV $^2$ . *Phys. Rev. Lett.* **104**, 242301(2010).

## INDEX

- Absolute Beam Energy, 22
- Accelerator, 19
- ADC, 22, 34
- BCM, 22
  - Uncer, 22
- Beam Energy, 22
- Beam Modulation, 23, 102
- Beam Monitoring, 20
- Beamline, 19
- BPM, 20
  - target BPM, 21
- CEBAF, 15
- CODA, 21
- Collimator, 30
- Detector System, 32
- Energy Asymmetry, 23
- EPICS, 20
- False Asymmetry, 24
- Halo Monitors, 24
- Helicity, 64, 123
  - Helicity, 123
  - Helicity Corelated Pedestal Analysis, 123
  - Helicity Reversal, 16
- Luminosity Monitors, 34
- Main Čerenkov Detectors, 32
  - Focal Plane Scanner, 34
  - Low Noise Electronics, 34
- Pedestal, 73
- Polarimetry, 24
  - Compton, 25
  - Moller, 24
- Polarized Source, 16
  - Circularly polarized, 16
  - GaAs, 16
- Q-weak
  - Kinematics, 14
- QTOR, 116
  - Corrector magnet, 117
  - hall probe, 31, 116
- QTor, 30
- Raster, 28
  - Fast Raster, 28
- regression schemes, 124
- RF, 20
- Shielding, 30
- superconductor, 5
- Superharp, 21
- Targets, 26
  - Liquid Hydrogen Target, 27
  - Solid Target, 29
- TJNAF, 15
- TOSCA, 118
- voltage-to-frequency, 20